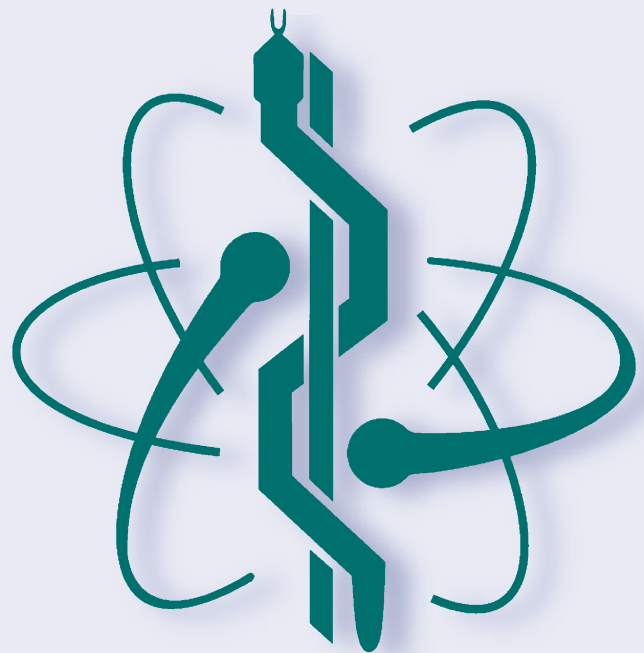# IFMBE Proceedings

Yuan-Ting Zhang · Paulo Carvalho
Ratko Magjarevic (Eds.)

Volume 64

International Conference on Biomedical and Health Informatics

ICBHI 2015, Haikou, China, 8–10 October 2015

Springer

IFMBE Proceedings

Volume 64

Series editor

Ratko Magjarevic

Deputy Editors

Fatimah Ibrahim
Igor Lacković
Piotr Ładyżyński
Emilio Sacristan Rock

The IFMBE Proceedings book series presents the results of IFMBE Conferences. These scientific conferences deal with various topics of medical, biological and clinical engineering, and biophysics. They are organized or endorsed by the International Federation for Medical and Biological Engineering (IFMBE).

The aims of the IFMBE conferences are to encourage research and the application of knowledge, and to disseminate information and promote collaboration. The papers of the IFMBE proceedings present research results of a high impact for the community and their high scientific standard is guaranteed by a double peer-reviewing of every published paper.

The topics included but are not limited to:

- Diagnostic Imaging, Image Processing, Biosignal Processing
- Modeling and Simulation, Biomechanics
- Biomaterials, Cellular and Tissue Engineering
- Information and Communication in Medicine, Telemedicine and e-Health
- Instrumentation and Clinical Engineering
- Surgery, Minimal Invasive Interventions, Endoscopy and Image Guided Therapy
- Audiology, Ophthalmology, Emergency and Dental Medicine Applications
- Radiology, Radiation Oncology and Biological Effects of Radiation

The IFMBE Proceedings series is an official publication of the International Federation for Medical and Biological Engineering.

IFMBE Proceedings are indexed by Google scholar. Thomson Reuters and Scopus index many volumes in their ISI Proceedings and the Scopus database, respectively.

More information about this series at http://www.springer.com/series/7403

Yuan-Ting Zhang • Paulo Carvalho
Ratko Magjarevic
Editors

International Conference on Biomedical and Health Informatics

ICBHI 2015, Haikou, China, 8–10 October 2015

Springer

Editors
Yuan-Ting Zhang
The Chinese University
of Hong Kong
Hong Kong, China

Ratko Magjarevic
Faculty of Electrical Engineering
and Computing
University of Zagreb
Zagreb, Croatia

Paulo Carvalho
Universidade De Coimbra
Coimbra, Portugal

Contents

Contents

Inter-limb Coordination Assessment and Fall Risk in ADL

Tomislav Pozaic, Anna-Karina Grebe, Michael Grollmuss, Nino Haeberlen, and Wilhelm Stork

Abstract

Fall risk assessment research has largely been focused on individual biomechanical measures or assessment in clinical setting. The goal of the study was to evaluate the fall risk from the inertial sensor data from activities of daily living (ADL) based on the inter-limb coordination assessment. Eight older adults with higher risk of falling and eight adults with no risk of falling were monitored for one week with hip and wrist sensor node. A one-way analysis of variance and 95% confidence interval were applied to investigate associations between extracted temporal inter-limb coordination measures for these two groups. Results have shown significantly higher asymmetry in lower limbs and between contralateral arm and leg for subjects with higher risk of falling, allowing us to reliably distinguish these two groups.

1 Introduction

A leading cause of injuries in older adults is falling, causing a heavy burden on the health care system. Each year, one in every three adults aged over 65 falls [1]. Fall risk factors can be divided into five domains [2]: sociodemographic factors, medical and psychological factors, medication risk factors, mobility factors and sensory risk factors. Epidemiological studies have shown that transitions and walking are main mobility fall risk factors causing 41% and 36% of all falls respectively [3].

Previous studies have investigated mobility factors in terms of variability of biomechanical measures, such as stride time, walking speed, stride length, stance and swing times and individual joint kinematics [4, 5]. The timing of gait events in the lower limbs is more asymmetric and less stable in older adults [6]. Additionally, gait stability and inter-limb coordination are very well correlated and as such good indicators for falls [7].

Inter-limb coordination primarily involves movements requiring sequential and simultaneous use of both sides of the body with a high degree of rhythmicity. More precisely, it involves the timing of motor cycles of the limbs in relation to one another [8]. Such actions are commonly divided into two categories [9]: bimanual coordination (involves skilled inter-limb coordination of the two arms or legs in a bimanual action) and coordination between hands and feet (involves the simultaneous coupling of the upper and lower limbs).

Many previous studies focused only on lower extremities [10], assessed inter-limb coordination using camera based tools [11] or in clinical settings during short periods of time [12, 13]. While camera assessment tools are expensive and subject of privacy concerns, clinical assessments oversimplifies geriatric fall risk, which can be more accurately described with fuzzy boundaries as a multifactorial disorder.

Our work focuses on assessment of coordination of upper and lower extremities in terms of fall risk in home environment during ADL using a system of two sensor nodes. A novel approach for inter-limb coordination assessment enables optimization of the number of sensors, thus enabling unobtrusive, user-friendly measurement during a longer period of time (one week). We hypothesize that fall-prone adults will have less coordinated movements and higher variability of gait than adults with no risk of falling on a weekly basis. Using features that uniquely describe inter-limb coordination it should be possible to reliably distinguish between these two groups.

T. Pozaic (✉) · A.-K. Grebe · M. Grollmuss · N. Haeberlen
Bosch Healthcare Solutions GmbH, Waiblingen, Germany
e-mail: tomislav.pozaic@de.bosch.com

W. Stork
Karlsruhe Institute of Technology, Karlsruhe, Germany

Table 1 Subject characteristics

Characteristic	Fallers	Non-fallers
N	8	8
Female (%)	75	25
Age (years)	68.5 ± 8.8	57.2 ± 6.5
Height (cm)	166.0 ± 13.8	173.9 ± 8.3
Weight (kg)	75.6 ± 18.4	81 ± 12.5
BMI, (kg/m^2)[a]	27.7 ± 7.7	26.8 ± 3.9
SOMC (0–28)[b]	2.0 ± 2.4	1.5 ± 3.5
Habitual gait speed, (m/s)	1.0 ± 0.2	1.1 ± 0.2
History of falls	0.8 ± 0.7	0
FRAQ[c]	7.4 ± 2.6	1.4 ± 1.2

[a]*BMI* Body Mass Index
[b]*SOMC* Short Orientation-Memory-Concentration test
[c]*FRAQ* Fall Risk Assessment Questionnaire

2 Methods

2.1 Subjects

Sixteen older adults were recruited with the characteristics as shown in Table 1. These show the mean values with corresponding standard deviations. The study was approved by the Ethical Committee of the Medical Faculty and the University Hospital of Tübingen. All participants signed informed consent according to the Declaration of Helsinki. Exclusion criteria for the study were more than 10 points on Short Orientation-Memory-Concentration (SOMC) test (cognitive impaired subjects), inability to walk or terminal diseases.

2.2 Experiment Setup

Subjects were wearing two sensor nodes, one attached on the wrist and one on the ipsilateral hip. Each sensor node consisted of a 3-axis accelerometer BMA280, gyroscope BMG160 and magnetometer BMC055 (all produced by Bosch Sensortec GmbH). Accelerometer measurement range was set to ±4 g, gyroscope to ±500°/s and magnetometer to ±1000 µT. 14-bit accelerometer and 16-bit gyroscope and magnetometer data were sampled with a sampling frequency of 100 Hz. Each data package was transmitted over a Bluetooth Low Energy (BLE) connection to an Android phone (LG2 mini) attached at the belt around the waist. Phone was requesting the time from the sensor nodes every minute and correlated it with the real time. The round trip between the phone and sensors is integrated into this mapping for synchronization purposes. Data corresponding to one measurement day was stored in one file in order to enable easier offline processing.

Data acquisition was performed for one week (seven consecutive days) in the home environment of each subject. Rechargeable lithium battery (170 mAh) supplying the sensor node lasts for approximately 8 h. Subjects put on the sensors in the morning and wore them during activities of daily living. The battery and phone are charged over night.

On the first day of the measurement week the subject's supervisors collected anthropometric measures. The habitual gait speed was determined by letting the subjects walk on a straight line not shorter than 3.5 m and measuring the elapsed time. The length of the walking line was adjusted to various conditions in subject's home (e.g. small apartments, obstacles etc.).

Additionally subjects answered a fall risk assessment questionnaire (FRAQ) containing 18 most significant factors for risk of falling indentified in [2]. Answers were graded with either 0 or 1 (depending if the indentified risk factor was present or not), except the number of prescript medications and number of falls in the last 12 months. Total score defined as the sum of all answers was used to split the subjects into two groups: fallers and non-fallers. Fallers are subjects with a total score of four or higher, while non-fallers are subjects with a total score lower than four points.

3 Data Analysis

3.1 Preprocessing

Data was preprocessed offline using MATLAB R2012b. Sensor data for the wrist and hip were synchronized using a (proprietary) method for mapping the phone and sensor times. Signals, particularly from the wrist, were affected with data loss due to various artifacts in BLE connection (e.g. various obstacles, distance between sensors and phone). Thus, before further processing, the missing data was interpolated using linear interpolation. Missing data is detected when the time difference between two consecutive BLE packages t_i and t_{i-1} is $t_i - t_{i-1} > 1.5 * T_S$, where T_S is defined sampling period. This action maintained data from both sensors synchronized during the whole day and enabled sample wise signal processing.

Inertial sensors (accelerometer, gyroscope and magnetometer) provide data in three perpendicular axes of their local coordination system. To describe the orientation of sensor's local system in relation to the geodetic coordination system approach with Euler angles (yaw, pitch and roll) estimated from all three inertial sensors was used. The relation is described with a Yaw-Pitch-Roll angle rotation matrix M_{YPR} defined by standard convention ("x-convention") rotation order:

$$a_t = M_{YPR}^{-1} a_t', \qquad (1)$$

where a_t' is one sensor sample at moment t and a_t is the corresponding value in the geodetic coordination system. Solving (1) for the acceleration signals the linear acceleration of human movement is calculated.

3.2 Walking Bouts

Acceleration based step detector was previously developed in C and used as binary *mex* file for processing sensor data in MATLAB. The step detector algorithm is based on an adaptive threshold approach over a sliding window of 300 samples. A walking bout is defined as the time between start and end of walking. Start of walking is depicted with three or more consecutively detected steps, while end of walking is determined when no steps for maximum step duration time (3 s) were detected.

Data for each day for each subject was processed and only walking bouts longer than 10 s were taken into consideration. Despite the fact that high step rate variability is present for short walking bouts, they were still taken into consideration due to the older age of subjects and the relatively small number of long walking bouts (100 or more steps).

3.3 Gait Speed

Linear acceleration (defined as an acceleration in the direction of human movement), was used to calculate gait speed of a particular walking bout. In order to remove tilt from the acceleration signal, a following filter proposed in [14] was applied:

$$x_{output} = \frac{x_a - \overline{x_a}}{\cos(a \, \sin(\overline{x_a}))}, \qquad (2)$$

where x_a is linear acceleration signal and x_{output} is signal without tilt. To reduce additionally the signal drift due to high frequency noise, data was filtered using moving average filter with window size of one second. The gait velocity was then calculated by integrating the filtered acceleration signal for each walking bout and then averaged over the particular interval.

Previous systematic review of gait speed values for long term care residents, which are at higher risk of falling, has shown that usual gait speed in clinical setting is 0.58 m/s [15]. Moreover, slow gait speeds have also been related to higher risk of institutionalization and mortality. Thus, only walking bouts with mean gait speed lower than 0.6 m/s were taken into further consideration.

3.4 Inter-limb Coordination Features

Features extracted in this study for assessment of inter-limb coordination and are as follows:

- inter-limb coordination index (IC),
- ipsilateral coordination index (YC),
- contralateral coordination index (CC),
- step time variability (STV),
- swing phase time variability (SPV).

STV and SPV features describe bimanual coordination, while IC, YC and CC features describe hands/feet coordination.

Gait cycle of human walking can be split into swing and stance phase, where swing phase starts with toe off event and ends with heel strike. Toe off event was detected from the hip acceleration signal as the first local minima following the heel strike of the opposite foot. SPV is defined as variability of swing time duration of steps in each walking bout. STV is defined as a variability of duration of steps detected for each walking bout.

IC parameter is defined for each walking bout as a mean time delay between highest backward or forward point in arm swing and corresponding heel strike. Highest backward point in the arm swing fits to the heel strike of ipsilateral foot, while highest forward point in arm swing fits to heel strike of contralateral foot.

Since it was defined that sensor should be worn always on the same hip (subject arbitrarily chooses on first day of measurement on which side the sensors will be worn), it is possible to distinguish between left and right heel strikes based on the gyroscope signal. Namely, empirically it has been noticed that rotation of the hip while walking happens before the heel strike and it is visible in the gyroscope signal (angular velocity) on the side where sensor is worn. By calculating the area under curve of the gyroscope signal between two consecutive heel strikes, left and right steps were distinguished. YC and CC features were then calculated as the mean time delay between arm swing and ipsilateral and contralateral heel strike, respectively.

3.5 Statistical Analysis

Analysis of the features was performed on a weekly basis, meaning that feature values for each particular subject were averaged for all walking bouts satisfying above described

conditions over the whole week (or at least for all days when recording was successfully performed). A one-way analysis of variance (ANOVA) was used to analyze the difference between two defined groups for all five features (*significance*, p). The mean (μ) values were extracted for each feature together with corresponding 95% confidence interval (95% CI). MATLAB built-in functions *anova1* and *paramci* were used for statistical analysis.

4 Results

From the total number of subjects, 8 were identified as non-fallers (57.2 ± 6.5 years) and 8 were identified as fallers (68.5 ± 8.8 years). There was no significant difference in habitual speed between the groups (p = 0.21). Non-fallers reported no previous falls in last 12 months, while fallers reported 0.8 ± 0.7 falls. There was a significant difference in FRAQ results (7.4 ± 2.6 and 1.4 ± 1.2 for fallers and non-fallers respectively, p < 0.01).

In average 4.4 days per subject out of seven days of recording were satisfying exclusion criteria. In total, non-fallers performed 899 walking bouts which were longer than 10 s and had mean gait speed lower than 0.6 m/s (53% of a total number of walking bouts), while fallers performed 1052 walking bouts with same features (81%).

Regarding our reference, STV and SPV features have shown moderate to good relation with results of the FRAQ questionnaire (Pearson's r = 0.72, p < 0.01 and r = 0.70, p < 0.01, respectively).

Figure 1 shows the difference between fallers and non-fallers for features describing bimanual coordination (STV and SPV). These features were significantly different for fallers and non-fallers (p < 0.01 for both features). More precisely, STV and SPV were significantly higher for fallers (μ = 0.035 s, 95% CI = 0.029–0.041 and μ = 0.036 s, 95% CI = 0.031–0.042, respectively) than for non-fallers (μ = 0.025 s, 95% CI = 0.021–0.030 and μ = 0.026 s, 95% CI = 0.022–0.031, respectively).
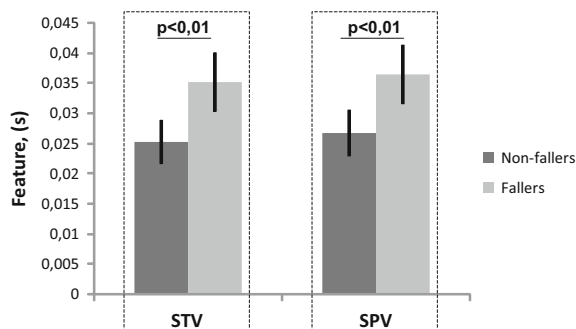
Fig. 1 STV and SPV values for non-fallers (N = 8) and fallers (N = 8). Differences for both features are p < 0.01
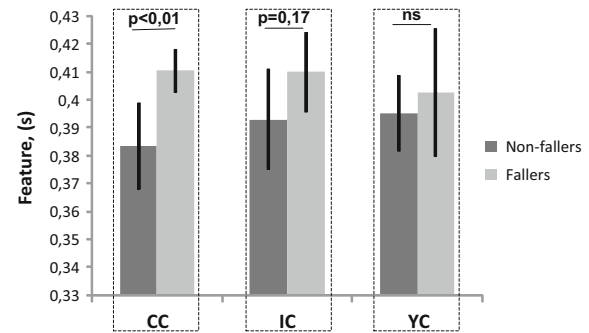
Fig. 2 CC, IC and YC values for non-fallers (N = 8) and fallers (N = 8). Differences for features are as follows: p < 0.01, p = 0.17 and ns (not significant)

Figure 2 shows relation of IC, YC and CC features for two defined groups. The most significant difference was for CC (p < 0.01). IC showed statistically moderate difference (p = 0.17), while there was no difference between groups for YC feature. CC was significantly higher for fallers than for non-fallers (μ = 0.41 s, 95% CI = 0.40–0.42 and μ = 0.38 s, 95% CI = 0.36–0.40, respectively). Although there were only moderate differences in mean values for IC (0.41 vs. 0.39 s, for fallers and non-fallers respectively), 95% CI were rather wide (CI = 0.39–0.43 and CI = 0.37–0.41). YC showed no difference between the two groups (μ = 0.40 s, 95% CI = 0.37–0.40 and μ = 0.39 s, 95% CI = 0.38–0.41, respectively).

5 Discussion

The proposed method for subjects identified at higher risk of falling has shown on a weekly basis significantly higher STV, SPV and CC, which is in accordance with previous clinical findings [4, 6, 7]. Results for the YC feature indicate that further possibilities for improvements in distinguishing between left and right steps should be investigated. Despite good assessment of CC feature, YC feature shows low performance probably due to poor hip rotation during walking, which could be related to weakness in lower limbs and slower gait speed characteristic for faller group. Additional features (e.g. frequency domain features) or features assessed on daily or even walking bout basis could give added value in distinguishing between the groups once the population number increases and boundaries between them become even more fuzzy.

Fallers have performed more walking bouts at mean gait speed lower than 0.6 m/s than non-fallers, but to confirm lower gait speeds as a good fall predictor further investigation on all walking bouts is necessary. Analysis of all walking bouts longer than 10 s might have included some other activities during the day, like climbing up or down the stairs, as these events are difficult to differentiate based on accelerometer data used by our

step detector. We used mean values of all walking bouts for particular subjects averaging the extremes, although they might be more indicative (but noisy) for high risk of falling.

Although proposed multi-sensor system has given us a better overview of the daily life activities of fallers and non-fallers, there are still some challenges that have to be overcome. For instance, improvement in the battery performance and reduction of data loss could be resolved by using internal memory (e.g. SD card) instead of BLE transfer of data. Focus on monitoring of movement of only one hand has still given us enough information for distinguishing subjects based on lower limb coordination and coordination between contralateral arm and leg (in respect to the side where sensor system has been worn).

Recalling of previous falls in last 12 months might be a challenging task (indicated by relatively small number of falls for fallers) even for subjects with no or low cognitive impairment (SOMC < 10) and has to be taken into account. This challenge we tried to overcome by assessing 18 different factors relevant for the fall risk. In respect to that results of the FRAQ were significantly higher (more than five times) for fallers.

In conclusion, our method with proposed features can reliably distinguish between fallers and non-fallers assessed on a weekly basis. Additionally, proposed method can be used for assessment of inter-limb coordination in cases where long term monitoring of motor features with high acceptance rate is required (Parkinson's Disease, post-stroke patients etc.).

References

1. A.M. Tromp, S.M.F. Pluijm, D.J.H. Deeg, L.M. Bouter, P. Lips, "Fall-risk screening test: A prospective study on predictors for falls in community-dwelling elderly", *J. Clinical Epidemiology*, vol. 54, pp. 837–844, 2001.

2. S. Deandrea, E. Lucenteforte, F. Bravi, R. Foschi, C. Vecchia, E. Negri, "Risk factors for falls in community-dwelling older people", *J. Clinical Epidemiology*, vol. 21, pp. 658–668, 2010.

3. K. Rapp, C. Becker, I.D. Cameron, H.H. Konig, G. Buchele, "Epidemiology of falls in residential aged care: Analysis of more than 70,000 falls from residents of Bavarian Nursing Homes", *J. Am Medical Directors Association*, vol. 13, pp. 187–193, 2012.

4. J.M. Hausdorff, "Gait dynamics, fractals and falls: finding meaning in the stride-to-stride fluctuations of human walking", *Human Movement Science*, vol. 26, pp. 555–589, 2007.

5. J. Verghese, R. Holtzer, R.B. Lipton, C. Wang, "Quantitative gait markers and incident fall risk in older adults", *J. Gerontology*, vol. 64A, pp. 896–901, 2009.

6. M. Plotnik, N. Giladi, J.M. Hausdorff, "A new measure for quantifying the bilateral coordination of human gait: effects of aging and Parkinson's disease", Experimental brain research, vol. 181, pp. 651–570, 2007.

7. T. Krasovsky, M.C. Bana, R. Hacmon, A.G. Feldman, A. Lamontagne, M.F. Levin, "Stability of gait and interlimb coordination in older adults", *J Neurophysiology*, vol. 107, pp. 2560–2569, 2012.

8. S.P. Swinnen, R.G. Carson, "The control and leaning of patterns of interlimb coordination: past and present issues in normal and disordered control", *Acta Psychologica*, vol. 110, pp. 129–137, 2002.

9. T. Bobbio, C. Gabbard, P. Cacola, "Interlimb coordination: An important facet of gross-motor ability", Early Childhood Reseach & Practice, vol. 11, 2009.

10. T. Tanahashi et al., "Noisy interlimb coordination can be a main cause of freezing of gait in patients with little to no Parkinsonism", PLOS One, vol. 8, pp. 1–10, 2013.

11. E.E. Stone, M. Skubic, "Evaluation of an inexpensive depth camera for passive in-home fall risk assessment", *Proc. 5th Intern. Conference on Pervasive Computing Technologies for Healthcare*, 2011, pp. 71–77.

12. T. Krasovsky, A. Lamontagne, A.G. Feldman, M.F. Levin, "Reduced gait stability in high-functioning poststroke individuals", *J. Neurophysiology*, vol. 109, pp. 77–88, 2013.

13. S.L. Chiu, L.S. Chou, "Variability in inter-joint coordination during walking of elderly adults and its association with clinical balance measures", *Clinical Biomechanics*, vol. 28, pp. 454–458, 2013.

14. R.M. Nilssen, J.L. Helbostad, "Trunk accelerometry as a measure of balance control during quiet standing", *Gait and Posture*, vol. 16, pp. 60–68, 2002.

15. S.S. Kuys, N.M. Peel, K. Klein, A. Slater, R.R. Hubbard, "Gait speed in ambulant older people in long term care: A systematic review and meta-analysis", *J. Am. Medical Directors Association*, vol. 15, pp. 194–200, 2014.

Optimization of the Amplicons Detection System of Loop-Mediated Isothermal Amplification on Microfluidic Compact Disk

Shah Mukim Uddin, Fatimah Ibrahim, Jongman Cho, and Kwai Lin Thong

Abstract

Salmonellosis caused by the bacteria in the genus *Salmonella* remains the most important foodborne disease in both developing and developed countries. Since several decades various microbial detection and quantification methods have been developed. One of recently developed gene amplification method is loop-mediated isothermal amplification (LAMP) which has been developed on tube-based platform. To facilitate the detection of pathogenic diseases in remote areas, a microfluidic platform has been developed called lab-on-a-CD. This paper presents an improved endpoint detection system for LAMP on Lab-on-a-CD platform. A set of ultraviolet (UV) emitter and color sensor have been used in this detection system to detect the emission level of LAMP amplicons. A LAMP assay has been performed with *Salmonella* bacteria DNA and calibrated the duty cycle of UV emitter to optimize the amplicons detection system.

1 Introduction

Most foodborne illnesses are caused by pathogenic bacteria or viruses in food. One of the major bacterial foodborne illness is Salmonellosis which is caused by *Salmonella* bacteria. The conventional methods of *Salmonella* bacteria diagnosis are limited by the high cost requirement with lower sensitivity and specificity performance [1]. Food contamination may cause a severe consequence with economic burden and human health risk, unless we can identify the source of contamination rapidly and accurately. Conventional methods of microbial detection and identification require special media to isolate the viable bacterial cells from food [2, 3]. Hence, these methods requires 2–3 days to achieve the initial results and 5–7 days for confirmation with laborious and cumbersome work [3, 4].

In 1980s a gene amplification method had been developed called polymerase chain reaction (PCR) which is being widely used for genetic testing [5, 6]. The steps required for PCR are nucleic acid extraction, gene amplification, and detection. These steps require skilled personnel, expensive equipment, and facilities. To overcome these drawbacks, in 2000s an alternative gene amplification method had been developed called loop-mediated isothermal amplification (LAMP) that combines rapidity, simplicity, high sensitivity and specificity [7–9]. The limitation to conduct LAMP assay is laboratory requirement which restrain from performing genetic test in remote places.

To overcome the drawbacks of accessibility, a microfluidic device called lab-on-a-chip (LOC) has been developed which can perform biochemical assays with advantages

S. M. Uddin · F. Ibrahim · J. Cho (✉)
Faculty of Engineering, Department of Biomedical Engineering, University of Malaya, 50603 Kuala Lumpur, Malaysia
e-mail: minerva@inje.ac.kr

S. M. Uddin
e-mail: shahmukim@gmail.com

F. Ibrahim
e-mail: fatimah@um.edu.my

S. M. Uddin · F. Ibrahim · J. Cho · K. L. Thong
Faculty of Engineering, Centre for Innovation in Medical Engineering (CIME), University of Malaya, 50603 Kuala Lumpur, Malaysia
e-mail: thongkl@um.edu.my

K. L. Thong
Microbiology Unit, Faculty of Science, Institute of Biological Sciences, University of Malaya, 50603 Kuala Lumpur, Malaysia

J. Cho
Department of Biomedical Engineering, Inje University, Gimhae, 621-749, South Korea

of low reagent consumption and sample requirements, precise microfluidic volume control, automated operations, and process integration [10, 11]. As an alternative microfluidic method, lab-on-a-CD has been developed which integrates all the biochemical steps onto a single disc-shaped microfluidic device [12, 13]. Conducting genetic test for food bacteria detection like LAMP in lab-on-a-CD platform can lead to develop a point-of-care testing (POCT) device in order to provide rapid services to patients at the point of care.

In this study, LAMP assay has been conducted following tube-based method utilizing thermal cycler and then the resultant DNA amplicons has been transferred to the detection chamber of microfluidic compact disk (CD). Then, the loaded microfluidic CD has been tested with the developed amplicons detection system to optimize the calibration of ultraviolet (UV) emitter excitation.

2 Methodology

The developed endpoint detection system of LAMP amplicons by Shah et al. [14] has been optimized by controlling the pulse-width modulation (PWM) signal for UV emitter. The optimization for the detection system was performed by conducting LAMP assay, fabricating microfluidic compact disk, developing the control circuit hardware and software, and improving the mechanical structure of the detection system.

2.1 LAMP Assay

The LAMP assay was conducted following the protocol by Thong et al. [15, 16]. The reaction mix composition and the *Bst* DNA polymerase was taken from Loopamp DNA Amplification Kit (Eiken Chemical Co., Ltd., Tokyo, Japan). The reaction mix contains 40 mM Tris-HCl (pH8.8), 20 mM KCI, 16 mM $MgSO_4$, 20 mM $(NH_4)2SO_4$, 0.2% Tween20, 1.6 M Betaine, and 2.8 mM each dNTPs. Each of the LAMP reaction of the LAMP assay was performed with 12.5 μL of reaction mix composition, 40 pmol of each FIP and BIP primer, 5 pmol of each F3 and B3 primer, 20 pmol of each LF and LB loop primer, 1.0 μL of 8 U Bst DNA polymerase,

2.0 μL of deionized water and 2.5 μL of DNA template of *Salmonella*. To conduct the negative control of LAMP assay, deionized water was used instead of DNA template. The primers were designed based on the *fadA* gene of *Salmonella enterica* Typhimurium (GenBank accession number NC003197.1) using the LAMP Primer Explorer V4 software [17]. The primer sequences are proprietary information. DNA extraction was performed by direct cell lysate boiling method and NanoDrop 2000 UV-Vis Spectrophotometer was utilized to measure the DNA concentration. The LAMP assay was conducted in a heat block at 65 °C for 60 min, then 80 °C for 2 min to inactivate the enzyme. At the end, LAMP assay was cooled off at 4 °C. 1 μL of tenfold diluted SYBR Green I dye was added with each of the resultant LAMP amplicons (25 μL) to distinguish the positive results from the negative one. The positive results turns from orange to yellowish green and negative results maintain its original color which is orange.

2.2 Microfluidic Compact Disk Fabrication

The microfluidic compact disk (CD) are featured with sixteen detection chambers. The geometry of each detection chamber is optimized on volume of 26 μL. The detection chambers have two inlet/outlet holes to facilitate the loading of LAMP amplicons. All detection chambers are arranged in four groups and each group has four individual chambers. The microfluidic CD has an interrupting edge which is cooperating with the detection system. Figure 1 shows the assembly of the microfluidic CD fabrication.

The features of microfluidic CD were designed with AutoCAD design software. The microfluidic CD has two transparent PMMA (poly methyl methacrylate) layers which are sticked together with one PSA (pressure sensitive adhesive) layer in the middle of them. The thickness of top and bottom PMMA layers are 2 mm and 4 mm, respectively. The features of PMMA layer and PSA layer was fabricated utilizing computer numerical control (CNC) machine and digitally controlled cutting plotter machine, respectively. In the bottom PMMA layer, the detection cambers was engraved in a depth of 1 mm. In the middle PSA layer, the detection chambers were cut-through. In the top PMMA layer, the inlets/outlets holes were cut-through.

Fig. 1 Assembly of the microfluidic CD
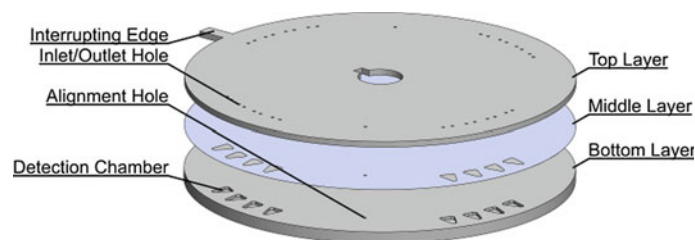
After fabricating, all the layers were positioned together on top of each other with the alignment hole and pressed all together with a custom manufactured screw-compressor-clamp to bind strongly.

2.3 Development of the Detection System

(1) *Overview*

The detection system has been developed in three stages; (a) design and construction of the electronic circuitry for the detection system, (b) design and fabrication of an optical noiseless mechanical structure of the detection system, and (c) developing a software for the control circuitry. The mixer of LAMP amplicons and SYBR Green emit green color light in UV excitation [14]. To excite the LAMP amplicons, a UV emitter (peak wavelength: 365 nm) has been used. To calculate the color light emission level from the LAMP amplicons, a color sensor has been used. A UV filter has been used on the light way to omit the unwanted UV wave passing through the detection chamber. Figure 2 shows the structure of the sensor holder which composites of a UV emitter, a UV filter, and a color sensor.

The developed detection system consists of a stepper motor with a motor driver, a photo interrupter, a LCD display, a microcontroller, a set of navigation keys (start, next, previous, and restart), and other supporting electronic components. To place the detection chamber aligning with the UV emitter and color sensor, a unipolar stepper motor has been used which is driven by a motor driver (darlington transistor arrays). The photo interrupter is acting as a position sensor which is cooperating the stepper motor to place the detection chamber on desire position. The LCD display is visualizing the detection results from the color sensor interpretation. The microcontroller is controlling the rotational direction, speed, and steps of the steeper motor, processing the photo interrupter output voltage, controlling the UV emitter which is driven by an IGBT transistor and LED driver IC, processing the color sensor output pulse train, processing the display of LCD, and processing the input
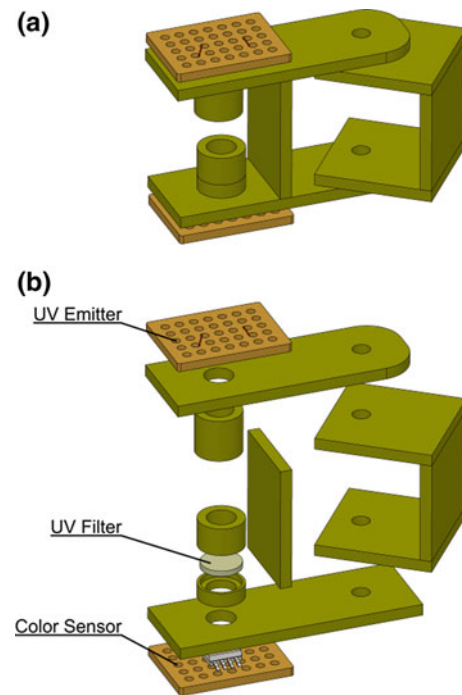
Fig. 2 Sensor holder of the detection system; **a** perspective view, **b** exploded perspective view

from the navigation keys. Figure 3 shows the developed amplicons detection system of LAMP for microfluidic CD platform.

(2) *Operation of the Detection System*

By pressing the start key of the detection system, the stepper motor starts to rotate stepwise. The motor continues its rotation cooperating with the photo interrupter until the first detection chamber of the microfluidic CD is placed aligning with the UV emitter and color sensor. Then the UV emitter is enabled and afterward the color sensor state is changed to enable by the microcontroller. The color sensor senses the emission level from the LAMP amplicons and generates the corresponding pulse train as an output. The microcontroller calculates the frequency of the color sensor output and compares with the detection condition. The frequency of the output pulse train is different for the positive

Fig. 3 Naked eye inspection of the LAMP amplicons in tube. Tubes 1–3 are negative control and tubes 4–6 are positive control
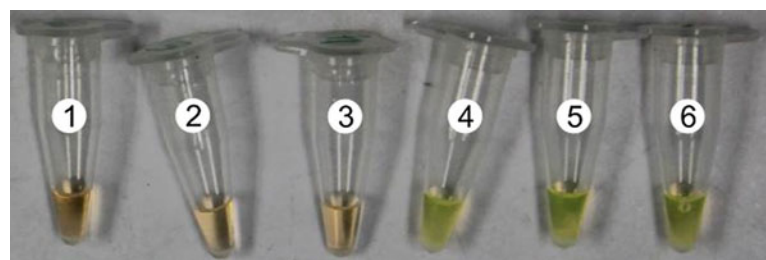
control and negative control of LAMP amplicons. The detection condition interpretation of LAMP amplicons detection is executed to display on LCD screen in terms of "Positive" or "Negative". Following the same fashion of detection, the system reads, processes, and displays the results for rest of fifteen detection chambers. To facilitate the review of detection results, the navigation keys can be utilized.

2.4 Optimization of the Detection System

The interpretation of the color sensor varies for different intensity levels of the UV emitter. To achieve the optimum intensity, the UV emitter (driving current 350 mA) is controlled by a microcontroller and an IGBT transistor. By changing the duty cycle (range of 10–100%) of the PWM signal generated by the microcontroller, the average current flowing through the UV emitter is controlled. The UV emitter intensity is proportional to the power consumption. Hence, the intensity level of UV emitter varies for the corresponding duty cycle of PWM signal.

3 Results and Discussion

A LAMP assay was performed with the DNA from *Salmonella* bacteria. The concentration of the DNA template was 25 ng/μL. Figure 4 shows the photograph of the resultant LAMP amplicons mixed with SYBR Green I in tube. Tubes 1–3 were negative controls (NC) (DNA template was replaced with deionized water) and tubes 4–6 were positive controls (PC). The negative controls maintained the original orange color of SYBR Green I and the positive controls changed to yellowish green color. After conducting the
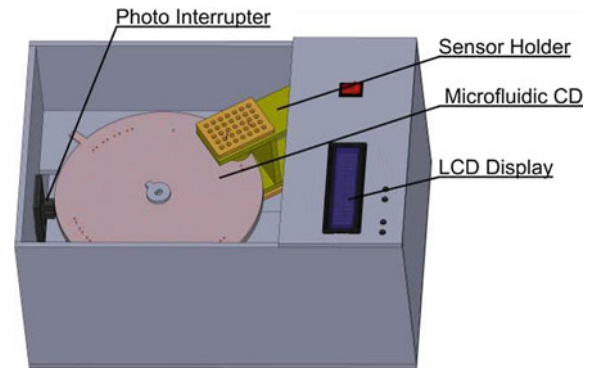
Fig. 4 Developed amplicons detection system of LAMP for microfluidic CD platform

LAMP assay, these LAMP amplicons were transferred to the detection chambers of the microfluidic CD.

The microfluidic CD loaded with LAMP amplicons was tested with the developed detection system at different intensity levels of the UV emitter. The intensity level of the UV emitter was controlled by changing the duty cycle of UV emitter. Table 1 shows the normalized sensor reading (following feature scaling method) for the corresponding UV emitter duty cycles.

It was reported earlier that the normalized pulse duration was greater than 0.8 for negative control and less than 0.1 for positive control [14]. As much the deference between the minimum pulse duration (Tmin) of NC and maximum pulse detection system will be in optimum calibration. Figure 5 shows the graph for the effect on sensor reading for different intensity levels of the UV emitter. From the Table 1 and Fig. 5, the maximum deference between Tmin of NC and Tmax of PC is 0.892 μs (normalized value) at 70% duty cycle. So, it can be concluded that the optimum excitation of the UV emitter can be achieved when the UV emitter duty cycle is 70%.

Table 1 Sensor reading for different duty cycles of UV emitter to detect LAMP amplicons with the developed detection system

Sample no.	Normalized pulse duration (T)						Diff[a]
	1	2	3	4	5	6	
Duty cycle (%)	Negative control (NC)			Positive control (PC)			
10	0.937	1.000	0.841	0.087	0.000	0.508	0.333
20	1.000	0.879	0.948	0.607	0.289	0.000	0.272
30	0.589	0.869	1.000	0.000	0.054	0.321	0.268
40	0.894	0.716	1.000	0.000	0.645	0.447	0.071
50	1.000	0.935	0.946	0.000	0.176	0.133	0.759
60	0.998	0.954	1.000	0.139	0.000	0.051	0.815
70	1.000	0.959	0.943	0.000	0.032	0.050	0.892
80	0.976	1.000	0.923	0.042	0.000	0.037	0.881
90	0.934	1.000	0.963	0.009	0.072	0.000	0.862
100	1.000	0.967	0.919	0.000	0.090	0.000	0.828

[a]Difference between minimum pulse duration (Tmin) of NC and maximum pulse duration (Tmax) of PC

Fig. 5 Effect of UV emitter excitation with different intensity level on sensor reading to detect LAMP amplicons with the developed detection system
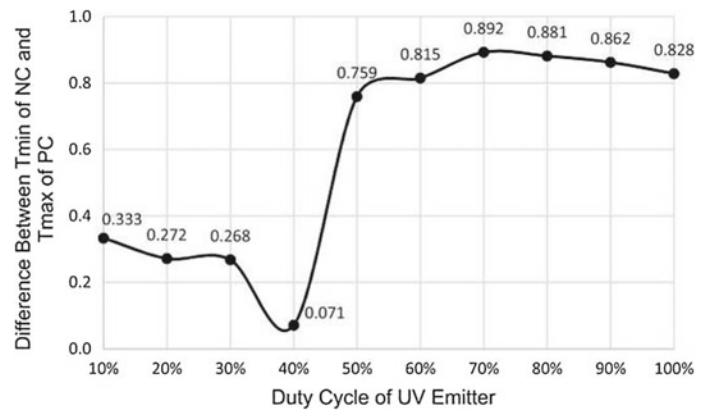
After analyzing the test results with *Salmonella* bacteria DNA to optimize the UV emitter excitation, it can be concluded that the developed detection system can perform the detection in optimum calibration when the duty cycle of UV emitter is 70%. Previously reported detection test results with *Salmonella* bacteria DNA were performed at 100% duty cycle of UV emitter.

4 Conclusion

In this paper, the amplicons detection system of LAMP to detect *Salmonella* bacteria DNA has been calibrated to its optimum UV excitation level and the mechanical structure has also been improvised. The detection test indicates that the optimum excitation could be achieved when the duty cycle of the UV emitter was 70%. This developed amplicons detection system can lead to develop a point-of-care testing (POCT) device to prevent food bacterial diseases by early pathogens detection in suspected remote areas. In future, this detection system can be further improved by compositing a feature like detection results transmission function to remote places through a smart phone.

References

1. K. G. Kuhn, G. Falkenhorst, T. H. Ceper, T. Dalby, S. Ethelberg, K. Mølbak, *et al.*, "Detecting non-typhoid Salmonella in humans by ELISAs: a literature review," *Journal of medical microbiology,* vol. 61, pp. 1–7, 2012.

2. P. Mandal, A. Biswas, K. Choi, and U. Pal, "Methods for rapid detection of foodborne pathogens: an overview," *Am. J. Food Technol,* vol. 6, pp. 87–102, 2011.

3. V. Velusamy, K. Arshak, O. Korostynska, K. Oliwa, and C. Adley, "An overview of foodborne pathogen detection: in the perspective of biosensors," *Biotechnology advances,* vol. 28, pp. 232–254, 2010.

4. A. K. Bhunia, "Biosensors and bio-based methods for the separation and detection of foodborne pathogens," *Advances in food and nutrition research,* vol. 54, pp. 1–44, 2008.

5. R. F. Wang, W. W. Cao, and C. Cerniglia, "A universal protocol for PCR detection of 13 species of foodborne pathogens in foods," *Journal of Applied Microbiology,* vol. 83, pp. 727–736, 1997.

6. G. Jeníková, J. Pazlarová, and K. Demnerová, "Detection of Salmonella in food samples by the combination of immunomagnetic separation and PCR assay," *International Microbiology,* vol. 3, pp. 225–229, 2010.

7. T. Notomi, H. Okayama, H. Masubuchi, T. Yonekawa, K. Watanabe, N. Amino, *et al.*, "Loop-mediated isothermal amplification of DNA," *Nucleic acids research,* vol. 28, pp. e63–e63, 2000.

8. C.-C. Chang, C.-C. Chen, S.-C. Wei, H.-H. Lu, Y.-H. Liang, and C.-W. Lin, "Diagnostic Devices for Isothermal Nucleic Acid Amplification," *Sensors,* vol. 12, pp. 8319–8337, 2012.

9. A. Niemz, T. M. Ferguson, and D. S. Boyle, "Point-of-care nucleic acid testing for infectious diseases," *Trends in biotechnology,* vol. 29, pp. 240–250, 2011.

10. S. Haeberle and R. Zengerle, "Microfluidic platforms for lab-on-a-chip applications," *Lab on a Chip,* vol. 7, pp. 1094–1110, 2007.

11. S. K. Sia and L. J. Kricka, "Microfluidics and point-of-care testing," *Lab on a Chip,* vol. 8, pp. 1982–1983, 2008.

12. M. Madou, J. Zoval, G. Jia, H. Kido, J. Kim, and N. Kim, "Lab on a CD," *Annual Review of Biomedical Engineering,* vol. 8, pp. 601–628, 2006.

13. R. Gorkin, J. Park, J. Siegrist, M. Amasia, B. S. Lee, J.-M. Park, *et al.*, "Centrifugal microfluidics for biomedical applications," *Lab on a Chip,* vol. 10, pp. 1758–1773, 2010.

14. S. M. Uddin, F. Ibrahim, A. A. Sayad, A. Thiha, K. X. Pei, M. S. Mohktar, *et al.*, "A Portable Automatic Endpoint Detection System for Amplicons of Loop Mediated Isothermal Amplification on Microfluidic Compact Disk Platform," *Sensors,* vol. 15, pp. 5376–5389, 2015.

15. K. T. Lim, C. S. J. Teh, and K. L. Thong, "Loop-mediated isothermal amplification assay for the rapid detection of Staphylococcus aureus," *BioMed research international,* vol. 2013, 2013.

16. C. S. J. Teh, K. H. Chua, Y. A. L. Lim, S. C. Lee, and K. L. Thong, "Loop-Mediated Isothermal Amplification Assay for Detection of Generic and Verocytotoxin-Producing Escherichia coli among Indigenous Individuals in Malaysia," *The Scientific World Journal,* vol. 2014, 2014.

17. (13 Nov 2014). *PrimerExplore V4.* Available: http://primerexplorer.jp/elamp4.0.0/index.html.

Implementation of an Electronic Prescription System for Ambulatory Care

Marc Nyssen and Yelina Piedra

Abstract

After a two-year pilot, including the ICT (Information and Communication Technology) developments and small scale tests, the Recip-e project for ambulatory electronic prescriptions is currently in national roll-out phase. Along with the operational secure data-flow, an important number of parameters are captured and taken along; these parameters are processed and archived, enabling us to make a first evaluation regarding the approach taken in Belgium, both from a technical point of view and from a methodologic point of view, regarding the technical developments and the involvement of all stakeholders.

1 Introduction

Prescriptions are a cornerstone in most health systems: in the paper world, the prescribing health worker (general practitioner, specialist, dentist) writes down a medical prescription on a pre-formatted piece of paper, signs it and usually hands it over to the patient. The patient then collects the medication, written on the paper prescription, in a pharmacy. Here, health systems may differ greatly: in some countries the choice of the pharmacy is not free (e.g., Denmark where this is determined at the time of prescribing, and often limited by physical constraints: islands with a single pharmacy [1]). In other countries, the choice of the pharmacy is free: the patient determines where he will collect the prescribed medication. This last case corresponds to the Belgian situation [2].

In this paper, we will highlight the main design features of the ambulatory electronic prescription system "Recip-e"

M. Nyssen (✉)
Vrije Universiteit Brussel, Brussels, Belgium
e-mail: mnyssenr@vub.ac.be; mnyssen@vub.ac.be

Y. Piedra
Havana University, Havana, Cuba

[3] in the Sects. 2 and 3, then in Sect. 4 (Results) the roll-out process is quantified and discussed in Sect. 5.

2 Materials and Methods

The objective set forward for the Recip-e project phase 0 was to realize an in depth study to identify the elements required to realize the theoretical model. This theoretical model resulted from a study performed in the context of the Belgian Ministry of Health and Social Affairs in 2002 [2].

The pilot study covered following topics:

(1) Evaluate the functional, technical and operational requirements for a realistic implementation
(2) Make a stakeholder analysis
(3) Benchmark equivalent projects abroad
(4) Study the financial implications
(5) Communication/Interaction with the stakeholders
(6) Propose a roll-out plan.

Figure 1 shows the current flows of the paper and electronic prescriptions in Belgium: from the prescribing physician via the patient to the pharmacy which he can choose freely.

Benchmarking with Sweden and Denmark, also the Netherlands [4–7], teaches us that the introduction of EPP (Electronic Pharmaceutical Prescriptions) can take several years. Innovations in the medical sector are confronted with the relatively high inertia of the sector.

This understanding leads to following eight border conditions for the technical solution of the "Electronic Medical Prescription" (EMP) in Belgium, where we need a system: Allowing perfect co-existence between paper and electronic prescriptions during the roll-out phase, which might take some time; at least allowing continuity in characteristics and identical functional possibilities versus the paper prescriptions; and requiring minimal legal modifications. These points were identified at the start of the project. They obtained a consensus within the project team and were acknowledged by

Fig. 1 Recip-e dataflows
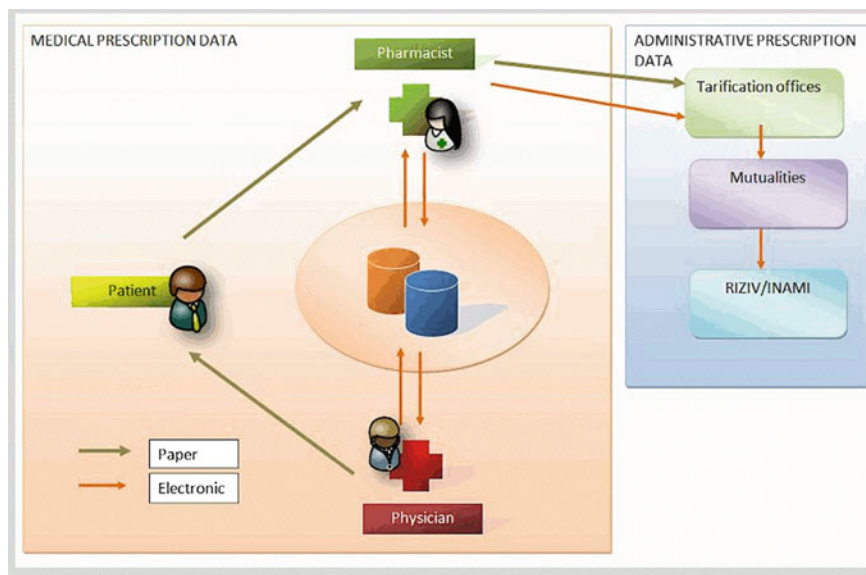
the sector representatives we consulted. Taking into account these border conditions, we designed the conceptual flow model, fitting into the Belgian health system and complying with the national and European privacy regulations [8, 9], resulting in the flow diagram of Fig. 1. The flow of the electronic medical prescription starts at the prescribing physician (generated by the prescription module of his medical package) and goes to the EPP system. While in the first phase (during roll-out), the patient still obtains his printed-out paper prescription, after the roll-out phase, paper tokens will become obsolete and identification at the pharmacy will be performed by the appropriate identification system selected by the sector in dialog with the authorities.

3 Technology Description

3.1 Data Format

The building blocks required to realize an electronic prescription system are based on an existing technology:

1. Internet communication protocols/web-services
2. The Kind Messages for Electronic Health Records (KMEHR-bis) XML format for medical messages [10], including the medical prescription
3. Patient and medical worker identification by the appropriate electronic cards (eID or equivalent) [11]
4. Advanced digital signature, via the eID signing certificate, recognized equivalent to handwritten signature [12]
5. Accessible and sound encryption technology
6. Adequate authentication portals, identifying the role of prescriber and pharmacist

7. Operational common medication databases. [13–15]

KMEHR-bis XML messages play a central role in Belgium: since 2002, about 30 XML formatted messages were defined, corresponding to the most used messages in the Belgian health system. Through labeling sessions, enforcing the implementation of relevant KMEHR-bis messages, the Ministry of Health's efforts and incentives resulted in the situation where all accredited software packages for general practitioners are now able to generate and read in the KMEHR-bis messages such as the pharmaceutical prescription. The pharmaceutical packages will reach this level mid-2015.

The KMEHR-bis message "pharmaceutical prescription" comprises an administrative header, followed by a folder (containing the data which are found on a paper prescription) such as the prescriber's identity, the patient and as many items elements as there are medications on the prescriptions.

This number would be limited to 9, due to space limits on the paper prescription. The items comprise the market name of the medication, the unique Belgian identifier code for a given drug (CNK), the packaging and quantity, posology, way of administration, and the frequency (daily, morning/afternoon, …) and free text instructions for patients.

3.2 Building Blocks

Modules realized are (Fig. 2):

The Recip-e portal allows access by individual patients to their pending electronic prescriptions.

Fig. 2 Recip-e components
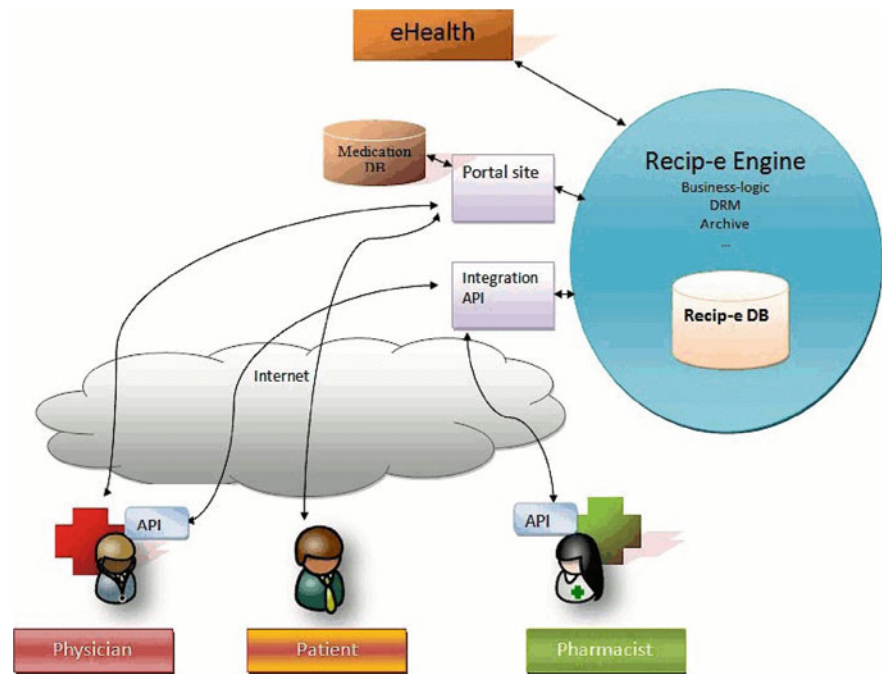
The Recip-e Application Programming Interface (API): Recip-e is mainly be accessed through the API of the physicians or the pharmacists software package.

The Recip-e engine contains modular building blocks, surrounding the secured prescription database.

Links to authentic sources for authentication and identification of roles will be made through the eHealth-platform (national infrastructure supporting the generic building blocks).

Some building blocks needed by the Recip-e engine are provided by the eHealth-platform (time-stamping, logging, authentication, encryption, …) as for the whole e-health sector.

3.3 Data Flows and Interactions

Step 1: Creation of a prescription by the prescriber. The prescriber creates an electronic prescription, normally via his medical package or via a web prescription program. The prescription is signed digitally (either each prescription is digitally signed or the prescriber's session is authenticated via the e-ID + pin code of the prescriber, if a similar procedure can be accepted as in the intra-muros prescription). Then the prescription is transmitted in encrypted format to the Recip-e server. See Fig. 2.

Here, some formal verifications are performed: identity of prescriber and patient´s identity. If all tests passed, a RID (Recip-e ID == unique identifier for each accepted prescription within the system) is attributed. The RID is sent in

response to the prescribing system within seconds (max. 5 s). The prescription is then printed, using the legal format, comprising the RID as a bar-code (Fig. 3). Otherwise, a meaningful error message is generated and transmitted to the prescribing system.

For security reasons, the prescription is divided into several data-blocks:

1. administrative (patient, RID)
2. administrative prescriber (ID, …)
3. medical: (medication, posology, …)

blocks 2 and 3 are encrypted with a key, kept by the eHealth-platforrm, while encrypted data are stored in the Recip-e database.

The prescriber will automatically add the prescription to the medical patient record [16] (outside the scope of Recip-e) and the patient obtains the printed-out prescription.

3.4 Technical Implementation

During the pilot phase (2011–2013), three infrastructures were set-up:

The test-environment at the software developer Accenture (main software developer of the project)

The acceptance environment, integrated into the eHealth-platform's acceptance bus, servers and database hosted by Belgacom (the national telecom company and commercial datacenter provider)

The production environment, integrated into the eHealth-platform's production bus, servers and database hosted by Belgacom, managed by Recip-e.

These three were maintained throughout the pilot phase of the project and the current roll-out phase. Developments are first made and tested on the test server of the software developer, then transferred to acceptance and made available for testing purposes by software vendors of EMR's and pharmaceutical softwares and the Recip-e team. After approval, updates are then transferred from the "acceptance" to the "production" servers, accessible to the end-users.

In the roll-out phase, a fourth environment was set-up on independent servers, on another location (Uniweb), for the logging and monitoring functions, exclusively accessible to the Recip-e technical team.

Authentication of end-users, both in acceptance and in production environments is performed by a combination of the following elements:

- The national identity card and associated pin-code to authenticate the individual

- A certificate associated with the health worker and attributed via the eHealth-platform.

which result in "sessions". During such session, the health worker can access the system and perform the actions, associated with his role in the health system: a GP can create prescriptions, a pharmacist can deliver and a patient can consult the pending prescriptions, for himself as shown in Table 1.

3.5 Management by the Patient

The patient can manage (list, delete, forward) the prescriptions, related to himself, residing on the Recip-e server via a portal, that will be made available via the network of mutual insurance instances of the country and other health portals.

Step 2: The patient selects the care provider (pharmacist in case of pharmaceutical prescription) of his choice. He identifies himself by his electronic ID and (in the transition period, while paper prescriptions remain the only legally

Table 1 Recip-e functions and permissions

Function	GP	Pharmacy	Patient
Create prescription	*		
Revoke (delete) prescription	*	*	*
List open prescriptions	*		*
Print prescription content	*	*	*
Mark as delivered		*	
Mark as undelivered		*	
Archive prescription		*	
Announce prescription	*		
Create feedback messages		*	
List feedback messages	*		

valid ones, he/she will then recover the pending prescription (s) via his professional package and will deliver what is written on the prescription). The electronic prescription is removed from the prescription server upon archiving by the care provider. This way, we avoid a huge accumulation of sensitive medical data in a single place.

4 Results

4.1 Deployment with the GP's

After the "pilot phase", national roll-out was prepared and effectively started in May 2013 by involving all recognized vendors of electronic medical records for general practitioners (17) and software for pharmacies (9), active in the country. Via the "registration procedure" managed by the Federal state's institution "eHealth-platform", vendors of GP software were required to implement access to the secure webservices of the health system and a number of applications, amongst which the electronic ambulatory prescriptions via Recip-e. Several mini-lab sessions were held to assist the software vendors and to assess the operation (end-to-end) via real-life scenarios. By November, all passed the tests.

Progressive end-user deployment resulted in a consistent increase in the generation of electronic prescriptions as shown in Fig. 4, taken on May 19th 2015. In May 2015, about one quarter of the GP's were active and half of the country's pharmacies.

We could also measure the rate of incoming prescriptions, versus the time of the day, as shown in Fig. 5. The most active part of the day is between 8:30 am. and 11:30 am., it is followed by a serious slow down between 12:00 and 16:00, then an active afternoon runs from 16:00 to about 20:00, be it at a slower pace than the morning period. These data should be taken into consideration to establish the required performance at full deployment.

Fig. 4 Daily produced e-prescriptions versus time
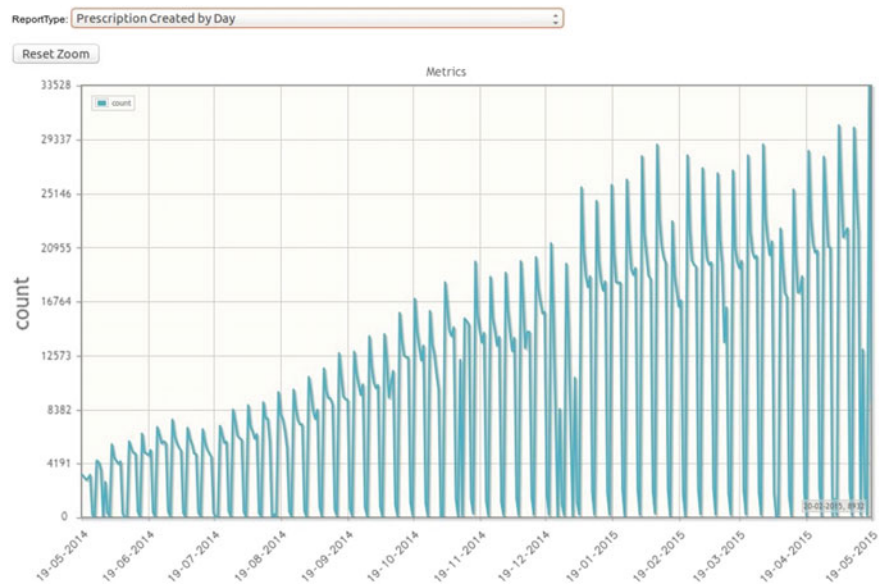
Fig. 5 Incoming prescriptions versus time of the day
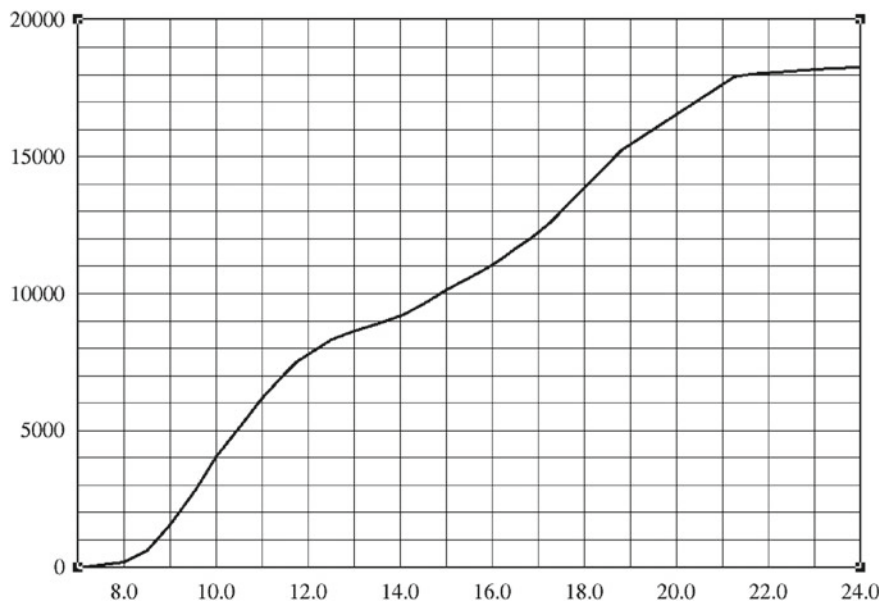
4.2 Informing Stakeholders

A major effort was deployed to inform all stakeholders, including the end-users of the introduction of electronic prescriptions.

Software vendors were invited to participate in info sessions and mini-labs. Software demos were prepared, showing all the Recip-e functions in full-source, readily down-loadable and operational within hours in the "acceptance environment". A technical help-desk, ticketing system and interactive follow-up were established.

For the end-users seminars, conferences and demos were performed together with the respective professional associations (mostly GP's and pharmacists) and on-line materials are made available.

4.3 Deployment in Other Sectors of the Health Care System

Next to deployment of ambulatory pharmaceutical prescriptions by GP's, following targets are in the pipe-line: Prescriptions by specialists, dentist, ambulatory prescriptions from hospitals and clinics, physiotherapy prescriptions, nursing prescriptions, prescriptions by midwives.

For each of these, the methodology, as followed for the pharmaceutical prescriptions by GP's is followed, be it at faster pace, because the same infrastructure and previous experience can readily be applied.

4.4 Remaining Work

The paper-based prescription with additional RID-bar-code was intended as a transition tool between the paper prescription and the electronic one. In view of fully paperless operation, the approach of how and when de-materialisation will take place needs to be addressed in dialogue with the stakeholders involved.

5 Discussion

The deployment of the electronic prescriptions evolves consistently and although we have little leverage to force the end-users to start sending in electronic prescriptions, they start moving in. Once prescribers have observed how little effort it takes, they continue to use the system.

For the benefits to become evident to the whole sector, we need to obtain a higher deployment degree and familiarity of the end-users with the more sophisticated functions such as the feed-back messages and the verification of "list open prescriptions" enabling GP's to verify weather the patient has at least collected previously prescribed medication.

Pharmacists have the possibility to link the electronic prescription to their "robots", but the ergonomy of their softwares is a key factor.

Although in very few cases, inconsistencies between the paper-based and the electronic prescription were observed, due to software bugs and due to manipulation errors, in general, the roll-out strategy works.

6   Conclusion and Future Work

The purpose of the Recip-e project is to go fully digital, thereby forcing prescribing in connection with the electronic patient record and avoiding fraud by copying printed or written prescriptions. After completing the roll-out of the pharmaceutical prescriptions (or in parallel with the final steps), we will move to the remaining types of prescriptions and decide how and when full "de-materialisation" will take place, liberating us from the paper-based prescriptions, except in emergencies such as power breaks or other catastrophes.

References

1. Theilgaard, J., "Message Implementation Guide for Prescription", version 1.0, 21.03.97 for the CoCo project, on behalf of Medcom, Denmark. Zipped file (120 K) of a Word- document of 117 pages.
2. English web report of the original theoretical EMP study http://minf.vub.ac.be/∼marc/rapemvnewe/ (last accessed December 8th 2014).
3. Recip-e project webpage http://recip-e.b (last accessed December 8th 2014).
4. Stroetmann, K. A., Jones, T., Dobrev, A. and Stroetmann, V. N., "eHealth is Worth it", The economic benefits of implemented eHealth solutions at ten European sites, European Commission, 2006, Information Society and Media, available via www.ehealth-impct.org, ISBN 92-79-02762-X.
5. Öhlund, S.-E., "ePrescribing Implementation in Sweden", WM-data Kalmar, Sweden, available via www.wmdata.com, 2006.
6. Ministry of Health, Welfare and Sport, Netherlands, "ICT in Dutch Healthcare: An International Perspective", May 2006, available via www.minvws.n (last accessed on May 24th 2013).
7. Stroetmann, K. A., Dobrev, A., Lilischkis, S. and Stroetmann, V. "eHealth priorities and strategies in European countries", eHealth ERA report, March 2007, http://ec.europa.eu/information_society/activities/health/docs/policy/200703/ehealthera-countries.pd   (last accessed June 1st 2014).
8. Data Protection Working Party, Article 29, "Working Document on the processing of personal data relating to health in electronic health records (EHR)", February 15 2007, http://europa.eu.int/comm/justice_home/fsi/privacy/index_en.htm (last accessed on December 8th 2014).
9. Belgian Privacy Commission: http://www.privacycommission.be/ (last accessed December 8th 2014).
10. Vandenberghe, A., Kmehr-Bis support site (KMEHR specifications) available via website: https://www.ehealth.fgov.be/standards/kmehr/ (last accessed December 11th 2014).
11. Beun, J. G., Jansen, P., Bakker, A. and Branger, P., "Zorg Identificatie/Identification Santé (ZIS), Vooronderzoek. Voorbereiding implementatie Zorg Identificatie nummer (ZIN) Een analyse van Aspecten die spelen bij implementatie van het persoonsgebonden nummer in de zorg", Netherlands, 2002.
12. Laws and decrees: K.B. 10 August 2005, B.S. 20 September 2005, KB 21 December 2001.
13. RIZIV: (Dutch) Geneesmiddelen en andere farmaceutische verstrekkingen – Reglementaire documenten – Het geneesmiddelenvoorschrift.
14. http://www.riziv.fgov.be/drug/nl/pharmacists/papers/prescriptions/index.htm (last accessed November 22nd 2014).
15. BCFI-CBIP: Belgisch Centrum voor Farmacotherapeutische Informatie, http://www.bcfi.be/, (last accessed December 8th 2014).
16. CEN-TC-251 Secretariat, "European Standardisation of Health Informatics, Results of the mandated work by CEN- TC-251", June 2001.

Quantitative Coronary Analysis Using 3D Coronary Reconstruction Based on Two Biplane Angiographic Images: A Validation Study

Panagiotis K. Siogkas, Lambros S. Athanasiou, Antonis I. Sakellarios, Kostas A. Stefanou, Themis P. Exarchos, Michail I. Papafaklis, Katerina K. Naka, Lampros K. Michalis, and Dimitrios I. Fotiadis

Abstract

The mortality rate due to Cardiovascular Diseases is constantly gaining ground worldwide. Therefore, the early detection of coronary hemodynamic abnormalities is a non-trivial matter in today's clinical practice. The assessment of coronary lesions is made using either invasive imaging techniques or by measuring the Fractional Flow Reserve value which also requires the use of a dedicated pressure wire. In this work, we present our newly developed novel 3-Dimensional Quantitative Coronary Analysis reconstruction method and its' validation by comparing it to an already validated commercial 3D-QCA software. We used the volumes of the 7 3D reconstructed arterial segments as well as the virtual Functional Assessment Index values as validation metrics to compare the two methods. The obtained results show a very high correlation between the two methods presenting very high r^2 values (0.98 and 0.99) and a very strong agreement between them.

P. K. Siogkas · L. S. Athanasiou · A. I. Sakellarios
D. I. Fotiadis (✉)
Unit of Medical Technology and Intelligent Information Systems, Department of Materials Science and Engineering, University of Ioannina, 45110 Ioannina, Greece
e-mail: fotiadis@cs.uoi.gr

P. K. Siogkas
e-mail: psiogkas@cc.uoi.gr

L. S. Athanasiou
e-mail: lmathanas@cc.uoi.gr

A. I. Sakellarios
e-mail: ansakel@cc.uoi.gr

K. A. Stefanou · T. P. Exarchos · D. I. Fotiadis
Biomedical Research Department, IMBB, FORTH, 45110 Ioannina, Greece
e-mail: kstefan@cc.uoi.gr

T. P. Exarchos
e-mail: exarchos@cc.uoi.gr

M. I. Papafaklis · K. K. Naka · L. K. Michalis
Department of Cardiology in Medical School, Michaelideion Cardiac Center, University of Ioannina, 45110 Ioannina, Greece
e-mail: m.papafaklis@yahoo.com

K. K. Naka
e-mail: anaka@cc.uoi.gr

L. K. Michalis
e-mail: lmihalis@cc.uoi.gr

1 Introduction

According to the latest stats from the World Health Organization (WHO), the most predominant causes of mortality worldwide are heart diseases, and more specifically CardioVascular Diseases (CVD), such as ischaemic heart diseases and strokes. Moreover, the mortality rate has followed an increasing trend when compared to the respective data from the past decade. The diseases of the coronary vasculature are considered to be the most fatal between CVD's. There are several invasive or semi-invasive imaging modalities that allow the clinician to assess the status of the coronary arterial network, the most common of which are Optical Coherence Tomography (OCT), IntraVascular UltraSound (IVUS), biplane angiography, Computed Tomography (CT) etc.

In many cases, these imaging techniques are not sufficient to draw a safe conclusion on the hemodynamic state of a coronary vessel. The most widely known technique to assess the hemodynamic status of a diseased coronary vessel is the Fractional Flow Reserve measurement (FFR). The FFR value is determined by calculating the ratio between the pressure distal from the lesion and the pressure proximal to the lesion, as it is shown in Eq. 1 [1]:

$$FFR_{myo} = \frac{P_d}{P_a}, \qquad (1)$$

where P_a is the pressure proximal (aortic pressure) and P_d the pressure distal to the stenosis. A stenosis is characterized as severe when the FFR value is below 0.8 (Fig. 1).

Fig. 1 Graphical representation of FFR assessment

The continuous enhancement of the aforementioned imaging techniques has constituted the accurate 3-dimensional (3D) reconstruction of the artery of interest a trivial matter. Numerous 3D reconstruction techniques have been documented in the literature. The most accurate combine the fusion of two imaging modalities such as CT and angiography [2], IVUS and angiography [3, 4] or OCT and angiography [5]. Recently, however, several efforts have been made to create 3D arterial models from a single modality [6].

The aforementioned 3D arterial models, when combined with Computational Fluid Dynamics (CFD) simulations allow the calculation of crucial hemodynamic parameters such as wall shear stress (WSS) as well as pressure values throughout the vessel. Several publications can be found in current literature on the aforementioned matter [7–19].

In this work, we validate our newly developed 3D-QCA reconstruction method, comparing it to an already validated 3D-QCA commercial software [6] for 7 arterial segments, regarding the volume of the generated 3D models, as well as the calculated virtual Functional Assessment Index (vFAI).

2 Materials and Methods

2.1 Dataset

Our dataset constitutes of 2 Right Coronary Arteries (RCA), 1 Left Circumflex Artery (LCx) and 4 Left Anterior Descending (LAD) arteries. Each patient was subjected to a biplane angiography exam under the consent of the Ethics Committee [20].

2.2 3D Reconstruction-QCA Method

The 7 arterial segments were reconstructed using our novel in-house developed method based on biplane coronary angiography. The user manually marks the luminal borders of the artery of interest in two angiographic projections. Then the centerline is automatically detected by our algorithm in each projection and n equidistant points are selected in each centerline. The centerline that is detected is extracted in 3D so that it can be used in the next step. For each

centerline, the respective perpendicular line in each of the n points is computed. In each projection, the perpendicular lines intersect the luminal borders of the artery projections in two points $P_1^{Ang}, P_1^{Ang'}$, having a distance r_1^{P1} and r_1^{P2} from the first and second luminal border, respectively. Then for each of the n points, n circles (contours) are computed having radius r_1 calculated as:

$$r_1 = \frac{r_1^{P1} + r_1^{P2}}{2}. \tag{2}$$

Figure 2 depicts the aforementioned reconstruction method. The generated contours are placed perpendicularly on the 3D centerline that was previously created, thus generating the 3D arterial model.

2.3 Blood Flow Simulations

In order to compare and validate our 3D-QCA reconstruction method, we calculated the vFAI value for each case using both 3D-QCA methods. In order to calculate the vFAI, we used the method proposed in [20]. The finite element blood flow simulation parameters are described below.

2.3.1 Rigid Wall Assumption
The Navier-Stokes and the continuity equations were used to model blood flow:

$$\rho \frac{\partial \mathbf{v}}{\partial t} + \rho(\mathbf{v} \cdot \nabla)\mathbf{v} - \nabla \cdot \boldsymbol{\tau} = 0, \tag{3}$$

$$\nabla \cdot (\rho \mathbf{v}) = 0, \tag{4}$$

where $\mathbf{v}$ is the blood velocity vector and $\boldsymbol{\tau}$ is the stress tensor, which can be defined as:

$$\boldsymbol{\tau} = -p\delta_{ij} + 2\mu\varepsilon_{ij}, \tag{5}$$

where δ_{ij} is the Kronecker delta, μ is the blood dynamic viscosity, p is the blood pressure and ε_{ij} is the strain tensor calculated as:

Fig. 2 3D reconstruction using the proposed 3D-QCA method
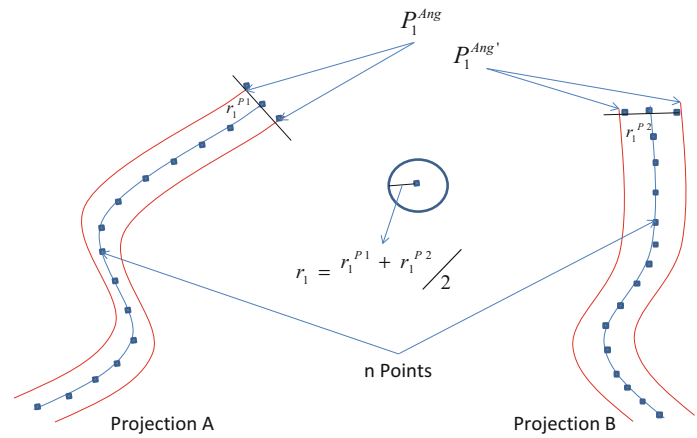
$$\varepsilon_{ij} = \frac{1}{2}\left(\nabla\mathbf{v} + \nabla\mathbf{v}^T\right). \tag{6}$$

Blood was treated as Newtonian fluid with density 1050 kg/m^3 and dynamic viscosity 0.0035 Pa s. Blood flow was considered laminar and incompressible. The Reynolds number ranged from 229 to 830.

2.3.2 Boundary Conditions

At the inlet, a pressure value of 100 mm Hg was used in all cases, corresponding to the average aortic pressure in humans.

At the outlet, we applied a fully developed flow (steady-state). In each case we performed two separate simulations, applying flows of 1 ml/s and 3 ml/s, respectively. These values correspond to the average blood flow during rest and under stress (as obtained under the induction of hyperemia using adenosine), respectively. Finally, the pressure gradient was calculated in each case using the pressure at the inlet (P_a) and the outlet (P_d). The obtained results were then used to create the artery-specific pressure gradient (ΔP)-flow relationship for each case. Then, using Eq. (7), we calculated the vFAI for each case, which corresponds to the actual FFR value of each case. The following quadratic equation was used in all cases:

$$\Delta P = 0 + f_v Q + f_s Q^2, \tag{7}$$

where ΔP is the pressure gradient, Q is the flow rate, f_v is the coefficient of pressure loss due to viscous friction and f_s is the coefficient of pressure loss due to flow separation [21]. Regarding the arterial wall, a no-slip boundary condition was employed, indicating that the velocity of blood at the interface between the wall and the lumen is equal to zero.

2.3.3 Mesh

All seven 3D models were discretized into tetrahedral elements with a minimum element face size 0.09 mm and a maximum element face size 0.12 mm. The element size was determined using a mesh sensitivity analysis. The maximum number of iterations for the convergence of the solution was set to 50 and the convergence criterion was set to 10^{-4}.

3 Results

To validate our novel reconstruction method, we chose to compare it to an already validated 3D-QCA commercial software. We reconstructed in 3D 7 arterial segments using the PIE Medical software [20] and then, using the exact same angiographic frames and the same path we performed the reconstruction with our in-house developed algorithm, comparing the volume of the generated 3D models as well as the calculated vFAI values from both methods. Figure 3

Fig. 3 Luminal border segmentation using PIE Medical software (left image) and our algorithm (right image)
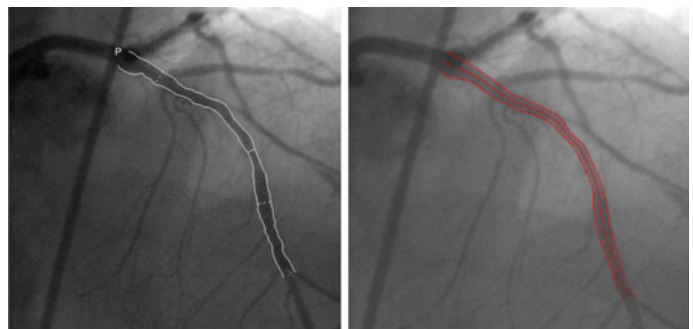
Table 1 Calculated volumes using both reconstruction methods

	Pie medical volume (mm^3)	In-house measured volume (mm^3)	Percentage difference (%)
Patient 1	162.2	165.3	−1.91
Patient 2	161.5	166.4	−3.03
Patient 3	248.5	249.2	−0.28
Patient 4	164.7	163.8	0.55
Patient 5	246.3	255.8	−3.86
Patient 6	108.4	101.8	6.09
Patient 7	246.4	231.2	6.17

depicts the luminal border segmentation for the exact same arterial segment using both methods (Table 1).

From the calculated volumes we can observe that the two methods produce similar results, with the worst case scenario having a difference of 6.17%. Figure 4 depicts the final 3D models for the same case using both methods.

From the correlation diagram (Fig. 5) we can observe a high correlation between the two reconstruction methods with an r^2 value of almost 0.98. Moreover, from the Bland-Altman plot in Fig. 6 we can observe that the two methods have a strong agreement since all produced values are within the range of $\pm 1.96 * SD$.

We also calculated the vFAI values for all cases in order to compare the two reconstruction methods. Table 2 depicts the obtained results. We can observe that the two methods produce almost identical results, presenting a difference of 4.41% in the worst case scenario.

A very high correlation is observed from the following correlation diagram (Fig. 7) between the two methods with the r^2 coefficient reaching a value of nearly 0.99. Furthermore, the respective Bland-Altman diagram (Fig. 8) shows a very high agreement between the two methods since all values are within the range of $\pm 1.96 * SD$.

Fig. 4 3D representation of the same reconstructed case from PIE Medical (left image) and our algorithm (right image)

Fig. 5 Correlation diagram of calculated 3D model volumes

Correlation between In House Method-PIE Medical

$y = 1.0032x - 1.2493$
$R^2 = 0.9793$

Fig. 6 Bland-Altman plot regarding the calculated volumes
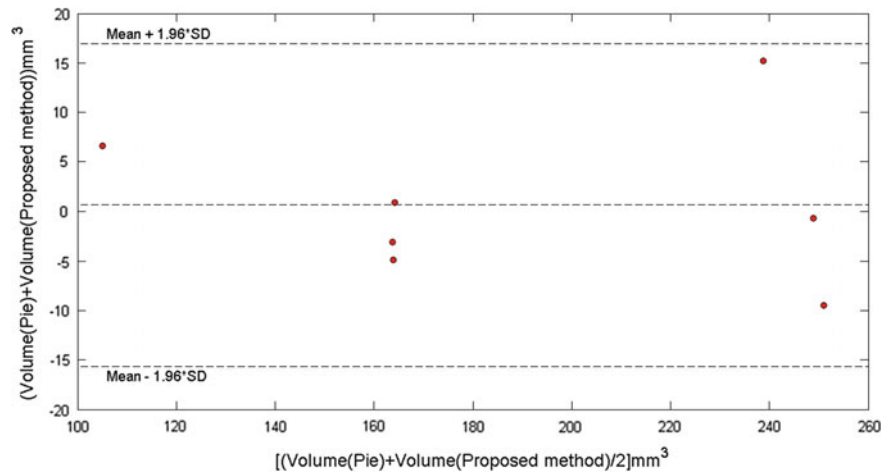
Table 2 Calculated vFAI values for both reconstruction methods

	vFAI pie medical	vFAI in-house method	Percentage difference (%)
Patient 1	0.68	0.65	4.41
Patient 2	0.26	0.26	0.00
Patient 3	0.64	0.66	−3.13
Patient 4	0.77	0.74	3.90
Patient 5	0.93	0.9	3.23
Patient 6	0.69	0.66	4.35
Patient 7	0.85	0.87	−2.35

Fig. 7 Correlation diagram of calculated 3D model vFAI values
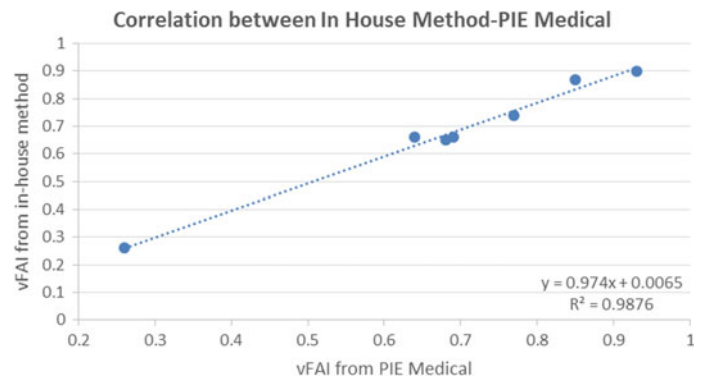
Fig. 8 Bland-Altman plot regarding the calculated vFAI values
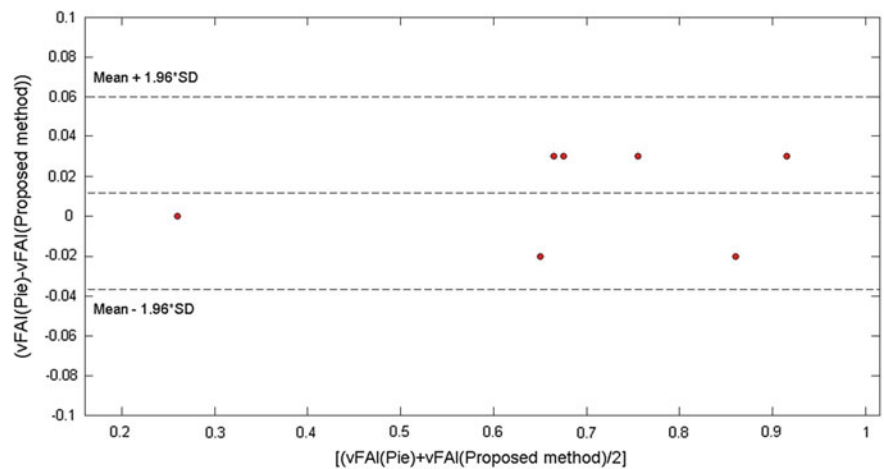
4 Discussion

In this work, we presented a validation study of our newly developed novel 3D-QCA reconstruction algorithm. Our dataset contained 7 arterial segments with mild or severe lesions. All cases were reconstructed using both methods and two validation metrics were used to examine the efficacy of our proposed reconstruction method. We compared the two modules by calculating the volumes of the final 3D models as well as the vFAI values for all cases. The obtained results showed an excellent correlation regarding both calculated values for the two methods with very high correlation coefficient values. Moreover, the generated Bland-Altman plots presented a very strong agreement between the two reconstruction methods. This fact constitutes our newly proposed reconstruction method a powerful tool for the clinician, since, when combined with the vFAI calculation process, it can assess the severity of a coronary lesion by utilizing only two biplane angiographic images.

The limitation of our study lies on the relatively small dataset that was used. However, we currently create a larger dataset to enhance the validation strength of our newly created 3D-QCA reconstruction method.

5 Conclusions

The present study validated the efficacy of our newly created 3D-QCA reconstruction algorithm by comparing it to an already validated 3D-QCA software. The use of the aforementioned algorithm makes the estimation of the severity of coronary lesions almost non-invasive, since it requires only an angiographic exam, which is a routine examination in everyday clinical practice.

Conflict of Interest The authors declare that they have no conflict of interest.

References

1. K. Govindarajua, I.A. Badruddina, G. N. Viswanathanb, *et al.*, "Evaluation of functional severity of coronary artery disease and fluid dynamics' influence on hemodynamic parameters: A review," *Physica Medica,* in press, 2012, https://doi.org/10.1016/j.ejmp.2012.03.008.

2. A.G. van der Giessen, M. Schaap, F.J. Gijsen, et al., "3D fusion of intravascular ultrasound and coronary computed tomography for in-vivo wall shear stress analysis: a feasibility study," *International Journal of Cardiovascular Imaging*, vol. 26(7), pp. 781–796, 2010.

3. C.V. Bourantas, I.C. Kourtis, M.E. Plissiti, *et al.*, "A method for 3D reconstruction of coronary arteries using biplane angiography and intravascular ultrasound images," *Computerized Medical Imaging and Graphics*, vol. 29(8), pp. 597–606, 2005.

4. C.V. Bourantas, F.G. Kalatzis, M.I. Papafaklis, *et al.,* "ANGIO-CARE: an automated system for fast three dimensional coronary reconstruction using angiographic and intracoronary ultrasound data," *Catheterization and Cardiovascular Interventions*, vol. 72 (2), pp. 166-75, 2008.

5. L.M. Athanasiou, C.V. Bourantas, P.K. Siogkas, *et al.,* "3D reconstruction of coronary arteries using Frequency Domain Optical Coherence Tomography images and biplane angiography," Conf Proc IEEE Eng Med Biol Soc, vol. 2012, pp. 2647–50, 2012.

6. J.C. Schuurbiers, N.G. Lopez, J. Ligthart, F.J. Gijsen, J. Dijkstra, P.W. Serruys, A.F. Van der Steen, J.J. Wentzel, "In vivo validation of CAAS QCA-3D coronary reconstruction using fusion of angiography and intravascular ultrasound (ANGUS)," *Catheter Cardiovasc Interv.,* vol. 73(5), pp. 620–626, 2009.

7. M. Malve, A. Garcia, J. Ohayon, *et al.*, "Unsteady blood flow and mass transfer of a human left coronary artery bifurcation: FSI vs. CFD," *International Communications in Heat and Mass Transfer,* vol. 39(6), pp. 745–751, 2012.

8. D. Bluestein, Y. Alemu, I. Avrahami, *et al.*, "Influence of microcalcifications on vulnerable plaque mechanics using FSI modeling," *Journal of Biomechanics*, vol. 41, pp. 1111–1118, 2008.

9. A. Borghi, N.B. Wood, R.H. Mohiaddin, *et al.*, "Fluid-solid interaction simulation of flow and stress pattern in thoracoabdominal aneurysms: A patient-specific study," *Journal of Fluids and Structures*, vol. 24(2), pp. 270–280, 2008.

10. S.A. Kock, J.V. Nygaard, N. Eldrup, *et al.*, "Mechanical stresses in carotid plaques using MRI-based fluid-structure interaction models," *Journal of Biomechanics,* vol. 41(8), pp. 1651–1658, 2008.

11. J.R. Leach, V.L. Rayz, M.R.K. Mofrad, *et al.* "An efficient two-stage approach for image-based FSI analysis of atherosclerotic arteries." *Biomechanics and Modeling in Mechanobiology,* vol. 9 (2), pp. 213–223, 2010.

12. B. Vahidi, and N. Fatouraee, "Large deforming buoyant embolus passing through a stenotic common carotid artery: A computational simulation," *Journal of Biomechanics*, vol. 45(7), pp. 1312–1322, 2012.

13. R. Torii, M. Oshima, T. Kobayashi, *et al.*, "Fluid-structure interaction modeling of a patient-specific cerebral aneurysm: influence of structural modeling," *Computational Mechanics*, vol. 43(1), pp. 151–159, 2008.

14. S.H. Lee, H.G. Choi, and J.Y. Yoo, "Finite element simulation of blood flow in a flexible carotid artery bifurcation," *Journal of Mechanical Science and Technology*, vol. 26(5), pp. 1355–1361, 2012.

15. M.X. Li, J.J. Beech-Brandt, L.R. John, *et al.*, "Numerical analysis of pulsatile blood flow and vessel wall mechanics in different degrees of stenoses," *Journal of Biomechanics*, vol. 40(16), pp. 3715–3724, 2007.

16. X.H. Wang, and X.Y. Li, "Fluid-structure interaction based study on the physiological factors affecting the behaviors of stented and non-stented thoracic aortic aneurysms," *Journal of Biomechanics*, vol. 44(12), pp. 2177–2184, 2011.

17. J. Lantz, J. Renner, and Karlsson M., "Wall Shear Stress in a Subject Specific Human Aorta - Influence of Fluid-Structure Interaction," *International Journal of Applied Mechanics*, vol. 3 (4), pp. 759–778, 2011.

18. Vavourakis, Y. Papaharilaou, and J.A. Ekaterinaris, "Coupled fluid-structure interaction hemodynamics in a zero-pressure state corrected arterial geometry," *Journal of Biomechanics*, vol. 44 (13), pp. 2453–2460, 2011.

19. S.J. Park, J.M. Ahn, N.H. Pijls, *et al.*, "Validation of functional state of coronary tandem lesions using computational flow dynamics." *Am J Cardiol.* 110(11): 1578–84, 2012.

20. M.I. Papafaklis, T. Muramatsu, P.W. Serruys, *et al.,* "Fast virtual functional assessment of intermediate coronary lesions using routine angiographic data and blood flow simulation in humans: comparison with pressure wire - fractional flow reserve," *Eurointervention*, vol. 10(5), pp. 574–583. 2014.

21. D.F. Young, "Fluid Mechanics of Arterial Stenoses," *J Biomech Eng*. Vol. 101, pp. 157–75, 1979.

mHealth Platform for Parkinson's Disease Management

Dimitrios Gatsios, George Rigas, Dragana Miljkovic,
Barbara Koroušić Seljak, Marko Bohanec, Maria T. Arredondo,
Angelo Antonini, Spyros Konitsiotis, and Dimitrios I. Fotiadis

Abstract

Parkinson's is a complicated, chronic disease that most people live with for many years/decades. For this reason, a multidisciplinary disease management, involving several professions working together (neurologists, physiotherapists, speech and language therapists, occupational therapists, dieticians), is important to ensure that the patient retains his/her independence and continues to enjoy the best quality of life possible. To address these needs we describe an mhealth ecosystem for Parkinson's disease (PD) management facilitating the collaboration of experts and empowering the patients to self-manage their condition.

D. Gatsios · G. Rigas · D. I. Fotiadis (✉)
Unit of Medical Technology and Intelligent Information Systems,
Department of Materials Science and Engineering, University of
Ioannina, 45110 Ioannina, Greece
e-mail: fotiadis@cc.uoi.gr

D. Gatsios
e-mail: dgatsios@cc.uoi.gr

G. Rigas
e-mail: rigas@cs.uoi.gr

S. Konitsiotis
Department of Neurology, Medical School, University of
Ioannina, 45110 Ioannina, Greece
e-mail: skonitso@cc.uoi.gr

A. Antonini
Department for Parkinson's Disease, IRCCS San Camillo, Via
Alberoni 70, 30126 Venice, Italy
e-mail: angelo.antonini@ospedalesancamillo.net

M. T. Arredondo
Life Supporting Technologies, Universidad Politécnica de Madrid,
Avenida Complutense 30, 28040 Madrid, Spain
e-mail: mta@lst.tfo.upm.es

D. Miljkovic · M. Bohanec
Department of Knowledge Technologies, Jozef Stefan Institute,
Jamova 39, 1000 Ljubljana, Slovenia
e-mail: dragana.miljkovic@ijs.si

M. Bohanec
e-mail: marko.bohanec@ijs.si

B. K. Seljak
Computer Systems Department, Jozef Stefan Institute, Jamova 39,
1000 Ljubljana, Slovenia
e-mail: barbara.korousic@ijs.si

1 Introduction

Parkinson's disease affects people of all races and cultures. The facts are startling. Around 6.3 million people have the condition worldwide—that's less than one percent of the total population [1]. More than one million people live with Parkinson's in Europe today and this number is forecast to double by 2030 [2]. It is the second most common neurodegenerative disease (after Alzheimer's disease) and its prevalence will continue to grow as the population ages. The economic impact of the disease is high and its annual European cost is estimated at €13.9 billion [3].

Even though many different studies can be found in the literature addressing specific aspects of the disease there are only a few research efforts that adopt a holistic approach in order to address the disease management. The PERFORM [4], the REMPARK [5] and the SENSE-PARK [6] systems are intelligent closed-loop systems that seamlessly integrate a range of wearable sensors (mainly accelerometers and gyroscopes) constantly monitoring several motor signals of the patients and enabling the prescribing clinicians remotely assess the status of the patients, adjust medication schedules and personalize treatment. In addition, the REMPARK system includes a belt-worn movement sensor that detects in real time movement alterations that activate an auditory cueing system controlled by a smartphone in order to improve patient's gait. CuPiD [7] is a closed-loop system for personalized and at-home rehabilitation focusing on freezing of gait.

The PD_manager system proposes a holistic mobile approach based on a set of unobtrusive, simple-in-use, off-the-self, co-operative, mobile devices (a smartphone, an insole and a wristband). It covers aspects such as patients' and caregivers training and focuses on adherence to the

medical recommendations. Moreover, the open, based on the Internet of Things concept, knowledge management platform that will be developed as well as the studies analysing the clinicians diagnostic and prescribing behaviour and the mobile apps for empowering patients adhere to nutrition and physiotherapy plans are novel and along with the effort to build a Decision Support System (DSS) that suggests modifications in the medication plan take the PD management a step beyond the existing systems.

The approach that is being followed for the development of the PD_manager system is:

Phase 1—Modelling of the behaviours of intended users of (patients, caregivers, prescribing neurologists and other healthcare providers). User needs analysis will examine current practices around every-day and specialist management of Parkinson's disease, and identify where these practices may be enhanced or complemented by technological and/or process support. Detailed studies of the analytical strategies and knowledge sets used by expert health-care providers (e.g., neurologists undertaking diagnosis activities) will inform the design of a DSS embedded within PD_manager. At the same time, the policy and ethical framework under which Parkinson's disease is managed will be assessed. These outcomes of behavioural modelling will be validated within a computational modelling framework, which will establish the viability of, and constraints on, the PD_manager support environment.

Phase 2—Assessment of symptoms (initially of motor with data collected prospectively from 20 advanced patients with motor complications). Obtaining long-term, objective information on motor status using an unobtrusive approach, that minimizes visits to the clinicians' office, is very important for the assessment of disease progression. Specifically, the patient, with the support of his/her caregiver, will be able to monitor occurrence of motor symptoms such as tremor, dyskinesia, bradykinesia, gait, posture, balance, with the sensor insole, as well as the accelerometers of the wristband and of the smartphone that will provide the necessary raw data needed for that purpose. Data for non-motor symptoms, including the emotional state, cognitive status, speech disturbances and sleep disorders the patient may be experiencing will provide to clinicians a more complete picture.

Phase 3—Analysis and validation of strategies that help physicians and healthcare professionals to search and evaluate the most diagnostic information (i.e., the information that is most relevant to help PD patients to cope with their symptoms, relief from them and make the best of their resources). Usually consultations are very short so the feedback needs to be short and integrated into the daily working routine of the health professional. Moreover, medical staff and patients usually decide the treatment plan

and its modifications together—shared decision making. This decision making is on the basis of subjective experiences by the patient/carer (self-report), and on the basis of objective assessment (available thanks to PD_manager) of motor, cognitive, and non-cognitive symptoms, as well as the level of adherence to the suggested management plan (with information about medication, nutrition, physiotherapy and daily activity). Furthermore, objective data ought to be combined with subjective symptoms (e.g., depression, impulse control disorders, and cognitive dysfunction) referred to by the patients to gain a holistic view on the patient's state. This holds true especially at the stage in which PD patients' response to medications becomes unpredictable and clinicians have to make decisions about whether and what changes in the disease management should be made. Thus personalized suggestions for an optimal PD management plan will be provided by the PD_manager DSS that will be based on expert decision-making strategies and data mining and will be calibrated by the treating neurologist before referring it to the patient.

Phase 4—System evaluation. 100 patients and 100 controls will be recruited during the pilot activities of the system. In addition to the evaluation of the usability and usefulness of the developed platform and mobile apps a detailed study for the potential of PD_manager as a new care model in terms of health outcomes, quality of life, care efficiency gains and economic benefits will also be conducted.

2 Materials and Methods

2.1 Overall Architecture

The PD_manager overall architecture is provided in Fig. 1. The mobile part, i.e. the gathering of data using as hub iOS, Android and Windows Phone devices and data transmission to the PD_manager cloud infrastructure, the implementation of mobile apps and their hosting will be handled by Globo's proprietary platform [8]. The cloud infrastructure (services, data management and storage etc.) will be hosted by Biotronics 3D [9].

The sensors, Clowdflows for data mining and analytics and Dexi for building DSS are presented in the next sections.

2.2 Data Collection

For the initial needs of the research activities, and especially for the monitoring and assessment of motor symptoms, data from 20 patients will be captured prospectively. Each of the Fondazione Ospedale San Camillo (in Venice), Fondazione Santa Lucia (in Rome), University of Ioannina and

Fig. 1 The overall PD_manager
architecture

University of Surrey, will enrol 5 patients. The consenting hospitalised, enrolled patients will be asked to use the wristband and the sensor insole for 30 days at their home environment. The annotated data, which will be captured 24/7, include:

- Measurements for distribution of pressure, acceleration, weight-bearing, balance and motion sequences that will become available from the insole sensor manufactured by Moticon [10].
- Continuous heart rate patterns (with optical blood flow sensor), motion (with 3-axis accelerometer and gyrometer), skin conductivity measurements (with galvanic skin response (GSR) sensors), activity (metrics for steps, calories burned, duration accurately measured thanks to the built in GPS) and periods of restful and light sleep that will be captured with the Microsoft Band [11].

2.3 Motor Symptoms Evaluation

Tremor, Bradykinesia, Dyskinesia, Gait and Postural Balance will be assessed mainly with the OpenGo system (Moticon). The OpenGo is based on a fully integrated, ultrathin and flexible sensor insole (that can measure frequencies at 5, 10, 25, 50, 100 Hz). With respect to the analysis of motor symptoms, the sensor insole is capable to continuously measure the centre of foot pressure (COP), the partial weight-bearing as well as the tri-axial acceleration. These parameters can serve for further analysis of staggering, dysbalance, gait variance, foot loading as well as for fall detection or position monitoring. Analysis of the motor

symptoms of the upper limbs and body will be based on signals received from the accelerometers and gyroscopes built in smartphones and the wristband.

The most interesting results of the relevant, on-going research by the involved groups include:

- a methodology for the automated levodopa-induced dyskinesia (LID) assessment [12, 13].
- a method detecting freezing of gait (FoG) events [14].
- an automated method for analysis and detection of gait parameters, i.e. gait modelling in PD [15].
- a smart algorithm for the bradykinesia detection [16].

2.4 Data Mining

The PD_manager data mining module will address the problem of prediction of PD symptoms and their severity. The goal is to monitor patient's status, evaluate existing therapy and, when necessary, suggest the new therapy plan.

The study will consist of two phases. In the first phase the work will be done with raw data for patient's symptoms, therapy, adherence to disease management plans and any other available data to analyse the patient's status. The analysis will be done throughout the rule discovery process mainly with association rule mining algorithms. In the second phase methods for the automatic recognition of symptoms based on time series data will be developed. This prediction will be performed mainly by using decision trees. To improve the predicting accuracy, the possibility of using some ensemble methods, like bagging and boosting, will be explored.

The PD_manager data mining module will be implemented as workflows of data processing and data mining algorithms and will be included into the novel web-based data mining platform ClowdFlows [17]. The implementation of this module in the form of workflows provides the benefits of repeatability of such workflows and potential sharing results between different users. The platform has user-friendly graphical user interface which facilitates efficient feature selection, and wider selection of applicable data mining and machine learning algorithms even from non-experts such as the intended end users, i.e. the clinicians.

2.5 Decision Support System

The PD_manager's DSS supports the physician their monitoring of patients and deciding about their therapies. The DSS will employ mechanisms (models) that transform the stream of measured patient's data into suggested therapy plans. This is a complex and typically a multi-stage process. In the context of PD_manager, the two most important stages are: (a) from patient data to recognise symptoms (to identify patient's status), and (b) from symptoms to proposed decisions (to formulate necessary actions, treatment plans, prescriptions). For both stages, corresponding models will have to be developed and implemented in the DSS. However, it is unlikely that all the needed information could be extracted from data, which could also suffer from other possible imperfections (incompleteness, insufficient quantity, various errors and noise). For this reason, we will supplement the data mining models with expert-developed models. There are several possible ways to combine the two, for instance by model revision [18], where an initial model is developed by an expert and then algorithmically modified to better correspond to some given data stream. A similar approach can be used to address another difficult challenge in PD_manager, the need to personalize the DSS models to features of individual patients.

In PD_manager, the primary method for the development of expert-developed models will be DEX [19]. DEX is a qualitative multi-criteria modelling approach, aimed at the assessment and analysis of decision alternatives. DEX models have a hierarchical structure, which represents a decomposition of some decision problem into smaller, less complex sub-problems. The hierarchy is formulated in terms of qualitative (symbolic) attributes and decision rules. DEX has already been successfully used in healthcare [20, 21].

2.6 Mobile Apps for Patients, Caregivers and Clinicians

The mobile apps that will expose the decision support functionalities are:

- The clinicians' app through which periodic reports with major events for the patients will be available and suggestions for modifications will be made, mainly, for the medication plan based on the holistic picture of the patient. Moreover, clinicians will be able to collaborate with the other healthcare providers (neurologists, physiotherapists, speech and language therapists, occupational therapists, dieticians) involved in the management of PD patients.
- The patients' app through which recommendations for modifications in medication, diet, physiotherapy and activity will be sent to the patient.
- The caregiver app will have alerts when the patient is in danger, e.g. in case of falls. The app will also provide feedback about symptoms as well as the patient's adherence to the management plan in order to motivate him comply with it and improve his condition. Recommendations for plan modifications will also be sent to the caregiver in order to ensure that the patient will adopt them.

2.7 Evaluation—Pilot Activities

The PD_manager system with the DSS in its core will be evaluated with the following approach:

Evaluation: outline of the stages of the clinical trial

- Ethical approvals and research governance will be completed in each site.
- Recruitment: 200 consenting patients with Parkinson's will be enrolled to the study through clinical centres in Ioannina, Surrey, Venice and Rome. Patients with motor fluctuations and significant disability (Hoehn and Yahr stage 3 or greater) and with at least 2 h off time during the day (based on MDS-UPDRS) will be eligible for the trial.
- Baseline data collection will be conducted in each site by a local researcher covering age, gender, indicator of social status, time since Parkinson's diagnosis, disease stage, medications, and comorbidities. Baseline recording of outcome measures will also be undertaken.

- Group assignment: Participants will be randomly assigned to receive either the PD_manager or to be in the control group (i.e. 100 patients in each group). Separate randomisation will be conducted for men and women to ensure an even gender distribution between the groups.
- Intervention: Participants and their caregivers will be trained in how to use the devices and the PD_manager apps. The devices will be unobtrusive. The insole and the wristband do not need to be initiated and they record 24/7. The responsible clinicians in each country will receive a monthly report with the most important information extracted for each patient and with the suggestions of the PD_manager DSS. On the basis of this information, the neurologist will be able to modify the management plan accordingly, and send these modifications to the patients and their caregivers through the mobile apps. The data captured by PD_manager for the 100 patients in the intervention group include: features from motor symptoms; emotional status data (stress, anxiety); sleep quality data; speech abnormalities; data for compulsive behaviours; cognitive status data; data for compliance with the suggested nutrition; adherence to medication data; activity data; physiotherapy data.
- Assessment of outcomes will be undertaken by researchers in each site at the end of the 60 day intervention period. Outcome measures are chosen to show effect of PD_manager:

(a) Clinical effectiveness (both groups)—a range of outcomes will be collected including PD disability, non-motor symptom scale, generic health related quality of life such as SF12, PD specific quality of life e.g. PDQ-8, psychological status, self-efficacy. For carers, the important measurement is the carer strain. Wherever possible, validated scales will be used.
(b) Views about the PD_manager will be collected from patients and carers by telephone interview (in intervention group only). Usefulness, usability and interaction with their neurologist will be explored. PD_manager will generate compliance data and this will be used to assess the extent to which the patients/carers valued using the devices.

(c) All health professionals involved in use of PD_manager will also be invited to take part in a telephone interview to gain feedback on their view of its usefulness, adaptability, interpretation of available data and interaction with the patients.

- An economic evaluation embedded in the clinical trial will assess the resource implications and costs of using PD_manager from the perspective of the health service provider. All health professionals will be asked to keep a log over the 60 day trial period of all activity and tasks they have completed related to the delivery of PD_manager. Using national pay scales, inclusive of on costs and overheads, the cost of the time spent for each professional will be calculated. The health professionals will be asked to keep a similar log for the patients in the control group so that an assessment of the cost difference in the delivery of care to the two groups over the trial period can be estimated. Patients and carers in both groups will also be asked to keep a diary of their use of health and social services during the study period (including that associated with PD_manager). Costs of this service use will be calculated and will be used to explore if PD_manager results in more or less overall service use.
- Data will also be collected from the PD_manager technical team about the costs of running the service (equipment and staff time).

3 Conclusions

The validated PD_manager system will be the first of its kind mhealth solution for the monitoring and management of patients suffering from Parkinson's. The system is applied and engages the whole healthcare ecosystem as it is shown in Fig. 2. The holistic approach described in this paper will combine traditional machine learning and decision support methods with modern mobile first and cloud based approaches in order to deliver an ecosystem for the management of Parkinsonian patients. Data on the clinical outcomes and from the qualitative feedback and economic evaluation will

Fig. 2 The patient-centric, holistic approach provided by the PD_manager ecosystem
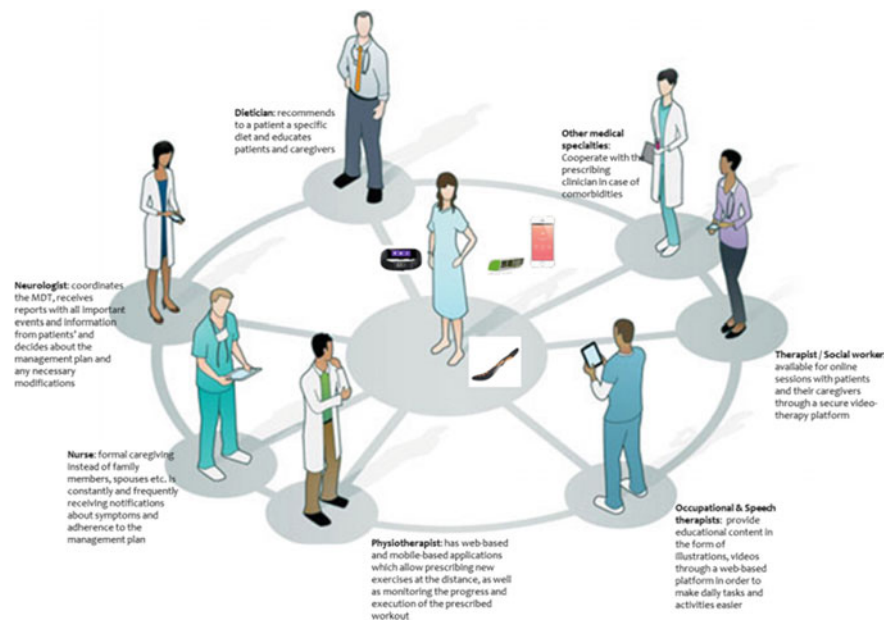
be brought together in a cost-consequences framework that will show the benefits and costs of the system to different groups (patients, carers, neurologists, other HCP). The implications of findings for practice and future research needs will be consolidated.

Conflict of Interest The authors declare that they have no conflict of interest.

References

1. www.epda.eu.com (accessed on 05-06-2015).
2. E. R. Dorsey, R. Constantinescu, J. P. Thompson, K. M. Biglan, R. G. Holloway, K. Kieburtz, F. J. Marshall, B. M. Ravina, G. Schifitto, A. Siderowf, C. M. Tanner, "Projected number of people with Parkinson's disease in the most populous nations, 2005 through 2030," *Neurology*, vol. 68, no. 5, pp. 384–386, 2007.
3. J. Olesen, A. Gustavsson, M. Svensson, H. U. Wittchen, B. Jönsson (on behalf of the CDBE2010 study group and the European Brain Council), "The economic cost of brain disorders in Europe," *European Journal of Neurology,* vol. 19, no. 1, Dec. 2011.
4. A. T. Tzallas, M. G. Tsipouras, G. Rigas, D. G. Tsalikakis, E. C. Karvounis, M. Chondrogiorgi, F. Psomadellis, J. Cancela, M. Pastorino, M. T. Waldmeyer, S. Konitsiotis, D. I. Fotiadis, "PERFORM: a system for monitoring, assessment and management of patients with Parkinson's disease," *Sensors*, vol. 14, no. 11, pp. 21329–57, Nov. 2014.
5. A. Samà, C. Pérez-López, D. Rodríguez-Martín, J. M. Moreno-Aróstegui, J. Rovira, C. Ahlrichs, R. Castro, J. Cevada, R. Graça, V. Guimarães, B. Pina, T. Counihan, H. Lewy, R. Annicchiarico, A. Bayés, A. Rodríguez-Molinero,

J. Cabestany, "A double closed loop to enhance the quality of life of Parkinson's Disease patients: REMPARK system," *Studies in Health Technology and Informatics*, vol. 207, pp. 115–124, 2014.
6. www.sense-park.eu (accessed on 05-06-2015).
7. www.cupid-project.eu (accessed on 05-06-2015).
8. www.globoplc.com/en-GB/overview/ (accessed on 05-06-2015).
9. www.3dnetmedical.com (accessed on 05-06-2015).
10. www.moticon.de (accessed on 05-06-2015).
11. www.microsoft.com/Microsoft-Band (accessed on 05-06-2015).
12. M. G. Tsipouras, A. T. Tzallas, G. Rigas, S. Tsouli, D. I. Fotiadis, S. Konitsiotis, "An automated methodology for levodopa-induced dyskinesia: assessment based on gyroscope and accelerometer signals," *Artificial Intelligence in Medicine*, vol. 55, no. 2, pp. 127–135, Jun. 2012.
13. M. G. Tsipouras, A. T. Tzallas, D. I. Fotiadis, S. Konitsiotis, "On automated assessment of Levodopa-induced dyskinesia in Parkinson's disease," *Engineering in Medicine and Biology Society, EMBC, 2011 Annual International Conference of the IEEE,* pp. 2679–2682, 2011.
14. E. Tripoliti, A. T. Tzallas, M. G. Tsipouras, G. Rigas, P. Bougia, M. Leontiou, S. Konitsiotis, M. Chondrogiorgi, S. Tsouli, D. I. Fotiadis, "Automatic detection of freezing of gait events in patients with Parkinson's disease," *Computer Methods and Programs in Biomedicine,* vol. 110, no. 1, pp. 12–26, Apr. 2013.
15. J. Cancela, M. Pastorino, M. T. Arredondo, K. S. Nikita, F. Villagra, M. A. Pastor, "Feasibility Study of a Wearable System Based on a Wireless Body Area Network for Gait Assessment in Parkinson's Disease Patients," *Sensors*, vol. 14, no. 3, pp. 4618–4633, Mar. 2014.
16. M. Pastorino, J. Cancela, M. T. Arredondo, M. Pansera, L. Pastor-Sanz, F. Villagra, J. A. Martin, "Assessment of bradykinesia in Parkinson's disease patients through a multi-parametric system. *Engineering in Medicine and Biology Society, EMBC, 2011 Annual International Conference of the IEEE,* pp. 1810–1813), 2011.
17. J. Kranjc, J. Smailović, V. Podpečan, M. Grčar, M. Žnidaršič, N. Lavrač, "Active learning for sentiment analysis on data streams: Methodology and workflow implementation in the ClowdFlows

platform," *Information Processing & Management*, Vol. 51, no. 2,, pp. 187–203, Mar. 2015.

18. M. Žnidaršič, M. Bohanec, "Automatic revision of qualitative multi-attribute decision models," *Foundations of Computing and Decision Sciences,* vol. 32, no. 4, pp. 315–326, 2007.

19. M. Bohanec, V. Rajkovič, I. Bratko, B. Zupan, M. Žnidaršič, "DEX methodology: Three decades of qualitative multi-attribute modelling," *Informatica*, vol. 37, no. 1, pp. 49–54, 2013.

20. M. Bohanec, B. Zupan, V. Rajkovič, "Applications of qualitative multi-attribute decision models in health care," *International Journal of Medical Informatics,* vol. 58–59, pp. 191–205, 2000.

21. O. Šušteršič, U. Rajkovič, D. Dinevski, E. Jereb, V. Rajkovič, "Evaluating patients' health using a hierarchical multi-attribute decision model," *Journal of international medical research*, vol. 37, no. 5, pp. 1646–1654, 2009.

Design of a Serious Game to Increase Physical Activity by Adding Direct Benefits to the Game for Conducting Sport Activities

René Baranyi, Dennis M. Binder, Nadja Lederer, and Thomas Grechenig

Abstract

"Dosis facit venenum," or "the dose makes the poison," as first expressed by Paracelsus, is a universally valid statement. Thus, being a little bit of a sedentary person makes a whole lot of difference when this behavior turns into a lifestyle. If combined with additional poor habits like imbalanced food intake, little physical activity becomes a number one risk factor in developing chronic diseases later on. What is lacking are motivational concepts and tools that pick up "active" as well as "less active couch potatoes" with the purpose to prevent serious health consequences by making sport activities more attractive, interactive, fun and engaging. Thus, lowering the barrier of overcoming one's weaker self is pivotal. In this paper, we propose a novel concept and Android-based prototype of a serious game called *Lazarus*, which aims to prevent chronic disease by using motivational boosts to enhance physical exercise. 117 people helped gathering basic information for the game and another 10 people evaluated the concept adhering to a User Centered Design. The application takes advantage of an approach to reward physical real-life activity (doing sports) with virtual in-game benefits.

1 Introduction

On regular weekdays, people (aged 15–98 years) spend a mean time of 309 min per day sitting according to a study involving 32 European countries [1]. In theory, this is not necessarily a bad thing. Much less so, one might think that an adequate degree of physical activity may balance it out.

However, research suggests that even "active couch potatoes"—people meeting physical activity level guidelines, while experiencing much sedentary time—are at risk in facing adverse health consequences. Breaks in-between longer sitting hours as well as reduced sitting hours overall are highly encouraged [2].

Sedentary behavior, which is defined as sitting or lying, while being awake and expending <= 1.5 metabolic equivalents in energy [3], together with physical inactivity and imbalanced diet are known risk factors for lifestyle diseases, including overweight and obesity, likely yielding nonalcoholic fatty liver disease, type 2 diabetes, certain types of cancer, hypertension, and stroke [4]. Poor lifestyle habits and stressful job routines are seemingly demanding on maintaining physical activeness.

Hence, motivation is probably a very important aspect in terms of regular physical exercises. To increase the motivation, the authors decided to develop the serious game *Lazarus*: by doing sports and "checking in" to a sports location people get benefits within the designed game.

Projects investigating the concept of rewarding physical activity with virtual in-game benefits are already known in the scientific community—a few of them are described below.

Play!Mate encourages users to perform exercises, like jumping up and down, during gameplay. Jumps are captured by accelerometers and, as a direct result, enhance time allowed to navigate a ball through a maze in an open-source game called NeverBall. To account for player-dependent gaming skills, difficulty levels were introduced. A refined *Play!Mate* concept was then applied to the mobile game *Run, Tradie, Run!*, where players may obtain in-game-commodity-boosts in return for physical activity performed during or outside of gameplay [5].

According to Consolvo et al., physical activity promoting applications should meet four key design requirements [6]. Their research project Houston, which consists of a mobile phone-based fitness journal, social interaction software and a pedometer, addresses these requirements, while focusing on increasing people's daily step count. A similar project setup

R. Baranyi (✉) · D. M. Binder · N. Lederer · T. Grechenig
Research Group for Industrial Software, Vienna University of Technology, 1040 Vienna, Austria
e-mail: rene.baranyi@inso.tuwien.ac.at

Fig. 1 Methodology

and goal was adhered to in *Chick Clique*, with the target population being teenage girls [7].

Physical outdoor activity is encouraged in both the application platform prototype *Fitness Adventure* and the prototype *FigureMeter* [8]. In Fitness Adventure, a mobile phone-based game uses location information via GPS to provide a person with a fictional story about people's surroundings, taking into account historic or architecturally relevant buildings, sights or nature trails while doing sports. The prototype *FigureMeter* lets users receive benefits (e.g. virtual assets, special skills) in games and online communities in return for physical activity.

The remainder of this paper is structured as follows: Sect. 2 summarizes the project methodology, Sect. 3 delineates results with the main focus on architectural details, requirements and presentation of the prototype. Finally, Sect. 4 presents a conclusion and Sect. 5 discusses positive aspects, challenges and limits of the project and outlines future work.

2   Methodology

The used methodology to gather requirements and to build a prototype was divided into three steps (analysis, implementation, and evaluation). First, a literature analysis was conducted to find any similar applications and gather more detailed information on the topic of serious games in the target area. After that, a brainstorming was conducted with people from the proposed target group which led to an online survey to get more quantitative feedback for the design of a serious game to increase motivation for doing sports. Based on the results of this survey, a User Centered Design (UCD) process was conducted with the help of a low fidelity prototype (throughout different iterations). Afterwards, a high fidelity prototype was sequentially implemented. Finally, this prototype was optimized and the results established. The methodology can be found in Fig. 1.

3   Results

Based on the aforementioned methodology, the main results are described in this chapter. First, an overview of the used software architecture is given. Afterwards, an overview of the basic results from the online-survey and the UCD is given. Finally, some of the identified and all implemented requirements are described and more details of the prototype are given.

3.1   Architecture

The proposed name for the application is Lazarus and its architecture (see Fig. 2) is divided into an application- and a server-part. Both are programmed with Java 1.7.

The server (back-end) is built with the Dropwizard framework [9]. Hibernate and MySQL is used for the database, Jetty as web server and Maven as build- management-tool. The back-end handles all retrieving, storing, editing and removing of the data in the database and does the complex calculation operations and algorithms, e.g. determines which user gained which achievement.

The Lazarus-Client is developed for the Android version 4.1 Jelly Bean, thereby ensures that at least 85.8% of all Android devices are able to run this app [10]. The client contains an open source module from GitHub [11], which provides the complete functionality to communicate and exchange data with the Foursquare-Application Programming Interface (API) [12].

The server as well as the client use a Representational State Transfer (REST)-Service to communicate between each other and with the Foursquare-API. This API was used to gather location based information for the check-ins like user proximity to a soccer court, swimming pool, gym and so on.

Fig. 2 Lazarus
system-architecture
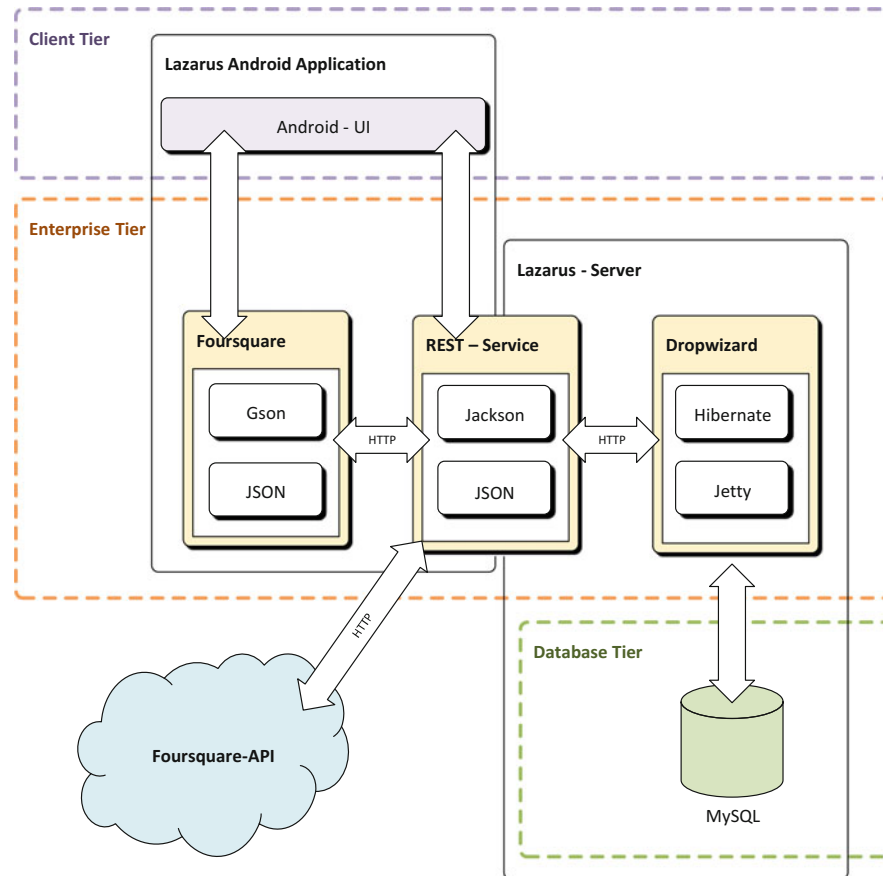
3.2 Online-Survey

A total number of 117 people took the online survey. They are divided into 83 male (70.94%) and 34 female (29.06%) individuals. The age range is from age 17 to 51 with a mean of 27.4 and a median of 26. The questionnaire was about the sports behavior and the concept of in-game feedback of the planned application. The authors also asked users about their favorite mobile games and sport applications. The participants had the choice to mention up to three favorite sports—beginning with their most favorite one—which gives a total number of 351 answers. Most people conduct running as activity (n = 50, 14.25%) followed by swimming (n = 37, 10.54%) and cycling (n = 35, 9.97%). Only 37.61% (n = 44) people do use an electronic device to track their sport activities. These people use a classic heart rate monitor/watch and different mobile applications like Runtastic, Nike + and Strava. The remaining 62.39% (n = 73) mentioned that they have not found a device or software fitting their needs, or they are not interested in tracking their activities. According to their opinion, only competitive

sports people should do that. Some of them also forget to start tracking before they work out, two people also mentioned that they track their sport data with pen and paper and some do not want to track their activities.

A total number of 67 (57.26%) participants can be motivated by achievements in a mobile game. Reasons mentioned why achievements motivate, are that the users like to target a concrete goal, like the appreciation, achievements unlock special features, the achievements reflect the users' performance only because they are there and the users like to collect them all.

Regarding some features and motivational aspects for the proposed game, users said it should provide the possibility to motivate the user. The participants could choose between 'achievements' (n = 49), 'advantage in the game' (n = 61) and 'other' (n = 43). Answers mentioned in the 'other' category were money, voucher, free pro account, being motivated by another person, no advertisement in the app, increase of character values like dexterity, strength, endurance, better equipment and other styling of equipment within the game. Overall, the online-survey delivered 13 base

requirements.

3.3 User-Centered Design

The whole UCD process was done with 10 people. Four of them participated in the low-fidelity and another six in the high-fidelity iterations. The low-fidelity process led to 27 additional requirements. One of the main findings was that the participants do want real benefits like money or coupons for online shops. All participants said that they enjoyed the chosen game concept. All of them would actually use the provided application—three of them with additional features implemented, e.g. training schedule, support of external sport apps and weight tracking. Another source of motivation are the provided achievements.

3.4 Requirements

During the online evaluation and the UCD, the authors identified a total number of 67 requirements. The main requirements, which were implemented, are shown in Table 1. The remaining ones were skipped, but were evaluated and should give a brief overview of the proposed functionality and overall scope of the app.

3.5 Prototype

All implemented requirements of the prototype can be divided into four categories: game, exercise, achievements, and highscore. The correlation of these categories is essential for the understanding of the in-game feedback.

Achievements were triggered from the played games and exercises of the users. Playing the game, doing sports and earning achievements increases the highscore. Real life sport activities generate a benefit, which can be used in the game and grants an advantage over those, who did not conduct sport activities. Doing a workout, which lasts at least 30 min, generates this benefit. In the app it is called 'item'. After the login, the user is redirected to the main screen. A game or a training session can be started directly from the home screen. Below those, the user can enter his/her training plans and the live ticker is shown, which contains the progress made by his/her friends. Information like a level up, earned achievements, completed workouts, friend requests are displayed there. At the top of the page the user's avatar, current level, progress until the next level up and his/her username is located. The game of the Lazarus app follows the rock-paper-scissors principle, which is also widely used and popular in a variety of games. It offers three possible actions or directions: up, front and down. Each user has to conduct an attack and a defense which is asynchronously

Table 1 Implemented requirements

ID	Description
01	The app should contain a game with a single-player mode against an Artificial Intelligence
02	To get a better overview of the completed exercises, there should be a management site for them
03	To track the conducted sport activity, the user needs a 'Check-In' before he starts to do his/her workout
04	For motivational reasons, there should be achievements which can be unlocked via sport activities/game playing
05	The GPS functionality of the mobile device should be used
06	The app should offer 'in-game feedback'. Doing sport generates something that the user can use in the game
07	For comparing all users and seeing which user has earned the most points, there should be a Highscore
08	The application should be integrated on the cellphone
09	A so called 'Autologin' should be implemented
10	The app should have a registration so that the user can create an user account and grant access to the app
11	Every sport activity should be supported by the app
12	The app should be free to download and at no charge
13	The app should not contain any ads

Fig. 3 Lazarus game procedure
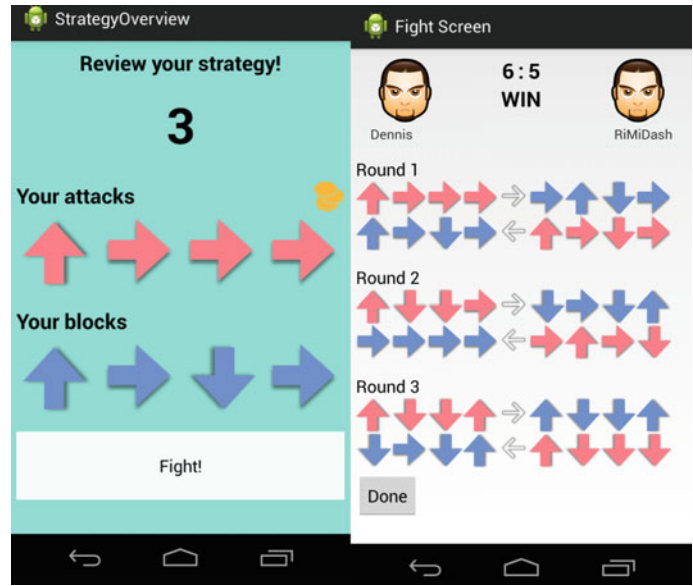
compared to the opponent's attack and defense. If player 1 hits 'up' in his/her attack phase, the opponent (player 2) must also hit 'up' to block his attack, otherwise player 1 gets a point. One game consists of three rounds, four attacks and blocks. The player with the most points wins the game. The sequence of one round can be seen in Fig. 3 and is as follows. First, the user chooses an opponent to play against. Now, the user chooses the attacks and blocks. If available, the user can choose an item (which is a specific reward granted for doing sports and checking in—see Fig. 4) either for the attacks or the blocks which is indicated by the coins in the strategy overview. After this, the actions of the user

and his/her opponent will be compared. Round one shows the attacks of the user on the left side (red arrows) and his/her blocks (blue arrows) underneath. On the right side, there are the blocks of the opponent and then his/her attacks. An attack is successful and counts as a point, if the blue arrow is not in the same direction as the red arrow. If not, the attack is blocked and the offensive player does not get a point. If an item was used for the attacks, the first attack hits regardless of whether the defender chose the right direction for the block. If an item is used for the defense, it blocks every attack in every direction.

Fig. 4 Sports tracking
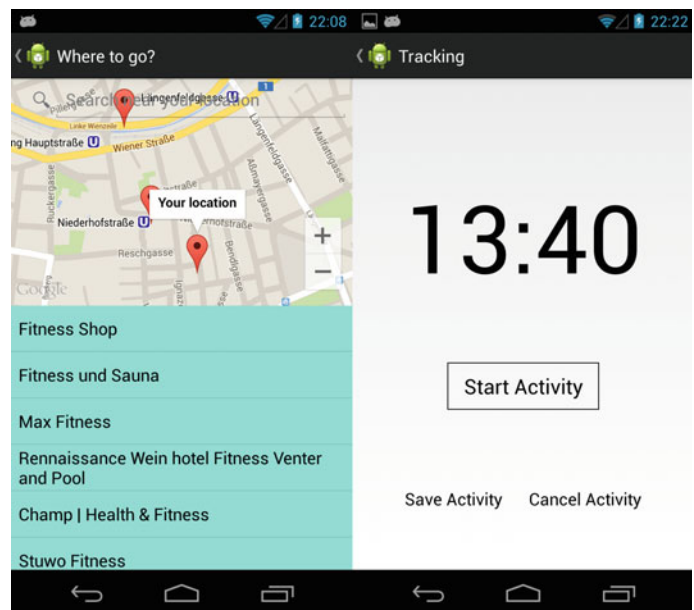
4 Conclusion

The here presented work tries to find a motivating way to combine physical activities with a serious game. By doing real life sport activities people get benefits within the game, which should have a positive effect on them doing even more sports. The results indicate that this approach might be helpful, but delivered no significant answer to this question.

5 Discussion

The results of this research may point out that people are not quite sure what motivates them to do sports more often. It seems that everybody has different reasons for doing sports as well as different ways to boost their motivation. The authors took special care to deliver a concept that allows tracking physical activity and engaging in gameplay as separate activities, while ensuring that only real-life exercise leads to in-game benefits. That way, experienced gamers stand no chance to boost their character skills without actually engaging in physical activity. Furthermore, the authors are aware that an approach to link active lifestyle with in-game benefits targets only those people, who are fond of playing in general. Nonetheless, we propose that the developed and herein presented serious game may be a good starting point to have less-active couch potatoes (who are not reluctant to play games) take charge in replacing their rather sedentary behavioral pattern with a lifestyle of increased physical activeness. Future research needs to evaluate this assumption and the proposed real-life benefit in practice. The results also suggest that people are competitive and tend to interact with each other—which might be used to motivate people further. People also like to see what they have accomplished—which might indicate that they are motivating themselves by just keeping track of their activities.

During this research some problems occurred, one of them being associated with using Foursquare for the check-in—there are not that many places to check-in within the city of Vienna, where the evaluation was conducted. It is also not possible to reduce search results for dedicated sport places.

In terms of future work, a few interesting aspects might be implemented in the prototype which were mentioned throughout the different phases by the users. Some of those features are a ranking board, to see the activity of other people, as well as the definition of goals for themselves. The developed application should also be tested and evaluated over a longer period of time. Also, the integration of different tracking devices is currently investigated.

References

1. J. A. Bennie, J. Y. Chau, H. P. van der Ploeg, E. Stamatakis, A. Do, and A. Bauman, "The prevalence and correlates of sitting in European adults - a comparison of 32 Eurobarometer-participating countries," Int. J. Behav. Nutr. Phys. Act., vol. 10, no. 1, p. 107, Sep. 2013.
2. D. W. Dunstan, G. N. Healy, T. Sugiyama, and N. Owen, "'Too much sitting' and metabolic risk - Has modern technology caught up with us?," European Endocrinology, vol. 6, no. 1, pp. 19–23, 2010.
3. Sedentary Behaviour Research Network, "Letter to the Editor: Standardized use of the terms 'sedentary' and 'sedentary behaviours'," Appl Physiol Nutr Metab, vol. 37, pp. 540–542, 2012.
4. Weight-control Information Network, "Overweight and Obesity Statistics," Oct-2012. [Online]. Available: http://win.niddk.nih.gov/publications/PDFs/stat904z.pdf. [Accessed: 06-Mar-2015].
5. S. Berkovsky, J. Freyne, and M. Coombe, "Physical Activity Motivating Games: Be Active and Get Your Own Reward," ACM Trans Comput-Hum Interact, vol. 19, no. 4, pp. 32:1–32:41, Dec. 2012.
6. S. Consolvo, K. Everitt, I. Smith, and J. A. Landay, "Design Requirements for Technologies That Encourage Physical Activity," in Proceedings of the SIGCHI Conference on Human Factors in Computing Systems, New York, NY, USA, 2006, pp. 457–466.
7. T. Toscos, A. Faber, S. An, and M. P. Gandhi, "Chick Clique: Persuasive Technology to Motivate Teenage Girls to Exercise," in CHI '06 Extended Abstracts on Human Factors in Computing Systems, New York, NY, USA, 2006, pp. 1873–1878.
8. A. Laikari, "Exergaming - Gaming for health: A bridge between real world and virtual communities," in IEEE 13th International Symposium on Consumer Electronics, 2009. ISCE '09, 2009, pp. 665–668.
9. Coda Hale, Yammer Inc., "Dropwizard Framework," 2013. [Online]. Available: http://dropwizard.io/. [Accessed: 09-Mar-2015].
10. "Android Developers Platform Versions." [Online]. Available: https://developer.android.com/about/dashboards/index.html. [Accessed: 03-Feb-2015].
11. Condesales, "Foursquare module from github." [Online]. Available: https://github.com/condesales/easyFoursquare4Android. [Accessed: 02-Mar-2015].
12. "Foursquare Application Programming Interface." [Online]. Available: https://developer.foursquare.com/. [Accessed: 02-Mar-2015].

An Adaptive Compression Algorithm for Wireless Sensor Network Based on Piecewise Linear Regression

Jia-Heng Li, Xiao-Lin Zhou, Rong-Chao Peng, and Feng Lv

Abstract

The wireless sensor network (WSN) has limited bandwidth, low power consumption, and may have redundantly collected data. The effective compression of data to reduce the energy consumption in transmission is of great importance. To this end, we proposed a new data-compression algorithm for WSN. The key idea of the algorithm is based on an adaptive threshold and piecewise linear fitting. The adaptive threshold is automatically adjusted by error after the fitting model was applied to the rationality of the adjusted model; subsequently linear fitting is used to determine the reasonable range of subsection based on the detection of continuous unfitting points. From the simulation results, the algorithm is realized in low time complex but with a good data compression effect, and then has a potential practicability.

1 Introduction

Wireless sensor network may consist of hundreds of nodes which are interrelated and communicate with each other. It is widely used in various healthy and environmental monitoring, disaster prevention, equipment diagnosis, target classification and other fields [1]. It also has potential applications in many industrial systems, and can be widely used in the Internet of Things. In the development of WSN, the energy consumption is the primary factor to be concerned, because the sensor node is equipped with the battery which has limited energy and cannot be charged or changed. According to related statistics, the transmission of collected data consumes about 80% of the battery energy. Therefore, it is of great importance to reduce the energy consumption on the data transmission process by compressing the amount of data [2].

The data collected from biomedical sensor nodes usually change slowly over time. According to this feature, the data can be compressed by linear regression. However, the data waveform usually does not have an obvious trend. In addition, the result of the commonly used polynomial approximation has poor performance of fit and large computation [3]. Therefore, we here in introduce the piecewise approximation of the data waveform, which used the method of piecewise linear fitting to compress the data in the present study.

There are many scholars have done a lot of research work about the data compression algorithm based on linear regression. In paper [4], an algorithm was proposed that used the nonlinear fitting compression on the streaming data, and set the fitting error threshold to reduce the number of fitting adjustment, resulting in reduction of the algorithm complexity and the transmission data. This algorithm can compress the data in many occasions, but if the data changes frequently, the performance of the algorithm may be obviously affected. In paper [5], a low complexity-regression method was developed, which has low variance of data reconstruction and was suitable for the environment with different types of noise and different density of WSN. In paper [6], a compression algorithm of the piecewise linear approximation was proposed, which reduced the complexity of the algorithm and improved the fitting accuracy. In paper [7], a linear regression model was adopted to fit the correlation of the data at a single node, and then further compressed the spatial redundancy at the collection node (ODLRST). In paper [8], a piecewise linear fitting algorithm

J.-H. Li (✉) · F. Lv
Wuhan University of Technology, Wuhan, 430070, China
e-mail: lijiaheng2015@outlook.com

F. Lv
e-mail: lufengwut@163.com

X.-L. Zhou · R.-C. Peng
SIAT-Institute of Biomedical and Health Engineering, Chinese Academy of Sciences, Shenzhen, 518055, China
e-mail: xl.zhou@siat.ac.cn

R.-C. Peng
e-mail: rc.peng@siat.ac.cn

(CIRA) based on confidence interval was developed, which well fitted the variation trend of data by determining the confidence interval in different cases.

In this study, an automatically adaptive piecewiselinear regression compression algorithm was proposed (ACPLR). This algorithm introduced an adaptive adjustment mechanism of fitting error and an optimized judgment mechanism of fitting model, processed the data in piecewise linear fitting, and tested regions of different density with different thresholds. Finally, the simulation experiments were carried out to compress the data with this algorithm and previous algorithms. The test results showed that the proposed algorithm could effectively reduce the amount of data and transmit these data effectively.

2 Methodology

2.1 Fitting Model of Time Series

In WSN nodes, a series of data sets collected in time sequence can be represented as S, and S = {(t_i, y_i)}, $(i = 1, 2, 3…n)$. (t_i, y_i) records the data y_i collected in the time of t_i and n represents the data number of the series. Because the collected data within a certain time interval can be approximated as a linear function, we can thus adopt a piecewise line to fit the trends of the data.

For an acquired data sequence S = {(t_i, y_i), $(i = 1, 2, 3… n)$}, the first order fitting regression line can be expressed as:

$$\hat{y} = \beta_0 + \beta_1 t + \varepsilon, \quad \varepsilon \in (0, \sigma^2) \tag{1}$$

where ε is the fitting error. β_0 and β_1 are the fitting coefficients. According to the least square theory, β_0 and β_1 can be represented as:

$$\beta_0 = \frac{1}{n}\sum_{i=1}^{n} y_i - \left(\frac{1}{n}\sum_{i=1}^{n} t_i\right)\beta_1 \tag{2}$$

$$\beta_1 = \frac{\sum_{i=1}^{n} t_i y_i - \left(\sum_{i=1}^{n} t_i\right)\left(\sum_{i=1}^{n} y_i\right)}{\sum_{i=1}^{n} t_i^2 - \frac{1}{n}\left(\sum_{i=1}^{n} t_i\right)^2} \tag{3}$$

2.2 The Feature Representation of Fitting Sequence

For the conventional linear fitting algorithm, the fitting sequence can be expressed as {$t_1, t_2, \beta_0, \beta_1$}. The first two parameters are the start and end time points of the sequence and the last two are fitting parameters. After linear fitting of continuous monitoring data, the fitting coefficients and start and end time points are used to represent the time data

information and can greatly compress the amount of transmission data.

In the proposed algorithm, we let the start time point of each segmented sequence start from $t_1 = 1$, then the sequence can be simplified as: S = {(i, y_i), $(i = 1, 2, 3…n)$}. Since the start time point of the feature sequence of each segmented sequence is 1, the start time point parameter t_1 can be removed and only the end time point parameter t_2 is preserved, so that the sampling data can be further compressed.

In addition, the proposed algorithm adds the judgment of the cut-off point and the non-fitting point. The cut-off point is the start data point for time series segments and the non-fitting point is the point whose fitting error exceeds a preset threshold in each segment. The non fitting points are added to the three feature parameters of the fitting line and then transmitted separately.

Finally, the feature of the segmented sequence is expressed as: {$t, \beta_0, \beta_1, (t_i, y_i)$}, where (t_i, y_i) is the non fitting points that need to be transmitted separately, and the number of non fitting points is unfixed.

2.3 Algorithm Implementation

The meanings of parameters in the algorithm are shown in Table 1.

Firstly, the normal range of the detection object is determined by [y_{min}, y_{max}]. Three normal data are taken for the generation of the initialization of the fitting model $\hat{y} = \beta_0 + \beta_1 t$. Subsequently, we read the next record, If it is out of the normal range, we cut it off and use the fitted values instead in the decoding process, which can play a role for filtering the noise. Otherwise, it is further judged whether the fitting error $\Delta y_i = y_i - \hat{y}_i$ is within the specified range or not;

Table 1 Meanings of parameters

Parameter	Meaning
t	The time point of sampling
y	The value of sample
y_{max}	Upper limit of normal sample
y_{min}	Lower limit of normal sample
n	n-2 is the number of adjustment times of fitting model
$flag$	The sign of the initialization of fitting model
$delta1$	Fitting error
$delta2$	Fitting error to judge the non fitting points
P	Line angle before model adjustment
Q	Line angle after model adjustment
E	Threshold for the fitting error
M	Threshold for the angle

If it is, the next record is followed to read; else, the fitting model is thus adjusted.

(1) *Adaptive Threshold for Fitting Error*: The threshold for fitting error is defined as a function of the slope of fitting curve: $E = \varepsilon_0 \log_2(|\beta_1| + 2)$, where ε_0 is a constant that can be adjusted according to the specific situations and accuracy requirements, so that the fitting error can be adjusted adaptively and the fitting model has an acceptable performance in the case of gentle waveform or heavy fluctuation.

After the adjustment of the model, the angle between the pre-adjusted and after-adjusted lines is calculated, and the model can be considered reasonably if it is lay within the specified angle threshold range.

(2) *Definition And Judgment of Non Fitting Point*: If the model is considered reasonably then the next record is read. Otherwise, the current point is temporarily labeled as non fitting point and the next point is read. If the fitting error between the next point and the fitting model before adjustment is within the threshold range, the current point is the non fitting point and need to be translated separately; else, a new initialization fitting model is set up from the current point.

Based on the judging mechanism of non fitting point, the adjustment number of the model can be greatly reduced, and then the time computational complexity of the algorithm can be reduced.

(3) *Pseudo Code of The Algorithm*:

Step 1: Initialization of the fitting model

(i)   if (!fin.eof()), algorithm ends.
(ii) if (*flag* == 1), read three normal records continuously and initialize the fitting model.
(iii) else if (*flag* == 0), read a normal record and initialize the fitting model with the last two records, set *flag* = 1. Output the fitting result.

Step 2: Read data and adjust the fitting model

① if (*flag* == 1), read the next record and calculate the fitting error.
② if (!eof()), output the fitting result; else if (*delta1* <= E), go to ①.
③ Adjust the fitting model, if (abs(P − Q) <= M), i.e., the angle of two linear model is within the threshold M, go to ①. else label it as non fitting point.

④ Read the next record, if (!eof()), output the fitting result.
   else if (*delta2* <= E), add the non fitting point to the end of the transmission data and adjust the fitting model, go to ①.
⑤ Set *flag* = 0, go to step 1.

3 Results and Analysis

3.1 Experimental Setup and Evaluation Model

In this section, the proposed algorithm ACPLR is compared with two other regression compression algorithms CIRA and ODLRST.

Testing clincial data is downloaded from the MIT-BIH Database (http://ecg.mit.edu/), this paper extracts 750 sampling points of the data which are representative enough.

The computational complexity of the three algorithms depends on the length of the fitting sequence. The space complexity of the algorithm ODLRST is $O(n)$, The space complexity of CIRA and the newly proposed algorithm ACPLR is $O(1)$. There is no obvious difference between the algorithm space complexity, and the performance of the algorithm is evaluated by the data compression ratio (CR) and the mean square of reconstruction error (RMSE). Under the same testing condition, the less the value of CAR and RMSE, the better the performance.

$$CR = \frac{\text{Data volume after compressed}}{\text{Data volume before compressed}} \quad (4)$$

$$RMSE = \frac{1}{N} \sum_{n=1}^{N} (x_i - y_i)^2 \quad (5)$$

3.2 Result Analysis

Three segments series of data with different features were extracted and applied in the fitting compression experiment. As shown in Fig. 1, Fig. 1a shows the arterial blood pressure (ABP) waveform which is slowly changing (signal 1) in periodic variation, Fig. 1b displays the fast changing data of central venous pressure (CVP) with unconspicuous linear trend (signal 2), Fig. 1c shows the data in 1(a) with artifical noise added (signal 3).

Using the three different algorithms to compress the data, the statistical results are shown in Table 2 and Fig. 2.

The experimental results are obtained under the high fitting accuracy with setting the threshold of fitting error 0.5. It shows that in the condition of normal sample data such as
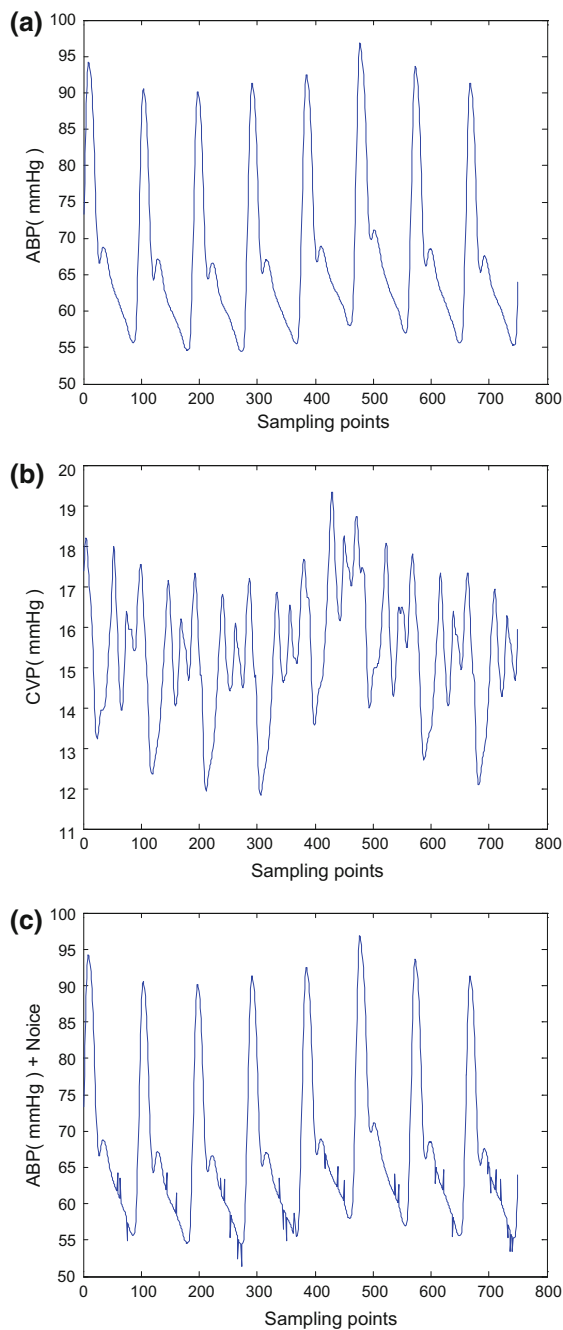
Fig. 1 Three original signals with different characteristics
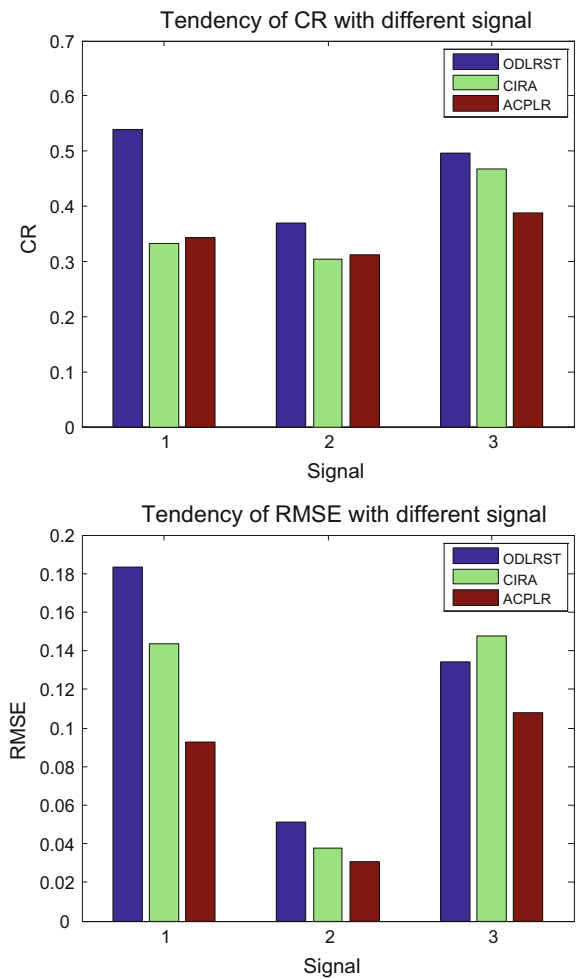
Fig. 2 Tendency graphics of experimental results

signal 1 and 2, the proposed algorithm ACPLR has almost the same compression ratio with CIRA but its reconstruction accuracy is higher than CIRA. In contrast, neither the compression ratio nor the reconstruction accuracy of ODLRST has a good result. Furthermore, as shown in signal 3, where the data has much noise, the proposed algorithm has a much better compression effect than CIRA and ODLRST, both in the compression ratio and the reconstruction accuracy. Therefore, it can be inferred that

Table 2 Comparison of the three algorithms

Algorithm	Parameters	Signal 1	Signal 2	Signal 3
ODLRST	CR	0.5400	0.3700	0.4970
	RMSE	0.1836	0.0510	0.1345
CIRA	CR	0.3330	0.3030	0.4670
ACPLR	RMSE	0.1436	0.0375	0.1476
	CR	0.3420	0.3130	0.3880
	RMSE	0.0927	0.0307	0.1078

the performance of the present algorithm is better than the other two algorithms in a noisy environment.

Overall, for the algorithm ODLRST, the maximum length of fitting model is determined, and the storage complexity and the computation quantity are decreased, but the compression rate is not improved. The parameters of algorithm CIRA are not flexible enough for the abnormal data compression. The proposed algorithm ACPLR uses adaptive fitting threshold judgment mechanism as well as the individual transmission mechanism of non fitting points, and make the algorithm compression effect more excellent.

4 Conclusion

The existing compression algorithms based on the regression model of WSN achieve excellent data transmission efficiency, but they do not consider the dynamic change of environmental monitoring data, and have an unflexible confidence interval of the fitting error and lack of adaptability in establishment of the linear model, leading to constrained practicality of the algorithm.

In this paper, an adaptive linear predictive coding algorithm was proposed to solve the existing problems. The algorithm utilized the adaptive adjustment mechanism of fitting error and the optimized judgment mechanism of fitting model, which enhances the applicability and robustness of the algorithm.

References

1. J. Yick, B. Mukherjee, D. Ghosal. Wireless sensor network survey [J]. Computer Networks, 2008, 52(12): 2292–2330.
2. G. Anastasi, M. Conti, M. D. Francesco, et al. Energy conservation in wireless sensor network: a survey[J]. Ad hoc Networks, 2009, 7 (3): 537–568.
3. J. M. Zhang, Y. P. Lin, M. Fu, S. W. Zhou. Piecewise Approximation Based Data Compression Algorithm with Error Bound in Wireless Sensor Networks[J]. Journal of Software, 2011, 22(9): 2149–2165.
4. X. Y. Liu, Y. Z. Wang, X. C. Yang. Study on Compression Technique for Streaming Data in Wireless Sensor Networks[J]. Computer Science, 2007, 34(2): 141–143.
5. A. L. Fernandes, M. Raginsky, T. P. Coleman. A low-complexity universal scheme for rate-constrained distributed regression using a wireless sensor network[J]. IEEE Transaction on Signal Processing, 2009, 57(5): 1731–1744.
6. E. Soroush, K. Wu, J. Pei. Fast and quality-guaranteed data streaming in resource-constrained sensor networks. In: Proc. of the MobiHoc. New York: ACM Press, 2008. 391–400.
7. L. C. Wang, C. X. Ma. A One-dimensional Linear Regression Model Based Spatial and Temporal Data Compression Algorithm for Wireless Sensor Networks. Journal of Electronics & Information Technology, 2010, 32(3): 755–758.
8. J. L. Wang, S. W. Zhou, H. Tang. Regression-based Wireless Sensor Network Data Compression Method. Computer Engineering, 2011, 37(23): 96–98.

Improving the Accuracy of the KNN Method When Using an Even Number *K* of Neighbors

Alberto Palacios Pawlovsky and Daisuke Kurematsu

Abstract

The kNN (k Nearest Neighbors) method is a classification method that could show low accuracy figures for even values of *k*. This paper details one method to improve the accuracy of the kNN method for those cases. It also shows one method that could improve the accuracy of it for biased classification sets and for odd values of *k*.

1 Introduction

There are many machine learning methods for data classification [1], and several of them have been used for breast cancer prognosis and diagnosis [2–5].

This paper deals with the improvement of the kNN (k-Nearest Neighbor) method [6]. It is a nonparametric classification method that has high accuracy. It has even been used to detect different stages of breast cancer [7, 8]. We have conducted research on the details of its use for breast cancer diagnosis and prognosis [9, 10].

When using the kNN method for breast cancer prognosis we have found that it has low accuracy when the number of neighbors *k* is small and even. When *k* takes an even value there are some cases where the data used for classification splits in equal sized groups and the class is not chosen by majority, but by the order of the groups used to determine the class. To improve the accuracy in those cases we have devised a method that is very effective for small even values of *k*. It is detailed in the following section. We show in section III the results of applying it to the breast cancer prognosis data of UCI [11].

A. P. Pawlovsky (✉)
Faculty of Biomedical Engineering, Department of Clinical Engineering, Toin University of Yokohama, Kanagawa, Japan
e-mail: pawlovsky@toin.ac.jp

D. Kurematsu
Department of Clinical Engineering, Toin University of Yokohama, Kanagawa, Japan

When evaluating the kNN method the target data is splitted into two sets. One is used for classification and the other one as a test set. Usually the test set is randomly chosen in a typical implementation and this way of forming it can give place to classification sets that contain data of only one class. This type of sets will completely bias the classification process and will also lower the average accuracy of the method when evaluating it. We also researched on the use of an implementation that helps avoid these cases. We also shown some details of its implementation and its combination with the method to improve the accuracy for even values of *k*.

2 The KNN Method

The k-Nearest Neighbor (kNN) method is an unsupervised nonparametric machine learning method used for classification tasks. To evaluate the accuracy of it and other classification algorithms we usually divide an already classified data in two sets. One is used for the classification task and the other one is used as a test set. Then one datum at a time is taken from the test set and compared with the data in the classification set. In Fig. 1 we show an example where an unclassified data is brought to the classification set and the similarity of it to the surrounding ones is measured.

Similarity is usually measured using the Euclidean distance between data, but other distances can also be used [12]. In this example we use three neighbors to decide the class or type of the datum. Since two of the three closest data used in the decision are of type **a**, the new datum will be assigned this class. In the kNN method if the number of neighbors *k* is even and the number of classes is also an even number, there will be cases where the class will not be determined by majority, but by the class closest to the datum to classify.

Figure 2 shows that the average accuracy of the kNN method lowers for even values of *k* (data obtained using the prognosis breast cancer data in the UCI repository). We have
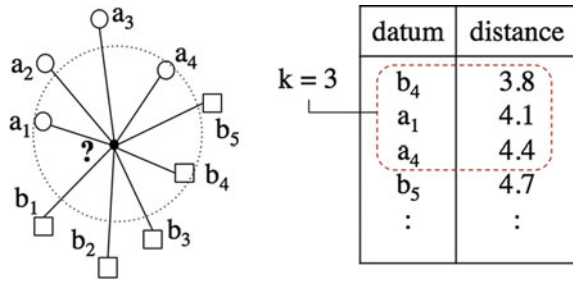
Fig. 1 kNN method: classification example

developed a method that in some of those cases it uses optional data to classify a new datum. Details of this method with its experimental results are shown in the following section.

3 Improvement Method for Even Values of *K*

We used in this work our own implementation of the kNN method. It uses the Euclidean distance as similarity metric. One method widely used to evaluate the accuracy of a kNN based method is ten-fold cross validation. In it a complete set of classified data is divided in ten parts and one is used as a test set and the remaining nine ones as the set for classification (the ones surrounded by the point-line enclosure in Fig. 3). Then the next part is used as a test set and so on, repeating this process 10 times. The accuracy is given as an average of the accuracies obtained in each step of the process.

To further reduce bias we evaluated the kNN algorithm and the method to improve it when *k* is even with nine different sizes of the classification set. They go from 10 to 90% in increments of 10%. We also evaluated each setting with its maximum number of possible neighbors.

Fig. 2 Prognosis results using the kNN method
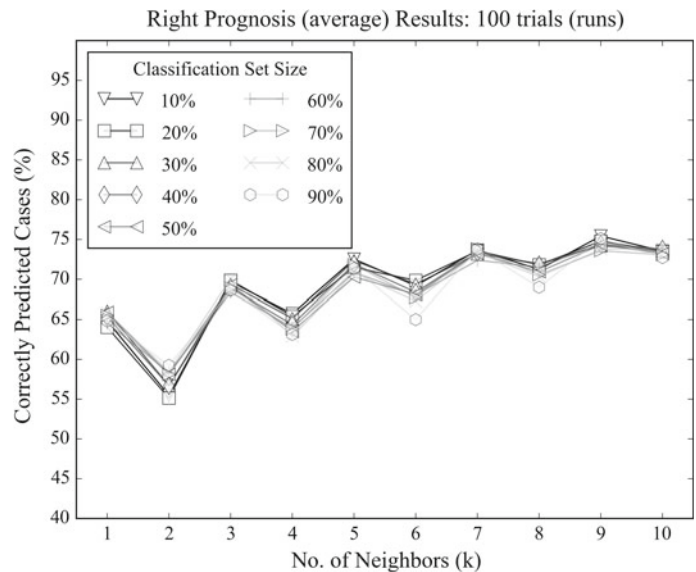
Fig. 3 Ten-fold cross validation scheme: first and last classification sets
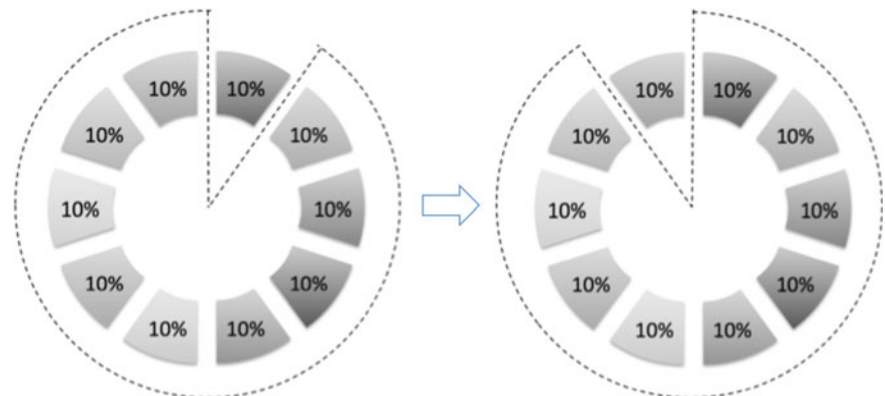
Fig. 4 Average accuracy results: 40% set size, all k values
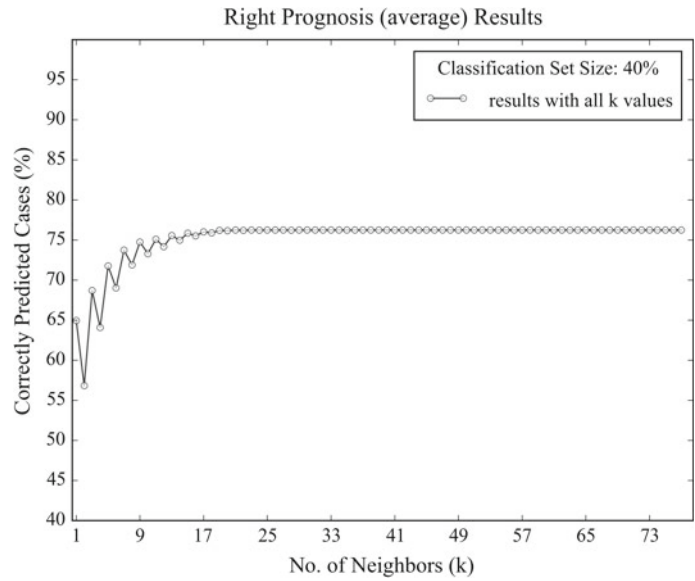
This maximum number is 19 for a classification set size of 10% and 174 for a classification set size of 90% of all available data (194 records). From this evaluation we found that average accuracy for all set sizes reaches a maximum before k reaches a value of 30 (Fig. 4). Low average accuracy values are seen for low even values of k for any classification set size. The method that helps to correct it is detailed in the following section.

3.1 Method to Improve Accuracy for Even Values of k

In our approach to improve the accuracy of the kNN method we first divide all the classified data in its corresponding classes. For the case of the UCI prognosis breast cancer data it will be into two classes, the non recurrent cases and the recurrent ones as depicted in Fig. 5.

Then, we calculate the average values of the items of them (**aN** and **aR**). We implemented the kNN method with an extension that detects the cases where the number of neighbors causes a tie and the class can not be decided by majority. In thoses case the datum to be classified is compared with the class reference values and the class is decided for the closests one (Fig. 6).

We evaluated this approach and found that we can obtain improvements that goes up to a 12% of increment in the accuracy. The corresponding results are shown in Fig. 7.

Fig. 5 Class reference averages
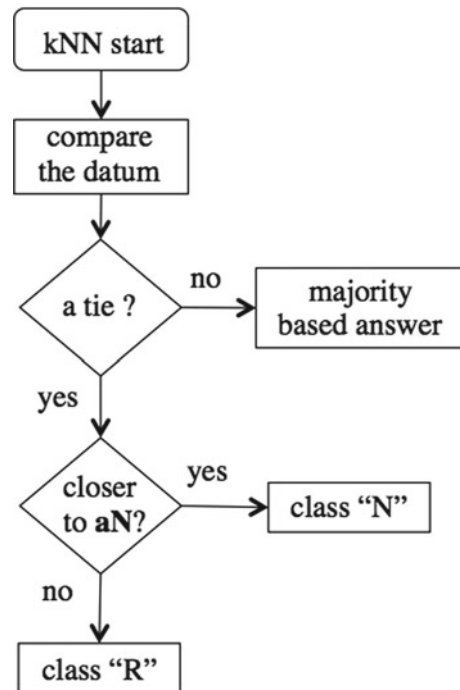
Fig. 6 Class processing when reaching a tie

Fig. 7 Improvements in the accuracy for all set sizes
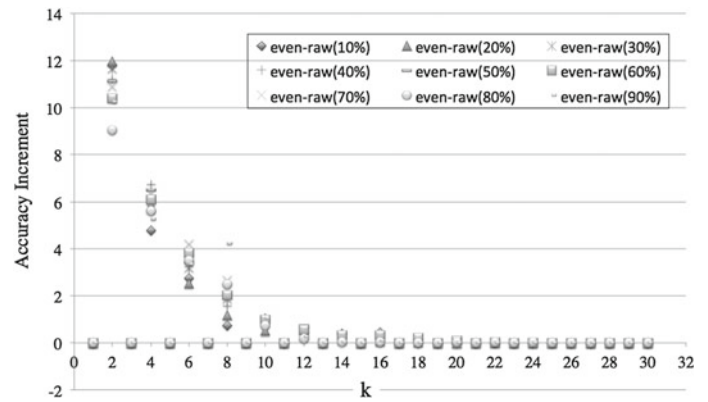
The accuracy obtained with an implementation without the improvement is called a raw one and the one with it even. The increments are shown as the differences between these two implementations and for the ten classification set sizes used in its evaluation. The increment in the accuracy is clearer for small values of k up to 16. After that the improvement is close to zero or zero.

While researching on this approach we found that there are some case where the classification set contained only one type of data or a large portion of it was only of one class. These sets also lower the average accuracy. One approach to deal with these cases is briefly explained in the following section.
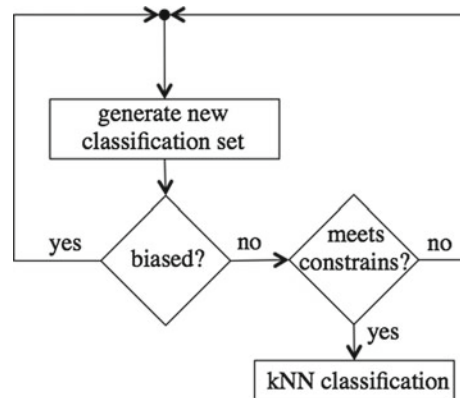
Fig. 8 Detection and reprocessing of biased classification sets

3.2 One Approach to Deal with Biased Classification Sets

In a kNN method the data used as the classification set is usually chosen randomly. This causes that some classification sets are highly biased, containing only one type of data or a large portion of the data is of only one type. We implemented a modification of the kNN method, Fig. 8, that checks if the classification set is biased and if it meets some requirements, and if not forces the generation of a new one.

Fig. 9 Accuracy Results for the fix rate approach: 60% set size
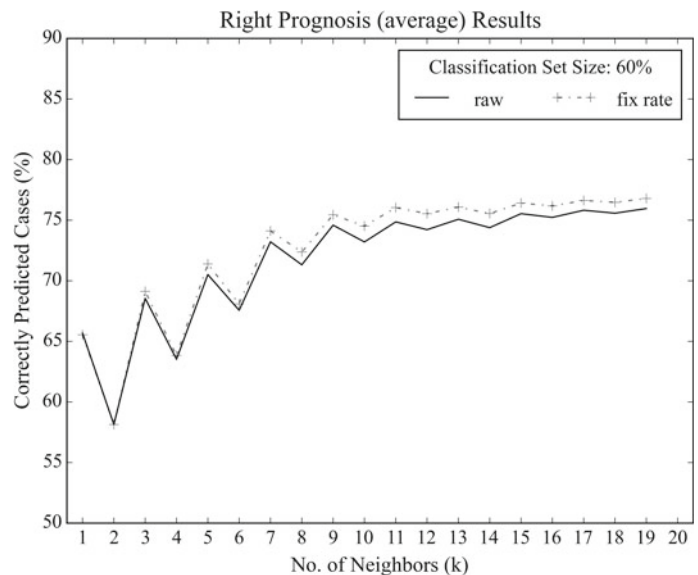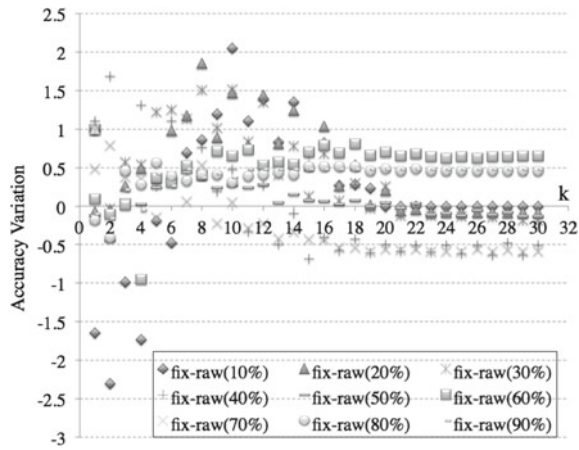
Fig. 10 Changes in the accuracy for the fix-rate approach

We set the requirement that the data in the classification set has the same type percentages found in the total data.

In the UCI breast cancer prognosis data we have 46 recurrent cases and 148 nonrecurrent ones, so the percentages are 23.7% and 76.3%, respectively.

The results for a classification set size of 60% are shown in Fig. 9. We can see that with the fix rate (percentage) constraint we can improve the accuracy for large values of k. The change in the accuracy for all the classification set sizes and for values of k up to 30 are shown in Fig. 10.

The fix rate approach in some cases lowers the accuracy in a small amount for small sizes of k and for small sizes of the classification set, but also brings improvements in the accuracy for classification sets sizes of 80% and higher.

Fig. 11 Accuracy for the combinations of approaches: 50% set size
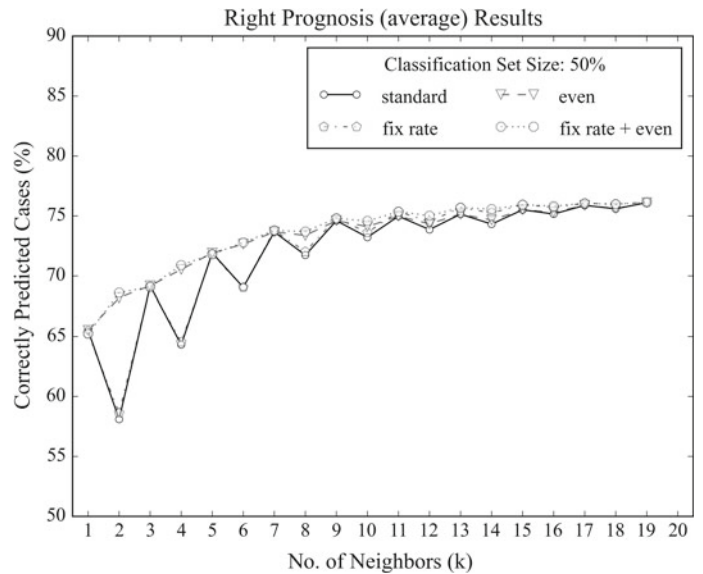
Fig. 12 Maximum and minimum accuracies range: 50% set size
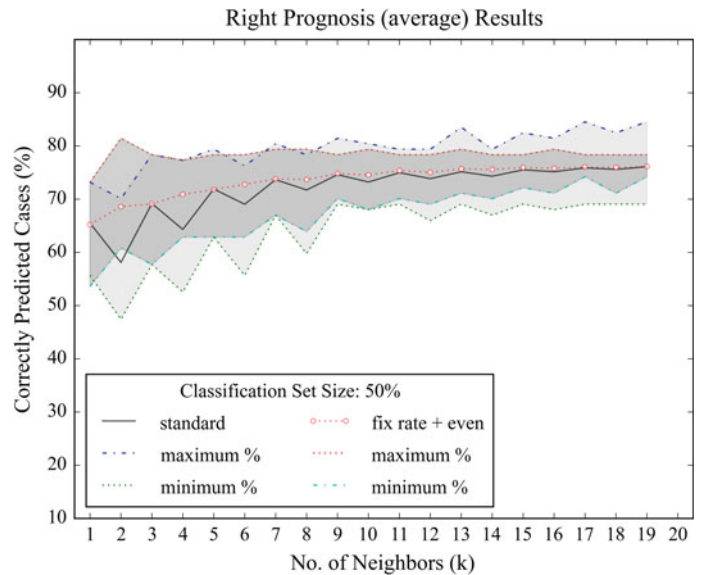
Table 1 Average (best) accuracies and the corresponding values of k

Classification	(Maximum) average accuracies							
Set size	Raw		Even		Fix rate		Even + fix	
(%)	Value	k	Value	k	Value	k	Value	k
10	76.27	19	76.27	19	76.51	13	76.51	13
20	76.27	23	76.27	23	76.19	19	76.19	19
30	76.61	29	76.61	29	76.47	19	76.47	18
40	76.61	29	76.61	29	75.97	19	75.97	19
50	76.34	29	76.34	29	76.21	25	76.21	25
60	75.99	25	75.99	24	76.64	29	76.64	29
70	75.74	25	75.74	25	75.16	25	75.16	25
80	75.77	23	75.77	23	76.23	23	76.23	23
90	76.53	23	76.53	23	77	23	77	23
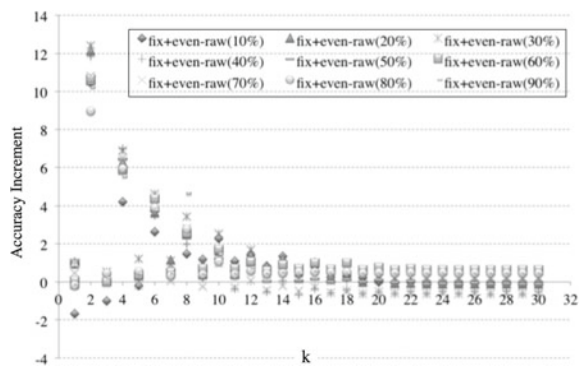
Fig. 13 Variation of the accuracy for the combined approach

We also evaluated the combination of both of our approaches. The results for a classification set size of 50% are shown in Fig. 11 (standard = raw implementation).

The combination of our approaches also makes smaller the differences between the maximum and minimum accuracy results, specially for large sizes of k (Fig. 12). Both approaches in some way complements each other and brings improvements to almost all the range of values of k and for all sizes of the classification set.

Figure 13 shows the increments in the accuracy for all the nine sizes of the classification set when combining the even and the fix rate approaches.

Details of the best average values of the accuracy and the number of neighbors to obtain them for all the classification set sizes are shown in Table 1.

From the values of this table we can say again that the even approach does not affect the best values of the accuracy. However, the fix-rate approach and the method that combines the even and fix approaches increase, for several classification set sizes, slightly the best values and lower the number of neighbors k to obtain them. Reducing the number of neighbors could help reduce the processing time when working with large classification data sets.

4 Conclusions

When forecasting the recurrence of breast cancer using the breast cancer prognosis dataset of the UCI repository we found that the accuracy reduces in some cases when an even number of neighbors k is used in the classification process using the kNN method. We have shown a method that helps to improve the accuracy in those cases. Experimental results show that it is useful for several small values of k. It improved the accuracy in almost 12% for values of k equal to 2.

We also found that there are cases where the classification set is biased and also introduced a method to handle them. We also show results of combining these two approaches. From them we can say that both could be very useful with similar data sets. They do not increase too much the best accuracies, but for several classification set sizes they reduce the number of neighbors needed to obtain the best accuracies.

References

1. P-N. Tan, M. Steinbach and V. Kumar, Introduction to Data Mining, Pearson Education Inc., 2006.
2. Shelly Gupta, Dharminder Kumar and Anand Sharma, " Data Mining Classification Techniques Applied for Cancer Breast Diagnosis and Prognosis," Indian Journal of Computer Science and Engineering, Vol. 2, No. 2, pp. 188–195, May 2011.
3. Shweta Kharya, " Using Data Mining Techniques for Diagnosis and Prognosis of Cancer Disease," International Journal of Computer Science and Information Technology, Vol. 2, No. 2, pp. 55–66, April 2012.

4. Gouda I. Salama, M. B. Abdelhalim, and Magdy Abd-elghany Zeid, "Breast Cancer Diagnosis on Three Different Data sets Using Multi-Classifiers," International Journal of Computer and Information Technology Vol. 1, Issue 1, pp. 36–43, September 2012.

5. Shomona G. Jacob and R. Geetha Ramani, "Efficient Classifier for Classification of Prognosis Breast Cancer Data Through Data Mining Techniques," Proceedings of the World Congress on Engineering and Computer Science 2012, Vol. I, October 2012.

6. Ethem Alpaydin, Introduction to Machine Learning 2nd. Edition, The MIT Press, 2010. Chap. 8.

7. Manish Sarkar and Tze-Yun Leong, "Application of k-Nearest Neighbors Algorithm on Breast Cancer Diagnosis Problem," Proceedings of American Medical Informatics Association (AMIA) Annual Symposium, pp. 759–763, 2000.

8. Jini R. Marsilin and G. Wiselin Jiji, "An Efficient CBIR Approach for Diagnosing the Stages of Breast Cancer Using KNN Classifier," Bonfring International Journal of Advances in Image Processing, Vol. 2, No. 1, pp. 1–5, March 2012.

9. Alberto Palacios Pawlovsky and Mai Nagahashi, "A Method to Select a Good Setting for the kNN Algorithm when Using it for Breast Cancer Prognosis," Proceedings of the 2nd. IEEE International Conference on Biomedical and Health Informatics (BHI 2014), pp. 189–192, Sevilla, Spain, June, 2014.

10. Katsuyoshi Odajima and Alberto Palacios Pawlovsky, "A Detailed Description of the Use of the kNN Method for Breast Cancer Diagnosis," Proceedings of the 7th International Conference on Biomedical Engineering and Informatics (BMEI 2014) Dalian, pp. 606–610, China, October 2014.

11. http://archive.ics.uci.edu/ml/datasets.html.

12. Seyyid A. Medjahed, Tamazouzt A. Saadi, and Abdelkader Benyettou, "Breast Cancer Diagnosis by using k-Nearest Neighbor with Different Distances and Classification Rules," International Journal of Computer Applications, Vol. 62, No.1, pp. 1–5, January 2013.

Effectiveness of Evidence-Based Venous Thromboembolism Electronic Order Sets Measured by Health Outcomes

Jacob Krive, Joel S. Shoolin, and Steven D. Zink

Abstract

In this retrospective causal comparative study, we analyzed 5 years of electronic medical records (EMR) data at two large teaching hospitals to determine effectiveness of evidence-based VTE prophylaxis physician order entry systems (CPOE) order sets, measured by acute VTE diagnosis, length of stay (LOS), and comorbidities outcomes. Results indicate lower VTE rate among non-surgical patients, while surgical patients did not benefit. Placing VTE orders via sets was not effective in influencing LOS and comorbidities outcomes. The study highlights the role of medical informatics in improving patient outcomes through reduction of variability in patient care practice.

J. Krive (✉)
Advocate Health Care, Downers Grove, IL, USA
e-mail: jkrive@valencehealth.com; jkrive@nova.edu;
krive@uic.edu

J. Krive
Valence Health, Population Health Technology, Chicago, IL, USA

J. Krive
Department of Biomedical Informatics, Nova Southeastern University, Fort Lauderdale, FL, USA

J. Krive
Department of Biomedical and Health Information Sciences, University of Illinois at Chicago, Chicago, IL, USA

J. S. Shoolin
Department of Family Medicine, Advocate Medical Group, Arlington Heights, IL, USA
e-mail: joel.shoolin@advocatehealth.com

S. D. Zink
Nevada System of Higher Education, Las Vegas, NV, USA
e-mail: steve_zink@nshe.nevada.edu

1 Introduction

The prevalence of VTE in the United States is estimated at 600,000 to 1 million cases annually [1, 2], while 300,000 deaths are directly attributed to VTE [3]. Half of all cases are related to hospitalization [4], while 18 to 65% of cases are preventable [5]. VTE is the third most common cause of hospital-related death and the most-common preventable cause of hospital-related death [6]. VTE is a candidate for technology enabled evidence-based prophylaxis guideline review process. Order set is a core component of CPOE that could have profound effect on ordering practices, leading to patient outcomes improvement [7]. Yet, majority of the VTE quality studies conducted to date focused on core measures compliance as a result of order set implementation [8–14], warranting a study dedicated to health outcomes.

2 Methods

Data was obtained via structured query language (SQL) queries from the Enterprise Data Warehouse (EDW) that receives information stored in EMR, patient registration, clinical and financial decision support, and other patient care and data analytics applications. The EDW uses Kimball architecture and runs on Microsoft SQL Server database. Paper sets, while still in limited circulation, were excluded from the study7, as it would require manual efforts to retrieve data and analyze outcomes. In this causal comparative study, we analyzed VTE patient data for the 2007–2011 period. We focused on prophylaxis as the most beneficial study of the potential CPOE impact on patient outcomes.

VTE prophylaxis sets ordered within 48 h of admission were selected for analysis of 92,000 EMR encounters that were organized under the "order set" and "no order set" groups. These groups were formed based on the EDW flag that identifies whether physicians utilized a set for placing

VTE orders in CPOE. Encounters selected for the study excluded psychiatric, obstetrics, pediatric, and chronic VTE patients. While organizational focus on utilization of the order sets during studied period of time was weak, with majority of the sets available in CPOE showing low use, VTE prophylaxis sets were popular with physicians, ensuring sizable comparison group: 39.6% of selected records were in the "order set" category. On average, monthly utilization of VTE sets hovered around 600 at one of the participating hospitals and 500 at another.

The independent variable in this study was utilization of the two order sets. Health outcomes—acute VTE, LOS, and comorbidities—were defined as the dependent variables. Race and sex were mediating variables analyzed in conjunction with order set utilization to determine combined significance in predicting health outcomes. De-identified patient encounters were obtained via queries against the EDW containing records from CPOE and patient accounting applications. The data were entered into and manipulated in Excel (filtering and cleanup), then loaded into the SPSS application for statistical analysis.

Due to the retrospective nature of the study and limited harm to patients, the internal review board (IRB) approval was obtained under the Expedited de-identified category, with a Health Insurance Portability and Accountability Act (HIPAA) privacy waiver form requiring no consent from patients. The data obtained from the EDW contained no identifying information, such as social security numbers or names. Records were identified via medical record number (MRN), which is internal to EMR/CPOE applications.

Acute VTE outcomes were analyzed using logistic regression, Pearson's chi-squared, and Fisher's exact methods. LOS and comorbidities (Charlson Comorbidity Index/CCI) were analyzed by applying One-Way ANOVA with Tukey and Bonferroni post hoc and Mann-Whitney U tests. Outcomes were organized by surgical classification via Agency for Healthcare Research and Quality (AHRQ)

PSI-12 standard defining technical VTE specifications, sex, and race. Patients were assigned to the "order set" and "no order set" groups based on VTE classification and physicians ordering preferences. The qualified non-surgical patient population N at the two hospitals was 28,271 and 38,813, and the surgical population was 10,237 and 17,329. Table 1 displays an example of the VTE prophylaxis order set content available for physicians' consideration and use in CPOE.

3 Results

The results indicated that VTE prophylaxis orders placed via electronic sets were effective in prevention of acute VTE for non-surgical patients at two participating hospitals [OR = 1.566; 95% CF 1.354–1.812; $P < 0.01$ and OR = 1.205; 95% CF 1.043–1.393; $P = 0.011$] and not effective for surgical patients [OR = 0.67; 95% CF 0.452–0.992; $P = 0.044$ and OR = 0.497; 95% CF 0.383–0.645; $P < 0.01$].

The relationship between CCI and order sets was significant [$F_{(3,28271)} = 94.297$, $P < 0.01$ and $F_{(3,38813)} = 410.373$, $P < 0.01$ non-surgical] and [$F_{(3,10237)} = 87.429$, $P < 0.01$ and $F_{(3,17329)} = 51.459$, $P < 0.01$ surgical], but the means indicated mixed results leading to inconclusive outcomes. Results were mixed due to no agreement between the actual means for comorbidity between the two hospitals within each of the surgical and non-surgical categories. In some cases comorbidity was higher, and in other cases it was lower, likely pointing to external factors influencing CCI beyond the scope of this study.

For LOS, the relationship was significant [$F_{(3,28271)} = 172.499$, $P < 0.05$ and $F_{(3,38813)} = 410.373$, $P < 0.05$ non-surgical] and [$F_{(3,10237)} = 101.509$, $P < 0.01$ and $F_{(3,17329)} = 686.291$, $P < 0.01$ surgical], but the mean LOS for the "order set" group was longer under both ANOVA and Mann-Whitney U test scenarios. Race and sex of the

Table 1 VTE prophylaxis order set content

Content	Details/Explanation
Patient activity	Nursing orders for patient activity, i.e. ambulation, assistance needed, etc.
Coumadin	Medication
Heparin	Medication
INR/PT	Labs
Lovenox	Medication
Nursing communication order	A set of nursing instructions for patient care
Platelet blood count (PLT)	Labs
Pulsation boot	DVT prophylaxis device
Sequential compression device	DVT prophylaxis device

patients, as mediating variables in this study, did not have significant effect on outcomes.

4 Limitations

A retrospective study performed on existing historical data from EMR and other information systems is not sufficiently flexible to offer ability for manipulating variables, controlling for all factors playing a role in the VTE diagnosis and prevention, and evaluating clinical factors beyond the scope of this patient data driven study. For example, CCI represented comorbidity. In this study, CCI could play a dual role: (1) it could help explain LOS as an index of pre-existing conditions, thus introducing comorbidity adjustment, or (2) it could serve as a measure of complications due to clinical interventions performed in the hospital. Therefore, comorbidity calculation is separate instead of being utilized as a mediating factor in the relationship between independent (order set use) and dependent (health outcomes) variables in this study. Comorbidities could potentially explain or provide better information about the differences between comparison groups of patients in this study.

Another factor that could represent a difference between comparison groups is risk for bleeding, warranting assignment to the "no order set" group for exclusion from standard anticoagulant therapy. Additionally, the mean LOS for the "order set" patients in both surgical and non-surgical groups was longer, compared to the "no order set" group, despite acute VTE rate showing favorable results for the non-surgical patients. Typically, prevention of VTE is expected to lead to a shorter hospital stay, as VTE could extend it by as many as a few days. This means that other factors or baseline characteristics outside of the scope of this study were in play.

5 Discussion

The study identified health outcomes measures where evidence-based VTE prophylaxis methods applied via CPOE sets were effective or lacked impact. Non-surgical patients benefitted from orders placed via sets, in terms of the acute VTE rate. Other measures were not positively affected, with the likely explanation that these outcomes were impacted by other variables beyond the scope of this study. Mortality was not investigated, as VTE sets are aimed at the deep vein thrombosis (DVT) and the pulmonary embolism (PE) preventative measures and therefore cannot be directly linked to cause of death. However, DVT can lead to serious complications and prolonged hospital stay. Unlike core compliance measures, health outcomes showed that effectiveness of VTE prophylaxis measures applied via

CPOE templates could be limited for certain categories of patients, in this case surgical ones, but still benefit a large patient population.

6 Recommendations for Future Research

Quantitative follow-up studies on VTE, and CPOE order sets effectiveness in general, should focus on observational or experimental studies designed with greater variable and baseline patient characteristics controls in mind. Such study design could account for all typical characteristics of the VTE patients, contain more focused list of exclusions, and form more closely comparable "order sets" and "no order sets" groups of patients. However, the study shall focus on health outcomes exclusively, as opposed to the subjects of core measures and clinical guidelines compliance, as the latter research has been conducted in the past and revealed positive results, yet core measures compliance may or may not translate into improved patient outcomes such as reduced VTE rate from following standardized clinical protocols for VTE prevention.

Additionally, a study into harmful effects for patients who get prescribed orders via standardized sets but do not conform to standard clinical prevention guidelines due to comorbidities or other baseline characteristics is warranted to discover potentially negative effects of the "one size fits all" solutions using CPOE applications. And on another accord, a qualitative study of reasons for physicians acceptance or resistance to using evidence-based ordering templates in CPOE could be beneficial in the process of understanding utilization and improving applications.

7 Conclusion

This VTE prophylaxis order sets study addressed the subject of medical informatics helping ensure that evidence-based guidelines are followed in an effort to reduce variability in patient care practices for situations and conditions where process standardization could help improve quality and reduce error rates. The study points to potentially promising outcomes from care standardization efforts implemented via CPOE templates for placing orders. At the same time, it revealed challenges in analyzing history data to account for all variables playing a role in following the entire continuum of care. New sophisticated EMR, CPOE, and EDW applications are necessary to collect more granular data. There are differences in the points of view among care providers on the subject of evidence-based guidelines implemented via medical informatics applications in patient care settings. Quantitative studies such as this VTE order sets research are necessary in order to produce tangible results in terms of the

patient outcomes, needed to convince clinicians in effectiveness of CPOE applications helping maintain evidence-based care protocols.

Some 54% of the United States hospitals have implemented CPOE by 2014 [15], and it is likely that many of these hospitals have capabilities for utilization of electronic VTE prophylaxis sets in their clinical workflows. This study could serve as a catalyst to encourage further collaboration between physicians and clinical informaticists in an effort to identify effective applications for CPOE-enabled tools grounded in methodology of evidence-based practices. Our findings could positively influence patient safety and cost of care. Improvements in these areas are important to healthcare facilities that are reviewing their evidence-based practices, CPOE investment, application utilization guidelines, and order set governance policies.

Rereferences

1. A. Qaseem, V. Snow, P. Barry, E.R. Hornbake, J.E. Rodnick, T. Tobolic, B. Ireland, J.B. Segal, E.B. Bass and K.B. Weiss, "Current diagnosis of venous thromboembolism in primary care: A clinical practice guideline from the American Academy of Family Physicians and the American College of Physicians," *Ann. Intern. Med.,* vol. 146, pp. 454–458, 2007.
2. F.A. Anderson, H.B. Wheeler, R.J. Goldberg, D.W. Hosmer, N.A. Patwardhan, B. Jovanovic, A. Forcier and J.E. Dalen, "A population-based perspective of the hospital incidence and case-fatality rates of deep vein thrombosis and pulmonary embolism: the Worcester DVT Study," *Arch. Intern. Med.,* vol. 151, pp. 933–938, 1991.
3. J.A. Heit, A.T. Cohen and F.A. Anderson Jr, "Estimated annual number of incident and recurrent, non-fatal and fatal venous thromboembolism (VTE) events in the US," in *ASH Annual Meeting Abstracts*, pp. 910, 2005.
4. J.A. Heit, W.M. O'Fallon, T.M. Petterson, C.M. Lohse, M.D. Silverstein, D.N. Mohr and L.J. Melton, "Relative impact of risk factors for deep vein thrombosis and pulmonary embolism: a population-based study," *Arch. Intern. Med.,* vol. 162, pp. 1245–1248, 2002.
5. C.E. Mahan, M.T. Holdsworth, S.M. Welch, M. Borrego and A.C. Spyropoulos, "Deep-vein thrombosis: a United States cost model for a preventable and costly adverse event," *Thromb. Haemost.,* vol. 106, pp. 405, 2011.
6. E. Kim, "The disease management project, Cleveland Clinic Foundation," in: *Venous Thromboembolism*, R. Hobbs, editor [Online]. Clevelend, OH: The Cleveland Clinic Foundation, 2010. Available: http://www.clevelandclinicmeded.com/medicalpubs/diseasemanagement/cardiology/venous-thromboembolism.
7. B.E. Dixon and M.A. Zafar. (2009, January). "Inpatient computerized provider order entry (CPOE)". Agency for Health Care Research and Quality [Online]. Available from: http://healthit.ahrq.gov/ahrq-funded-projects/emerging-lessons/computerized-provider-order-entry-inpatient/inpatient-computerized-provider-order-entry-cpoe.
8. S.B. Anderson, S.N. Lin, J. Reiss, D. Skupski, and D. Grunebaum, "Peripartum thromboprophylaxis before and after implementation of a uniform heparin protocol," *J Perinat. Med.*, vol. 42, pp. 219–223, 2014.
9. C.P. Bourdeaux, K.J. Davies, M.J. Thomas, J.S. Bewley and T.H. Gould, "Using 'nudge' principles for order set design: a before and after evaluation of an electronic prescribing template in critical care," *BMJ Qual. Saf.,* vol. 23, pp. 382–388, May. 2014.
10. M.R. Cassidy, P. Rosenkranz and D. McAneny, "Reducing postoperative venous thromboembolism complications with a standardized risk-stratified prophylaxis protocol and mobilization program," *J. Am. Coll. Surg.,* vol. 218, pp. 1095–1104, 2014.
11. C.M. Formea, A.F. Picha, M.G. Griffin, J.A. Schaller and M.R. Lee, "Enhancing participant safety through electronically generated medication order sets in a clinical research environment: A medical informatics initiative," *Clin. Transl. Sci.,* vol. 3, pp. 312–315, Dec. 2010.
12. M.H. Kroll, A. Ferrajoli, L. Cheng, J.L. Watkins and M.A. Rodriguez, "Incidence rate of venous thromboembolism (VTE) and utilization of a VTE prophylaxis order set module In hospitalized patients with leukemia," *Blood*, vol. 122, pp. 2946–2946, 2013.
13. D. Vyas, D. Bearelly and B. Boshard, "A multidisciplinary quality improvement educational initiative to improve the rate of deep-vein thrombosis prophylaxis," *International Journal of Pharmacy Practice*, vol. 22, pp. 92–95, 2014.
14. A.M. Zeidan, M.B. Streiff, B.D. Lau, S. Ahmed, P.S. Kraus, D.B. Hobson, H. Carolan, C. Lambrianidi, P.B. Horn and K.M. Shermock, "Impact of a venous thromboembolism prophylaxis "smart order set": Improved compliance, fewer events," *Am. J. Hematol.,* vol. 88, pp. 545–549, 2013.
15. *United States EMR Adoption Model* [Online], Chicago, IL: HIMSS Analytics, 2014. Available from http://www.himssanalytics.org/home/index.aspx.

The Diabino System: Temporal Pattern Mining from Diabetes Healthcare and Daily Self-monitoring Data

Eleni I. Georga, Vasilios C. Protopappas, Eleni Arvaniti, and Dimitrios I. Fotiadis

Abstract

In this study, we present an intelligent clinical diabetes management system to support the processes of follow up and treatment of diabetic patients. In addition, temporal pattern mining is proposed as a tool for explaining and predicting the long-term course of the disease. In particular, a fast time-interval pattern mining algorithm is utilized for knowledge discovery from a multivariate dataset concerning not only long-term clinical diabetes data but also daily self-monitoring data.

1 Introduction

Medical data mining aims at identifying established relationships among the recorded variables, determining potential risk factors and extracting new medical knowledge regarding a disease. Diabetes data mining can be applied to: (i) diagnosis, (ii) prognosis, (iii) therapy, (iv) monitoring and (v) management of the disease [1]. The sequential nature of diabetes data necessitates the utilization of association analysis techniques able to handle both co-occurrence and dynamic relationships. Moreover, modelling of Electronic Health Record (EHR) data is very challenging because the time series of clinical variables are acquired asynchronously at irregular time intervals (i.e. at different frequencies). For this purpose, innovative temporal data mining algorithms have been proposed that consider the temporal dimension of the data in opposite to typical data mining which treats data statically [2–5].

Existing clinical information systems are limited to the collection of purely medical data (i.e. clinical examinations or laboratory results) and do not include knowledge about the daily routine of the patient (e.g. glucose measurements, medication adherence, physical activity, diet, etc.) [6, 7]. As a result, they are not able to extract individualized and quantitative knowledge that can support the interpretation of the patient's status and the individualization of treatment. Nevertheless, the advances in mobile health devices and cloud services have enabled monitoring of personal health information on a more ubiquitous level [8, 9].

In this study, we present an innovative information system that supports clinicians in the management of Type 1 and 2 diabetic patients by the efficient integration of health and lifestyle data into its monitoring system [10]. In particular, we focus on the temporal analysis of the data which is attempted through a recently published pattern mining algorithm [11].

E. I. Georga · V. C. Protopappas · D. I. Fotiadis (✉)
Unit of Medical Technology and Intelligent Information Systems, Materials Science and Engineering Department, University of Ioannina, 45110 Ioannina, GR, Greece
e-mail: fotiadis@cc.uoi.gr

E. I. Georga
e-mail: egeorga@cs.uoi.gr

V. C. Protopappas
e-mail: vprotop@cc.uoi.gr

D. I. Fotiadis
Institute of Molecular Biology and Biotechnology, Biomedical Research Department, FORTH, University of Ioannina, 45110 Ioannina, GR, Greece

E. Arvaniti
Department of Endocrinology, Hatzikosta General Hospital, 45445 Ioannina, GR, Greece

2 The Diabino System

Diabino is a clinical system which has been designed to provide an integral management of diabetic patients [10]. It combines parameters that are usually disaggregated in order to correlate them and extract knowledge out of them. The system provides the following functionalities:

- recording of clinical, laboratory and daily self-monitoring data,
- clinical reasoning and interpretation of the status of diabetic patients,
- setting goals and customization of the treatment plan,
- extraction of new medical knowledge and prediction of the long-term status of the patient.

The system, as it is shown in Fig. 1, consists of (i) peripheral devices including the Medtronic continuous glucose monitoring system (CGMS), the activity trackers from Withings, Fitbit, and Bodymedia and the Withings smart body analyser, (ii) the Data Management Subsystem integrating data stored on third-party computing cloud infrastructures and the Hospital Information System, (iii) the Data Analysis and New Knowledge Extraction subsystem incorporating temporal data mining algorithms to identify meaningful patterns and relationships either for an individual patient or for a group of patients, (iv) the Treatment Planning component concerning the intuitive representation of data and the development of the treatment program including clinical reasoning and setting of goals, and (v) the Graphical User Interface through which physicians can access the above-described functions.

It should be mentioned that the HL7 and the ICD-10 interoperability standards as well as the epSOS guidelines are followed in the overall design of the Diabino system. More specifically, the HL7 Reference Information Model (HL7-RIM) is supported at a database level and the ICD-10 diabetes coding is used in the classification of diabetes types and diabetic complications. Moreover, the oAuth security protocol and JSON lightweight data interchange standard are used for communication with third parties and importing data from them, respectively. Moreover, drugs naming is in accordance with the National Drug Organization.

3 Temporal Pattern Mining

3.1 The Dataset

Data were collected at the "Hatzikosta" General Hospital of Ioannina during routine clinical visits. Diabetic individuals who have been diagnosed at least 5 years ago were included. The majority of cases are of non-insulin dependent Type 2 diabetes. We have digitized 114 health records acquired from hard copy. Table 1 presents the baseline characteristics of the dataset. The medical record of each patient, as it is shown in Table 2, includes information on patient profile, glucose-insulin control, therapy, laboratory and clinical tests, and medical surveillance of comorbid conditions. In addition, the feature set has been extended with self-monitoring information (e.g. physical activities, blood glucose, weight).

3.2 Problem Formulation

The process of temporal pattern mining in the Diabino system is illustrated in Fig. 2. The raw time series of each variable V is first transformed into an interval-based representation [4, 11]:

$$\langle v_1[b_1, e_1], v_2[b_2, e_2], \ldots, v_n[b_n, e_n]\rangle, \tag{1}$$

where $v_i \in \Sigma$ is a temporal abstraction that holds from b_i to e_i and Σ is the abstraction alphabet. Medication orders and clinical diagnoses are already represented in a time-interval

Fig. 1 Diabino data flow diagram and system's components
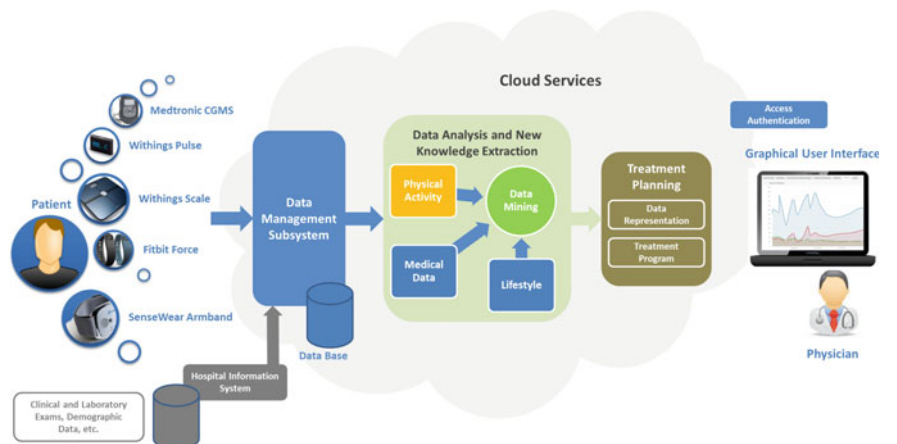
Table 1 Patient baseline characteristics

Gender	
No. Female	71
No. Male	43
Age (years)	
Mean ± SD	68.7 ± 10.4
Range	29–85
Monitoring period (years)	
Mean ± SD	10.0 ± 5.1
Range	2–28
Number of visits per patient	
Mean ± SD	32.0 ± 21.3
Range	3–103

Table 2 Description of the feature set

Demographic and clinical data	
Patient profile	Gender, Age, Diabetes duration, Family history, Obesity, Weight, Birth weight, Habits (e.g. smoking)
Glucose-insulin control	Glycated hemoglobin (HbA1c), Hypoglycemia, Fasting blood glucose, Insulin concentration
Therapy	Oral medication, Insulin therapy
Laboratory examinations	Serum creatinine, Calculated GFR, Microalbumin, Potassium, Systolic and diastolic blood pressure, Low- and high-density lipoprotein, Triglycerides, Hepatic enzymes: AST, ALT, gGT, etc.
Clinical examinations	Abdominal ultrasound, Skin and foot examinations, Fundus examination, Weight, Body Mass Index, Systolic and diastolic blood pressure, Complications
Comorbidities	Hypo/hyperthyroidism, Pernicious anemia, Celiac disease
Self-monitoring data	
Physical activity	Number of steps, Total distance, Total energy expenditure, MET levels, Physical activity levels and duration, Lying down time etc.
Health and lifestyle data	Continuous glucose concentration, Weight, Body composition, Sleep duration and efficiency (Sleep Classification: showing minutes of light, deep and very deep sleep)

format and $\Sigma = \{True, False\}$. For numeric variables, the trend and value abstractions are applied: (i) trend abstractions describe the local trends in each time series, and (ii) value abstractions discretize the time series based on its values [4]. Figure 3 illustrates an indicative example of temporal abstractions for HbA1c parameter, whereas Table 3 presents the value abstractions for a number of laboratory and clinical variables, which have been provided by expert physicians from the General Hospital of Ioannina.

An abstraction for a specific variable i.e. $V = v$ is called a state, whereas a state that holds during an interval i.e. $(V = v, b, e)$ is called a state-interval.

Therefore, the health record of each patient is represented as a multivariate state sequence [4, 11]:

$$\langle (S_1, b_1, e_1), \ldots (S_l, b_l, e_l) \rangle : b_i \leq e_i \wedge b_i \leq b_{i+1}, \quad (2)$$

where S_i is a state and (S_i, b_i, e_i) is a state interval.
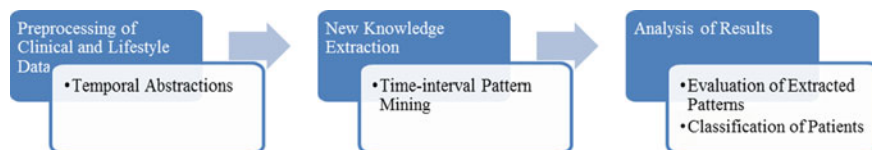
Fig. 2 Diabetes data temporal pattern mining process

Fig. 3 An indicative example of temporal abstractions for the HbA1c parameter
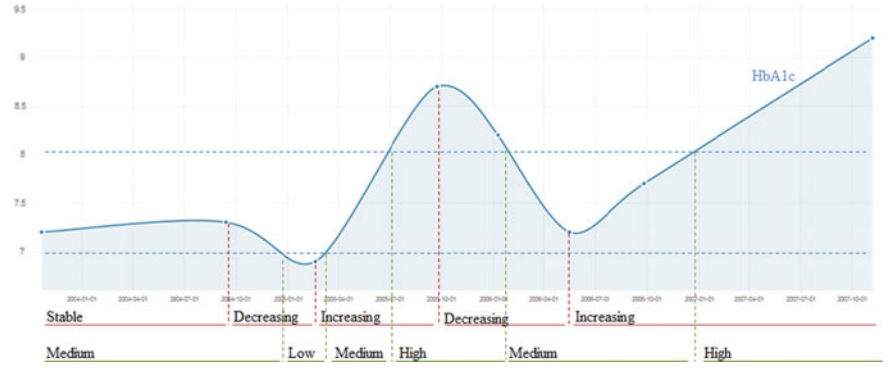
Table 3 Knowledge-based value abstractions defined by the expert physicians

Feature	Unit	Value abstractions
Glycated hemoglobin (HbA1c)	mg/dl	(−Inf, 6), [6, 6.5), [6.5, 7), [7, 7.5), [7.5, 8), [8, 9), [9, Inf)
Fast blood glucose	mg/dl	(−Inf, 100), [100, 125), [125, 200), [200, Inf)
Microalbumin	mg/dl	(−Inf, 0.2), [0.2, 1), [1, 1.9), [1.9, 5), [5, 10), [10, 20), [20, 30), [30, 120), [120,Inf)
Glomerular filtration rate	mL/min/1.73 m^2	(−Inf, 15), [15, 30), [30, 45), [45, 60), [60, 90), [90, Inf)
Low-density lipoprotein	mg/dl	(−Inf, 100), [100, 130), 130, 160), [160, 190), [190, 230), [230, 300), [300, Inf)
High-density lipoprotein	mg/dl	(−Inf, 20), [20, 35), [35, 55), [55, Inf)
Triglycerides	mg/dl	(−Inf, 100), [100, 130), [130, 200), [200, 250), [250, 500), [500, 800), [800, 1000), [1000, Inf)
Systolic blood pressure	mm Hg	(−Inf, 130), [130, Inf)
Diastolic blood pressure	mm Hg	(−Inf, 80), [80, Inf)
Body mass index	kg/m^2	(−Inf, 18.5), [18.5, 25), [25, 30), [30, Inf)

A time-interval pattern is defined as [4, 11]:

$$P = (\langle S_1, S_2, \ldots, S_k \rangle, R), \quad (3)$$

where S_i is the ith state of the pattern and R is defined as:

$$R : R_{i,j} = r, i \in \{1, \ldots, k-1\} \wedge j \in \{i+1, \ldots, k\}, \quad (4)$$

where r is a temporal relation between S_i and S_j [12]. Allen's temporal logic is used to describe the relation for any pair of state intervals (Fig. 4).

Given a database of $|E|$ distinct entities described by a symbolic time-interval series, the support of a temporal pattern P is given by:

$$\text{sup}(P) = \frac{|E^P|}{|E|}, \quad (5)$$

where E^P is the set of distinct entities within which P holds at least once. The pattern mining algorithm outputs all frequent temporal patterns:

$$\{P \in TP : \text{sup}(P) \geq \text{min\_sup}\}, \quad (6)$$
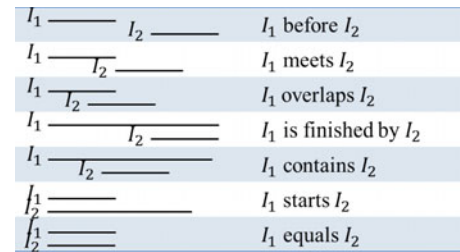
Fig. 4 Allen's temporal operators

where TP is the space of all temporal patterns and min_sup is a minimum support threshold.

3.3 The KarmaLego Algorithm

We have implemented the KarmaLego time-interval pattern mining algorithm, which consists of two phases [11]. In the first phase, all of the frequent patterns of size 2 are generated using a breadth first approach. In the second phase, a recursive process extends the frequent 2-sized patterns into a tree of longer frequent patterns. KarmaLego algorithm uses a flexible version for all of Allen's temporal relations which is defined as:

$$t_1 =^\varepsilon t_2 \; iff \; |t_2 - t_1| \leq \varepsilon \text{ and } t_1 <^\varepsilon t_2 \; iff \; t_2 - t_1 > \varepsilon, \quad (7)$$

where t_1 and t_2 are two time points. In addition to Allen's relations, it defines three abstract temporal relations:

$$\begin{aligned} BEFORE = \{before|meets\}, OVERLAP, CONTAINS \\ = \{is\ finished\ by|contains|starts|equals\}. \end{aligned} \quad (8)$$

Moreover, the before temporal relation is limited by a maximum allowed gap time between consecutive events in a pattern.

4 Conclusions

Temporal patterns of EHR data can reveal statistically significant associations over time and, eventually, predict the long-term course of the disease. The incorporation of self-monitoring health and lifestyle information into the pattern mining algorithm is also expected to enable clinical experts to reason and quantify the effect of daily patient's context on his glycemic and overall clinical status.

Conflict of Interest The authors declare that they have no conflict of interest.

References

1. N. Esfandiari, M. R. Babavalian, A. M. E. Moghadam, and V. K. Tabar, "Knowledge discovery in medicine: Current issue and future trend," *Expert Systems with Applications,* vol. 41, pp. 4434–4463, Jul 2014.
2. K. Orphanou, A. Stassopoulou, and E. Keravnou, "Temporal abstraction and temporal Bayesian networks in clinical domains: A survey," *Artificial Intelligence in Medicine,* vol. 60, pp. 133–149, Mar 2014.
3. S. Concaro, L. Sacchi, C. Cerra, P. Fratino, and R. Bellazzi, "Mining Healthcare Data with Temporal Association Rules: Improvements and Assessment for a Practical Use," in *Artificial Intelligence in Medicine.* vol. 5651, C. Combi, Y. Shahar, and A. Abu-Hanna, Eds., ed: Springer Berlin Heidelberg, 2009, pp. 16–25.
4. I. Batal, H. Valizadegan, G. F. Cooper, and M. Hauskrecht, "A Temporal Pattern Mining Approach for Classifying Electronic Health Record Data," *ACM Trans Intell Syst Technol,* vol. 4, Sep 2013.
5. S. Concaro, L. Sacchi, C. Cerra, and R. Bellazzi, "Mining administrative and clinical diabetes data with temporal association rules," *Stud Health Technol Inform,* vol. 150, pp. 574–8, 2009.
6. O. El-Gayar, P. Timsina, N. Nawar, and W. Eid, "Mobile applications for diabetes self-management: status and potential," *J Diabetes Sci Technol,* vol. 7, pp. 247–62, 2013.
7. R. Jeffery, E. Iserman, and R. B. Haynes, "Can computerized clinical decision support systems improve diabetes management? A systematic review and meta-analysis," *Diabet Med,* vol. 30, pp. 739–45, Jun 2013.
8. E. Georga, V. Protopappas, C. Bellos, and D. Fotiadis, "Wearable systems and mobile applications for diabetes disease management," *Health and Technology,* pp. 1–12, 2014/05/10 2014.
9. R. Bellazzi, A. Dagliati, L. Sacchi, and D. Segagni, "Big Data Technologies: New Opportunities for Diabetes Management," *J Diabetes Sci Technol,* Apr 24 2015.
10. E. I. Georga, V. C. Protopappas, C. V. Bellos, V. T. Potsika, D. I. Fotiadis, E. Arvaniti, *et al.*, "Development of a smart environment for diabetes data analysis and new knowledge mining," in *Wireless Mobile Communication and Healthcare (Mobihealth), 2014 EAI 4th International Conference on*, 2014, pp. 112–115.
11. R. Moskovitch and Y. Shahar, "Classification of multivariate time series via temporal abstraction and time intervals mining," *Knowledge and Information Systems,* pp. 1–40, 2014/10/01 2014.
12. J. F. Allen, "Towards a General-Theory of Action and Time," *Artificial Intelligence,* vol. 23, pp. 123–154, 1984.

Adaptive Latent Space Domain Transfer for Atrial Fibrillation Detection

Xing-Bin Qin, Yan Yan, Jianping Fan, and Lei Wang

Abstract

Atrial fibrillation (AF) is characterised by disorganised atrial electrical activity and contraction. The complications of atrial fibrillation is varied, so it shows several modalities in the Electrocardiogram (ECG). According to our statistics, the beat features and duration time of AF are different from person to person. The distribution of available annotated source ECG date is not as the target. Due to the rapid development of portable monitor, the ECG data explodes. The existing algorithms for the detection of AF perform well only in the training database. Training a general used model requires a great deal of labeled data for every user, this is a huge amount of work that is almost impossible. In order to make full use of the limited labeled ECG data and training a general model, we propose an adaptive latent space domain transfer method for the detection of AF. The model learned from the source data is automatically adapted with little annotated or none in the target data. The MIT-BIH Atrial Fibrillation Database is regard as standard reference for classifier. Then we carry the experimental verification on the MIT-BIH Normal Sinus Rhythm Database and the Long-Term AF Database. The transfer method shows better performance than directly applied. It does make sense for detection and analysis of clinical dynamic electrocardiogram and individual ECG monitoring.

1 Introduction

Atrial Fibrillation is the most common sustained arrhythmia. Lifetime risk over the age of 40 years is near to 2.5%. The complications of AF include haemodynamic instability, cardiomyopathy, cardiac failure and embolic events such as stroke. The exact mechanisms behind AF reminds uncertain, But it mainly contains two parts: focal activation in which AF originates from an area of focal activity; multiple wavelet mechanism in which multiple small wandering wavelets are formed. So The AF shows irregularly irregular rhythm, no P waves, absence of an isoelectric baseline, variable ventricular rate in the ECG wavelet. There are also other complex shapes in AF signals. Detecting the different kinds of AF with high accuracy become a hard problem.

Several algorithms have been proposed for detecting AF. The wavelet transforms have been use to detect and filter the discrete data. The analysis of AF mainly uses the time domain and frequency domain methods. Some methods which measure the absence of P-waves [1, 2] or RR variability [3] are mature. But the accuracy is far from clinical application. Rodrigo [4] presents an original hidden Markov model approach for ECG signal analysis and obtains high beat detection performance. Dash [5] describes a robust Algorithm for automatic detection of AF and employs three statistic parameters to characterize this arrhythmia. Most of the methods work well in the standard ECG library, but perform poor on other database or real application due to the distributions of the dataset change.

In this paper, a method of latent space domain transfer for AF detection is presented. It can take advantage of existing well labeled signal and use them as sources into a new target AF detection task. Here we apply transfer learning [6, 7] for target ECG databases. The MIT-BIH Atrial Fibrillation Database [8] is regard as source to train the model. The MIT-BIH Normal Sinus Rhythm Database and the Long-Term AF Database are used to verify the performance.

X.-B. Qin
University of Chinese Academy of Sciences, Beijing, China

Y. Yan · J. Fan · L. Wang (✉)
Shenzhen Institutes of Advanced Technology, Chinese Academy of Sciences, No. 1068, Xueyuan Road, Shenzhen, Guangdong Province, Nanshan District, China
e-mail: wang.lei@siat.ac.cn

The transfer method shows better result than directly applied the model to target database.

The main contributions of our works are:

- Adapt a novel strengthen of R peak detection algorithm with Mexican-Hat wavelet.
- Fix a window before R peak and mix with RR interval informations as the features space to train the models and automatically classify the atrial behavior types.
- Propose an adaptive latent space domain transfer method for the detection of AF and generalizing the model to different target dataset.

2 Features Space Transfer Towards Atrial Fibrillation

In the preprocessing method, the R peak detection is most important for RR interval and extracting the atrial activity waves. But this is not the focus of this work, the algorithm is described in brief. Instead, We aim at the transfer learning method for AF detection and adapt it to the different distribution dataset. The problem can be defined as: given a target users, get an ECG data with n instances $T = \{t_i | i \in [1, n]\}$ to be classified into AF and normal segments. A source labeled data $S = \{s_i | i \in [1, m]\}$ will be used to help learn a mapping $f = T \rightarrow Y$ in which $Y = \{y_i | y_i \in \{-1, 1\} i \in [1, m]\}$, where -1 represents normal signal and $+1$ represents AF signal.

2.1 The Strengthen of R Peak Detection Algorithm

To locate the waves in the ECG signal more accurately, the Mexican Hat wavelet is used to strengthen the R peak in the signal and week others. By reconstructing the ECG signal with the Mexican Hat wavelet adapted to the different sampling rate and make the R peak more noticeable. Then the wavelet transform method with high accuracy is used to detect R peak. Mexican Hat wavelet is define as:

$$\psi(t) = \frac{2}{\sqrt{3}} \pi^{-\frac{1}{4}} (1 - t^2) e^{-\frac{t^2}{2}} \qquad (1)$$

The transfer of the Mexican Hat wavelet is defined by a scaling factor $a = 2^{\frac{r}{180}}$ and a translation factor $\tau = 2^{(\frac{r}{180}-1)}$ as:

$$\psi_r(t) = 2^{-\frac{r}{360}} \psi \left(2^{-\frac{r}{180}} t - \frac{1}{2} \right) \qquad (2)$$

where r is the sampling rate of the ECG collector. The proposed Algorithm is done by fast Fourier transform (fft) and rebuilt in the frequency domain:

$$f(t) = \frac{1}{\sqrt{a}} fft(\psi_{a,\tau}) \cdot conj(fft(ECG)[t])) \qquad (3)$$

where conj() is the complex conjugate of the parameter. Then we apply the inverse discrete Fourier transform to get the better ECG signal. The performance is shown in Fig. 2.

2.2 Transferring Knowledge of Instances

The case that the source ECG data cannot be reused directly, Parts of this data still be useful together with a few labeled data by the experts in the target ECG data. But the labeled data in the target is tiny, so those data are not enough to train a best model. The source data whose distribution may differ from the target, perhaps because of out-dated, collecting device or the difference of group. To enable transfer learning, part of the source data that has the same distribution to the target plays a role in building the classification model. These data are assumed to be abundant, but the classifiers learned from these data cannot classify the test data well due to different data distributions.

Specifically, in the source ECG database, let X_s be the same distribution instance space, X_d be the different distribution instance space, Y = {−1, +1} be the set of labels. The decision function f mapping X to Y, where $X = X_s \bigcup Xd$. The test ECG data set is denoted by $T = \{(x_i^t)\}$, where $x_i^t \in X_s (i = 1, \ldots, k)$. Here, k is the size of the test set which is unlabeled.

In another case that the source ECG data cannot be reused directly and no labeled data in the target ECG data. if we directly use the classifier learned from source ECG data in the target data, most of the signal will be classified incorrectly due to the different distribution. Transfer learning aims to improve the learning of the target predictive function $f_T(.)$ in target data using the knowledge in source data. However, it is hard to estimate the probability distribution in the target ECG data, the empirical risk can be used to measure the distribution of the source and target domain data. The problem changes to minimize the empirical risk:

$$\theta^* = arg \min_\theta L(\theta) \sum_{(x,y) \in D_T} P(D_T) l(x, y, \theta) \qquad (4)$$

where $l(x, y, \theta)$ is the loss function of parameter θ. But the $P(D_S) \neq P(D_T)$, the above optimization (4) has to be

modified with high generalization ability for the target ECG data, as below:

$$\theta^* = arg \min_{\theta} \sum_{(x,y) \in D_S} \frac{P(D_T)}{P(D_S)} P(D_S) l(x, y, \theta)$$
$$\approx arg \min_{\theta} \sum_{i=1}^{n} \frac{P_T(x_{T_i}, y_{T_i})}{P_S(x_{S_i}, y_{S_i})} l(x_{S_i}, y_{S_i}, \theta) \quad (5)$$

By assigning each instance (x_S, y_S) a corresponding weight $\frac{P_T(x_{T_i}, y_{T_i})}{P_S(x_{S_i}, y_{S_i})}$, we can learn a precise model for the target ECG data. Since $P(Y_T | X_T) = P(Y_S | X_S)$, $\frac{P_T(x_{T_i}, y_{T_i})}{P_S(x_{S_i}, y_{S_i})} = \frac{P(x_{S_i})}{P(x_{T_i})}$. So the problem is to estimate $\frac{P(x_{S_i})}{P(x_{T_i})}$ for each instance. Here, we use the method of kernel-mean matching (KMM) proposed by Huang et al. [9] to estimate $\beta = \frac{P(x_{S_i})}{P(x_{T_i})}$. Each instance is weighted by β for knowledge transferring. For the source instances that close to the target distribution get a higher weight. Then we user instances with high weight to adjust the learner, transfer the classifier to classify the target ECG data.

2.3 Weight Transductive Using Adaptive SVM

Cores and Vapnik [10] proposed the SVM which uses the constrained optimization method to find the best margin of two different classes in the feature space. Given a set of training data $(x_i, t_i), i = 1, \ldots, N$, where $x_i \in R^d$ and $t_i \in \{-1, +1\}$. The problem is to minimize the separating margin and to minimize the training errors ξ_i:

$$
\begin{aligned}
Mimimize: & \quad L_{SVM} = \frac{1}{2} \|w\|^2 + C \sum_{i=1}^{N} \xi_i \\
Subject\ to: & \quad t_i(W \cdot \phi(x_i) + b) \geq 1 - \xi_i \\
& \quad \xi_i \geq 0 \quad i = 1, \ldots, n
\end{aligned} \quad (6)
$$

Based on the Karush-Kuhn (KKT) theorem, to train the SVM is solving the dual optimization problem.

Adaptive SVM [7] extends the standard SVM to identify the mathematical relation from classifier that has trained from the source domain to an adapted one. The classifier is adapted to learn the similarity to the features of the target domain and then used to categorize the ECG signal in the target database. The delta function is $f(x) = f'(x) + w^T \phi(x)$. The formulation of the adaptive SVM (aSVM) is defined as follow:

$$
\begin{aligned}
Mimimize: & \quad L_{aSVM} = \frac{1}{2} \|w\|^2 + C \sum_{i=1}^{N} \xi_i \\
Subject\ to: & \quad y_i f'(x_i) + y_i w^T \phi(x_i) \geq 1 - \xi_i \\
& \quad \xi_i \geq 0 \quad i = 1, \ldots, n
\end{aligned} \quad (7)
$$

where $f'(x)$ is the classifier learned from the auxiliary dataset. $f(x)$ is the classifier learned from the source domain. w is the parameter learned using the Adaptive SVM. The experiments is discussed below.

3 Electrocardiography Datasets and Arrhythmia Annotation

In the presented method for AF detection, The MIT-BIH Atrial Fibrillation Database (MIT-AF) [8] is regard as source and use the labeled signal to train the ActiveTransfer and Adaboosting classifiers. Then we transfer them to MIT-BIH Normal Sinus Rhythm Database (MIT-NSR) and Long-Term AF Database (LT-AF) to verify the performance.

3.1 The Database

The MIT-AF database [8] includes 25 long-term ECG recordings with AF (mostly paroxysmal). Of these, 23 records are each 10 h in duration with two leads and sampled at 250 samples per second with 12-bit resolution over a range of 10 mV. Recording 04043, 08405 and 08434 isolated data blocks from the original tapes were unreadable, those records are removed. The MIT-NSR database includes 18 long-term ECG recordings of subjects that were found to have had no significant arrhythmias, they are used to verify the specificity of the models. The LT-AF database contains 84 long-term ECG recordings of subjects with paroxysmal or sustained AF. Each record contains two simultaneously recorded ECG signals digitized at 128 Hz with 12-bit resolution over a 20 mV range. We randomly pick 10 records to test the transfer methods.

3.2 Arrhythmia Classes and Labels

The MIT-AF database contains rhythm annotations of types (AFIB-atrial fibrillation, AFL-atrial flutter, J-AV junctional rhythm and N-indicates all other rhythms). The annotations in this database have been revised for consistency with those used for the other two databases. All the annotations are mapped to AF segments or normal.

4 Experimental Results

In this section, the experimental results of the R detection and transfer learning algorithm are presented to evaluate the accuracy of the methods.

4.1 Data Proportion and Distribution

According to our statistics, 10 recordings of the MIT-AF database used each has 10 h in duration. Among them, there are 204 atrial fibrillation fragments, total time of 83.42 h. The MIT-BIH Normal Sinus Rhythm Database has no significant arrhythmias, so all the signals in this database are regarded as normal data and used to verify the specificity of the classifiers. We randomly pick 10 recordings from the LT-AF database. Record durations vary but are typically 24–25 h and there are 373 atrial fibrillation fragments, total time of 103.05 h. The proportion of the segments that contain AF beat is 41.34% in the MIT-AF database and 43.43% in the Long-Term AF Database. The Fig. 1 shows the feature distribution of different database. The blue color represents the data draw from the MIT-BIH Atrial Fibrillation Database and the green is from the Long-Term AF Database. The symbols *, + indicate the AF segments and the other is normal. The distribution is various from each other.

4.2 R Detection and Features Extraction

R peak detection is the most important work in our experience. A reliable algorithm is necessary, especially to the signal with high noise. According to the characteristics of the QRS wavelet, we propose a frequency adaptive
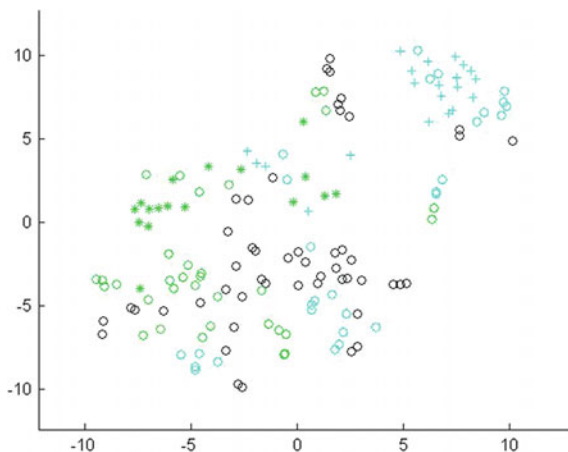
Fig. 1 The features distribution of the different ECG database visualizing with t-SNE [11]
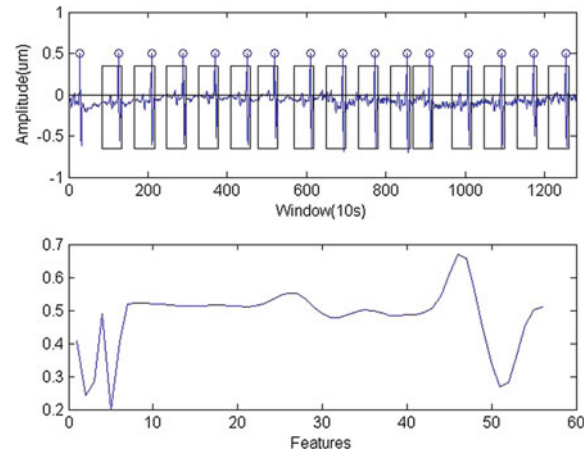
Fig. 2 Capture the windows depends on R and features extraction

algorithm to strengthen the R peak in the waves and weak others signal with the Mexican Hat wavelet.

The AF shows irregularly irregular rhythm and no P waves in the electrocardiogram. So we split the signal with window size of 10 s and use R detection algorithm to find the R peaks. Then we adapt another window to cut the signal that contains P wave. Also manually extract some features that reflect the RR gaps and combine those features with the mean of the P wave windows. The Fig. 2 shows the progress of features extraction. The features well express the RR gaps and P waves information.

4.3 Performance Study

In the experiments, the MIT-AF database is divided into two parts. 80% of the data is added to train the distinct models and the left is used to test the model. All the MIT-NSR database and the LT-AF database are acted as target test data. The classifiers' performance are evaluated in terms of specificity (SPC) which describes proportion of the normal segments divided into norm and accuracy rate (ACC) which denotes the proportion of correctly classified segments. The logical regression (LR) gets the accuracy of 86.96%, the specificity is stable in the MIT-NSR and lower in the LT-AF database. The extreme learning machine (ELM) with Gauss kernel has the highest accuracy of 97.05% and same in the target dataset. The neural network (NN) is similar with the ELM. The SVM with Gauss kernel function works well on the source database, but very low performance in the target. At last, we use the transfer learning method to reweight the SVM model and get a better result.

Table 1 illustrates the detail performance of the different classifiers. The accuracy is remarkably improved with the transfer learning by adaptive SVM. The test accuracy is very high in the source database and the highest is 97.050%, but

Table 1 Comparisons with different learning methods

Approaches	Source (MIT-AF) (%)	Target (MIT-NSR) (%)	Target (LT-AF) (%)
LR	86.960	86.995	76.365
ELM	**97.050**	87.315	87.715
NN	96.070	87.590	**89.365**
SVM	96.670	32.290	47.690
TL (aSVM)	96.670	**96.580**	72.440

the accuracy of those classifiers significantly decreases in the other two target databases. By transfer learning, the accuracy in the MIT-NSR database is 96.58% and the LT-AF database is 72.440%.

5   Conclusions

Atrial fibrillation automatic Detection is a big challenge to the massive Holter ECG signal. The proportion of occurrence and feature space distribution are diverse. So the algorithms used for AF detection are not stable. Training a general model requires a abundant labeled data for every user, so we propose the adaptive latent space domain transfer method for the detection of AF. We implement the transfer learning using Adaptive SVM to utilize these labeled source ECG database into the classification of target ECG signal for AF detection.

The experimental results show that the proposed method could outperform the directly use of the classifiers on different target dataset. Using the transfer learning method, the promotion in the MIT-NSR database is 64.29 and 24.75% in the LT-AF database. Moreover, this method enhances the classification accuracy with limited annotation ECG signal.

References

1. M. Stridh and L. Sornmo, "Spatiotemporal QRST Cancellation Techniques for Analysis of Atrial Fibrillation." IEEE Transactions on Biomedical Engineering, vol. 48, No. 1, Jan. 2001
2. M. Fukunami, T. Yamada, M. Ohmori, K. Kumagai, K. Umemoto, A. Sakai, N. Kondoh, T. Minamino, and N. Hoki, "Detection of Patients at Risk for Paroxysmal Atrial Fibrillation During Sinus Rhythm by P Wave-Triggered Signal-Averaged Electrocardiogram." Aug 1990
3. Xiaolin Zhou, Hongxia Ding, Benjamin Ung, Emma Pickwell-MacPherson and Yuanting Zhang, "Automatic online detection of atrial fibrillation based on symbolic dynamics and Shannon entropy." BioMedical Engineering OnLine, 2014
4. Rodrigo V. Andreao, Bernadette Dorizzi, and Jerome Boudy, "ECG Signal Analysis Through Hidden Markov Models." IEEE Transactions on Biomedical Engineering, vol. 53, No. 8, Aug. 2006
5. S. Dash, K.H. Chon, S. Lu, and E.A. Raeder, "Automatic Real Time Detection of Atrial Fibrillation." Annals of Biomedical Engineering, Vol. 37, No. 9, Sep 2009, pp. 1701–1709
6. Linda Argote, Paul Ingram, John M. Levine and Richard L. Moreland, "Knowledge Transfer in Organizations: Learning from the Experience of Others." Organizational Behavior and Human Decision Processes, vol. 82, No. 1, May. 2000, pp. 1C8
7. Jun Yang, Rong Yan, and Alexander G. Hauptmann, "Cross domain video concept detection using adaptive svms." 15th International Conference on Multimedia, pages 188–197, ACM, 2007
8. Goldberger A.L., Amaral L.A.N., Glass L., Hausdorff J.M., Ivanov P.Ch., Mark R.G., Mietus J.E., Moody G.B., Peng C.-K., Stanley H.E. PhysioBank, PhysioToolkit and PhysioNet: Components of a New Research Resource for Complex Physiologic Signals. Circulation 101(23):e215–e220 [Circulation Electronic Pages; http://circ.ahajournals.org/cgi/content/full/101/23/e215]; 2000 (June 13)
9. J. Huang, A. Smola, A. Gretton, K. M. Borgwardt, and B. Scholkopf, Correcting sample selection bias by unlabeled data. In Proceedings of the 19th Annual Conference on Neural Information Processing Systems, 2007
10. C. Cortes and V. Vapnik, "Support vector networks." Machine Learning, Vol. 20, No. 3, pp. 273–279, 1995
11. L.J.P. van der Maaten and G.E. Hinton, "Visualizing High-Dimensional Data Using t-SNE." Nov. 2008, pp. 2579–2605

Detection of Chewing Motion Using a Glasses Mounted Accelerometer Towards Monitoring of Food Intake Events in the Elderly

Gert Mertes, Hans Hallez, Tom Croonenborghs, and Bart Vanrumste

Abstract

A novel way to detect food intake events using a wearable accelerometer is presented in this paper. The accelerometer is mounted on wearable glasses and used to capture the movements of the head. During meals, a person's chewing motion is clearly visible in the time domain of the captured accelerometer signal. Features are extracted from this signal and a forward feature selection algorithm is used to determine the optimal set of features. Support Vector Machine and Random Forest classifiers are then used to automatically classify between epochs of chewing and non-chewing. Data was collected from 5 volunteers. The Support Vector Machine approach with linear kernel performs best with a detection accuracy of $73.98\% \pm 3.99$.

1 Introduction

Studies have shown that up to 15% of community dwelling and home-bound adults aged over 65 are malnourished and up to 45% are at risk [1, 2]. It is estimated that between 20 and 60% of hospitalised elderly and up to 85% of nursing home residents are malnourished [3]. Malnutrition is most frequent in the frailest of people, particularly those who are less autonomous and require help performing daily tasks.

Furthermore, malnutrition has been identified as one of four causes of frailty [4]. Frailty is considered to be a distinct syndrome, characterised by weakness, a slow walking speed, a low level of physical activity, unintentional weight loss and exhaustion.

Nutrition is an important factor in the elderly's health status. Malnourishment is associated with decreased muscle strength, poorly healing wounds, an increased hospital admission length and increased hospital mortality rate [5]. Furthermore, malnourished elderly are more prone to develop pressure ulcers and infections [6]. Preventing malnutrition by means of a targeted nutritional intervention could greatly improve the quality of life. Early recognition and treatment should therefore be included in the routine care of every elderly [7].

1.1 Food Intake Monitoring

Determining malnutrition can be done in a few ways. The first is by means of a self-report diary. These have been used to measure pain, sleep, illness or injury and health care use, as well as eating-related issues such as binge eating, energy intake and expenditure in weight loss treatment [8]. In the case of malnutrition, the diary provides insight into two aspects of nutritional intake. The first is to monitor a person's eating behaviour and food consumption on a daily basis in order to see if enough meals are consumed, and second, to record in detail all foods consumed for a nutrient analyses. The person is instructed to record all food intake, usually including location, time of day, quantity eaten, and nutrient values. A self-report diary is typically in paper-and-pencil format, but computerised solutions using a tablet-pc or terminal specifically catered to elderly people also exist [9]. It is clear, however, that a self-report diary has several limitations when used to self-monitor elderly people. First and foremost, keeping track of food intake and the need to look up foods in a nutrient guide and record the amount of intake is a time consuming task. The self-monitoring protocol is seldom

G. Mertes (✉) · T. Croonenborghs · B. Vanrumste
KU Leuven, Technology Campus Geel, AdvISe, Geel, Belgium
e-mail: gertmertes@gmail.com

G. Mertes · B. Vanrumste
KU Leuven, ESAT-STADIUS, Leuven, Belgium

G. Mertes · B. Vanrumste
iMinds Medical Information Technology Department, Leuven, Belgium

H. Hallez
KU Leuven, Technology Campus Oostende, ReMI, Leuven, Belgium

H. Hallez · T. Croonenborghs
Department of Computer Science, KU Leuven, Leuven, Belgium

followed adequately, resulting in an incomplete diary [8]. Furthermore, limited literacy skills or bad handwriting also play an important role. Similar techniques such as 24-hour recalls, food records or food frequency questionnaires share the same limitations, especially in elderly care.

A different type and the most widespread tool for nutritional screening and assessment is the Mini Nutritional Assessment (MNA) [5]. The MNA contains 18 questions grouped into 4 parts: anthropometry, general status, dietary habits, and self-perceived health and nutrition states. Each question is graded and summed up to a total of 30 points. The result is defined by the following thresholds: a score below 17 indicates malnutrition; a score between 17 and 23.5 indicates a risk of malnutrition; scores above 24 indicates a good status.

Other tools such as the Geriatric Nutritional Risk Index (GNRI) [10] and Cumulative Illness Rating Scale (CIRS) [11] have also been used in combination with the MNA to provide further insight into the person's health status [1, 5].

An important limitation, however, that instruments such as the MNA all share is the requirement for a health care professional to assist in taking and completing the test. Neither are they taken at routine intervals due to their time consuming nature [12]. They are therefore not used as a preventative tool to detect malnutrition at an early stage. In case of home-bound elderly receiving home care, tests such as the MNA are typically never administered unless ordered by a GP or after admission to a hospital. The results of these tests are also not always on par with what care-takers observe on a day to day basis.

1.2 Detecting Food Intake

A potential solution to replace manual self-monitoring methods is through the use of wearable devices. A wearable device that is able to detect food intake events and determine the amount of food ingested could replace manual food diaries and questionnaires. Sazonov and Fontana [13] demonstrated the use of a piezoelectric strain gauge sensor fixed to the lower jaw to detect epochs of chewing with high accuracy. In [14], the strain gauge sensor is incorporated in a larger system together with a hand gesture sensor and an accelerometer worn on a lanyard around the neck. In [15], 3D surface reconstruction from pictures taken with a mobile phone was used to determine the amount and type of food ingested. Detection of chewing and swallowing using a wearable microphone was presented in [16] and [17].

In this paper, the use of an accelerometer mounted on wearable glasses is proposed to measure the chewing motion as part of a system to measure food intake. The use of an accelerometer integrated into an already worn pair of glasses would have little impact on the elderly's comfort and is less stigmatising than other alternatives. Glasses are typically taken off to sleep, during which the sensor could be wirelessly charged on the night stand.

2 Methods

2.1 Glasses Mounted Accelerometer

Figure 1 shows the prototype setup used to capture the data. We used the low-noise tri-axial accelerometer of a Shimmer3 unit with a sample frequency of 128 Hz to capture the movements. The raw accelerometer signal is first filtered using a 10th order Chebyshev band-pass filter with $f_L = 1$ and $f_H = 45$ Hz in order to discard DC offset and high frequency noise and prevent aliasing.

In order to determine the feasibility of this method to detect chewing motion, the researcher himself consumed a meal while recording the accelerometer signal. The meal was recorded with a camera for annotation purposes. Figure 2 shows the captured signal in each of the three dimensions. The overlaying square wave is the annotation signal indicating an epoch of non-chewing (0) or chewing (1). As soon as chewing starts around the 6 mark, distinct peaks can be observed in all three dimensions, although different in amplitude. After comparing the accelerometer signal with what was visible in the video, we found that these peaks are the result of the chewing motion: a peak is captured each time the jaw is closed. The first four such peaks are highlighted in blue in Fig. 2. Since these peaks are visible in the time domain, it should be possible to extract characterising features from the signal to be used for classification.

2.2 Dataset

To construct the training and test dataset, data was collected from 5 volunteers who were asked to consume a meal while

Fig. 1 Setup used for data collection. The Shimmer sensor is firmly attached to the frame using cable ties
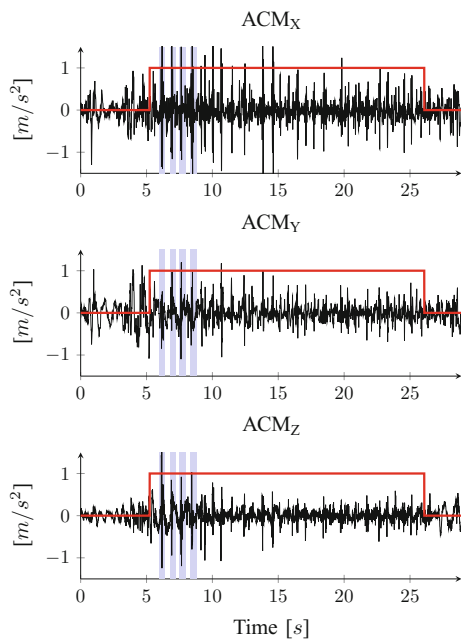
Fig. 2 Illustration of the captured tri-axial accelerometer signal while eating. The red annotation signal indicates epochs of chewing (1) and not chewing (0). The highlighted peaks represent the closing motion of the jaw (only the first four are highlighted) (Color figure online)

wearing the acquisition setup. Annotation was done by an observer. Two states were annotated: chewing (1) and not-chewing (0). As soon as the food entered the mouth and chewing started, the annotation was set to *chewing* until the food was swallowed, after which the annotation was set to *not-chewing*. Examples of activities that fall under the *not-chewing* class are: talking to the observer, bringing food to mouth, cutting food, etc. In order to get a representation of every day meals, food items with different properties were selected. The following meals were consumed: a crunchy deli sub sandwich, a mixed salad with bread (two times), mashed potatoes with vegetarian burger, and a hamburger.

Test subjects were also asked to walk around the room for roughly 1 min. This was done to determine if we are able to distinguish the chewing motion from other types of daily activities. This resulted in a total of three classes: *chewing*, *not-chewing* and *walking*.

2.3 Feature Extraction and Selection

From the triaxial accelerometer signal (x, y and z), the resultant net acceleration r is calculated using Eq. 1.

$$r = \sqrt{x^2 + y^2 + z^2} \qquad (1)$$

All data is then split up according to the recorded annotation. For example, all data containing *chewing* is concatenated serially to produce one signal containing only the *chewing*

Table 1 List of extracted features. Highlighted in bold are those selected by the forward feature selection

	Name
1	Standard deviation
2	Mean
3	Power
4	Range
5	Skewness
6	**# of zero-crossings of r**
7	# of zero-crossings of $\frac{d^2r}{dt^2}$
8	25th percentile value
9	50th percentile value
10	**75th percentile value**
11	**Dominant frequency**

activity. Likewise for the *not-chewing* and *walking* activity. As discussed in Sect. 2.1, the signals are then filtered with a band-pass filter with $f_L = 1$ Hz and $f_H = 45$ Hz. The filtered signal is segmented into non overlapping windows of 5 s. Concatenation is done to prevent windows containing data from different classes in the training dataset. Window size was experimentally determined to allow for enough windows that don't contain data from different classes when the detector is used in real-time. Chewing typically takes between 10 and 20 s, a window size of 5 s ensures that enough windows completely contain data of only one class. Features are subsequently extracted from the net acceleration signal on a per window basis. Table 1 shows an overview of the extracted features.

A forward feature selection based on [18] is performed on the dataset to eliminate redundant features. This method selects features with high correlation to the class, while discarding those having high intercorrelation. The total of 11 features is reduced by the algorithm to a final set of three, as shown in bold in Table 1: zero crossing rate, 75th percentile value and dominant frequency (determined via FFT).

2.4 Classification

Equivalent to the feature extraction as described in the previous section, classification is done on a per window basis. Two classifiers are evaluated: the Support Vector Machine (SVM) and the Random Forest (RF) decision tree. Classifier parameters were experimentally tuned to produce the highest accuracy. For the SVM, we chose a linear kernel with cost parameter $C = 1$ and the RF was constructed with a maximum of 100 trees. It is worth noticing that a feature selection is typically not required when using decision trees such as Random Forest due to their already selective nature in

features. However, we evaluated this and found that the RF performed better using only the three features selected by the feature selection.

Due to the limited size of the dataset, validation of the classifiers is done using the leave-one-out method. One person is excluded from the training set and used to test the classifier. This is done for each of the five participants and the results are averaged. We use the accuracy as performance metric. This method provides the added value that the classifiers can be tested on each person individually and evaluate how well they work as a group model.

To construct the training dataset, the method described in Sect. 2.3 is used. To construct the test set, a slightly altered version is used. Because we want to simulate the use of the classifiers in a real life setting, we segment the original signal into windows of five seconds without the concatenation step. This means, however, that a single window could potentially contain data from different classes. When this is the case, a choice is made: when a window contains data of a certain class for over 50% of the time, this class label is assigned to the window.

3 Results

Two experiments are conducted. In the first experiment, only two classes are included: *chewing* and *not-chewing* while the *walking* class is omitted from both the training and test set. In the second experiment, the *walking* class is also included together with *chewing* and *not-chewing*. Leave-one-out validation as described in Sect. 2.4 is used in both cases. Table 2 shows the results of these two experiments. The table contains the accuracy and standard deviation of the leave-one-out validation. We can see that the SVM classifier performs slightly better than the RF classifier in both cases, although the difference is statistically insignificant, with an average accuracy of 73.98% $\pm$ 3.99.

Table 3 shows the confusion matrices of the two experiments for the SVM classifier. These matrices contain the summed result of the leave-one-out validation, i.e. the confusion matrix values for each participant that was left out are added together.

Table 2 Results of the leave-one-out validation (acc. $\pm$ std.dev.)

Included classes	SVM	RF
Chewing–not-chewing	**73.98% $\pm$ 3.99**	72.39% $\pm$ 6.51
Chewing–not-chewing–walking	71.93% $\pm$ 5.03	69.79% $\pm$ 8.79

Table 3 Confusion matrices for the SVM classifier. Sum of all leave-one-out results

	Chewing	Not-chewing	
Chewing	**373**	93	
Not-chewing	120	**230**	
	Chewing	Not-chewing	Walking
Chewing	**361**	98	7
Not-chewing	115	**228**	7
Walking	6	9	**23**

4 Discussion and Conclusion

The average detection accuracy of 73.98% $\pm$ 3.99 obtained with the SVM indicates that our approach is able to correctly classify chewing events, but a considerable amount of false positives are still present. This can be seen in the confusion matrices in Table 3. Averaged over the five participants, the amount of false positives does not bias towards one specific activity. However, we found the false positive rate to be very person-specific. For example, when using the SVM classifier and classifying between *chewing* and *not-chewing*, for two out of five participants the *chewing* activity was frequently incorrectly classified as *not-chewing*, while for the other three participants the opposite was true. Likewise for the *walking* activity: for three participants there were no false positives for this activity, while the remaining two did have roughly 30% false positives. For all five participants, however, the true positive rate remained higher than the false positive rate.

This difference in false positives per person can be attributed to a couple of reasons. First, there is the fact that the annotation is done by an observer during the meal and is therefore not perfect. While this is not a problem for the *walking* activity, some errors could be made when annotating between *chewing* and *not-chewing*. Secondly, the dataset which was used to train and validate the classifiers is limited to only five participants. It is also worth noticing that our dataset is unbalanced, with less activities of the *not-chewing* class and only a few of the *walking* class. In order to further reduce the amount of false positives, a larger dataset would have to be recorded.

Adding the *walking* activity to the list of included classes lowers the detection accuracy. This indicates that there is still room for improvement in our proposed method. Looking towards future work, a possible improvement could be to further incorporate features from the frequency domain in the classifier or look into methods such as wavelet transforms. Furthermore, while the five second window was

chosen based on a motivated choice, the effect of the window size on the accuracy still stands to be determined.

Different studies have shown that it is possible to detect chewing motion using a group model with a jaw strain gauge sensor or microphone system with accuracies ranging from 80 to 90% [14, 16, 17]. While our system did not improve on these accuracies, it does offer the fact that the sensor can be incorporated into an existing pair of glasses, either by using a custom frame with the sensor built in or using a clip-on system. This would have little impact on the comfort of the wearer and makes the system more suitable for elderly people. Before this can happen, however, more research specifically targeting elderly people is required, starting with a case-study examining the elderly's and care givers' willingness to use such a system and the acquisition of a dataset with test subjects in this demographic group.

Conflict of Interest The authors declare that they have no conflict of interest.

References

1. L. Donini, P. Scardella, L. Piombo, B. Neri, R. Asprino, A. Proietti, S. Carcaterra, E. Cava, S. Cataldi, D. Cucinotta, G. Di Bella, M. Barbagallo, and A. Morrone, "Malnutrition in elderly: Social and economic determinants," *The Journal of Nutrition, Health & Aging*, vol. 17, pp. 9–15, 2013.
2. Nutricia, "Results of the NutriAction II study," 2013.
3. L. Donini, C. Savina, M. Piredda, D. Cucinotta, A. Fiorito, E. Inelmen, G. Sergi, L. Dominguez, M. Barbagallo, and C. Cannella, "Senile anorexia in acute-ward and rehabilitation settings," *The Journal of Nutrition Health and Aging*, vol. 12, no. 8, pp. 511–517, 2008.
4. R. DiMaria-Ghalili and E. Amella, "Nutrition in older adults: Intervention and assessment can help curb the growing threat of malnutrition." *American Journal of Nursing*, vol. 105, pp. 40–50, 2005.
5. E. Cereda, C. Pedrolli, A. Zagami, A. Vanotti, S. Piffer, A. Opizzi, M. Rondanelli, and R. Caccialanza, "Nutritional screening and mortality in newly institutionalised elderly: a comparison between the geriatric nutritional risk index and the mini nutritional assessment," *Clinical Nutrition*, vol. 30, no. 6, pp. 793–798, 2011.
6. D. Volkert, L. Pauly, P. Stehle, and C. C. Sieber, "Prevalence of malnutrition in orally and tube-fed elderly nursing home residents in Germany and its relation to health complaints and dietary intake," *Gastroenterology research and practice*, 2011.
7. H. Lochs, C. Pichard, and S. Allison, "Evidence supports nutritional support," *Clinical Nutrition*, vol. 25, no. 2, pp. 177–179, 2006.
8. L. Burke, M. Warziski, T. Starrett, J. Choo, E. Music, S. Sereika, S. Stark, and M. Sevick, "Self-monitoring dietary intake: Current and future practices," *Journal of Renal Nutrition*, pp. 281–290, 2005.
9. J.-M. Wu, H.-J. Yu, T.-W. Ho, X.-Y. Su, M.-T. Lin, and F. Lai, "Tablet pc-enabled application intervention for patients with gastric cancer undergoing gastrectomy," *Computer methods and programs in biomedicine*, vol. 119, no. 2, pp. 101–109, 2015.
10. O. Bouillanne, G. Morineau, C. Dupont, I. Coulombel, J.-P. Vincent, I. Nicolis, S. Benazeth, L. Cynober, and C. Aussel, "Geriatric nutritional risk index: a new index for evaluating at-risk elderly medical patients," *The American journal of clinical nutrition*, vol. 82, no. 4, pp. 777–783, 2005.
11. P. A. Parmelee, P. D. Thuras, I. R. Katz, and M. P. Lawton, "Validation of the cumulative illness rating scale in a geriatric residential population." *Journal of the American Geriatrics Society*, 1995.
12. G. Mertes, G. Baldewijns, P.-J. Dingenen, T. Croonenborghs, and B. Vanrumste, "Automatic fall risk estimation using the nintendo wii balance board," in *Biomedical Engineering Systems and Technologies*, 2015.
13. E. Sazonov and J. Fontana, "A sensor system for automatic detection of food intake through non-invasive monitoring of chewing," *IEEE Journal of Sensors*, vol. 12, pp. 1340–1348, 2012.
14. J. Fontana, M. Farooq, and E. Sazonov, "Automatic ingestion monitor: A novel wearable device for monitoring of ingestive behavior," *IEEE Transactions on Biomedical Engineering*, pp. 1772–1779, 2014.
15. M. Puri, Z. Zhiwei, Y. Qian, A. Divakaran, and H. Sawhney, "Recognition and volume estimation of food intake using a mobile device," in *Workshop on Applications of Computer Vision*, 2009.
16. S. Passler and W.-J. Fischer, "Food intake activity detection using a wearable microphone system," in *Intelligent Environments (IE), 2011 7th International Conference on*. IEEE, 2011, pp. 298–301.
17. O. Amft, "A wearable earpad sensor for chewing monitoring," in *Sensors, 2010 IEEE*. IEEE, 2010, pp. 222–227.
18. N. Z. Hamilton, "Correlation-based feature subset selection for machine learning," 1998.

Intra-operative Tumor Tracking Using Optical Flow and Fluorescent Imaging

Daniel Y. Kim, John H. Phan, and May D. Wang

Abstract

Image-guided surgery (IGS) can assist surgeons by modeling and visualizing objects of interest (tumors, nerves, etc.) that may be obstructed or difficult to recognize during surgery. Models based on pre-operative images are often not applicable during surgery because of motion and deformation. Therefore, real-time updates to IGS models are required. We propose an automated intra-operative tumor tracking system in which the initial tumor location is predicted using near infrared (NIR) fluorescence with indocyanine green (ICG), and the tumor is tracked using the Lucas-Kanade (LK) algorithm, a multi-resolution coarse-to-fine optical flow method. We simulate various conditions of intra-operative tumor movement, including movement speed and variations in image brightness. The LK method can accurately track tumors when speed of tumor movement and image brightness changes are low. However, when the speed of tumor movement increases or when image brightness changes by more than 30%, the LK method fails to track the tumor location. We compare the LK method to several other optical flow algorithms and find that LK has relatively high accuracy and tolerance in both speed and brightness changes, although each algorithm has strengths and weaknesses. In addition to the proposed intra-operative system, the simulations and metrics that we use in this study may serve as benchmarks to assess the performance of intra-operative tumor tracking algorithms.

1 Introduction

Tumor motion is a major challenge during surgical tumor resection. Because of breathing and cardiac motion, the location of the tumor can change. Thus, identification and resection of tumor margins can be difficult, resulting in the possibility of residual tumor remaining after surgery. Therefore, medical imaging technology is required for tracking the tumor location and providing this information to surgeons in real time.

Systems for image-guided surgery (IGS) can produce accurate, detailed, and specific models, providing real-time visualization of tumors or internal structures during surgery [1]. Previously, surgeons used pre-operative imaging information during surgery. For example, the tumor location was predicted by MRI before surgery, and the pre-operative imaging information was used during surgery. However, such systems could not account for deformations and organ motion during surgery [1]. As a result, about 40% of patients leave the operating room without complete resection of their tumor [2]. Intra-operative systems were developed to address these challenges. For example, using a pre-operative imaging data set that is correlated with the operative field, MRI or CT can detect and register tumor locations in real time [1]. CT and ultrasound can be combined to assess correlation of a combination of signals extracted intra-operatively [3]. In addition, advances in nanotechnology have made it possible to visualize the tumor in vivo intra-operatively. For example, quantum dots or indocyanine green (ICG) are fluorescent nanoparticles that can bind to specific biomarkers to detect tumors [4, 5]. The near infrared (NIR) fluorescence signals from such nanoparticles can be analyzed by systems such as FLARE^{TM} [6]. These intra-operative systems can guide

D. Y. Kim · J. H. Phan · M. D. Wang (✉)
Biomedical Engineering Department, Georgia Institute of Technology and Emory University, Atlanta, GA 30332, USA
e-mail: maywang@bme.gatech.edu

D. Y. Kim
e-mail: dkim304@gatech.edu

J. H. Phan
e-mail: jhphan@gatech.edu

M. D. Wang
Electrical and Computer Engineering Department, Georgia Institute of Technology, Atlanta, GA 30332, USA

surgeons in locating tumors to improve the results of surgery.

We propose an intra-operative system that uses ICG to locate a tumor pre-operatively, then uses optical flow to track the tumor during surgery. We also develop benchmark metrics for evaluating the performance of optical flow tumor tracking systems. ICG is an FDA approved tumor marker that binds to proteins in blood plasma and is excited by an NIR wavelength of 780 nm [5]. Optical flow can accurately track the movement of objects between successive images without the continued use of the NIR system. Prolonged exposure to NIR laser emissions may be hazardous [7]. Thus, the use of ICG and optical flow reduces exposure time of the NIR laser and simplifies the optical system. Optical flow methods include several classes: intensity-based differential methods, phase-based methods, region-based methods, and energy-based methods [8]. The Horn-Schunck (HS) method assumes constant intensity and smoothness [9]. The phase-based method computes optical flow from the phase behavior of band-pass filter outputs [10]. Brox et al. [11] proposed a rotationally invariant model for optical flow computation based on nonlinear constancy assumptions. We evaluate one of the intensity-based differential methods, Lucas-Kanade (LK), because of its computational efficiency, accuracy, and robustness to noise [12]. In addition, we compare it to two constant intensity based algorithms (i.e., HS and nonlinear constancy-based) and a non-constant intensity based algorithm (i.e., phase-based). We compare these methods under two scenarios that are expected to occur during surgical operations: (1) varying tumor movement speeds and (2) varying brightness of surgical field of view. Although varying the brightness of the surgical field of view violates the constant intensity assumption of the HS and nonlinear constancy-based methods, we include these methods as a baseline comparison of algorithm robustness.

2 Methods

2.1 Identification of Initial Tumor Location

To identify and visualize the initial tumor location, we use two types of videos. The first type of video captures the visible spectrum. The second type of video captures the NIR spectrum to monitor the scanned tumor in the tissue. First, ICG is injected into the tissue to identify the tumor region. The tissue is scanned with an NIR laser, and its fluorescence is detected in the NIR spectrum. From the fluorescence, the initial tumor location is predicted and updated in the visible spectrum video (Fig. 1). Scanning the ICG-injected tissue enhances the tumor region to more than three times brighter than the normal tissue region [5]. Using the brightness difference, the boundary of normal tissue and tumor tissue is obtained. A portion of the highly brightened tumor region within the boundary is shown in Fig. 2.

Fig. 1 Intra-operative tumor tracking using optical flow
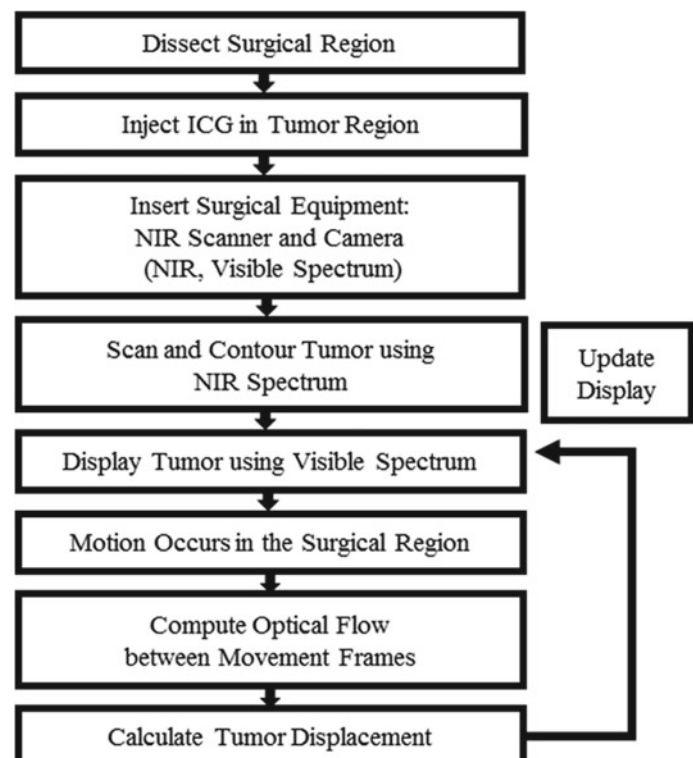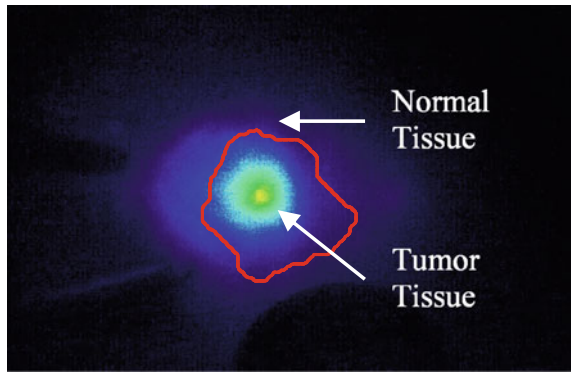
Fig. 2 ICG-enhanced tumor region highlighted within the boundary line between normal and tumor tissue (red outline). The boundary is obtained after adding all of the highly brightened tumor regions (Color figure online)

2.2 Optical Flow Analysis

Optical flow is a technique that calculates a motion vector field to predict the apparent motion of an object [12, 13]. To find a motion vector, the optical flow between the reference (before movement) frame and the incoming (after movement) frame is calculated. The motion vector is used to track the location of the tumor in the incoming frame (Fig. 3). We compare four optical flow methods: LK, HS, phase-based, and nonlinear constancy-based methods [9–13].

2.3 Evaluation of Tumor Tracking Algorithms

In a surgical environment, multiple variables can change simultaneously, causing difficulty in tumor tracking. These variables include tumor shape, location, brightness, and interrupting objects in the surgical field of view. To avoid these confounding variables, we evaluate optical flow tumor
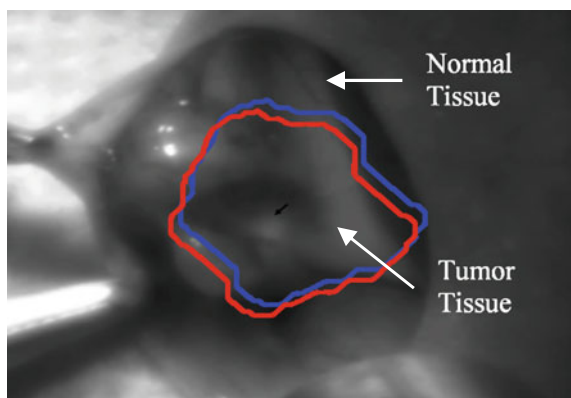
Fig. 3 Updating tumor location using optical flow. The location of the tumor in the new frame (red line) is obtained by displacing the original tumor position (blue line). The black center arrow indicates the average motion vector (Color figure online)

tracking algorithms in a simulated environment that focuses on only two variables: (1) varying tumor movement speeds and (2) varying brightness. In this initial study, we assume that tumor deformation and interrupting objects in the surgical field of view do not occur. We use two simulated surgical scenarios to evaluate tumor tracking algorithms. In the first scenario, we generate four videos with different movement speeds, 1×1–8×8, 8×8–19×19, 20×20–28×28, and 30×30–50×50 (pixel) in each frame, in which 1×1–8×8 (pixel) indicates that tumors can shift randomly from 1 to 8 pixels in both the x and y directions. Each pixel represents approximately 1–2 mm. Each video is generated with randomly shifted pixel movement in each frame, and optical flow is calculated in each frame. We use the same movement patterns for each of the four videos to maintain comparability. In the second scenario, we generate three different videos. Each video uses the same movement speed and pattern (i.e., 1×1–8×8 pixel), but varies in terms of brightness changes (i.e., up to 10, 20, and 30%). To validate the tracking accuracy of optical flow, we compare actual movement to calculated movement in terms of mean displacement error (in pixels) across all frames in the each video.

3 Results and Discussion

The comparison between the actual and calculated displacements using the LK method is shown in Fig. 4. The red line indicates the actual displacements in each frame, and the black line indicates the tracked displacements in each frame. Figure 4a compares the displacement for 1×1–8×8 (pixel) speed. For 8×8–19×19 (pixel) and 20×20–29×29 (pixel) speeds, the results are similar to Fig. 4a. However, for 30×30–50×50 (pixel) speed, optical flow fails to calculate displacement when speed is over 40×40 (pixel) (Fig. 4b). In Fig. 4b, 40×40 (pixel) speed begins at the 9th frame, so LK results in inaccurate tumor location and fails to calculate the next tumor location after frame 9. Therefore, the calculated tumor location using LK is accurate when movement speed is less than 40×40 (pixel). Moreover, tolerance (i.e., percent of video frames successfully processed) of LK in the 30×30–50×50 (pixel) speed video is low.

Figure 5 compares actual and calculated displacements using the LK method with respect to different brightness changes. As the change in brightness increases, tumor tracking accuracy decreases. Changes in brightness of up to 10% have little effect on tumor tracking accuracy. For 20% and 30% brightness changes (Fig. 5), tumor tracking fails after frames 328 and 176 frames, respectively. Therefore, tumor tracking using LK is accurate when brightness changes are less than 30%.

Fig. 4 Comparison between actual displacement and calculated displacement (LK algorithm) **a** for 1×1–8×8 (pixel) and **b** for 30×30–50×50 (pixel) speeds. The solid red line indicates the actual displacement and the dashed black line indicates the calculated displacement. The x-axis is video frame number and the y-axis is displacement. In (**b**), the algorithm cannot calculate when movement speed is over 40×40 (pixel) (Color figure online)
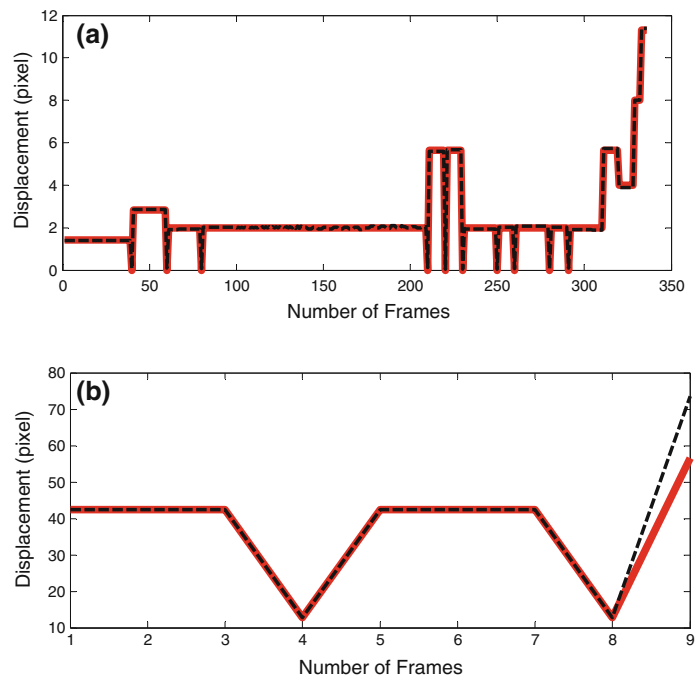
Fig. 5 Comparison between actual displacement and tracked displacement (LK algorithm) for **a** 20% and **b** 30% brightness changes. Changes in brightness of up to 10% have little effect on tracking accuracy. The solid red line indicates the actual displacements and the dashed black line indicates the tracked displacements. The x-axis is video frame number and the y-axis is displacement (Color figure online)
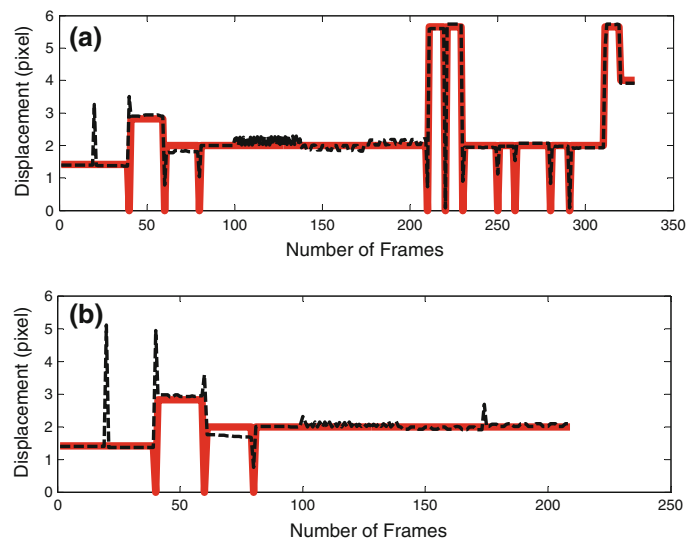
We calculated mean errors of each optical flow algorithm with different movement speeds. In a comparison of four optical flow methods, we found that HS is the least accurate, and nonlinear constancy-based is the second best accurate algorithm (Fig. 6). Phase-based is the most accurate algorithm but only has high tolerance (i.e., percent of frames successfully processed) for movement speeds of up to 20×20 (pixel), whereas other algorithms have high tolerance for movement speeds up to 40×40 (pixel). The order of accuracy (from highest to lowest) is phase-based, nonlinear constancy-based, LK, and HS. The order of tolerance (from the highest to lowest) is nonlinear constancy-based, LK, HS, and phase-based.

The phase-based algorithm is the most accurate method when video brightness changes, and the nonlinear constancy-based algorithm is intolerant to brightness changes (Fig. 7). Compared to LK and HS, LK is more tolerant and accurately tracks movement when brightness changes are less than 30%. The order of accuracy in brightness changes (from the highest to lowest) is phase-based, LK, HS, and nonlinear constancy-based. The order of tolerance (from the highest to lowest) is phase-based, LK, HS, and nonlinear constancy-based.
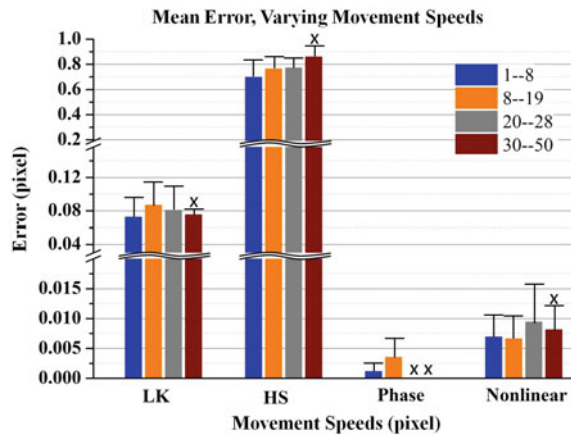
Fig. 6 Comparison among different optical flow algorithms with different movement speeds (1×1–8×8, 8×8–19×19, 20×20–28×28, and 30×30–50×50 pixels). Mean errors across frames from different movement speeds are compared among 4 different algorithms (LK, HS, phase-based, and nonlinear constancy-based algorithm). The X indicates that only 0–25% frames were successfully processed
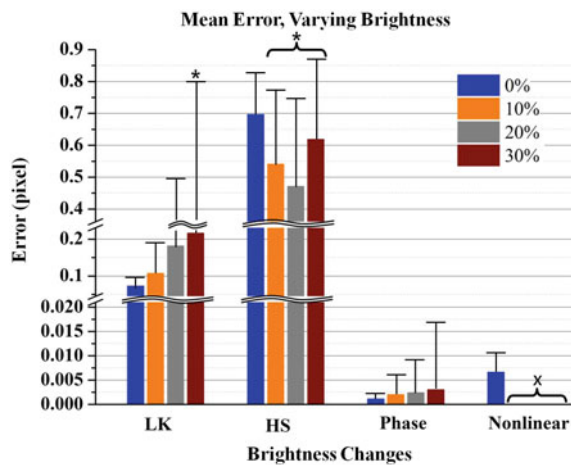
Fig. 7 Comparison among different optical flow algorithms with different brightness changes (10, 20, and 30%). Mean error across frames from different brightness are compared among 4 different algorithms (LK, HS, phase-based, and nonlinear constancy-based algorithm). The * and X indicate that 25–75% and 0–25% frames were successfully processed

4 Conclusion

We developed an intra-operative tumor tracking system that uses ICG to find the initial tumor location and tracks the tumor by using optical flow algorithms. We also developed benchmark metrics to evaluate tumor tracking algorithms using two surgical scenarios: varying tumor movement speed and varying brightness. The novelty of this study is that the initial tumor location is detected by ICG and the location is registered into tumor surgical videos to initialize

the optical flow. The combined intra-operative tumor tracking system using optical flow and ICG is ideal because it is accurate and it eliminates the need for continuous use of an NIR system during surgery. This is beneficial because (1) prolonged exposure to NIR could be hazardous, and (2) it simplifies the optical system. By using the benchmark metrics for evaluating the performance of optical flow algorithms, we identified the strengths and weaknesses of each algorithm. The phase-based algorithm is the most accurate with the highest tolerance to changes in brightness. However, it has the lowest tolerance to fast movement speeds. The nonlinear constancy-based algorithm has high accuracy and tolerance when movement speeds are fast, but it is intolerant to changes in brightness. The HS method has low accuracy and low tolerance to changes in brightness compared to other algorithms. The LK method has high accuracy and tolerance to both fast movement speeds and large changes in brightness. Thus, our results indicate that the LK method is robust in terms of movement speed and variations in brightness, conditions that may arise during surgical procedures.

There are some limitations to this study that may be addressed in the future. First, the computed motion vectors were averaged to shift the tumor location. However, in some scenarios the tumor may also be deformed during surgery. The current implementation of tumor tracking does not account for such deformations when calculating tumor displacement. Second, instead of using real tumor motion, the data was artificially produced. Therefore, the current data analyzed motion and brightness changes but did not consider other variables such as interrupting objects in the field of view during surgery. In the future, tumor tracking in a real surgical environment with the possibility of deformation or interrupting objects should be considered.

References

1. T. Sielhorst, M. Feuerstein, "Advanced Medical Displays: A Literature Review of Augmented Reality," *Journal of Display Technology,* vol. 4, no. 4, pp. 451–467, 2008.
2. L. A. Aliperti, J. D. Predina, "Local and Systemic Recurrence is the Achilles Heel of Cancer Surgery," *Ann Surg Oncol,* vol. 18, no. 3, pp. 603–607, 2011.
3. J. M. Blackall, "Alignment of Sparse freehand 3-D Ultrasound with preoperative images of the liver using models of respiratory motion and demoration," *IEEE Trans. Image Process,* pp. 83–90, 2005.

4. X. Qian, X. H. Peng, "In vivo tumor targeting and spectroscopic detection with surface-enhanced Raman nanoparticle tags," *Nature biotechnology,* pp. 83–90, 2007.

5. B. E. Schaafsma, J. S. Mieog, "The clinical use of indocyanine green as a near-infrared fluorescent contrast agent for image-guided oncologic surgery," *Journal of Surgical Oncology,* vol. 104, no. 3, pp. 323–332, 2011.

6. S. L. Troyan, V. Kianzad, "The FLARETM Intraoperative Near-Infrared Fluorescence Imaging System: A First-in-Human Clinical Trial in Breast Cancer Sentinel Lymph Node Mapping," *Society of Surgical Oncology,* vol. 10, pp. 2943–52, 2009.

7. CFR - Code of Federal Regulations Title 21 (2014, April 1). In U. S. Food and Drug Administration. Retrieved February 16, 2015, from Code of Federal Regulations (21CFR882.1480).

8. J. L. Barron, D. J. Fleet, "Systems and Experiment Performance of Optical Flow Techniques," *International Journal of Computer Vision,* vol. 12, no. 1, pp. 43–77, 1994.

9. B. K. P. Horn, B. G. Schunck, "Determining Optical Flow," *Artificial Intelligence,* pp. 185–203, 1980.

10. T. Gautama, M. Marc, "A Phase-Based Approach to the Estimation of the," *IEEE,* pp. 1127–1136, 2002.

11. T. Brox, A. Bruhn, N. Papenberg, J. Weickert, "High Accuracy Optical Flow Estimation Based on a Theory for Warping," In *Proc. 8th European Conference on Computer Vision,* pp. 25–36, 2004.

12. Q. Xu, R. Hamilton, "Lung tumor tracking in fluoroscopic video based on optical flow," *Medical physics,* p. 5351, 2008.

13. E. L. T. Amiaz, "Coarse to Over-Fine Optical Flow Estimation," *Pattern Recognition,* vol. 40, no. 9, pp. 2496–2503, 2007.

Measuring Physiological Stress Using Heart-Related Measures

An Luo, Siyi Deng, Michael J. Pesavento, and Joseph N. Mak

Abstract

Stress is an emergency response of our organism. Although stress may be necessary in case of life threatening situations, most of the stress experienced by modern day human is misplaced, and spur from evolutionary pressure that is not relevant in our societies. Finding ways to monitor, control, and reduce stress has become critical for the well-being of human societies. For the purpose of developing real time applications to assess and reduce stress for the general public using portable devices, we designed an experiment to trigger stress in laboratory conditions. Our results show that we successfully induced stress and that heart-related measures such as heart rate, heart rate variability and spectral estimation based on heart beats were reliable indicators of stress.

1 Introduction

Stress has been shown to speed up human aging and hinder quality of life [1]. Finding ways to reduce stress has become important for the well-being of human populations. It is not easy to elicit stress in laboratory conditions since according to a landmark review [2], stressful episodes involve: (1) novel, and/or unpredictable circumstances; (2) the individual must have the feeling that he/she does not have control over the situation.

A recent meta–analytical review, performed using 208 stress studies, concluded that a stressor that involves social-evaluative threat (e.g. when performance can be evaluated by others) is the most powerful way to induce stress in laboratory conditions [3, 4]. The Trier Social Stress Test (TSST) is one of the best-standardized tools to evoke stress responses in a laboratory setting. Salivary cortisol levels after the TSST reliably show a 2–4-fold elevation in cortisol above baseline within 30 min. The TSST consists of delivering a public speech in front of a 'team of experts', following a period of 5 min of preparation. At the end of the speech, participants are asked to serially subtract numbers as fast and as accurately as possible. If a mistake occurs, the participant is stopped and asked to start over from the initial number. Altogether, the TSST lasts approximately 10 min. Saliva samples are usually collected prior to the TSST (baseline, 0 min), after the speech preparation, immediately after the speech and arithmetic performance, and several times afterwards.

Multiple scientific studies [5–9] concluded that heart rate (HR) and heart rate variability (HRV) derived from ECG are strong markers of stress. Many derivatives of HRV, such as the high frequency (HF) and low frequency (LF) components of HRV and the ratio between them, have also been shown to be indicators of stress levels. A portable device capable of calculating these measures in real time would help quantify stress for better stress management. Before this can be done, it is however necessary to validate these measures in realistic data collection conditions. This is the goal of this study.

2 Methods

2.1 Protocol

Cortisol should show a peak in concentrations within 10–30 min after the end of the TSST [10]. We have therefore adapted the experiment timing to this constraint.

A. Luo · S. Deng
NeuroSky Inc., 125 S Market St., Suite 900, San Jose, CA 95113, USA
e-mail: aluo@neurosky.com

S. Deng
e-mail: sdeng@neurosky.com

M. J. Pesavento
NeuroSky Inc., 3scan Inc., 2122 Bryant St., San Francisco, CA 94110, USA

J. N. Mak (✉)
NeuroSky (Hong Kong) Co., Ltd., Unit 317, Lakeside 1, Hong Kong Science Park, Pak Shek Kok, Tai Po, New Territories, Hong Kong
e-mail: jmak@neurosky.com

First, we asked subjects to sign the consent form. Then we asked them to rinse their mouth with water. The experiment then started. We collected subjective stress at 7 points during the experiment (using questionnaire 2—Q2) and we collected saliva samples 6 times. Questionnaire Q2 contains 4 questions: (1) "Rate your stress (S) level now" from 0 to 5; (2) "Rate your excitement (E) level now" from 0 to 5; (3) "Rate your fatigue (F) level now" from 0 to 5; (4) "Rate your relaxation (R) level now" from 0 to 5. 0 indicated "totally without", 1 indicated "the least" and 5 indicated "the most". Subjects also filled a more general questionnaire Q1 before starting the task—to indicate their age, gender, height, weight, average hours of work/study per day, average number of hours of sleep per night, stress level of their lifestyle from Relax 1 to Stressful 5, how much physical activity per week, daily caffeine intake, smoking habits, alcohol intake, pregnancy, diabetes, hormone intake, steroid intake.

Each subject performed two tasks in the experiment. The first task was to do a 5-min presentation on a random topic given by the experimenter. The performance in the first task determined the time given in the second task. The experimenter tells the subject that he/she will move to task 2 only if what he/she says during the interview (task 1) is convincing enough. In the second task, subjects were asked to perform a mental arithmetic task: they had to keep subtracting 13 from a given number. The duration of the second task ranged from 3 to 6 min depending on the subject performance—the experimenter stopped the experiment when too many errors were made. Each subject received a compensation of HKD $5, $4, $3, and $2 for the 1st, 2nd, 3rd, and 4th to 6th min respectively.

The outline of the experiment with the duration of each phase is outlined below. (E*x*) indicates event *x* and these are tagged in the ECG data record manually for subsequent analysis (time 1–7 in Fig. 1):

- (E1) Saliva collection and subject fills Q2 and Q1, 2 min
- Place ECG electrode; connect ECG, 3 min
- (E2) Saliva collection and subject fills Q2, 2 min
- (E3) Saliva collection and subject fills Q2, 2 min
- Subject prepares for presentation, 5 min
- (E4) Subject fills Q2
- Task 1: subject presentation, 5 min
- (E5) Subject fills Q2
- Task 2: subject subtracts out loud, 3 to 6 min
- Rest, 5 min
- (E6) Saliva collection and subject fills Q2, 2 min
- Rest, 3 min
- Saliva collection, 2 min
- Rest, 3 min
- (E7) Saliva collection and subject fills Q2, 2 min.
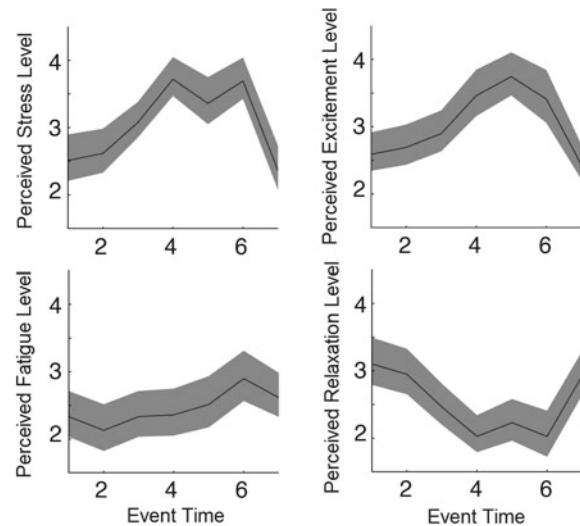
Fig. 1 Questionnaire results for the 7 data collection periods. From left to right, the stress, excitement, fatigue and relaxation levels. Data collection 4 and 5 correspond to the stress induction period. We can clearly see an increase in perceived stress and excitation as well as a decrease in relaxation during the stress induction

2.2 Participants

47 subjects were recruited for the experiment. Subjects' mean age was 22 years old (±3 years). Informed consent was obtained from all participants in accordance with the guidelines and approval of the NeuroSky Institutional Review Board. Three subjects were pilots and 6 subjects did not complete the experiment, thus were not included in the data analysis. Our final pool of subject for data analysis was 38. All of these subjects were considered for the purpose of data analysis.

2.3 ECG Data Collection

ECG data was collected using a proprietary Bluetooth ECG data collection device based on the NeuroSky BMD101 chip [11]. ECG signal was collected with a recording electrode placed in the middle of subjects' sternum and reference electrode on their left clavicle. The custom device was worn as a necklace and communicated with Bluetooth to a standalone computer running a custom data collection program. The data collection program allowed entering events as keystroke to mark different event in the data (events E1–E7 as indicated in the protocol section).

2.4 Cortisol Data Collection

We used saliva swab and test service from ZRTlab, Inc. Subjects were instructed to masticate the swab for about

2 min. Then the swab was placed in a plastic tube, sealed, labeled and refrigerated below −5 °C. Once all the swabs from all the subjects had been collected, we sent the data to ZRTlab by international refrigerated 2-day shipping. ZRTlab assessed cortisol level using proprietary methods.

3 Results

3.1 Entry Questionnaire (Q1) Results

We first processed the questionnaire results for the general questionnaire Q1. In particular we were interested to assess which response was correlated with perceived stress. Some questions were ignored because it did not concern any of the subjects. None of the subject smoked, none were pregnant, and none were taking hormones. 2 subjects were taking steroids for minor injuries, and 3 were drinking minor amount of alcohol on a weekly basis—these subjects were included in our pool but we did not process these two questions for lack of statistical power. Weight and height were combined to calculate each subject's body mass index according to the formula BMI = Weight (kg)/Height (m)^2.

Some variables were continuous and not normally distributed, so we used the nonparametric Spearman rank correlation coefficient to assess their relationship with stress. Some variables were ordinal so we used a chi square test of independence to assess any dependence between the variables. Table 1 indicates the correlation between stress level and the variables we recorded. In the table we also indicate the sign of the correlation in the last column. We also examined the correlation with the average subject response across the seven Q2 questionnaires as indicated in the last 5 rows of Table 1.

Table 1 shows independent variables correlation with baseline subjective stress level as recorded in Q1. Table 1 shows that daily caffeine was positively correlated with stress ($p < 0.01$; df = 37). Average fatigue of the subject during the experiment was also correlated with baseline stress ($p < 0.02$) as well as the average stress during the experiment ($p < 0.04$), the average excitation during the experiment ($p < 0.04$), and the standard deviation of the stress during the experiment ($p < 0.05$). This last measure indicates that more variation in perceived stress during the experiment is correlated with increased perceived baseline stress.

Other trends observed were a positive correlation between the number of work hour per day and baseline stress ($p < 0.09$) and a negative correlation between physical health and stress ($p < 0.08$).

3.2 Short Questionnaire (Q2) Results

For each subject, we assessed if their subjective ratings using Q2 were affected by the task. Figure 1 shows the evolution of the responses on the 4 questions of the 7 recurrent short questionnaires Q2. We clearly observe perceived stress increasing and relaxation decreasing over the course of the experiment. Excitement has a similar profile to stress with a later onset. Fatigue increased slightly over the course the course of the experiment although it decreased at the very end. Shaded areas indicate the 95% confidence intervals for each measure. 95% confidence intervals were calculated using a bootstrap method [12].

Table 1 Correlation between stress level in Q1 and other psychometric responses

Variable	Statistical test	Significance
Q1 Gender	χ^2	ns
Q1 Age	Spearman	ns
Q1 BMI	Spearman	ns
Q1 Work hour per day	Spearman	0.09 (+)
Q1 Sleep hour per day	Spearman	ns
Q1 Activity hour per week	χ^2	ns
Q1 Daily Caffeine	χ^2	0.01 (+)
Q1 Physical health	χ^2	0.08 (−)
Q1 Mental health	χ^2	ns
Q2 average stress	Spearman	0.04 (+)
Q2 average excitement	Spearman	0.04 (+)
Q2 average fatigue	Spearman	0.02 (+)
Q2 average relaxation	Spearman	ns
Q2 standard dev stress	Spearman	0.05 (+)

3.3 Cortisol Results

We collected Cortisol at six different times during the experiment as indicated in the method section: three times during the baseline period and three times after the stress induction. We failed to observe significant difference between pre and post-experiment cortisol levels, although cortisol level between time 3 (rest) and 4 (after the stress period) reached p = 0.1 (degree of freedom (df) = 37), and subjects' perceived stress levels were significantly higher during the experiment. Since saliva cortisol reflects the stress level 20–30 min prior to the saliva collection [4], we suspect the first three saliva cortisol readings were more related to the subjects' physiological stress condition while they were going to the data collection facility, thus were not a good indicator of their no-stress cortisol levels.

3.4 Heart Measure Results

Figure 2 presents the heart related measures averaged across subjects when the subjects filled up the psychometric Q2 questionnaires. The measures included HR, HRV in the form of standard deviation of the inter beat intervals (SDNN), log of the high frequency spectral power (HF) from 0.15 to 0.4 Hz, low frequency spectral power (LF) from 0.04 to 0.15 Hz, and the log of the ratio of HF and LF (LF/HF). Only 30 beat-to-beat intervals were used to calculate these measures, so they are expected to be quite different from those based on 24-hour recordings.

The abscissa scale ranging from 1 to 7 is the same as the one used for psychometric measures in Fig. 1. Event times 1, 2 and 3 are baseline (before the experiment starts). Event times 4 and 5 are during the experiment. Event times 6 and 7 are after the rest period. So real stress only occurs at point 4 and 5. The shaded region indicates 95% confidence interval calculated using the bootstrap method after removing each subject mean measure value over all considered time periods [12].

All measures are estimated using the NeuroSky Software Development Kit, which has been validated against Matlab implementations, and the Kubios HRV software [12].

Throughout our analysis, the calculation of HR, SDNN, HF, LF and LF/HF are based on 30 beat-to-beat intervals (one segment). For each subject, we had in between 65 and 220 (mean 126 ± 34) EKG segments throughout the

Fig. 2 Heart measurements averaged across subjects, including HR, SDNN, log of the high frequency (HF) inter beat interval from 0.15 to 0.4 Hz, log of the low frequency (LF) inter beat interval from 0.04 to 0.15 Hz, and the log of the ratio of LF and HF. Time axis same as in Fig. 1
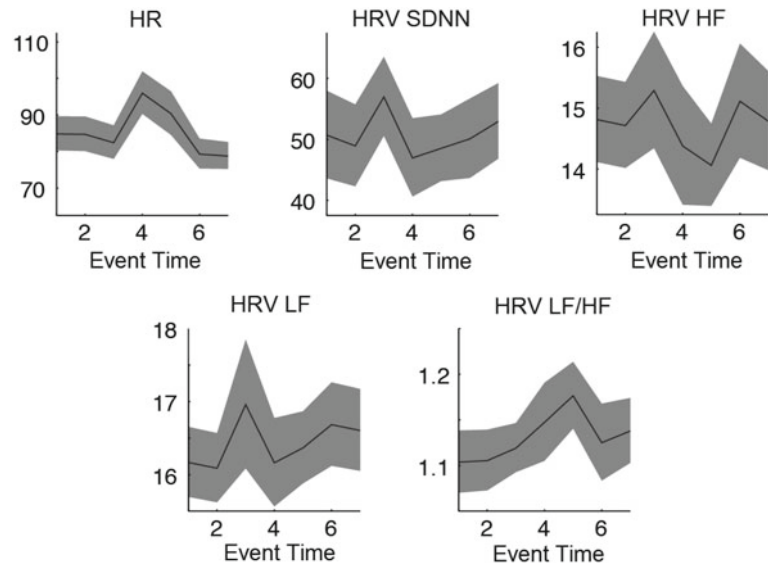
Table 2 Heart measures during the stress and the no-stress periods

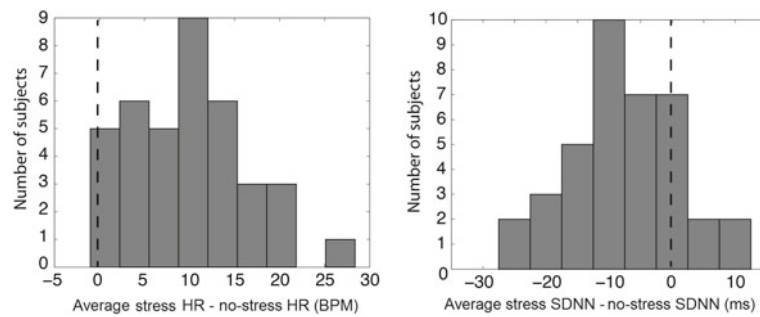|	p	df	Stress	No stress
HR (BPM)	3.0E−11	37	92.9	83.0
SDNN (ms)	4.0E−6	37	44.3	51.9
LF	0.01	37	8.48	8.74
HF	6.6E−4	37	5.89	6.22
LF/HF	0.015	37	1.51	1.46

Fig. 3 Distribution of the difference in average HR (left) and SDNN (right) between the stress and the no-stress periods. Most subjects showed a positive difference in HR indicating elevated HR during stress and a negative difference in SDNN indicating lower HRV during the stress periods

experiment. Some subject had fewer segments than others because of missing or bad data. Some of these data segments where during stress periods and some other during relax periods (see Methods). For each subject, we computed the mean SDNN for all the stress periods (periods 4, 5) for each individual, and we also computed the mean SDNN for all the non-stress periods (periods 1, 2, 3 as well as 6, 7). Paired t-test showed that HR and the LF/HF ratio were significantly larger in the stress than in the non-stress periods (see Table 2). Other measures, including SDNN, HF and LF also showed significant decrease during the stress period (Table 2). Figure 3 further shows the difference between the distribution of the difference in SDNN between the stress and the no-stress periods.

4 Conclusion

In this study we investigate how heart related measures, such as heart rate and heart rate variability, are affected by stress. We adopted the widely used Trier Social Stress Test and observed significantly elevated stress perceived by the subjects. We found statistically significant increase in heart rate and LF/HF, as well as significantly decreased SDNN, LF and HF during the stress test, comparing to periods before and after the test. These heart-related measurements respond much faster to stress than hormonal ones such as cortisol, and can be conveniently measured using a single-lead ECG at much lower cost. These findings enable the development of a real-time stress monitoring and tracking system to better understand, assess and manage stress for the general public.

References

1. R. M. Lawrence, "Stress management in work settings: a critical review of the health effects," *American Journal of Health Promotion*, vol. 11, no. 2, pp. 112–135, Nov., 1996.
2. J. W. Mason, "A review of psychoendocrine research on the sympathetic-adrenal medullary system," *Psychosomatic Medicine*, vol. 30, no. 5 (Suppl), pp. 631–653, Sep., 1968.
3. S. S. Dickerson, M. E. Kemeny, "Acute stressors and cortisol reactivity: a meta-analytic review," *Psychosomatic Medicine*, vol. 54, pp. 105–123, 2002.
4. C. Kirschbaum, K. M. Pirke, D. H. Hellhammer, "The 'trier social stress test'–a tool for investigating psychobiological stress responses in a laboratory setting," *Neuropsychobiology*, vol. 28, no. 1–2, pp. 76–81, 1993.
5. N. Hjortskov, D. Rissén, A. K. Blangsted, N. Fallentin, U. Lundberg, K. Søgaard, "The effect of mental stress on heart rate variability and blood pressure during computer work," *European Journal of Applied Physiology*, vol. 92, no. 1–2, pp. 84–89, Feb., 2004.
6. C. Schubert, M. Lambertz, R. A. Nelesen, W. Bardwell, J. B. Choi, J. E. Dimsdale, "Effects of stress on heart rate complexity—a comparison between short-term and chronic stress," *Biol Psychol.*, vol. 80, no. 3, pp. 325–332, Mar., 2009.
7. T. G. Vrijkotte, L. J. van Doornen, E. J. de Geus, "Effects of work stress on ambulatory blood pressure, heart rate, and heart rate variability," *Hypertension*, vol. 35, no. 4, pp. 880–886, Apr. 2000.
8. L. Tonello, F. B. Rodrigues, J. W. Souza, C. S. Campbell, A. S. Leicht, D. A. Boullosa, "The role of physical activity and heart rate variability for the control of work related stress," *Front Physiol.*, vol. 21, no. 5, article 67, Feb. 2014.
9. R. Orsila, M. Virtanen, T. Luukkaala, M. Tarvainen, P. Karjalainen, J. Viik, M. Savinainen, C. H. Nygård, "Perceived mental stress and reactions in heart rate variability–a pilot study among employees of an electronics company," *Int. J. Occup. Saf. Ergon*, vol. 14, no. 3, pp. 275–283, 2008.
10. M. Walser, R. Fischer, T. Goschke, C. Kirschbaum, F. Plessow, "Intention retrieval and deactivation following an acute psychosocial stressor," *PLoS One*, vol. 8, no. 12:e85685, De. 2013.
11. N. P. Bobra, Z. Wang, W. Zhang, A. Luo, "A high-quality, low-energy, small-size system-on-chip (SoC) solution enabling ECG mobile applications," in *Proc. Industrial Electronics Society*,

IECON 2013 – 39th Annual Conference of the IEEE, Vienna, 2013, pp. 8406–8409.

12. R. Wilcox, "Modern statistics for the social and behavioral sciences: a practical introduction. CRC press, 2011.

13. M. P. Tarvainen, J. P. Niskanen, J. A. Lipponen, P. O. Ranta-Aho, P. A. Karjalainen, "Kubios HRV–heart rate variability analysis software,", *Comput Methods Programs Biomed.*, vo. 113, no. 1, pp. 210–20, 2014.

Associating Protein Interactions with Disease Comorbidity to Prioritize Colorectal Cancer Genes

Sayedeh Razieh Abdollahi Demneh, Sama Goliaei, and Zahra Razaghi Moghadam

Abstract

Identification of disease causing genes is one of the most important topics in human health that affects disease therapy and understanding disease mechanism. Genome-wide association studies focus on chromosomal locus which contains many suspected disease genes. Gene prioritization methods identify the most probable unknown disease genes due to this locus. In this study a network-based approach is proposed to prioritize colorectal cancer genes. Different methods involved in this approach are random walk with restart, network propagation and shortest path algorithms, which are separately applied on protein-protein interaction network to prioritize genes. Then these methods are combined in different ways to find the best combination of them for identifying disease genes. Finally by looking through comorbid diseases to colorectal cancer and extracting their causing genes, the proposed approach is reconsidered. The method is validated by cross-validation analysis and its results are compared with other prioritization methods. This comparison shows the better performance of this new approach.

1 Introduction

Cancer is a genetic disorder that is one of the leading causes of death in the world. Early detection and treatment of cancer may prevent the death of patients. So, discovery of involved genes and related drugs is important. Recently, linkage analysis is used to identify chromosomal intervals which contain many disease suspected genes, but investigating these genes with experimental methods is an expensive and time consuming process and is not always possible. Computational methods help us to prioritize and identify more possible disease genes for further studies. Prioritization algorithms use known disease causing genes (achieved by experimental methods, such as linkage analysis) as seed genes to predict candidate genes for further analysis. These methods integrate available data from different sources to solve the problem. With the increase in available data of human protein-protein interaction (PPI), considering human PPI network with other disease information may help to discover new disease related genes. This is because, genes involved in the same or similar disease phenotypes tend to have interactions with each other in PPI network [1]. So, many approaches such as molecular triangulation [2], shortest path [3] and direct neighbors [4] use the network topological features to identify candidate genes. All these methods use local information of the network and because of considering direct interactions (not indirect functional relationships) [5] their final accuracies are vulnerable. Random walks with restart (RWR) [6] and network propagation [7] are methods that use global network information, so overall effects of known disease gene to other genes are taken into account. Therefore they have better performance than local methods but worth mentioning that they do not consider genes with poor connections in the network [8].

In some previous studies such as Endeavor [9] and MetaRanker [10] many heterogeneous data sources are used and overall information is utilized to prioritize genes. These methods rank genes based on each data source and finally combine their results. Some methods most use technical strategies and network topological information such as RWR and network propagation but the other ones are knowledge-based and often utilize different gene information and combine them for example Endeavour and MetaRanker.

In this paper, a hybrid method that uses local and global information of the network and the disease comorbidity knowledge is proposed to overcome disadvantages of

S. R. A. Demneh · S. Goliaei · Z. R. Moghadam (✉)
University of Tehran, Tehran, Iran
e-mail: razzaghi@ut.ac.ir

S. R. A. Demneh
e-mail: s_r_abdollahi@ut.ac.ir

S. Goliaei
e-mail: sgoliaei@ut.ac.ir

aforementioned methods. RWR, shortest path and network propagation, separately and in different combinations, are applied on PPI network to prioritize genes. Then by considering comorbid diseases to colorectal cancer and their causing genes, the prioritization is finalized. By this strategy both advantages of knowledge-based and technique-based methods are used. For the evaluation of the proposed method, it is applied on colorectal cancer datasets. The evaluation shows that using local and global network information and the other disease knowledge leads to more successful approach for identifying disease related genes in comparison to other previous methods.

2 Methods

2.1 Protein-Protein Interaction Network

In this method, the PPI network which is constructed on proteins interaction information and expert knowledge [11] is used. In the construction of this PPI network, protein interactions extracted from several of the largest databases and weighted interactions by network topology and expert knowledge. This network is an undirected and unconnected network in which nodes represent proteins and edges are interactions between them. By removing isolated nodes (nodes with degree of zero), 12,884 nodes are remained. For this proposed method, 1121 colorectal cancer genes are extracted from DisGeNET [12] and mapped to the PPI network as seed nodes (genes).

2.2 Disease Genes Prioritization

RWR, network propagation and shortest path algorithms are applied separately on the PPI network. Also, disease comorbidity information is used in this approach. All these algorithms and information are briefly described in the following:

(1) *Random walk with restarts algorithm*—RWR is an algorithm for calculating proximity of nodes with random walks on network. It defines by:

$$P^{t+1} = (1 - r)WP^t + rP^0 \qquad (1)$$

Where W is weighted adjacency matrix with normalized columns. P^0 is a vector of primary probabilities of nodes. In this vector equal probabilities are assigned to seeds and zero probability to all other genes. P^t is a probability vector of nodes at time t and r is a free parameter which determines the probability of restarting at seed genes. In this proposed approach, r is set to be 0.15. RWR repeats until the difference between P^t and P^{t+1} becomes less than 10^{-6} [6].

(2) *Network propagation algorithm*—Network propagation uses network flow propagation to prioritize genes. Its idea is very similar to RWR with a difference, in network propagation matrix rows are normalized too, in other words, both input and output flows of each node are normalized [7].

(3) *Shortest path algorithm*—In this given approach, Dijkstra [13] algorithm is applied to calculate the lengths of shortest paths between seed genes and all other genes. Then for each non-seed node, the minimum lengths of all seed ones are selected. Obviously, the smaller this score is, the more possible the node is to be a disease gene. After calculating these three scores for each non-seed node (gene), a total score based on these three are assigned to each of them [3].

(4) *Disease comorbidity information*—Here, MalaCards [14] database is used to find comorbid diseases to colorectal cancer. Their causing genes are extracted from DisGeNet database; these diseases are listed in Table 1. The previously assigned score of a gene is added by one, if it is a causing gene of a comorbid disease. For example, if a gene is a common causing gene of five comorbid diseases, it's previously score is added by five.

Previous steps are depicted in Fig. 1.

2.3 Comparison to Other Methods

For evaluating the performance of our proposed method, leave-one-out cross-validation analysis is done and the results are compared to other methods results. In leave-out cross-validation analysis, each seed gene is removed from seed genes set, one at a time and an artificial linkage interval is constructed on its 99 chromosomal neighbors obtained from UCSC database [15]. These 99 genes and the seed one is considered as the candidate set and the remaining seed genes make the new seed set. Our algorithm is applied on this new seed set and its result is compared with the candidate set. To show the performance of the algorithm, Receiver Operating Characteristic (ROC) curve is drawn to plot sensitivity versus 1-specificity. Also, Area Under Curve (AUC) is calculated for each curve. Here, sensitivity is defined by the percentage of disease genes which are ranked above a specific threshold while specificity is the percentage of all genes ranked below the threshold. Additionally, Mean Reciprocal Rank (MRR) is calculated which is defined by:

$$MRR = \frac{1}{|Q|} \sum_{i=1}^{|Q|} \frac{1}{rank_i} \qquad (2)$$

Table 1 Comorbid disease to colorectal cancer

Disease name
Adenoma
Breath cancer
HIV infections
Familial adenomatous polyposis
Lunch-syndrom
Ovary cancer

Comorbid disease to colorectal cancer extracted from MalaCards database

Fig. 1 Our method summarization, we apply RWR, shortest path and network propagation on PPI network to rank genes separately then added score of genes which are shared between comorbid diseases to colorectal cancer and merge results. With this strategy we use advantage of knowledge-based and technique-based method simultaneously
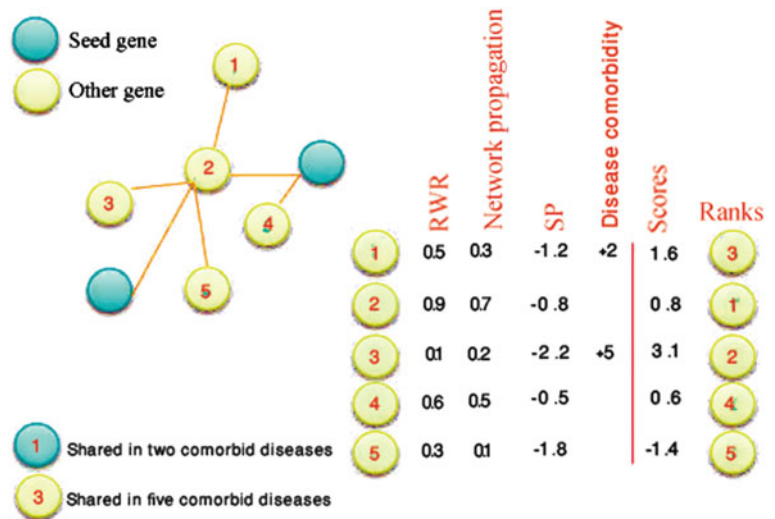
Q is count of candidate sets and $rank_i$ is rank of removed seed gene in ith candidate set. An average rank criterion is the other measure to show the performance of an algorithm and it is the average rank of seeds in their corresponding candidate sets. 1% and 5% are also the other measures which represent the percentage of seed genes that are respectively ranked in top 1% and 5% of candidate sets. All aforementioned measures for different methods are shown in Table 2.

3 Results and Discussion

In this paper, a new prioritization method is proposed which integrates disease comorbidity knowledge with PPI information to use benefits of both. Comorbid disease probably have same causing genes, in the other hand disease proteins tend to have interactions with each other. Our PPI network

Table 2 Comparison different methods

Methods	AUC	MRR	Average rank	1%	5%
Our methods	0.92	0.35	8.04	0.22	0.52
Endeavour	0.76	0.25	10.5	0.10	0.40
ToppGene	0.70	0.28	10.94	0.14	0.34
DIR	0.91	0.28	9.6	0.18	0.38
RWR	0.90	0.25	10	0.12	0.40
SP	0.90	0.14	10.1	0	0.18
Network propagation	0.91	0.25	9.8	0.12	0.40

Summary of performance comparison in various disease gene prioritization methods

Fig. 2 Comparison of prioritization methods, performance comparisons for different prioritization methods have done in a leave one-out cross-validation for each seed genes. The figure shows sensitivity versus 1-specificity with k threshold that changed between 1 and 100
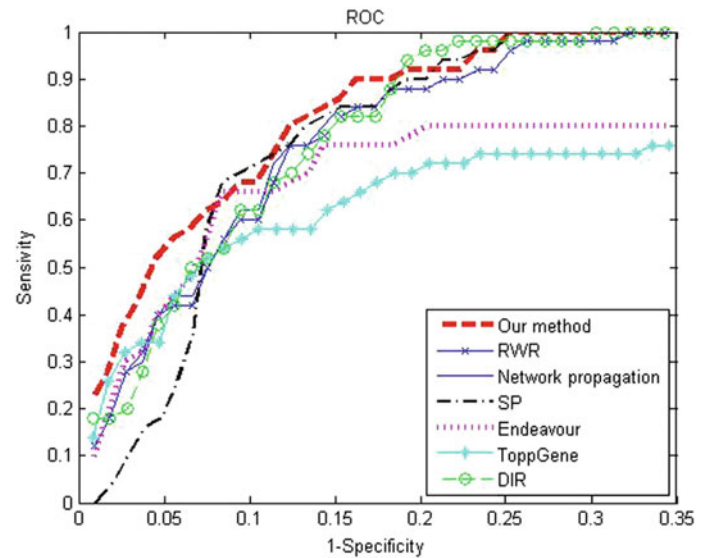
has 12,894 gens in which 1121 genes are seed ones. RWR and network propagation algorithms use network global information to calculate proximity of two nodes and the shortest path algorithm is based on network local information. All these three algorithms are applied on PPI network to overcome disadvantage of each method. Our method is evaluated and compared with other algorithms and tools such as Endeavour, ToppGene [16] and DIR [17] which use different data sources to prioritize disease genes. ROC analysis has used to compare different methods (shown in Fig. 2). For more accurate comparison, AUC is calculated for each curve. As it is shown in Table 2, the AUC of our method is higher than the others. In %22 cases our method ranks seed gene as the first candidate gene and its average rank is the lowest amon all examined algorithms. Additionally its MMR is 0.35 which is higher than the other methods MMR. Overall, it shows that our method has better performance comparing to the other examined algorithms.

4 Conclusions

We applied RWR, network propagation and shortest path algorithm separately on PPI network and combine results, then added comorbidity knowledge to rank genes. Our results show that considering different information of genes is important in disease gene identification and disadvantages of exciting methods can be decreased by combining various methods.

Conflict of Interest We have no conflict of interest to declare.

References

1. T. K. Gandhi, J. Zhong, S. Mathivanan, L. Karthick, K. N. Chandrika, S. S. Mohan, *et al.*, Analysis of the human protein interactome and comparison with yeast, worm and fly interaction datasets, *Nat Genet,* vol. 38, pp. 285–293, Mar 2006.
2. M. Krauthammer, C. A. Kaufmann, T. C. Gilliam, and A. Rzhetsky, Molecular triangulation: bridging linkage and molecular-network information for identifying candidate genes in Alzheimer's disease, *Proc Natl Acad Sci U S A,* vol. 101, pp. 15148–15153, 19 Oct 2004.
3. R. A. George, J. Y. Liu, L. L. Feng, R. J. Bryson-Richardson, D. Fatkin, and M. A. Wouters, Analysis of protein sequence and interaction data for candidate disease gene prediction, *Nucleic Acids Res,* vol. 34, p. e130, 2006.
4. M. Oti, B. Snel, M. A. Huynen, and H. G. Brunner, Predicting disease genes using protein-protein interactions, *J Med Genet,* vol. 43, pp. 691–698, Aug 2006.
5. S. Erten, G. Bebek, R. M. Ewing, and M. Koyuturk, DADA: Degree-Aware Algorithms for Network-Based Disease Gene Prioritization, *BioData Min,* vol. 4, p. 19, 2011.
6. S. Kohler, S. Bauer, D. Horn, and P. N. Robinson, Walking the interactome for prioritization of candidate disease genes, *Am J Hum Genet,* vol. 82, pp. 949–958, Apr 2008.
7. O. Vanunu, O. Magger, E. Ruppin, T. Shlomi, and R. Sharan, Associating genes and protein complexes with disease via network propagation, *PLoS Comput Biol,* vol. 6, p. e1000641, Jan 2010.
8. N. T. Doncheva, T. Kacprowski, and M. Albrecht, Recent approaches to the prioritization of candidate disease genes, *Wiley Interdiscip Rev Syst Biol Med,* vol. 4, pp. 429–442, Sep–Oct 2012.
9. S. Aerts, D. Lambrechts, S. Maity, P. Van Loo, B. Coessens, F. De Smet, *et al.*, Gene prioritization through genomic data fusion, *Nat Biotechnol,* vol. 24, pp. 537–544, May 2006.
10. T. H. Pers, N. T. Hansen, K. Lage, P. Koefoed, P. Dworzynski, M. L. Miller, *et al.*, Meta-analysis of heterogeneous data sources for genome-scale identification of risk genes in complex phenotypes, *Genet Epidemiol,* vol. 35, pp. 318–32, Jul 2011.
11. K. Lage, E. O. Karlberg, Z. M. Storling, P. I. Olason, A. G. Pedersen, O. Rigina, *et al.*, A human phenome-interactome

network of protein complexes implicated in genetic disorders, *Nat Biotechnol,* vol. 25, pp. 309–316, Mar 2007.

12. J. Pinero, N. Queralt-Rosinach, A. Bravo, J. Deu-Pons, A. Bauer-Mehren, M. Baron*, et al.*, DisGeNET: a discovery platform for the dynamical exploration of human diseases and their genes, *Database (Oxford),* vol. 2015, p. bav028, 2015.

13. E. W. Dijkstra, A note on two problem in connexion with graphs, *Numerische Mathematik,* pp. 269–271, 1959.

14. N. Rappaport, N. Nativ, G. Stelzer, M. Twik, Y. Guan-Golan, T. Iny Stein*, et al.*, MalaCards: an integrated compendium for diseases and their annotation, *Database,* vol. 2013, pp. bat018–bat018, 2013.

15. T. R. Dreszer, D. Karolchik, A. S. Zweig, A. S. Hinrichs, B. J. Raney, R. M. Kuhn*, et al.*, The UCSC Genome Browser database: extensions and updates 2011, *Nucleic Acids Res,* vol. 40, pp. D918–D923, Jan 2012.

16. J. Chen, H. Xu, B. J. Aronow, and A. G. Jegga, Improved human disease candidate gene prioritization using mouse phenotype, *BMC Bioinformatics,* vol. 8, p. 392, 2007.

17. W. Wang, Y. Chen, Y. Zhou, R. Shields, S. K. Chanda, R. C. Elston, and J. Li, In Silico Gene Prioritization by Integrating Multiple Data Sources, *PLoS ONE,* vol. 6, 2011.

Synchronization Analysis of EEG Using the Hilbert Huang Coherence

Eiji Kondo, Masatake Akutagawa, Takahiro Emoto, Yoshio Kaji,
Fumio Shichijo, Kazuhiko Furukawa, Hirofumi Nagashino,
Shinsuke Konaka, and Yohsuke Kinouchi

Abstract

The short periods of synchronization of different brain regions in particular frequency ranges during cognitive activities is reported. In this study, the Hilbert Huang Coherence (HHC) for analyzing the degree of synchronization by using a Hilbert Huang transform with high temporal frequency resolution is proposed. The authors intended to verify the availability of the HHC. According to computer simulation, it was found that temporal frequency resolution of HHC is higher than that of traditional coherence analysis for non-stationary signals. Furthermore, the HHC was applied to EEG during closed eyes rest. As results of them, the change of coherence in α band was obtained higher temporal frequency resolution than that of traditional coherence analysis.

1 Introduction

Cognition activities requires the integration of activities from the many different regions of the brain and it has been obtained research result that binding takes place through short periods of synchronization in particular frequency ranges [1]. Moreover, neural synchronization has been demonstrated as having an important role in pathological conditions such as epilepsy [2]. Therefore, it is considered to be important that to capture the change of synchronization.

Although there are methods using the Fourier transform and the Wavelet transform as methods for the temporal frequency analysis, these methods have a trade-off between temporal frequency resolution. Therefore, the frequency resolution decreased in the short analysis time length.

In case of analysis for non-stationary signals, such as whose characteristics are changing rapidly.

Analysis in a short period is required in order to capture the change for the signal that to be constantly changing from time to time as of the EEG, but since the frequency resolution is decreased, the analysis method of no trade-off is required. In this study, the synchronization analysis of the Hilbert Huang Coherence (HHC) for analyzing the degree of synchronization by using the Hilbert Huang transform (HHT) [3] with high temporal frequency resolution is proposed. We intended to verify the effectiveness of the HHC to apply to the simulation using the non-stationary signals and to α waves of EEG.

2 Hilbert Huang Coherence

2.1 Hilbert Huang Transform

The Hilbert Huang transform (HHT) [3] is effective method for the temporal frequency analysis of the unsteady and non-linear signal.

The HHT has the high frequency resolution to determine the instantaneous frequency from the analytic signal obtained by Hilbert transform (HT) to the Intrinsic Mode Function (IMF) to decompose the signal to the IMF without using the base by using the Empirical Mode Decomposition (EMD).

The signal $s(t)$ decomposed to the IMF by the EMD is shown as (1) in the residuals $r(t)$ and N number of IMF.

E. Kondo (✉) · M. Akutagawa · T. Emoto · H. Nagashino
S. Konaka · Y. Kinouchi
Tokushima University, 2-1, Minami Josanjima-Cho,
Tokushima-Shi, Tokushima, 770-8506, Japan
e-mail: k-eiji-sorairo@ee.tokushima-u.ac.jp

Y. Kaji
Faculty of Technology and Science, Tokushima Bunri University,
Shido 1314-1, Sanuki-Shi, 769-2193, Kagawa, Japan

F. Shichijo
Suzue Hospital, 2-1, Minamijosanjima-Cho, Tokushima-Shi,
Tokushima, 770-8506, Japan

K. Furukawa
Tokushima Prefecture Naruto Hospital, 32-1, Muya-Cho,
Naruto-Shi, Tokushima, 772–8503, Japan

97

$$x(t) = \sum_{i=1}^{N} c_i(t) + r(t) \tag{1}$$

Also, if (1) is transformed analytic signal, it is shown (2). (j: the imaginary unit)

$$z(t) = \sum_{i=1}^{N} a_i(t) \exp\left(j \int \omega_i(t)dt\right) + r(t) \tag{2}$$

Here, the instantaneous amplitude is $a_i(t)$ and the instantaneous angular frequency is $\omega(t)$ of the time t in i-th IMF. The spectrum H of temporal angular frequency obtained from these called the Hilbert Huang Spectrum. ($i = 1, 2, \ldots, N$)

$$H(t, \omega) = \begin{cases} a_i(t) & (\omega_i(t) = \omega) \\ 0 & (\text{otherwise}) \end{cases} \tag{3}$$

2.2 Hilbert Huang Coherence

Although typically the coherence analysis is performed using the Short Time Fourier transform (STFT) and the Wavelet transform (WT), there is a trade-off between temporal frequency resolution in these methods, if either resolution is increased, another resolution is decreased. In other words, if you want to know the synchronization for each frequency in the short period, it is necessary to take shorter analysis time length of coherence, but the frequency resolution is decreased.

Therefore, the coherence analysis of EEG using the HHT that the frequency resolution does not depend on the analysis time length has been proposed the HHC.

The HHT is decomposed into the narrow band signals called the IMF signals using the EMD, but the IMF comprises what frequency is varied by the waveform of the signal before decomposed, as it calculated the synchronization between the IMF even the frequency shown synchronization do not know only roughly. Also, when the degree of synchronization calculated between two signals, IMF must be selected whether to calculate the synchronization between any IMF. If the frequency band of the IMF were divided clearly in each of the IMF, it is easy to select the combination of the IMF but sometimes difference IMF have the same frequency band.

Therefore, it is availabling that the coherence analysis of each frequency by the HHT through selecting the time to perform the coherence analysis based on instantaneous frequency obtained by the HHT.

Then the specific analysis algorithm of the HHC shows below.

For example, Fig. 1 is shown one of the IMF(upper) when it was decomposed to the IMF by the EMD to a certain EEG and the instantaneous frequency(lower). From Fig. 1, this IMF can be seen to include the instantaneous frequency of approximately 10–60 Hz.

The IMF consist of the multiple frequency bands do not analyze the coherence of each frequency as it is. Here, if the amplitude and the phase difference averaged to calculate by extracting only the time to the instantaneous frequency of the band that interest analyzed is 20–30 Hz band, the coherence can be calculated of the specific frequency band within the time period to be analyzed.

Figure 2 shows a flowchart for calculating the coherence at the analysis frequency band λ of the time series signal $x(t)$ and $y(t)$.

(1) First, two signal $x(t)$ and $y(t)$ which the time series signal are decomposed the $\tilde{x}(k,t)$ and $\tilde{y}(l,t)$ which the IMF by the EMD.($k = 1, 2, \ldots, K, l = 1, 2, \ldots, L$)

(2) The analytic signals of all of the IMF by the HT and the instantaneous frequency $u(k,t)$ and $v(l,t)$ are calculated.

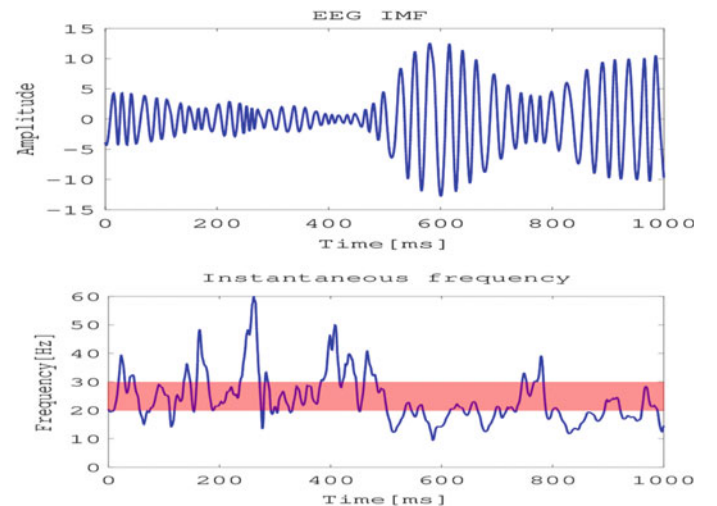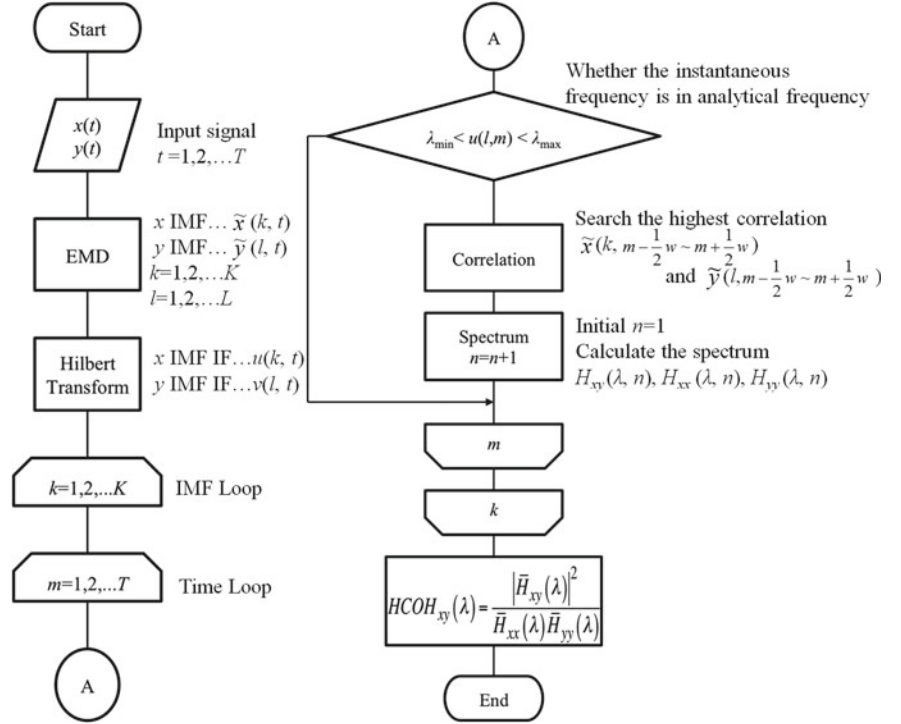**Fig. 1** The IMF of EEG and the instantaneous frequency

Fig. 2 The algorithm of the Hilbert Huang Coherence

(3) Then, it extracts the time m in the frequency band of the interest for the instantaneous frequency $u(k, t)$ and to calculate the correlation between all of the $\tilde{x}$ and $\tilde{y}$ in the time band $m - \frac{1}{2}w \sim m + \frac{1}{2}w$. w is calculated by (4) so that the calculated length the cross-correlation becomes the one period length of the instantaneous frequency. (Fs: Sampling frequency, f: instantaneous frequency)

The cross-correlation is calculated in order to identify the combinations of the IMF with most similar characteristics in all of the IMF.

$$w = \frac{F_s}{f} \quad (4)$$

(4) The cross-spectrum $H_{xy}(\lambda)$ that $\tilde{y}$ is highest correlation with k-th $\tilde{x}$ is calculated in the time band $m - \frac{1}{2}w \sim m + \frac{1}{2}w$.

The n-th cross-spectrum $H_{xy}(\lambda)$ is shown by (5) when $H_x(\lambda, n)$ and $H_y(\lambda, n)$ are Hilbert Huang Spectrum of $x(t)$ and $y(t)$. $*$ is the conjugate.

$$H_{xy}(\lambda, n) = H_x(\lambda, n) \cdot H_y^*(\lambda, n) \quad (5)$$

(5) When it has finished the calculation at all $\tilde{x}$, the basis of the $\tilde{y}$ perform the same operation. However, the analysis for the time that cross-spectrum has been already calculated at $\tilde{x}$ is excluded.

(6) Finally, $H_{xy}(\lambda)$ was averaged the number of samples that have been extracted, the power spectrum $H_{xx}(\lambda, n)$ and $H_{yy}(\lambda, n)$ of x and y are normalized by the averaged

product of them and $HCOH_{xy}(\lambda)$ that the coherence of the analyzed frequency between x and y is calculated.

$$HCOH_{xy}(\lambda) = \frac{\left| \bar{H}_{xy}(\lambda) \right|^2}{\bar{H}_{xx}(\lambda) \bar{H}_{yy}(\lambda)} \quad (6)$$

3 The Comparison with the Conventional Methods for Numerically Generated Non-stationary

First, best performance is compared conventional coherences using the signals in order to verify those features. Conventional coherences are derived from the STFT and from the WT. (The following is represented as STFT-C and the WT-C)

So, it is compared the case of synchronized component of 10 Hz. The coherences analyzed between x_1 and x_2. Sampling frequency is 500 Hz and parameters are shown Table 1.

$$x_1(t) = \sum_{i=0}^{M} \left\{ A_i \sin(2\pi f_i t) \cdot h\left(\frac{t}{T} - \tau\right) \right\} + \varepsilon_1(t) \quad (7)$$

$$x_2(t) = \sum_{j=0}^{M} \left\{ A_j \sin(2\pi f_j t) \cdot h\left(\frac{t}{T} - \tau\right) \right\} + \varepsilon_2(t) \quad (8)$$

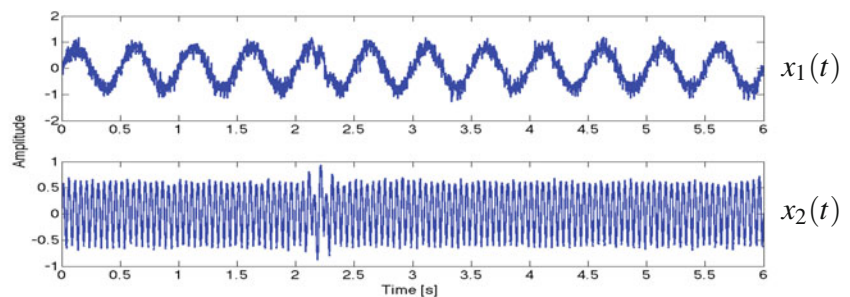**Table 1** Parameters in examined signals of simulation 1

i	A_i	f_i(Hz)	t(s)	τ(s)	T(s)
0	0.8	2	0–6	0	∞
1	0.4	10	0–6	2.2	0.4
j	A_j	f_j (Hz)	t (s)	τ (s)	T (s)
0	0.6	20	0–6	0	∞
1	0.4	10	0–6	2.2	0.4

Table 2 Parameters in examined signals of simulation 2

i	A_i	f_i (Hz)	t (ms)	τ (s)	T (s)
0	0.8	2	0–6000	0	∞
1	0.4	10	0–6000	2.2	0.4
2	0.4	10	0–6000	1.7	0.4
j	A_j	f_j (Hz)	t (ms)	τ (s)	T (s)
0	0.6	20	0–6000	0	∞
1	0.4	10	0–6000	2.2	0.4
2	0.4	10	0–6000	2.7	0.4

$$h(u) = \begin{cases} \frac{1+\cos(2\pi u)}{2} & \left(-\frac{1}{2} \le u \le \frac{1}{2}\right) \\ 0 & \left(u < -\frac{1}{2}, \frac{1}{2} < u\right) \end{cases} \quad (9)$$

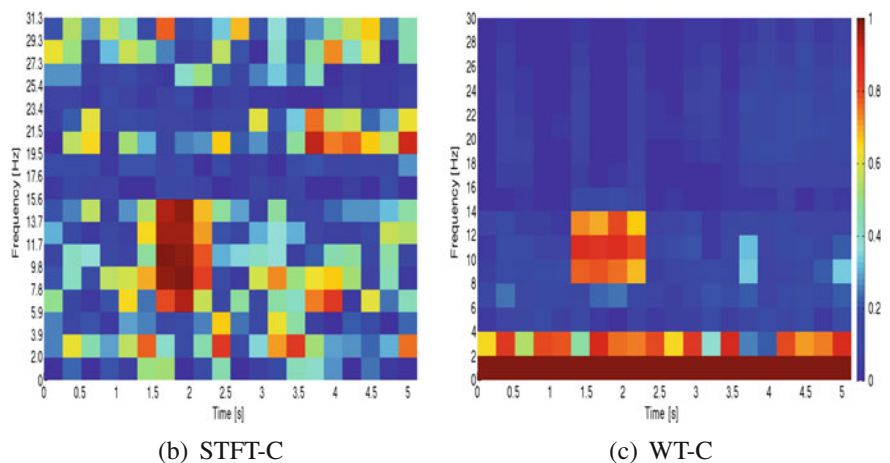ε_1 and ε_2 are white Gaussian noises where SNRs are 10 and 20 dB. $h(u)$ is Hanning window. $h(u)$ is used for extracted the signal of 10 Hz. In the case of $i = 0$, $T = \infty$ because $h(u)$ is not used.

The coherence analysis was performed in the analysis width is 1.024 s and the overlap is 0.768 s. In the case of the STFT-C, the analysis was performed by shifting every 0.004 s the Hanning window which the window width is 0.512 s. In the case of the WT-C, the analysis was performed by shifting every 0.004 s the Gabor window as the Mother Wavelet. σ parameter determined the temporal frequency resolution of the Gabor window was 5 in this time.

As shown in Fig. 3, it is easy to identify which frequency bands are synchronizing for the WT-C. This results show that WT is effective for the analysis of non-stationary signal.

Then, best performance of the HHC is compared WT-C that effectively in the analysis of non-stationary signal. Used signals are changed to verify features of the HHC.

It is compared the case of the including both synchronized component and unsynchronized component of 10 Hz. The coherences analyzed between x_1 and x_2. Sampling frequency is 500 Hz and parameters are shown Table 2.

The HHC was performed that the coherence analysis width is 0.512 s and the overlap is 0.384 s.

As shown in Fig. 4, it is easy identify which time and frequency bands are synchronizing for the HHC. Although the WT-C is effective for the analysis of non-stationary signal, it is necessary to increase the analysis width in order to analyze better resolution in the low frequency band. For that reason, it is difficult to identify which time and

Fig. 3 x_1, x_2 and compare of the analysis results of simulation 1

(a) The signals of analysis target

(b) STFT-C

(c) WT-C

Fig. 4 x_1, x_2 and compare of the analysis results of simulation 2
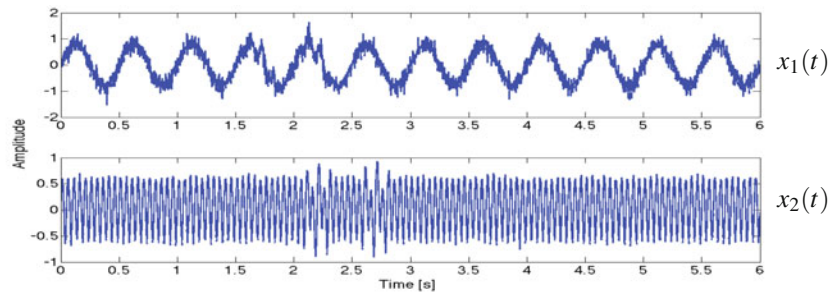
(a) The signals of analysis target
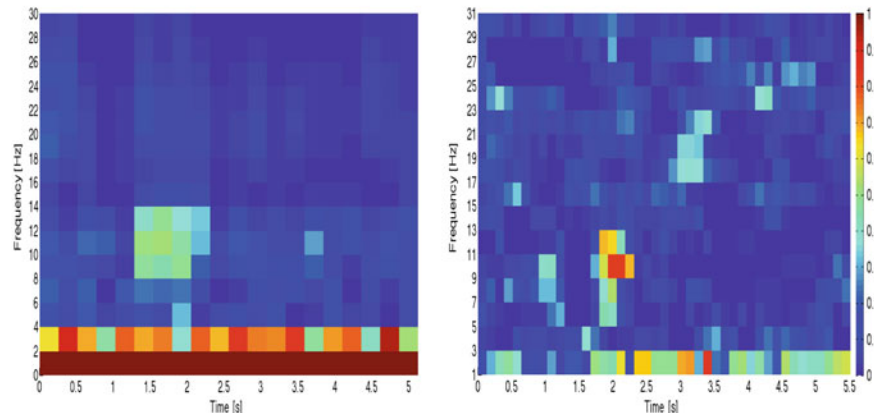
(b) WT-C

(c) HHC

frequency bands are synchronizing in the case of the including both synchronized component and unsynchronized component of the same frequency. In contrast, it is easy to identify even the short analysis width for the HHC.

4 The Comparison with the Conventional Method Using Measured EEG

As shown in Sect. 3, it is necessary to analyze in short analysis width which to identify synchronizing in the case of the signal including both synchronized component and unsynchronized component of the same frequency. For that reason, short analysis width is used for EEG analysis.

Coherencegrams are compared indicating the results of the coherence analysis using the STFT-C, the WT-C and the HHC. The coherencegram is drawn the coherence obtained at each time period which separated the signal in a short time length.

The analysis uses measured EEG of the healthy adult men (22 years old) who was measured at rest with eyes closed in anechoic chamber (Sampling frequency is 500 Hz). The EEG measured in the P3 and P4 electrodes of ten-twenty electrode system are used because α wave with most descriptive in change is seen remarkable.

The Fig. 5 shows segments of extracted EEG in P3 and P4 where α waves seem to be synchronized in short period. The length of each segment is 1.024 s.

The temporal frequency resolution of the coherences are examined for the segments. The coherence analysis is performed the STFT-C and the WT-C but it is expected that temporal frequency resolution is insufficient because it is analyzed in a short period of 0.256 s. The analysis results compared in consideration of them.

The analysis condition was the analysis width of coherence to 0.256 s and shifting the analysis width to every 0.064 s. The Hanning window, which the window width is 0.128 s, shift step 0.004 s, are used for STFT-C. The Gabor window as the mother Wavelet, which shift step 0.004 s, σ parameter determined the temporal frequency resolution of Gabor window was 4 in this time, used for WT-C.

Coherencegram of STFT-C, shown in Fig. 6a, is difficult to identify the synchronization in the frequency because the frequency resolution compared the WT-C and the HHC is lower.

The frequency resolution of coherencegram of WT-C, shown in Fig. 6b, is higher than STFT-C but high coherence region is spread wider than the others. Particularly, the coherence is highest in α band (8–13 Hz). The coherence is higher in the low frequency band because it does not obtain sufficient number of samples.

Fig. 5 Segment of extracted
EEG for coherence analysis
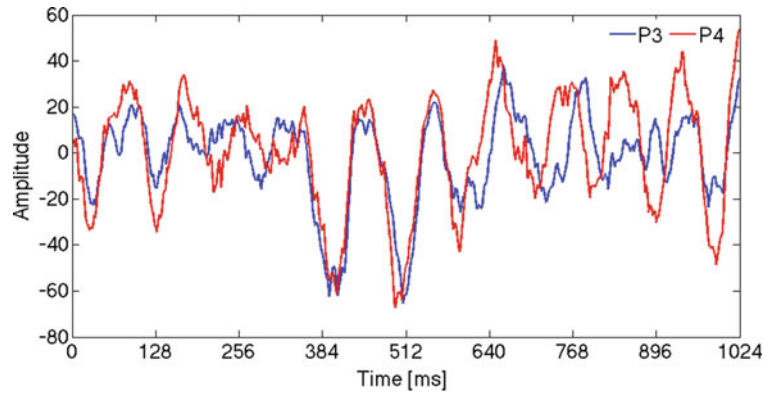
(a) Segment 1
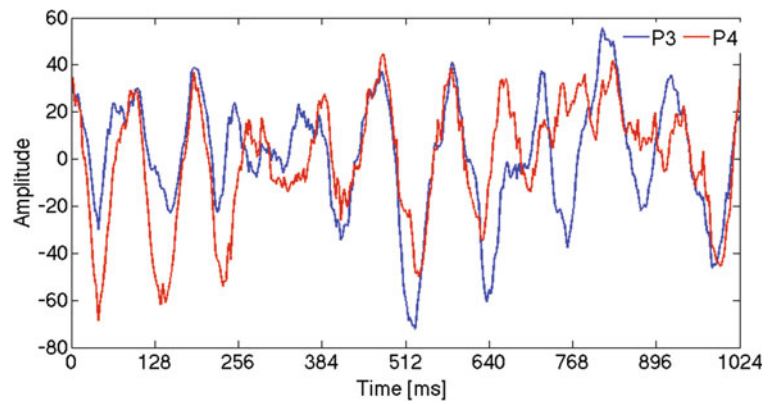
(b) Segment 2

Fig. 6 Coherencegrams of
segment
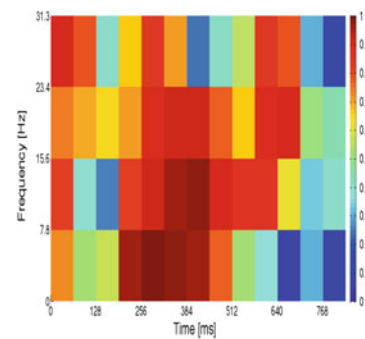
(a) STFT-C
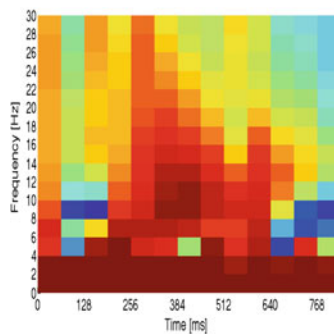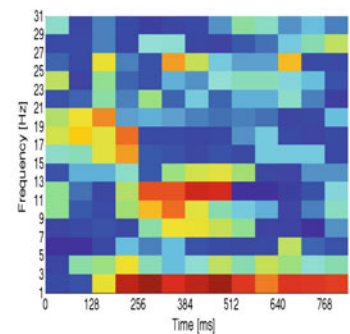
(b) WT-C (c) HHC

Coherencegram of HHC, shown in Fig. 6c, is considered to be easy to identify the synchronization of the time and frequency because the coherence is higher around the α band. The coherence is higher in low frequency band because the HHC is to capture the change of the instantaneous phase which the change of the phase with time is small.

5 Discussion

The HHC is expected to be used to evaluated the degree of synchronization in multiple brain regions even if its duration is short because the temporal frequency resolution is high. As a future tasks are to investigate the limit of the noise immunity, to investigate optimal analysis width so that significant HHC can be obtained and to apply the HHC to analysis of EEG that synchronization in the short period is occurred in order to confirm availability of the HHC more clearly.

References

1. Varela F, Lachaux J-P, Rodriguez E, Martinerie J (2001), "The brainweb: phase synchronisation and large-scale integration." Nature Rev. Neurosci. 2: 228–239.
2. Kandel E, Schwartz J, Jessell T (1991),"Principles of Neural Science, 3rd edn." Appleton and Lange, Norwalk, CT.
3. Norden E. Huang, Zheng Shen, Steven R. Long, Manli C. Wu, Hsing H. Shih, Quanan Zheng, Nai-Chyuan Yen, Chi Chao Tung and Henry H. Liu. (1998). The empirical mode decomposition and the Hilbert spectrum for nonlinear and nonstationary time series analysis. Proceedings of the Royal Society of London, A454, 903–995.

Identifying Cancer Subnetwork Markers Using Game Theory Method

Saman Farahmand, Sama Goliaei, Zahra Razaghi Moghadam Kashani, and Sina Farahmand

Abstract

In this paper, a novel game theory method is proposed to identify subnetwork markers by integrating gene expression profile and protein-protein interaction network. The proposed method has been evaluated on different cancer datasets in order to classify cancer phenotypes. To verify the performance of our approach, the identified subnetwork markers are compared with a greedy search method. The proposed method is capable of identifying robust subnetwork markers and presents higher classification performance.

Keywords

Cancer subnetwork markers • Microarray data analysis • Game theory • Cancer classification

1 Introduction

Genetic mutations in human cells are fundamental reason which lead to cancer diseases [1]. Cancer diagnosis at earlier stages using cancer markers empowers researchers to cure, or delay the progression of cancer in human body [2].

S. Farahmand · S. Goliaei
Research Laboratory for Computational Biology, Network Science and Technology Department, University of Tehran, Tehran, Iran
e-mail: saman.farahmand.1990@ieee.org

S. Goliaei
e-mail: sgoliaei@ut.ac.ir

Z. R. M. Kashani
Life Science Engineering Department, University of Tehran, Tehran, Iran
e-mail: razzaghi@ut.ac.ir

S. Farahmand (✉)
Laboratory of Neural Engineering Research, Biomedical Engineering Department, Illinois Institute of Technology, Chicago, IL, USA
e-mail: sfarahma@hawk.iit.edu

Therefore, it is of crucial importance to identify genetic markers involved in cancer diagnosis in system biology. Numerous studies in the literature have reported differentially expressed genes (DEGs) as cancer markers using gene expression profiles between cancer and normal phenotypes [3]. However, noisy data, small sample-sizes, and heterogeneous experimental platforms make cancer markers identification's procedure arduous and dataset-specific [4]. Several methods have been proposed to identify cancer markers from biological contexts. Proposed methods in [5] and [6] rely on identification of single genes expressed differentially across different phenotypes. However, cancer markers recognized by this approach is less efficient in terms of reproducibility among independent datasets [7, 8]. Using context in molecular levels has been considered as a main strategy to overcome the aforementioned drawback, in which genes with specific functional roles interact with each other [9]. Two different approaches have been reported using the context in molecular levels. In the first approach, genes are analyzed in pathways in order to identify cancer markers, which called pathway markers. Pathway-based methods yield more reliable and accurate markers than single gene markers. Furthermore, they provide biological and functional insight into the target diseases [10–14]. However, pathways used in pathway-based methods cover only a limited number of genes and may not include key genes with significant expression changes across different phenotypes [15]. In the second approach, gene expression profile is integrated with protein-protein interaction network (PPIN), which results in better covering over genes [15, 16]. In this approach, microarray data and the PPIN are evaluated in order to identify cancer marker as an individual connected component, which called subnetwork marker. The subnetwork marker provides better performance and reproducibility across cancer datasets [17]. Greedy search method proposed in [15] is a well-known method based on identifying subnetwork markers. However, this method may not be the optimal one in terms of classification performance.

In this study, we propose a novel method relied on game theory to identify robust subnetwork markers for predicting cancer phenotypes. In the most experiment's evaluation criteria, the discriminative power of identified subnetwork markers using the proposed method has been proved to be higher than the greedy search method.

2 Materials and Methods

2.1 Data Sources

In this study, we investigated three types of cancer, in which two independent datasets have been analyzed in each type to perform cross-dataset classification experiment. Table 1 shows six different datasets used in this paper. A scored network of human PPI data pooled from different PPIN databases has been used as our network data [18]. Furthermore, a 0.154 cut-off threshold has been utilized to reduce noise, interactions with confidence score below this threshold, from high-confidence data. Eventually, it generated a network with 169,810 unique, high-confidence interactions between 12,879 unique human proteins. We overlaid the six cancer datasets with the generated PPI network by mapping each gene to the corresponding protein.

Then, proteins which do not have any corresponding genes in cancer datasets were removed which leads to a new network generation with 146,293 interactions and 11,893 proteins.

2.2 Game Theory

Game theory is a branch of mathematics that models the behavior of rational agents in a strategic location. A game consists of a set of agents, or players, that each takes a specific strategy. The benefit and loss of each agent depends on its own and others' strategies chosen during the game which are basically defined by a payoff function. All of the agents choose a strategy that increase the benefit of their own payoffs. In cooperative games, the player's payoff determined by individual member, and the main purpose is to achieve an optimal set of players in order to maximize the

final score. Finally, all players should reach to an equilibrium called Nash equilibrium [19]. Assuming payoff function π_i and set of all possible strategies Σ_i for i-th agent, a Nash equilibrium (e.g. for two players) is a pair of strategies, (σ_1^*, σ_2^*), which has to satisfy both of the Eqs. (1) and (2).

$$\pi_1(\sigma_1^*, \sigma_2^*) \geq \pi_1(\sigma_1, \sigma_2^*) \quad \forall \sigma_1 \in \Sigma_1 \tag{1}$$

$$\pi_2(\sigma_1^*, \sigma_2^*) \geq \pi_2(\sigma_1^*, \sigma_2) \quad \forall \sigma_2 \in \Sigma_2 \tag{2}$$

That is, in Nash equilibrium no player is able to gain a better payoff by changing its own strategy alone. The detailed calculation regarding Nash equilibrium has been described in [19].

2.3 Payoff Function and Scoring

Given a PPI network as an undirected graph $G(V, E)$, the main objective is to identify a subnetwork as a group of nearly connected genes. Ideally, this subnetwork should be highly relative to the disease of interest, and is achieved using several scoring schemes [17]. In this study, we propose a scoring scheme based on a payoff function. Some criterions are considered to define payoff function as a combination of gain function and loss function. It should be noted that joining, or leaving a subnetwork are the main strategies that can be chosen by each player. Suppose in a subnetwork $G_s = (V_s, E_s)$, there are $|V_s| = n$ unique genes with m different samples. $x_i = (x_i^1, x_i^2, \ldots, x_i^m)$ is the expression vector of gene i, in which $i = 1, 2, \ldots, n$ and x_i^j is the expression level of gene i in sample j. The discriminative power of i-th gene is evaluated by t-test statistics score (t-score) of its expression. Furthermore, a local scoring (LS) function is introduced for each gene in order to score disease genes connecting DEGs in PPIN. The LS function for gene i with joining strategy is defined as Eq. (3), in which k is the number of neighbor genes of the gene i in the subnetwork G_s.

$$LS_i = \sum_{l=1}^{k} tscore(x_l) \tag{3}$$

Table 1 Six datasets that used in this study

Cancer	Dataset	#Tumour	#Normal	GEO ACC #	Platforms
Colon	Colon64	32	32	GSE8671	HG-U133_Plus_2
	Colon23	15	8	GSE4183	HG-U133_Plus_2
Breast	Breast185	42	143	GSE10780	HG-U133A
	Breast58	31	27	GSE10810	HG-U133A
Lung	Lung107	58	49	GSE10072	HG-U133_Plus_2
	Lung52	26	26	GSE7670	HG-U133_Plus_2

Fig. 1 Conceptual diagram of the candidate subnetwork
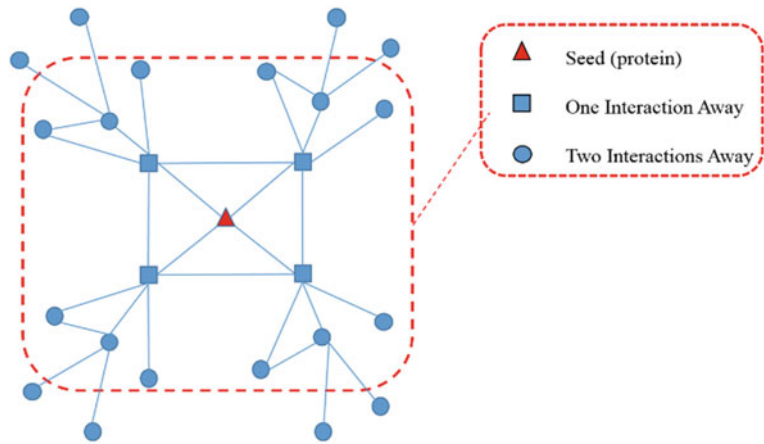
The gain function (GF) is determined for i-th gene as Eq. (4), in which α is a constant.

$$GF(i, G_s) = \alpha \cdot tscore(x_i) + LS_i \qquad (4)$$

The loss function (LF) for i-th gene with joining strategy is defined in Eq. (5), where c is a constant.

$$LF(i, G_s) = c \cdot (n - 1) \qquad (5)$$

Eventually, the payoff function (PF) for a given agent i and the subnetwork G_s is calculated as follows:

$$PF(i, G_s) = GF(i, G_s) - LF(i, G_s) \qquad (6)$$

2.4 Subnetwork Markers Identification

In the proposed method, proteins involved in the PPI network were sorted in decremental order according to their t-test statistics scores. Proteins with degree above the average degree of the PPI network were chosen as seeds. Furthermore, all proteins by at most two interactions away from each seed were selected to form a candidate subnetwork as illustrated in Fig. 1. In this subnetwork, all seed's neighbors with one interaction away were selected and sorted in incremental order according their degrees, and were iteratively removed while increasing local clustering coefficient of the seed. The remaining proteins, with two interaction away of the seed were sorted and the same procedure was performed while increasing the local clustering coefficient. In the candidate subnetwork with n genes, each gene's PF was calculated for all 2^n possible states including both joining and leaving strategies by setting $\alpha = 1.2$ and $c = 2$. Then, Nash equilibrium was measured and was selected as optimized subnetwork. It should be noted that for a subnetwork with multiple Nash equilibriums, averaged absolute values of t-scores of its involved genes have been calculated

for each Nash equilibrium, and the one with the highest value has been chosen to be the optimized subnetwork.

3 Results

The within-dataset and cross-dataset experiments were performed in order to evaluate the performance of the identified subnetwork markers using support vector machine (SVM) classifier. The results of the proposed method have been compared with the subnetwork markers obtained by the greedy method. In the within-dataset experiment, the top 50 subnetwork markers were used from each cancer dataset to train and test the SVM classifier. The five-fold cross-validation experiment was repeated ten times and averaged to validate its performance. In this experiment, the datasets were divided into five folds of equal size, in which four folds were used for training the classifier and the remaining fold was used for testing it. In each dataset, the results for two evaluation criteria, accuracy (ACC) and area under the curve (AUC), are shown in Table 2. According to the Table 2, the ACC and AUC of the classifier obtained using our identified subnetwork markers are higher than those of the classifier constructed by the greedy method ones. Thus, the proposed game theoretic algorithm is more effective than the greedy method in terms of identifying optimal subnetwork markers. To verify the reproducibility of identified subnetwork markers, the cross-dataset experiment was performed. In this experiment, the top 50 subnetwork markers were extracted from the first dataset, and then the five-fold cross-validation experiment was repeated for ten times on the second one. Table 3 shows the results of cross-dataset experiment for the both evaluation criteria. According to the Table 3, in the most cases, the classifier constructed based on our extracted subnetwork markers outperforms the one which is based on the greedy method. Therefore, it suggests that the extracted subnetwork markers

Table 2 Performance comparison of the within-datasets experiment

Datasets	Criteria	Proposed method		Greedy method [15]		Improvement (%)
		Mean	Variance	Mean	Variance	
Breast185	ACC	0.9508	0.001	0.9281	0.001	2.27
	AUC	0.9851	0.004	0.976	0.007	0.91
Breast58	ACC	0.8827	0.0011	0.8497	0.0027	3.3
	AUC	0.9467	0.0054	0.8831	0.0054	6.36
Colon64	ACC	0.9387	0.013	0.889	0.0019	4.97
	AUC	0.9845	0.001	0.9675	0.008	1.7
Colon23	ACC	1	0	0.9583	0	4.17
	AUC	1	0	0.9732	0.058	2.68
Lung107	ACC	0.985	0.017	0.9907	0.0001	−0.57
	AUC	0.9996	0.0006	0.9997	0.0002	−0.01
Lung52	ACC	0.9576	0.007	0.8636	0.01	9.4
	AUC	0.9736	0.0008	0.9219	0.0028	5.17

Table 3 Performance comparison of the cross-datasets experiment

Datasets	Criteria	Proposed method		Greedy method [15]		Improvement (%)
		Mean	Variance	Mean	Variance	
Breast185 → Breast58	ACC	0.8536	0.004	0.8382	0.012	1.54
	AUC	0.9195	0.005	0.9251	0.061	−0.56
Breast58 → Breast185	ACC	0.9471	0.004	0.9374	0.001	0.97
	AUC	0.9901	0.002	0.9809	0.005	0.92
Colon64 → Colon23	ACC	0.9571	0.006	0.9506	0.009	0.65
	AUC	0.9387	0.058	0.93	0.047	0.87
Colon23 → Colon64	ACC	1	0	1	0	0
	AUC	1	0	1	0	0
Lung107 → Lung52	ACC	0.9058	0.0002	0.8428	0.0013	6.3
	AUC	0.9581	0.0014	0.8972	0.001	6.09
Lung52 → Lung107	ACC	0.8729	0.002	0.8517	0.006	2.12
	AUC	0.9346	0.004	0.9316	0.001	0.3

using the proposed method have better reproducibility than the subnetwork markers identified by the other comparative method.

4 Conclusions

In this paper, we proposed a novel game theory method to identify subnetwork markers in order to predict cancer phenotypes. It has been proved that the discriminative power of the identified subnetwork markers using the proposed method is higher, and has better classification performance than the greedy search method.

Conflicts of Interest The authors declare that they have no conflict of interest.

References

1. P. Dao, R. Colak, R. Salari, F. Moser, E. Davicioni, A. Schönhuth, and M. Ester, Inferring cancer subnetwork markers using density-constrained biclustering, J. of Bioinformatics, vol. 26, no. 18, pp. 625–631, Sept. 2010.
2. S. J. Nass, Cancer biomarkers: the promises and challenges of improving detection and treatment. committee on developing biomarker-based tools for cancer screening, diagnosis, and treatment, The National Academies Press, 2007.
3. A. Berchuck, E. S. Iversen, J. Luo, Microarray analysis of early stage serous ovarian cancers shows profiles predictive of favorable outcome, J. of Clinical Cancer Research, vol. 15, no. 7, pp. 2448–2455, Mar. 2009.

4. M. J. Jahid, J. Ruan, A Steiner tree-based method for biomarker discovery and classification in breast cancer metastasis, J. of BMC Genomics, vol. 13, no. 6, pp. 38–49, Oct. 2012.

5. M. J. Vijver, Y. D. He, L. Veer, H. Dai, A gene-expression signature as a predictor of survival in breast cancer, The New England Journal of Medicine, vol. 347, no. 25, pp. 1999–2009, Dec. 2002.

6. Y. Wang, J. G. M. Klijn, Y. Zhang, A. M. Sieuwerts, M. P. Look, F. Yang, D. Talantov, Gene-expression profiles to predict distant metastasis of lymph-node-negative primary breast cancer, J. of Lancet, vol. 365, no. 9460, pp. 671–679, Feb. 2005.

7. L. Ein-Dor, I. Kela, G. Getz, D. Givol, Outcome signature genes in breast cancer: Is there a unique set?, J. of Bioinformatics, vol. 21, no. 2, pp. 171–178, Jan. 2005.

8. L. Ein-Dor, O. Zuk, E. Domany, Thousands of samples are needed to generate a robust gene list for predicting outcome in cancer, Proc. Natl. Acad. Sci. USA., vol. 103, no. 15, pp. 5923–5928, Apr. 2006.

9. E. E. Schadt, Molecular networks as sensors and drivers of common human diseases, Nature, vol. 461, no. 7261, pp. 218–223, Sept. 2009.

10. L. Tian, S. Greenberg, S. W. Kong, J. Altschuler, I. S. Kohane, Discovering statistically significant pathways in expression profiling studies, Proc. Natl. Acad. Sci. USA., vol. 102, no. 38, pp. 13544–13549, Sept. 2005.

11. A. H. Bild, G. Yao, J. T. Chang, Q. Wang, A. Potti, D. Chasse, Oncogenic pathway signatures in human cancers as a guide to targeted therapies, Nature, vol. 439, no. 6351, pp. 353–357, Jan. 2006.

12. Z. Guo, T. Zhang, X. Li, Q. Wang, J. Xu, H. Yu, J. Zhu, H. Wang, Towards precise classification of cancers based on robust gene functional expression profiles, J. of BMC Bioinformatics, vol. 6, no. 58, pp. 194–201, Mar. 2005.

13. J. Su, B. J. Yoon, E. R. Dougherty, Accurate and reliable cancer classification based on probabilistic inference of pathway activity, PLoS One, vol. 4, no. 12, p. e8161, Dec. 2009.

14. J. Tomfohr, J. Lu, T. B. Kepler, Pathway level analysis of gene expression using singular value decomposition, J. of BMC Bioinformatics, vol. 6, no. 21, p. 225–234, Sept. 2005.

15. H. Y. Chuang, E. Lee, Y. T. Liu, D. Lee, T. Ideker, Network based classification of breast cancer metastasis, J. of Mol. Syst. Biol., vol. 3, no. 140, p. 141, Oct. 2007.

16. J. Su, B.-J. Yoon, and E. R. Dougherty, Identification of diagnostic subnetwork markers for cancer in human protein-protein interaction network., BMC Bioinformatics, vol. 11 Suppl 6, no. Suppl 6, p. S8, 2010.

17. B. Jiang. M. Gribskov, Assessment of subnetwork detection methods for breast cancer, J. of Cancer Inform., vol. 13, no. 36, pp. 221–229, Dec. 2014.

18. K. Lage, E. O. Karlberg, Z. M. Størling, P. I. Olason, A. G. Pedersen, O. Rigina, A. M. Hinsby, A human phenomeinter-actome network of protein complexes implicated in genetic disorders, J. of Nat. Biotechnol., vol. 25, no. 3, pp. 309–316, Mar. 2007.

19. J. N. Webb, Game theory, decisions, interaction and evolution, Springer London, 2007.

On Fabrication of a Shoe Insole: 3D Scanning Using a Smartphone

Tomislav Pribanić, Tomislav Petković, Matea Đonlić, and Vedran Hrgetić

Abstract

The generation of 3D models from still images has been a long term goal in computer vision. Acquiring high quality 3D models is no longer restricted to processing on desktop computers and high end laptops. Modern and powerful smartphones open up the possibilities designing new methods for 3D reconstruction. The scope of this work is the development of the prototype system on a smartphone for the efficient active stereo 3D reconstruction. Acquired 3D results are apparently no different from 3D results using a standard structured light scanner. Extending smartphone's functionality towards an active stereo 3D scanning device is interesting both for the medical applications and for the industrial (economic) exploitation as well. Namely, combining 3D reconstruction capabilities with the present smartphone features sets the foundations for numerous other functionalities.

1 Introduction

At the moment, one of the most powerful trends in the IT industry is the wide availability of high-performance smartphones. Starting with Apple's iPhone in the 2007, the era of modern smartphones begins, resulting in a visual computing powerhouse. Modern smartphone has a high speed multi-core CPU, a 3D graphic processor, a DSP for image and video processing, a high resolution camera, a high quality color display, and quite impressive local storage capabilities enhanced with external storage possibilities (SD card). Therefore, turning a smartphone into a powerful 3D reconstruction device opens additional application and research avenues which are beyond a simple gadget. Namely, 3D measurement constitutes an important topic in computer vision, having different applications such as range sensing, industrial inspection of manufactured parts, reverse engineering (digitization of complex, free-form surfaces), object recognition, 3D map building, biometrics, clothing design, and others. The matter of fact is that a vast majority of research using smartphones for 3D reconstruction is devoted to smartphones using a single camera only [1]. That may be quite expectable and understandable since most smartphones do not have additional imaging or projection sensors, e.g. a built in video projector. Nevertheless, on the market there are smartphones which have a built in video projector [2]. From the computer vision perspective, and in particular considering the possibilities of using it for 3D reconstruction, an additional smartphone projector is underutilized. However, it is well known that a camera-projector pair defines a powerful active 3D reconstruction tool under the strategy named structured light (SL) [3]. The basic principle of SL approach can be summarized as follows: a projector projects a certain number of image(s) on the object of interest. The projected images have a particular structure (code) which can be decoded on the grabbed camera images. Hence, provided code allows dense correspondence between the projector and camera image pixels and ultimately sets the basis for the 3D triangulation (reconstruction).

Nowadays accurate CAD/CAM systems are frequently used in biomedical applications, for manufacturing of all kinds of parts, based on the provided 3D digitized model of some kind. In this work we propose 3D SL reconstruction system using Samsung Galaxy Beam smartphone with an embedded pico projector [4]. We demonstrate its potential use for one popular medical application: 3D scanning of the

T. Pribanić (✉) · T. Petković · M. Đonlić · V. Hrgetić
Faculty of Electrical Engineering and Computing, University of Zagreb, Zagreb, Croatia
e-mail: tomislav.pribanic@fer.hr

T. Petković
e-mail: tomislav.petkovic.jr@fer.hr

M. Đonlić
e-mail: matea.donlic@fer.hr

V. Hrgetić
e-mail: vedran.hrgetic@fer.hr

sole (foot) that could be eventually used during a CAD/CAM shoe insole production process.

2 Related Work

The field of 3D reconstruction on smartphones was until recently relatively poorly investigated and therefore there are not many works dealing with this topic. Because of the emerging need for new applications and all the commercial potential this area has, the situation is rapidly changing. Klein and Murray [5] have presented the Parallel Tracking and Mapping (PTAM) system on a mobile phone which aims at enabling different augmented reality applications of the mobile phone. The goal to give the users the possibility to create and maintain the Augmented Reality (AR) content without the need for complex and expansive tools has also motivated Hartl et al. [6] to design a 3D reconstruction system on the smartphone based on the shape-from-silhouette approach. In [7] Won et al. have presented the work where they implemented an active 3D shape acquisition method based on photometric stereo. They used a pair of smartphones which collaborated as master and slave where the slave was engaged to illuminate the scene (using the flash) from the appropriate viewing points while the master recorded images. In [1] Tanskanen et al. have presented a complete on-device 3D reconstruction pipeline for mobile monocular hand-held devices, which generates dense 3D models. To make the tracking and mapping process more resilient to rapid motions and to estimate the metric scale of the captured scene, the on-device inertial sensors are utilized. On the other hand we propose a method using smartphone with an embedded pico projector. To the best of our knowledge the idea of combining smartphone's camera and projector into one SL system has not been considered before. This is strongly suggested by a fact that smartphones have projector and camera positioned at different sides of its casing (see figures in the next section for more info), most likely to simplify using the touch screen menu before and during the content projection. To overcome this difficulty we propose using a mirror. It should be noted that the mirrors have been already routinely exploited even in more demanding 3D scanning applications [8, 9].

3 Proposed Method and Results

Figure 1 shows the chosen smartphone where evidently camera and projector have no common field of view. To overcome this difficulty we have made a small adapter with a mirror. The adapter is easily re-attached to the smartphone and it successfully re-directs projections rays into camera's field of view (Fig. 2). During a shoe insole production it is a

Fig. 1 The appearance of Samsung Galaxy Beam smartphone, equipped with a camera and a projector pointing in directions comprising an angle of 90°

customary to ask an individual to step in a special type of foam, leaving his/her imprint of the sole (foot). Our 3D smartphone scanner was used to reconstruct the imprint of the patient's sole (foot) in a special type of foam (Fig. 3).

Out of more than a dozen SL different projection strategies [3], we have chosen the multiple phase shifting approach (MPS) [10]. In brief, MPS consists of projecting a periodic sine pattern (Fig. 4b), shifted by some period amount and sequentially projected with a projector for $N \geq 3$ number of times. The corresponding $N \geq 3$ grabbed images are processed in order to compute a wrapped phase map (Fig. 4c). MPS assumes projecting at least one more set of $N \geq 3$ images using a periodic sine pattern with *a different period* than before providing in turn an additional wrapped phase. Using two such wrapped phase maps is sufficient to recover the unwrapped phase map (Fig. 4d) and to undertake 3D triangulation in the case of calibrated

Fig. 2 Smartphone on a small tripod and with a deflection adapter for projectors rays. Note a mirror image of the projector, i.e. a virtual projector

Fig. 3 **a** Taking patient sole imprint; **b** the proposed 3D system during 3D scanning
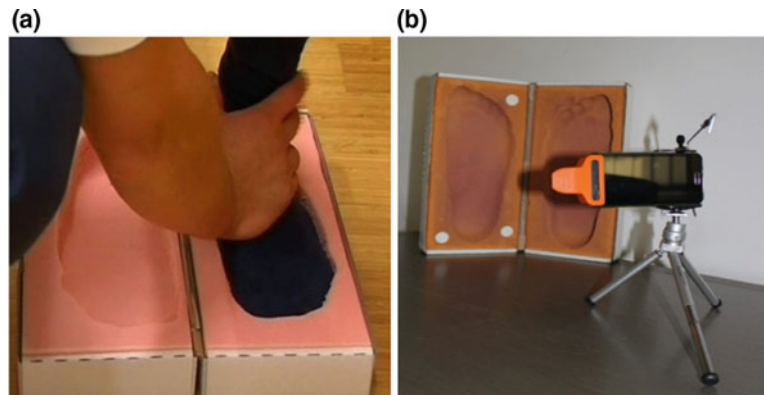
Fig. 4 **a** Camera image of the object to be scanned; **b** projected sine pattern during MPS; **c** computed wrapped phase map; **d** recovered unwrapped phase map
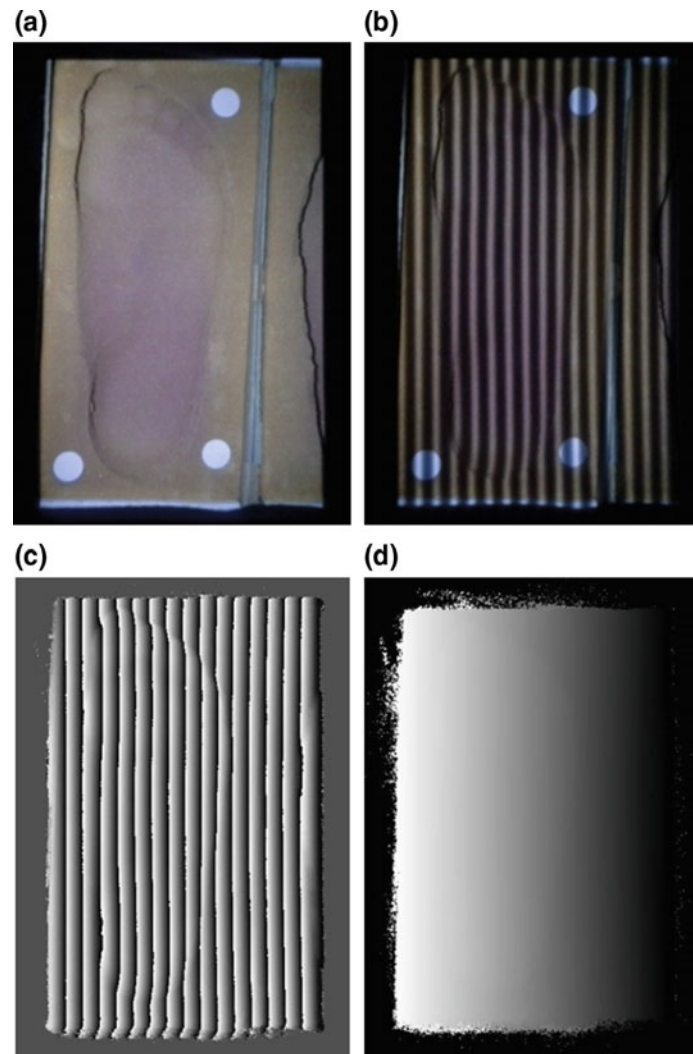
camera-projector pair. The proposed smartphone 3D system was calibrated using a plane calibration as described in [11]. Due to limited space, for more details about the implemented MPS method we refer a reader to [10].

We have scanned a foam (an imprint of the sole) from five different spatial positions/orientations with respect to the smartphone scanner. The number of reconstructed points per view varied between 50 and 80 k. Figure 5 shows a point
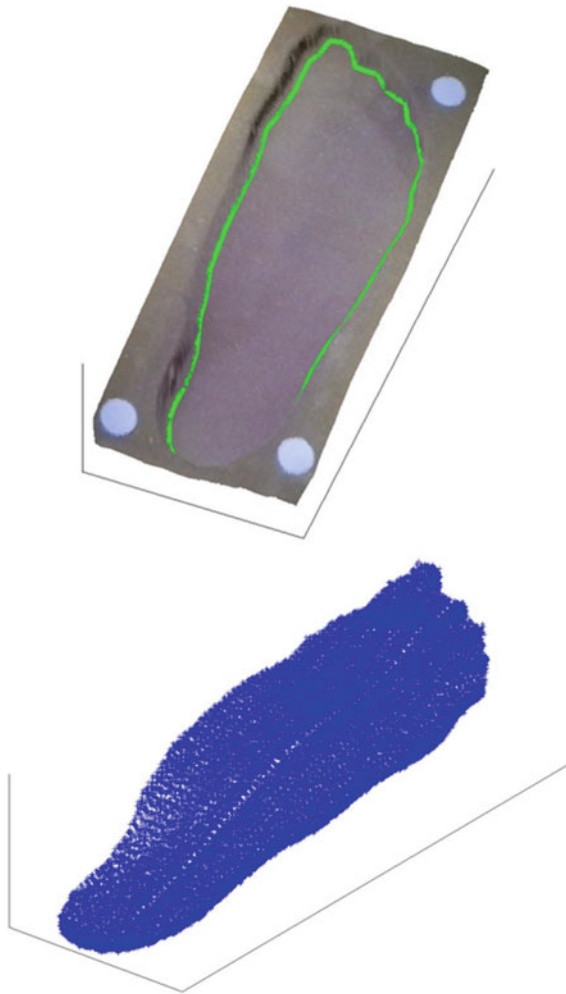
Fig. 5 Top: 3D reconstructed textured model of the entire foam. Green line presents extracted region of interest area (sole). Bottom: sole presented as a down sampled (for better visualization) point cloud (Color figure online)

cloud and the corresponding generated textured mesh from one of the scans.

To evaluate 3D results of the proposed smartphone scanner we have performed 3D scanning using a standard camera and projector set up, typically a state of the art approach in SL scanning (hereafter referred standard scanner Fig. 6). The foam was positioned in space with 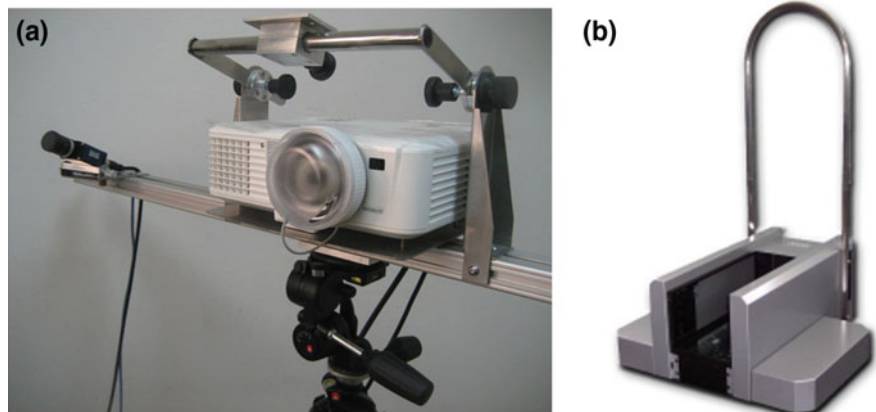the respect to the standard scanner approximately the same as in the case of the proposed smartphone scanner. Afterwards, 3D point clouds for all five spatial positions and for two types of scanners were compared through a process of 3D registration. 3D surface registration is usually used to fuse 3D point clouds acquired from two or more different views into a common point cloud [12]. There are various hardware and software approaches to compute 3D registration parameters between two reconstruction views, but in principle it is sufficient to identify three corresponding pairs of points from two scanned views. This was exactly the purpose of three circular markers labeled on foam (e.g. see Fig. 4a), establishing a minimal point pairs correspondence to compute an initial registration between 3D scans of two types of scanners involved. To acquire even more accurate registration parameters we have refined the initial registration by the well-known registration algorithm: iterative closet points or ICP [13]. Figure 7 shows an example of the registration between 3D point clouds reconstructed by the proposed smartphone scanner and the standard scanner, qualitatively demonstrating there is seemingly no difference in acquired scans between those two. To further appreciate the proposed method, we show 3D results when scanning upper body of mannequin and, from a closer distance, head and neck section (Fig. 8).

Finally, to provide a quantitative measure of agreement between registered point clouds we provide the absolute mean distance between corresponding points from the registered views at the final stage of registration process. We have considered two cases: first when the smartphone point cloud was registered to the standard scanner and second when the standard scanner point cloud was registered to the smartphone scanner (Table 1). Figures in the table strongly indicate that 3D output of two types of scanners is basically the same.
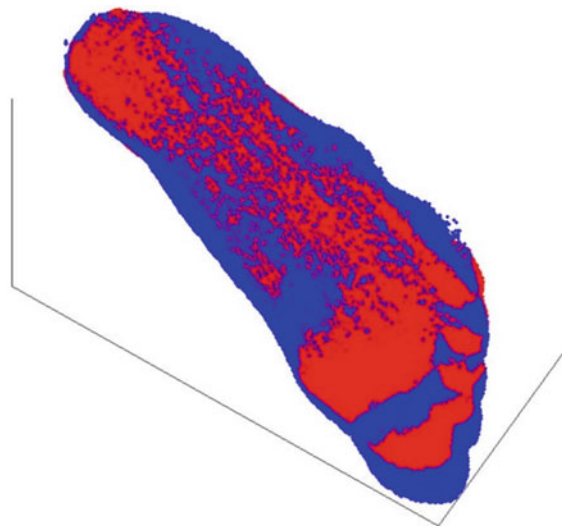
Fig. 6 **a** Standard scanner consisting of industrial camera and projector fastened on a tripod; it can be used as general purpose scanning device **b** example of specially designed foot scanner usable basically for scanning foot only

Fig. 7 Two clouds of points, red and blue, initially reconstructed from two different types of scanners and afterwards registered in the common coordinate system. Both clouds successfully overlap (Color figure online)

Fig. 8 **a** Mannequin model image **b** 3D textured mesh of upper body **c** 3D textured mesh of head and neck section
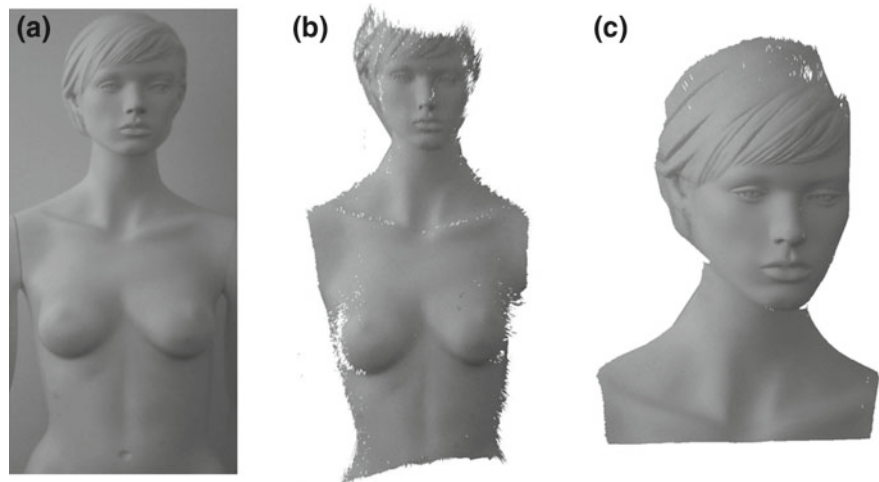
Table 1 Absolute mean distances (expressed in millimeters) between two corresponding points (nearest neighbor) from the registered views

	View 1	View 2	View 3	View 4	View 5
Smartphone to standard scanner (mm)	0.57	0.54	0.50	0.67	0.57
Standard scanner to smartphone (mm)	0.53	0.51	0.52	0.62	0.61

4 Discussion and Conclusion

The shown 3D reconstruction results, both qualitatively and quantitatively, demonstrate there is seemingly no difference between the proposed smartphone scanner and a standard scanner. The results are in particular surprisingly good given the modest characteristics of a smartphone's pico-projector compared to standard scanner projectors. One of the obvious advances of the proposed scanner is certainly the size and easy manipulation than more cumbersome and specially designed alternatives (Fig. 6). Additionally, it is useful to recall that a smartphone is more than just a 3D scanner whereas a standard scanner may only perform 3D scanning. Furthermore, combining smartphone's capabilities and sensors with the 3D data opens opportunities for numerous new applications. For example, smartphone's magnetic sensor and accelerometer (nowadays present in most smartphones)

could be used to register 3D point clouds without explicitly provided registration points [14, 15]. The obstacle of having smartphone projector and camera originally pointing in different directions is solved conveniently using an adapter with a mirror. Unfortunately, pico projectors are still not routinely embedded in smartphones. However, the list of smartphones which do have embedded projector is not small after all [2]. Besides, the fact that Samsung recently put on the market a new smartphone model with a pico projector shows the manufactures are still considering such options [16]. More importantly, the need to turn a smartphone into a 3D device with depth sensing capabilities is certainly recognized by a wider community. Google's Project Tango, a specially designed Android smartphone with an embedded infrared projector for depth perception [17], certainly proves that. To the best authors' knowledge Project Tango operates on the same principle as the well known original version of Microsoft's Kinect device [18]. On the other hand, our solution uses a general purpose projector normally used to project other consumable content which is now augmented by 3D scanning. Therefore, our solution could project Kinect like SL patterns, becoming Kinect like device too. In fact, one of the future research avenues about the proposed solution, will be directed to testing other SL patterns and in particular those for dynamic (moving) objects.

Conflict of Interest The authors declare that they have no conflict of interest.

References

1. Tanskanen, P., Kolev, K., Meier, L., Camposeco, F., Saurer, O., Pollefeys, M., 2013. Live Metric 3D Reconstruction on Mobile Phones. In IEEE International Conference on Computer Vision (ICCV) December 2013 Pages 65–72. IEEE.

2. List of projector phones. Accessed: June, 2015. https://en.wikipedia.org/wiki/Projector_phone.

3. J. Salvi, S. Fernandez, T. Pribanic, X. LLado. A state of the art in structured light patterns for surface profilometry. Pattern Recognition 43 (2010) 2666–2680.

4. http://www.samsung.com/global/microsite/galaxybeam/feature.html. Samsung Galaxy Beam. Accessed: June, 2015.

5. Klein, G., Murray, D., 2007. Parallel Tracking and Mapping for Small AR Workspaces. In 6th IEEE and ACM International Symposium on Mixed and Augmented Reality.

6. Hartl, A., Gruber, L., Arth, C., Hauswiesner, S., Schmalstieg, D., 2011. Rapid reconstruction of small objects on mobile phones. In IEEE Computer Society Computer Vision and Pattern Recognition Workshops (CVPRW) June 2011 Pages 20–27. IEEE.

7. Won, J. H., Lee, M. H., Park, I. K., 2012. Active 3D shape acquisition using smartphones. In IEEE Computer Society Computer Vision and Pattern Recognition Workshops (CVPRW) June 2012 Pages 29–34. IEEE.

8. S. Molkenstruck, S. Winkelbach and F. M. Wah. 3D Body Scanning in a Mirror Cabinet DAGM 2008, LNCS 5096, pp. 284–293.

9. I. Reshetouski and I. Ihrke. Mirrors in Computer Graphics, Computer Vision and Time-of-Flight Imaging. In Time-of-Flight and Depth Imaging. Sensors, Algorithms, and Applications. Lecture Notes in Computer Science Vol. 8200, 2013, pp. 77–10.

10. T. Pribanic, S. Mrvos, J. Salvi. Efficient multiple phase shift patterns for dense 3D acquisition in structured light scanning Image and Vision Computing 28 (2010) 1255–1266.

11. Z. Zhang, A Flexible New Technique for Camera Calibration IEEE Transactions PAMI, Vol. 22 (11), 2000, pp. 1330–1334.

12. C. Salvi, D. Matabosch, F. Fofi, Forest, A review of recent range image registration methods with accuracy evaluation, Image and Vision Computing 25 (2007) 578–596.

13. S. Rusinkiewicz, M. Levoy, Efficient variants of the ICP algorithm, in: 3rd International Conference on 3-D Digital Imaging and Modeling, 2011, pp. 145–152.

14. Shirmohammadi, B., Taylor, C.J., 2011. Self-localizing smart camera networks. ACM Transactions on Embedded Computing Systems, Vol. 8, pp. 1–26.

15. T. Pribanić, Y. Diez, S. Fernandez and J. Salvi. An Efficient Method for Surface Registration. VISIGRAPP 2013, February 21–24. 2013, Barcelona Spain, 114–118.

16. Samsung Galaxy Beam2 Accessed: June, 2015. http://www.gsmarena.com/samsung_galaxy_beam2-6328.php.

17. https://www.google.com/atap/project-tango/. Accessed: June, 2015.

18. http://gizmodo.com/google-tango-an-experimental-android-phone-with-kinect-1527065386. Accessed: June, 2015.

Development of an Electronic Patch for Falls Detection and Elderly Tracking

Bouchta Hajjine, Christophe Escriba, Eric Campo,
Sabeha Fettouma Zedek, Pascal Acco, Georges Soto-Romero,
Anne Hemeryck, and Jean-Yves Fourniols

Abstract

Considering the population aging all over the world, that leads to an increasing rate of Alzheimer's troubles, patients suffer from problems, like restless sleep for instance, which causes recurring falls. Such falls can be seen as a disease marker and thus could help diagnosis. This new field of research is known as Human Health Monitoring. The developed systems must be able to provide in real time information about weakness and vulnerability of elderly people. This paper presents the design of an electronic patch dedicated to the monitoring of elderly suffering from Alzheimer disease. This device ensures falls detection and geolocation in the case of fugues via GPS with the integration of wireless charging function. Different antennas were simulated and fabricated simultaneously with the PCB patch to reduce the total cost and present quite good simulated and measured performances.

B. Hajjine (✉) · C. Escriba · E. Campo · S. F. Zedek
P. Acco · G. Soto-Romero · A. Hemeryck · J.-Y. Fourniols
LAAS, CNRS, 7 Avenue du Colonel Roche, 31400 Toulouse, France
e-mail: bhajjine@laas.fr

C. Escriba
e-mail: cescriba@laas.fr

E. Campo
e-mail: campo@laas.fr

S. F. Zedek
e-mail: sfzedek@laas.fr

P. Acco
e-mail: pacco@laas.fr

G. Soto-Romero
e-mail: gsotorom@laas.fr

A. Hemeryck
e-mail: anne.hemeryck@laas.fr

J.-Y. Fourniols
e-mail: fourniols@laas.fr

B. Hajjine · C. Escriba · E. Campo · P. Acco · J.-Y. Fourniols
INSA, Univ de Toulouse, UT2J, 31100 Toulouse, France

G. Soto-Romero
ISIFC—Génie Biomédical—Université de Franche Comté, 23 Rue Alain Savary, 25000 Besançon, France

1 Introduction

AGING of the French population becomes a deeply rooted problem due to the baby boom generation who currently reaches the retirement age: over than 24% persons are older than 60 years in 2015 [1]. This growing class involves health problems, frailty, and dependence. Among the solutions proposed to alleviate this issue, we can cite the use of health monitoring systems either as a network of sensors implemented in residences or wearable devices like electronic patches that are designed to be glued directly on the skin [2–5].

Innovations in HHM (Human Health Monitoring) know an increasing growth and lead to development of new technologies helping to improve existing medical organization practices.

Elders are equipped with multiple sensors which enable the acquisition of different vital signs such as ECG, temperature, and daily activities in addition to the detection of anomalies requiring immediate interventions like fall or heart attack. To reach all these functionalities, various criteria must met to ensure a good implementation of the monitoring operation: accuracy of sensors, performances of communication modules, biocompatibility, integration, and reliability of used algorithms. This paper presents the design of a patch for elderly tracking and falls detection as a part of a research project named SACHA (Search And Computerize Human Acts). We will start with the description of the device and its various features then we will go through different results obtained during the tests, and finally show the interest of this approach.

Fig. 1 Representation of the operating principle of SACHA patch
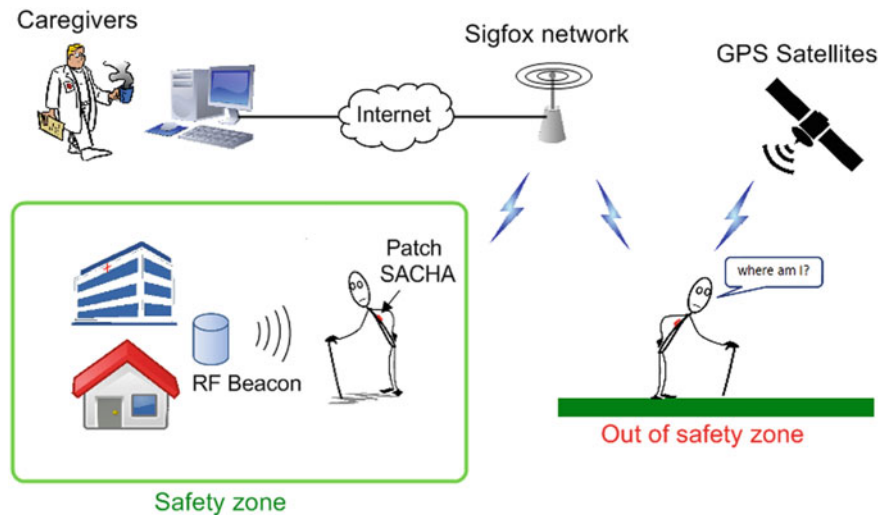
2 Features of Sacha Patch

The SACHA patch is designed to be worn on the back between the shoulder blades. It aims at the monitoring of elderly suffering from Alzheimer and who are residents in specialized institutions. According to the evolution of this disease these old people may be lost and forget the way back. The problem of falls threatens also the lives of elderly and can be considered as a significant cause of mortality [6].

The SACHA patch has two functionalities: the first one is dedicated to the falls detection to ensure an immediate intervention if an accident occurs and the second one is the GPS geolocation in the case of fugues.

Falls detection is guaranteed by the use of a 3D accelerometer that allows to recover the acceleration measurements to compare with thresholds and identify anomalies. The geolocation function is enabled when the followed person exceeds a safety zone determined by the communication between the patch and an RF beacon. This link permits to activate the GPS module and triggers the tracking operation (Fig. 1).

The SACHA patch is intended to be sandwiched by two medical dressings to avoid any biocompatibility problem, the package was also 3D printed to provide waterproof characteristic (plastic component). It is equipped with a thin battery (30 mAh) to ensure a reliable operation during 13 h in the case of fugues and GPS activation. Otherwise the normal working period is 3 days with a charging time of 4–5 h.

Figure 2 is a picture of the SACHA patch highlighting the most efficient positioning of the patch for reducing the risk of a lifting.
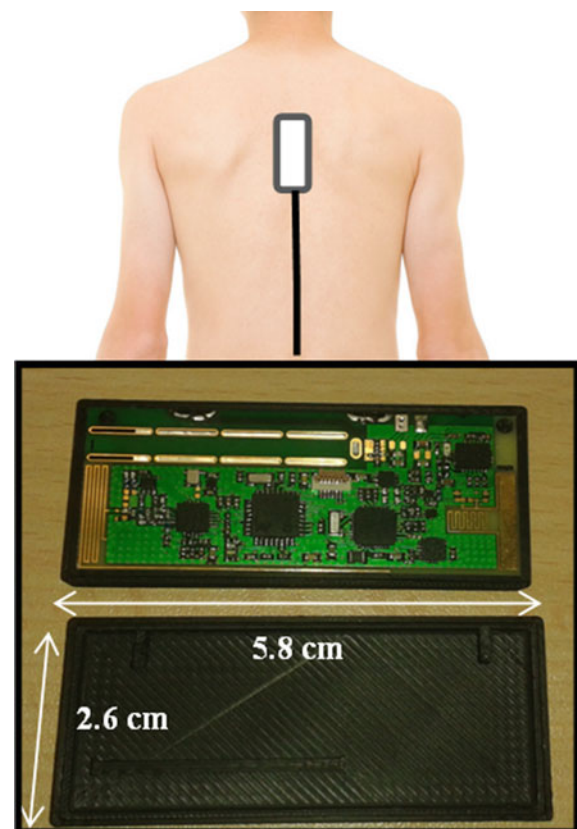

Fig. 2 Picture of the developed patch with its packaging

3 Antennas for Geolocation and Data Transfer

The SACHA Patch includes 2 antennas: the first one has an operational frequency of 868 MHz used to communicate with Sigfox low consumption network for data transfer. The second is a GPS antenna (L1 band: 1575.42 MHz) for tracking and geolocation. Both antennas are PIFA (Printed Inverted F Antennas) and were simulated and validated using ADS Software [7].

Figure 3 represents the simulation of our antennas modeled by ADS that permits to take into account the coupling between the two PIFAs.

With the aim to reduce the size of the SACHA patch, the two PIFAs were meandered many times. This technique guarantees a minimization of the total area occupied by the antennas. Simulated and measured reflection coefficients and bandwidths are given in Table 1.

The simulated gains of the ISM and GPS antennas are −6.9 dBi and 0.6 dBi respectively.

The variation of the reflection coefficient in function of the frequency is plotted on Figs. 4 and 5. We can see that the measurements meet the simulated results and that both antennas provide good performances.

Both antennas were tested and validated on real operation conditions, i.e. worn on the human body: the GPS module fix and the communication with Sigfox stations. One of these tests consists in verifying the patch ability to transmit an alarm in different falls positions especially when it is placed under the human body like in the case of a fall on the back. This test enables also to validate the operation of the patch with the presence of the ground effect due the reduction of the distance that separates the antennas and the ground after the fall. The operation principle is to send 10 frames emitted from 4 different body postures and then compare the total number of the received frames. Results tests are given in Fig. 6.

4 Wireless Charging

As its name indicates, wireless power transfer consists in transmitting electrical energy from one point to another without using any wires or any other conductor. Recently, this technology has gained much more attention and becomes a main research axis in different studies to develop wireless batteries chargers for various domains including electric vehicles [8, 9], implanted medical systems [10, 11], and handheld electronic devices. The problem of huge amount of incompatible and bulky chargers can be solved by using a single and universal charging pad. This interoperability was the main aim behind the creation of some
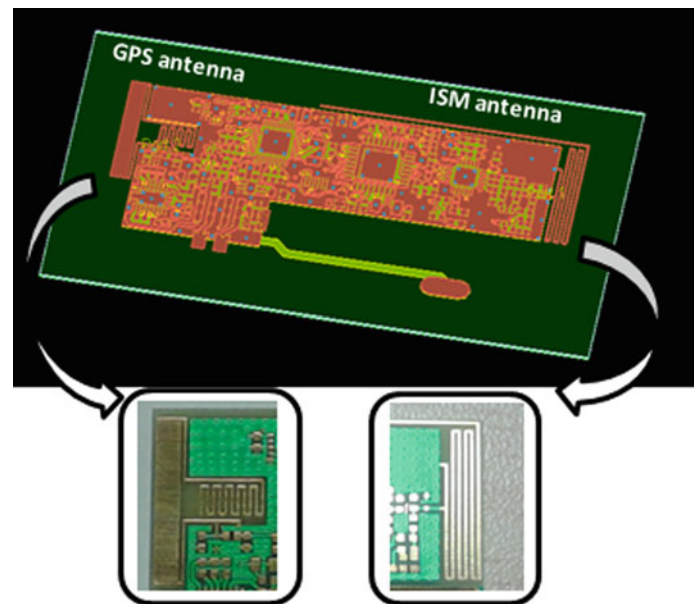

Fig. 3 PIFAs simulation with ADS

Table 1 Reflection coefficients and bandwidths of the designed PIFAs

	ISM antenna		GPS antenna	
	S11 @ 868 MHz (dB)	BW (MHz)	S22 @ 1575.42 MHz (dB)	BW (MHz)
Simulated	−38	7.3	−36.8	25
Measured	−16.4	16.2	−19.8	39

Fig. 4 Simulated and measured S_{11} of the ISM 868 MHz antenna

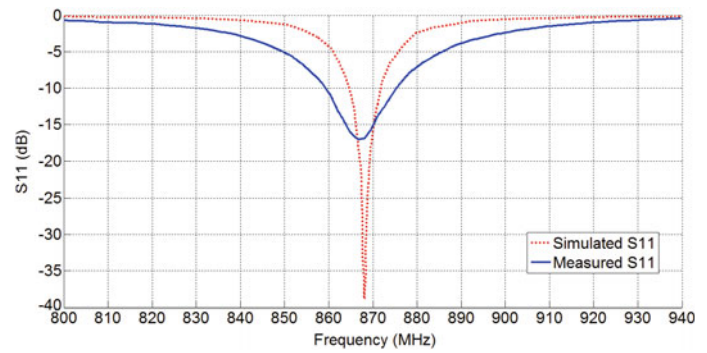**Fig. 5** Simulated and measured S_{22} of the GPS antenna
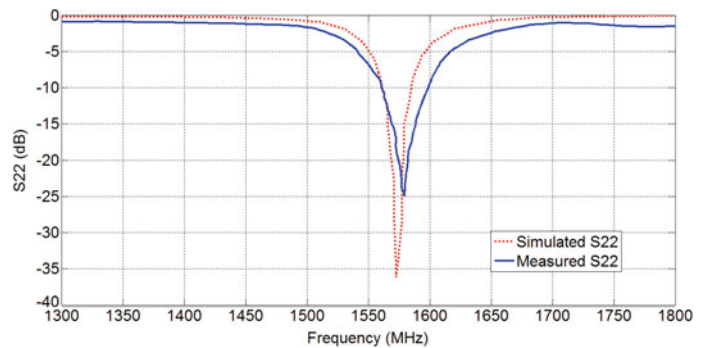
Posture	Total received frames
On the stomach	9/10
On the back	9/10
On the left side	8/10
On the right side	9/10

Fig. 6 Tests of the communication Patch-Sigfox network for different body postures

organizations which work on the development of different protocols to provide guidelines, requirements and communication techniques for the contactless battery charging like the Wireless Power Consortium (WPC). This has been developed under the standard named "Qi" and based on inductive power transfer [12]. The charging system is composed of two main parts: a transmitter and a receiver as in Fig. 7. The power transfer takes place using magnetic induction when the transmitting and receiving coils are closer from each other.

The frequency used by Qi standard for the lower power chargers (up to 5 W) is located between 110 and 205 kHz. This protocol provides a one-direction communication from the receiver to the transmitter enabling to control the battery power need and the state of charge.

For SACHA project, the receiving coils available in the market for wireless chargers development are voluminous compared to the patch dimensions. This is why, we have chosen to design a smaller coils based on copper wires.

Figure 8 is an image of the characterization process of the different tested coils using the impedance analyzer Agilent 4294 A that provides inductance, resistance and quality factor values.

Several copper wires were tested with different lengths and diameters to form two parallel coils to reduce the total resistance and get a better quality factor. The final coil has an inductance of 10.48 μH and a total resistance of 338 mΩ. It is designed to be placed under the battery with the adding of a ferrite layer to improve the energy transfer and solve the disturbances problems due to magnetic field lines when the coil is directly glued to the battery (Fig. 9).

Fig. 7 Qi wireless charging of the SACHA patch

Fig. 8 Characterization of a receiver coil for wireless charging
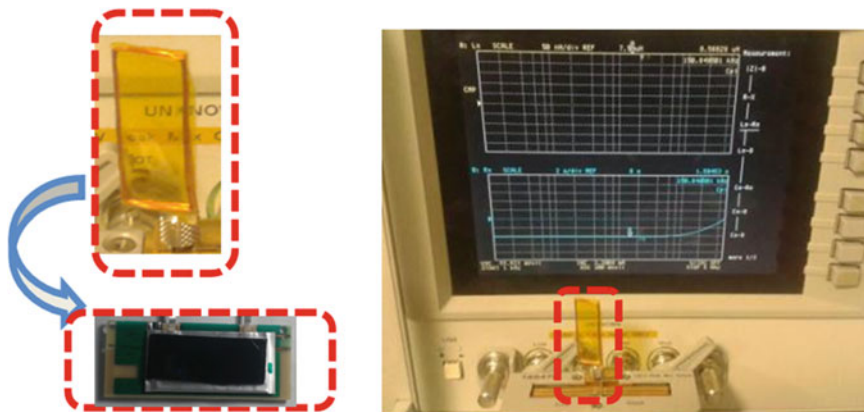

Fig. 9 Different layers stacking of the SACHA patch

For our project, we have chosen the Qi receiver-charger BQ51050b [13] from Texas Instrument that allows to get a charging current with a ripple of 10% as represented in the test results. Figure 10 represents the measured charging current that validates the wireless power transfer of the proposed patch.

Fig. 10 Patch charging current
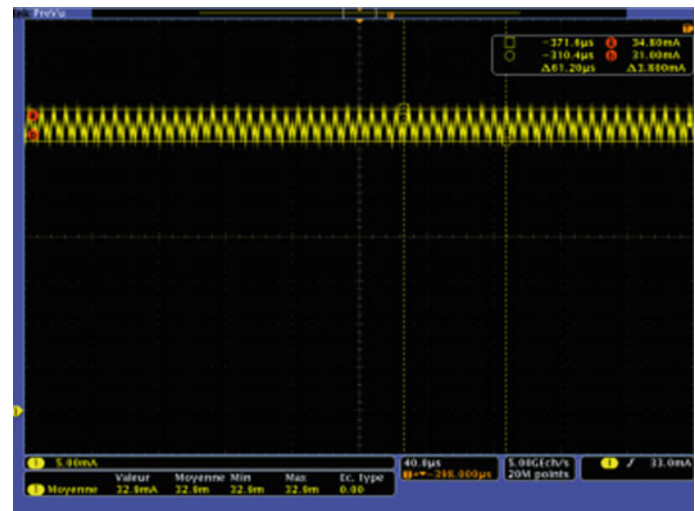
5 Conclusion and Outlook

Considering the exponential growth of the Human Health Monitoring needs and those new challenges especially for the elders, we focused our research on a tracking device which helps the relatives of the patient and hospital staff. We focused in this paper on one of the major challenge of our society toward the well being of Elderly.

The designed and integrated tracking patch for Alzheimer patient is a powerful tool to ensure their safety. In addition to the geolocation, this device provides the function of falls detection, waterproof characteristic and wireless battery charging in the aim to ensure an easy and daily use. The measurement results validate the simulated performances of the PIFAs designed to be manufactured with the PCB patch to reduce the total cost. Tests in real conditions with volunteers from a specialized institution will be carried out soon. This phase will be essential to certify the monitoring process and judge on the patch functionalities.

References

1. http://www.Esa.un.org, World Population Prospects, the 2012 Revision, 2015. [Online]. Available: http://esa.un.org/unpd/wpp/unpp/panel_indicators.htm. [Accessed: 18- Jul- 2015].
2. T. Suzuki, H. Tanaka, S. Minami, H. Yamada, and T. Miyata, Wearable wireless vital monitoring technology for smart health care, 7th Int. Symp. Medical Inform. Commun. Technology (ISMICT), 6–8 March 2013, pp. 1–4.
3. E. Hyun, S. Noh, C. Yoon, and H. C. Kim, Patch type integrated sensor system for measuring electrical and mechanical cardiac activities, IEEE Sensors Applicat. Symp. (SAS), 18–20 Feb. 2014, pp. 94–96.
4. M. Li, and Y. T. Kim, Development of patch-type sensor module for wireless monitoring of heart rate and movement index, Sensors and Actuators A: Physical, vol. 173, Issue 1, Jan. 2012, pp. 277–283.
5. Securafone.com, 'SecuraFone', 2015. [Online]. Available: https://www.securafone.com/subpages/health.php. [Accessed: 18-Jul-2015].
6. Chutes—maisons-de-retraite.fr, Maisons-de-retraite.fr, 2015. [Online]. Available: http://www.maisons-de-retraite.fr/La-sante-des-seniors/Chutes. [Accessed: 18-Jul-2015].
7. http://www.keysight.com, Advanced Design System. [online]. Available: http://www.keysight.com/en/pc-1297113/advanced-design-system-ads?cc=FR&lc=fre. [Accessed: 18- Jul- 2015].
8. S. A. Sabki, and N. M. L. Tan, Wireless power transfer for electric vehicle, IEEE 8th Int. Power Eng. and Optimization Conf. (PEOCO), 24–25 Mar. 2014, pp. 41–46.
9. F. Musavi, and W. Eberle, Overview of wireless power transfer technologies for electric vehicle battery charging, Power Electronics, IET, vol.7, no.1, Jan. 2014, pp. 60–66.
10. H. Jiang, S. Liang, J. Zhang, S. Liou, and H. Shahnasser, Design and optimization of printed spiral coils in wireless power transfer for biomedical implants, 4th Int. Conf. on Biomedical Eng. and Informatics (BMEI), vol. 2, 15–17 Oct. 2011, pp. 1064–1067.
11. S. Hached, A. Trigui, I. El Khalloufi, M. Sawan, O. Loutochin, and J. Corcos, A bluetooth-based Low-Energy Qi-compliant battery charger for implan medical devices, IEEE Int. Symp. On Bioelectronics and Bioinformatics (ISBB), 11–14 Apr. 2014, pp. 1–4.
12. 'wireless Power Consortium'. [online]. Available: http://www.wirelesspowerconsortium.com/. [Accessed: 18-Jul-2015].
13. http://www.Ti.com, 'BQ51050B| Wireless Power Solutions| Battery Management Products|Description & parametrics, 2015. [Online]. Available: http://www.ti.com/product/bq51050b. [Accessed: 18-Jul-2015].

Spatial Interactions of Electrically Evoked Potentials in Visual Cortex Induced by Multi-retinal Electrical Stimulation in Rats

Hui Xie, Yi Wang, and Leanne Lai-Hang Chan

Abstract

Retinal prostheses are designed to electrically stimulate retinal neurons to generate artificial vision in patients with degenerative diseases such as retinitis pigmentosa (RP) or age-related macular degeneration (AMD). Considering hundreds of microelectrodes may be applied in the future retinal prosthesis to provide enough spatial information for precise perception, it is crucial to investigate the spatial properties of the visual cortex in response to retinal electric stimulation via in vivo studies, especially in multi-stimulating manner by adjacent electrodes. In this study, we use retinal multi-stimulating electrodes to stimulate retinal ganglion cells (RGCs) and record electrically evoked potentials (EEPs) in contralateral visual cortex by a 32-channel Utah array. The threshold of eliciting current for EEPs was determined with 20% of the maximum response in visual cortex. The spatial map with 32 grids for single retinal stimulation was obtained firstly, which showed the different spatial distribution to different retinal stimulation. Then the combination of two stimulation from two adjacent retinal stimulating electrode was applied to examine the spatial responses of visual cortex.

1 Introduction

Retinitis pigmentosa (RP) or age-related macular degeneration (AMD) are the two major degenerative diseases which are involved with the degeneration of rod cells and cone cells, ultimately resulting in the loss of peripheral vision or total blindness without effective pharmacological treatments due to the regeneration disabilities of rods and cones [1–3]. However, recent findings revealed that the survival rates of macula core layer and ganglion cell layer in the retina can reach 80% and 30% in patients with RP [4, 5], and that of inner retinal cells of the retina in AMD patients is up to 90% [6]. The survival of retinal ganglion cells (RGCs) provide the possibility for restoration of visual function considering the survival inner nuclear layer and RGCs could be activated to generate nerve impulses by electrical discharge from an extracellular electrode in close proximity to those retinal cells [7, 8]. Thus, to put forward a visual prosthesis via stimulating retinal neurons holds great promises for the alternative treatment. Investigations have been gone through for decades and better understanding for retinal visual prosthesis via animal in vitro [9, 10] and in vivo experiments [11–13]. Several retinal devices have been developed with successful clinical trials [8, 14–17]. However, to understand and develop a precise stimulation strategy on retina, animal experimentation will be needed to provide more insights. A single stimulating electrode with different sizes which have recorded responses of retinal cells had been applied in most previous animal studies, which provided the basic understandings on the threshold values to activate the retinal neurons [18–20]. Only a few studies have examined the responses of RGCs to multiple electrode stimulation, which are limited within in vitro studies [21, 22]. Since the future retinal prosthesis may apply hundreds of microelectrodes to stimulate the retina to provide detailed spatial information for recognizing objects and text, it is crucial to investigate the spatial response properties of the visual cortex in response to retinal electric stimulation in in vivo studies, especially via multi-stimulating manner by adjacent electrodes, which will provide understanding for later optimal design of stimulating strategies and parameters of retinal visual prosthesis.

H. Xie · Y. Wang · L. L.-H. Chan (✉)
Department of Electronic Engineering, City University of Hong Kong, Hong Kong SAR, China
e-mail: leanne.chan@cityu.edu.hk

2 Materials and Methods

2.1 Animals

Long-Evans (LE) rats were used in all experiments. All animals were obtained from The Laboratory Animal Services Centre of The Chinese University of Hong Kong and housed with a 12 h light/dark cycle and with food and water available ad libitum. All experimental procedures were approved by the Animal Subjects Ethics Sub-Committees of City University of Hong Kong.

2.2 Retinal Preparation for Electrical Stimulation

Rats were anesthetized using combination of Ketamine (70 mg/kg, Alfasan, Holland) and Xylazine 2% by 2:1 (7 mg/kg, i.p.) and maintained with an anaesthesia machine (SurgiVet, Smiths Medical PM, Inc., USA) by isoflurane throughout stereotaxic surgery and later neuronal recordings. The body temperature was monitored and kept at approximately 38 °C by a heat pad (Model#TP702; Gaymar industries, Inc., NY, U.S.A).

Two drops of tropicamide (Mydrin-P; Santen Pharmaceutical Co. Ltd., Osaka, Japan) were used to dilate the pupil and eye gel (Lubrithal, Dechra Veterinary Products A/S, Mekuvej, Denmark) was applied regularly throughout the experiment to maintain the moisture and clarity of the stimulated eye. A 2 × 2 cm rubber membrane with a small hole in the middle was used to protrude the stimulated eye ball. After that, a needle penetrated the upper sclera near the margin of cornea for the convenience of later penetration of the stimulating electrodes (Fig. 1a). Then the stimulating electrodes penetrated through that hole made by previous needle, close to the ventral retina near the macular with the help of an articulated holder (Noga, Noga Engineering Ltd., Israel). The tip of the electrodes that we used for electrical stimulation contains cluster electrodes (2 × 2, diameter for each electrode: 50 μm) connecting with four wire in different color, namely yellow, black, red, and blue (Fig. 1b). The impedance of the stimulating electrodes was monitored (Reference 600, Gamry Instruments, Warminster, USA) throughout the insertion progress to ensure a close proximity from the electrode tip to the retina [23].

2.3 Surgical Procedures for Recording

Briefly, rats were mounted in a stereotaxic device, and a midline incision was made in the scalp. A craniotomy was performed at the occipital lobe ($\sim$2.5 to 5.5 mm posterior and $\sim$4.5 to $\sim$7.5 mm ventral to bregma) to access the visual cortex contralateral to the stimulated eye with the skull piece and dura carefully removed in this opening.

A 32-channel Utah array (Omnetics array: length of electrode: 1 mm, arrangement: 4 × 8, size of array: 2.8 mm × 1.2 mm; Blackrock Microsystems, Salt Lake
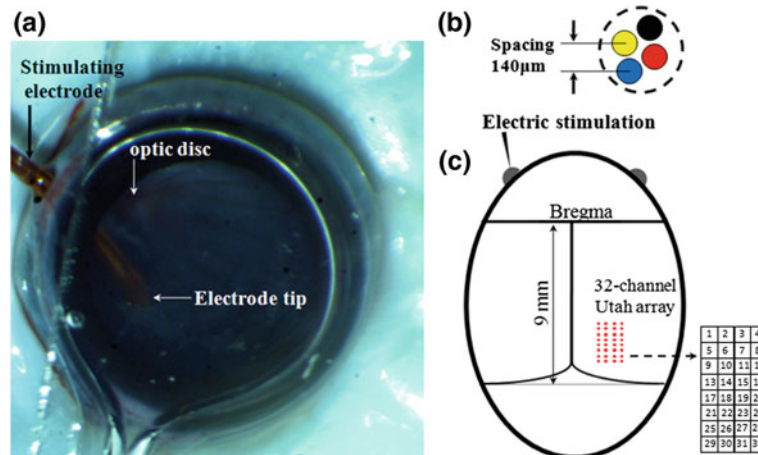
Fig. 1 **a** Captured image of stimulation electrode implantation under microscope. The stimulating electrodes (black arrow), penerates through the upper sclera near the cornea. The upper white arrow points the optic disc where a number of blood vessels converged in radial pattern. The lower white arrow is the position where the stimulating electrodes tip reached the retina surface. The distance between the stimulating electrodes tip and retina is monitored and determined by the impedance of the stimulating electrodes during the penetration progress [23]. **b** Cross section of the retinal stimulating electrodes, which contains cluster electrodes (2 × 2, yellow, black, red and blue) with electrodes spacing as 140 μm. The dotted cycle is the outer layer of the cluster electrodes. **c** Placement of the recording electrode array. A 32-channel Utah array (red dot array) was placed in the exposed visual cortex at the occipital lobe ($\sim$2.5 to 5.5 mm posterior and $\sim$4.5 to $\sim$7.5 mm ventral to bregma) contralateral to the stimulated eye. The arrangement of the Utah array was illustrated by the 4 × 8 grids with numbers in the right bottom corner (Color figure online)

City, USA) was inserted 1.0 mm depth quickly in the exposed visual cortex using an inserter (Blackrock Microsystems, Salt Lake City, USA) for in vivo electro-physiological recording to retinal electric stimuli (Fig. 1c). At least 15 min recovery was allowed before the retinal electric stimulation.

2.4   Electrical Stimulation

Charge-balanced, cathodic first, biphasic currents (20–200 µA, 1 ms/phase) were applied to the epiretinal surface. In all experiments, the platinum-iridium stimulating cluster electrodes (2×2) were positioned in the ventral sector of the retina. The current pulses were generated by a stimulus generator (STG 2004, Multichannel Systems MCS GmBH, Germany). The position of the return electrode was above the eyelid. The impedance of the electrode was measured by a potentiostat (Reference 600, Gamry Instruments, Warminster, PA) using a 10 mV (r.m.s.) AC sinusoid signal at 100 kHz. The stimulation began from single electrode (yellow, black, red, or blue), followed by the combination of two of those electrodes (red + blue, red + black, red + yellow, yellow + black) stimulating simultaneously.

2.5   Data Process and Analysis

Electrically evoked potentials (EEPs) were band-passed (0.3–500 Hz) and amplified (A-M system, Inc. Model 3600,

UK) using micro1401 data acquisition system (version 7.1, Cambridge Electronic Design Limited, UK). EEPs were distinguished by Spike-2 and analyzed in Matlab (R2013a, Mathworks, Natick, MA, USA) software. To determine the spatial distribution of EEP responses, we first obtained the strength-response curves (Figs. 3 and 4), which were later represented by color-coded maps to compare the spatial responses from different electrodes.

3   Results

3.1   Thresholds for Electrically Evoked Potentials

Firstly, electrically evoked potentials (EEPs) were recorded from the contralateral visual cortex using a 32-channel Utah array after retinal electrical stimulation to determine the threshold current. EEPs were obtained for each current amplitude. Figure. 2a illustrates a series of recorded EEPs from one channel as the stimulating current intensity was increased from 20–200 µA. The amplitude of each EEP was measured. Peak-to-peak voltage (N1-P2) was extracted for each current amplitude and the strength-response curve was plotted. A sigmoid curve was obtained to fit each input-output function (Fig. 2b). The amplitude of EEP was normalized with respect to the largest amplitude of each current to reduce the variations among experimental subjects. The responses saturated after the retinal stimulation current reached 120 µA . In this study, we chose the current
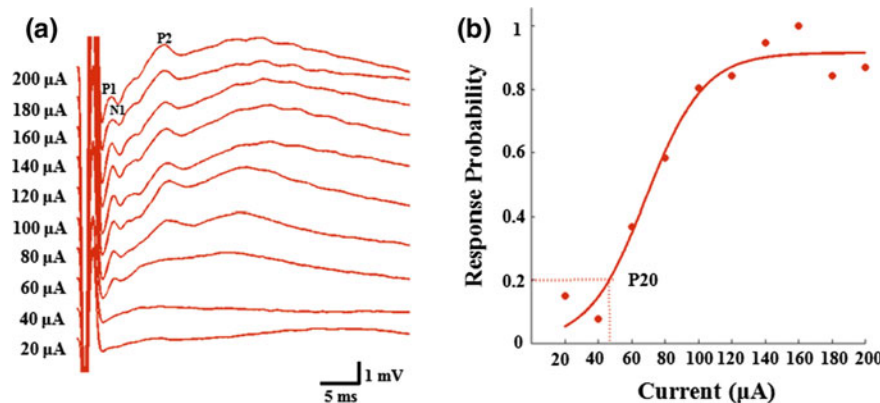
Fig. 2 Determination of stimulus threshold. **a** A series of stimulus pulses of 10 current amplitudes (20–200 µA) with 10 trials for each current level was applied to the retina after positioning the stimulating cluster electrodes on the retina surface. All data came from the same recording channel of one rat. The distance between the two peaks (N1-P2) represents the peak-to-peak voltage, which was measured for

each current amplitude to obtain the strength-response curve. **b** A sigmoid curve was fitted to each input-output function, from which current threshold was determined. In this study, threshold (red dotted line) was defined as the current required a potential equal to 20% of the maximum response (Color figure online)

required a potential equal to 20% of the maximum response as the threshold for EEP.

3.2 Spatial Correspondence of EEP Responses to Single Retinal Stimulation

The spatial activation of EEP responses to single retinal stimulation was examined in this study. As shown in Fig. 3, the corresponding area in the visual cortex for the blue stimulating electrode is the Utah array site 27, with the threshold of EEP for this channel is about 70 μA. The corresponding location to the black stimulating electrode is the site 18 and of higher threshold (90 μA). The corresponding site to red and yellow stimulating electrode are also different with that of blue and black electrode, locating in sites 32 and 17, respectively. Interestingly, their threshold to induce EEPs are about 42 and 43 μA, which are lower than those of blue and black. It may suggest a closer proximity between blue/yellow electrodes and retina than that of blue/black ones. Therefore, the spatial distribution to different single electrode are distinct and independent, together with the different threshold for EEPs.

3.3 Spatial Distribution of EEP Responses to Two Adjacent Retinal Electric Stimulation

Spatial discrimination of EEPs to simultaneous stimulation from two adjacent sites in retina is important to optimize the design of the distance between electrodes of retinal visual prosthesis. Therefore, we examined the spatial responses induced by a series of stimuli from two adjacent (140 μm apart) retinal stimulating electrodes and obtained the corresponding spatial map (Fig. 4). We may notice that, with the increase of retinal stimulation, the spatial responses also increased, with different increment ratio, until the spatial responses merged together. Different spatial mapping of responses in visual cortex were elicited by pair combinations of the retinal stimulating electrodes.

4 Discussion and Conclusion

Visual prosthesis devices have been implanted in various locations, including epiretinal, subretinal, and suprachoroidal space, and stimulation via the epiretinal electrodes has proven to be a safe and efficient method for visual perception in
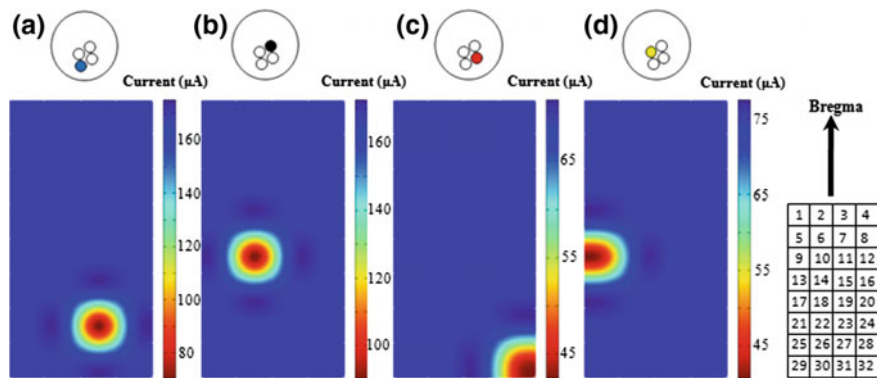
Fig. 3 Spatial distribution of responses in visual cortex induced by single-channel retinal stimulation. The color dot in the upper part of this figure represents the electric stimulation from different retinal stimulating electrode, while the lower part is the spatial map of the contralateral visual cortex to the corresponding stimulation. The spatial map was divided into 32 grids and illustrated by the right most rectangle with numbers. **a**–**d** showed the spatial interaction between responses recorded in visual cortex elicited by blue, black, red and yellow retinal electrode. The approximate corresponding area for blue, black, red and yellow stimulating electrode are site 27, 18, 32 and 17, respectively. Note that their threshold to induce EEPs are different (blue channel: 70 μA, black channel: 90 μA, red channel: 42 μA, yellow channel: 43 μA) (Color figure online)
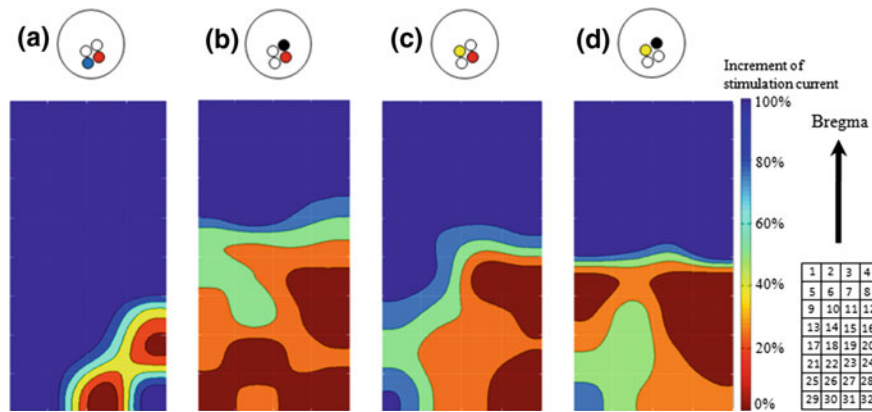
Fig. 4 Spatial distribution of EEP responses to two adjacent retinal electric stimulation. The retinal stimulating electrodes for simultaneous stimulation are indicated by the color dots in the upper row. The lower part with blue background is the spatial map divided into 32 grids to corresponding responses, which was illustrated by the right most rectangle containing grids with number. **a–d** The spatial interaction of responses recorded in visual cortex and the retinal co-stimulating from two electrodes. To better understand the spatial interaction and reduce variations among electrodes, we use percentage of increment as the color index. Dark brown in all four maps are the area induced by the initial retinal stimulation current. In most of the spatial maps, the responses to co-stimulating currents from two retinal electrodes merged when the current increased by above 10% (indicated by orange in the color map) (Color figure online)

clinical trials [8]. Factors appear to limit the spatial resolution of the visual prosthesis include the size of the stimulation electrodes and the capability to generate patterned perception. It is critical to investigate the spatial properties of the visual cortex in response to retinal electric stimulation. In our study, we first used single retinal stimulating electrode to obtain the spatial maps for each retinal electrode, and successfully showed that each electrode could uniquely elicit their own spatial response. Later, we carried out the co-stimulation simultaneously from paired retinal electrodes and acquired the corresponding spatial distribution in the visual cortex. The results showed that the responses which were induced by the two retinal electrodes merged when the initial stimulation current increased above 10%. The merging of response in the visual cortex induced by the paired retinal stimulating electrodes, with the distance of 140 μm apart, may suggest the merged response are considered to be elicited by a single stimulating area, rather than stimulating two distinct areas in retina, which provides a rudimentary understanding of the patterned perception for epiretinal prostheses.

Our in vivo results of interaction between spatial response of visual cortex and retinal stimulation provide a preliminary and an insightful clue for understanding the parameters of epiretinal stimulation, such as electrodes spacing and stimulating current levels. Further experiments are planned to use retinal microelectrode-array with different electrode spacings to investigate the spatial interactions in rodents' visual cortex.

References

1. Hartong, D.T., E.L. Berson, and T.P. Dryja, *Retinitis pigmentosa.* Lancet, 2006. **368**(9549): p. 1795–1809.
2. Lim, L.S., et al., *Age-related macular degeneration.* Lancet, 2012. **379**(9827): p. 1728–1738.
3. Tochitsky, I. and R.H. Kramer, *Optopharmacological tools for restoring visual function in degenerative retinal diseases.* Curr Opin Neurobiol, 2015. **34C**: p. 74–78.
4. Santos, A., et al., *Preservation of the inner retina in retinitis pigmentosa. A morphometric analysis.* Arch Ophthalmol, 1997. **115**(4): p. 511–515.
5. Humayun, M.S., et al., *Morphometric analysis of the extramacular retina from postmortem eyes with retinitis pigmentosa.* Invest Ophthalmol Vis Sci, 1999. **40**(1): p. 143–148.
6. Kim, S.Y., et al., *Morphometric analysis of the macula in eyes with disciform age-related macular degeneration.* Retina, 2002. **22**(4): p. 471–477.
7. Weiland, J.D., W. Liu, and M.S. Humayun, *Retinal prosthesis.* Annu Rev Biomed Eng, 2005. p:**7**. 361–401.
8. Weiland, J.D., A.K. Cho, and M.S. Humayun, *Retinal prostheses: current clinical results and future needs.* Ophthalmology, 2011. **118**(11): p. 2227–2237.
9. Ryu, S.B., et al., *Temporal response properties of retinal ganglion cells in rd1 mice evoked by amplitude-modulated electrical pulse trains.* Invest Ophthalmol Vis Sci, 2010. **51**(12): p. 6762–6769.
10. Tsai, D., et al., *Direct activation and temporal response properties of rabbit retinal ganglion cells following subretinal stimulation.* J Neurophysiol, 2009. **102**(5): p. 2982–2993.
11. Chan, L.L., et al., *Both electrical stimulation thresholds and SMI-32-immunoreactive retinal ganglion cell density correlate with age in S334ter line 3 rat retina.* J Neurophysiol, 2011. **105**(6): p. 2687–2697.

12. Elfar, S.D., et al., *A cortical (V1) neurophysiological recording model for assessing the efficacy of retinal visual prostheses.* J Neurosci Methods, 2009. **180**(2): p. 195–207.

13. Sun, J., et al., *Spatiotemporal properties of multipeaked electrically evoked potentials elicited by penetrative optic nerve stimulation in rabbits.* Invest Ophthalmol Vis Sci, 2010. **52**(1): p. 146–154.

14. Zrenner, E., et al., *Subretinal electronic chips allow blind patients to read letters and combine them to words.* Proc Biol Sci, 2010. **278**(1711): p. 1489–1497.

15. Rizzo, J.F., 3rd, et al., *Perceptual efficacy of electrical stimulation of human retina with a microelectrode array during short-term surgical trials.* Invest Ophthalmol Vis Sci, 2003. **44**(12): p. 5362–5369.

16. Humayun, M.S., et al., *Visual perception in a blind subject with a chronic microelectronic retinal prosthesis.* Vision Res, 2003. **43**(24): p. 2573–2581.

17. Perez Fornos, A., et al., *Temporal properties of visual perception on electrical stimulation of the retina.* Invest Ophthalmol Vis Sci, 2012. **53**(6): p. 2720–2731.

18. Fried, S.I., H.A. Hsueh, and F.S. Werblin, *A method for generating precise temporal patterns of retinal spiking using prosthetic stimulation.* J Neurophysiol, 2006. **95**(2): p. 970–978.

19. Sekirnjak, C., et al., *High-resolution electrical stimulation of primate retina for epiretinal implant design.* J Neurosci, 2008. **28**(17): p. 4446–4456.

20. Barry, M.P. and G. Dagnelie, *Use of the Argus II retinal prosthesis to improve visual guidance of fine hand movements.* Invest Ophthalmol Vis Sci, 2012. **53**(9): p. 5095–5101.

21. Sekirnjak, C., et al., *Electrical stimulation of mammalian retinal ganglion cells with multielectrode arrays.* J Neurophysiol, 2006. **95**(6): p. 3311–3327.

22. Stett, A., A. Mai, and T. Herrmann, *Retinal charge sensitivity and spatial discrimination obtainable by subretinal implants: key lessons learned from isolated chicken retina.* J Neural Eng, 2007. **4**(1): p. S7–S16.

23. Ray, A., et al., *Impedance as a method to sense proximity at the electrode-retina interface.* IEEE Trans Neural Syst Rehabil Eng, 2011. **19**(6): p. 696–699.

An Approach for Body Motion Registration Using Flexible Piezoelectret Sensors

Rui Xu, Qifang Zhuo, Xiangxin Li, Haoshi Zhang, Yanhu Cai, Lan Tian, Xiaoqing Zhang, Peng Fang, and Guanglin Li

Abstract

Body motion registration can be applied to control computer interfaces or real devices, and force myography (FMG) is a promising modality to register real-time body motions. In this work, an approach for FMG recording was developed by using flexible piezoelectret sensors, and different lower-limb motions of three able-bodied subjects were captured. The experimental results demonstrated that the piezoelectret sensors were a suitable approach for FMG recording, and the five-channel data were possible to register the motions of leg raising, knee flexion, and knee extension. An average motion classification accuracy of 92.1% was achieved, which would be useful for the FMG-based device control in future work.

1 Introduction

BODY motion registration can provide some useful information that is related to muscle activities, which may be applied in diagnostics, rehabilitations, and sports [1]. Accelerometers [2] and data-gloves [3] have been developed for body motion registration, but they are sometimes restricted due to the limited acquirable information or the inconvenience in wearing during body motions. Surface electromyography (sEMG) is also a tool to register body motions, which can directly convey motor commands [4]. Several sEMG-based systems have been developed to control human-machine interfaces [5], to monitor rehabilitation procedures for patients [6], and to operate prostheses for amputees [7]. However, some shortcomings may prevent the further applications of sEMG [8], e.g. an exact placement of sEMG electrodes is required, the signal stability is usually limited, and the conductivity change on skin surface would influence the signal precision. Force myography (FMG) is another method that can directly register real-time body motions [8, 9] by measuring the radially directed force distributions caused by the volumetric change of muscles. FMG is an easy-to-perform method with relatively high motion classification accuracy, and there are fewer application limits.

Currently, the force-sensitive resistors (FSR) are mostly used to measure force distributions in FMG recording [8, 10, 11]. FSRs own several strong points such as simple structure and interface, but with relatively low measurement precision. Piezoelectrets is another kind of force-sensing material, with some specific properties such as strong sensitivity (~ 600 pC/N), small thickness (< 100 µm), light weight (~ 330 kg/m^3), low cost, flexibility, and stretchability [12–14], and therefore they are considered as an appropriate alternative for force sensing in FMG recording.

In this work, we applied flexible piezoelectret sensors for FMG recording to registered lower-limb motions. A preliminary analysis was performed based on the acquired FMG signals, and some possible future work was discussed.

2 Experiments

2.1 Participants

Three male able-bodied subjects (21–24 years old) were recruited in the experiments. The protocol was approved by the Institutional Review Board of Shenzhen Institutes of

R. Xu · Q. Zhuo · X. Li · H. Zhang · Y. Cai · L. Tian · P. Fang (✉) · G. Li
Key Laboratory of Human-Machine Intelligence-Synergy Systems, Shenzhen Institutes of Advanced Technology, Chinese Academy of Sciences, Shenzhen, 518055, China
e-mail: peng.fang@siat.ac.cn

R. Xu · Q. Zhuo · X. Li
Shenzhen College of Advanced Technology, University of Chinese Academy of Sciences, Shenzhen, 518055, China

Y. Cai
University of Science and Technology of China, Hefei, 230026, China

X. Zhang
Tongji University, Shanghai, 200092, China

Fig. 1 A flexible piezoelectret film as prepared (left and middle) and a packaged piezoelectret sensor ready for use (right)

Advanced Technology. All subjects gave the written informed consent and provided permission for publication of photographs with a scientific and educational purpose.

2.2 Sensors and Data Acquisition

Piezoelectret sensors were prepared from polypropylene, as introduced elsewhere [14]. Each packaged sensor was 1.2 cm × 1.2 cm in area and 0.24 mm in thickness, and could be bent flexibly when needed. Figure 1 shows a piezoelectret sensor before and after packaging.

Five piezoelectret sensors were used for FMG recording. The sensors were attached at five selected points on the surface of thighs, as shown in Fig. 2. A bandage was used to fasten the sensors on muscle surface. Three lower-limb motions of leg raising, knee flexion, and knee extension were tested, as shown in Fig. 3. Each motion class was performed for 30 repeats by all the subjects for data acquisition.

Five-channel outputs were recorded in real time with a data acquisition system developed in lab. The outputs of the sensors were amplified and filtered with a passing band of 0.7–75 Hz. A notch filtering was applied to remove the 50 Hz power interference. A data acquisition card (*USB-*

0816) was used to collect the signals with sampling rate of 100 Hz. Then the signals were transmitted to a computer for analysis.

2.3 Motion Classification

For motion classification, first half of the data was used as the training set, and the second half as the testing set. The data was segmented into a series of 300-ms analysis windows with an increment of 200 ms. For each analysis window of training and testing set, five time-domain features [15–17], including mean absolute value, simple square integral, third temporal moments, log detector, and kurtosis coefficient, were extracted. The Linear Discriminant Analysis (LDA) algorithm was employed to classify the three lower-limb motions.

3 Results

The sensor outputs for different subjects show similar results, and only the representative data are discussed here. Figure 4 shows the typical force distribution signals of different lower-limb motions. Different from FSRs, piezoelectrets only generate outputs upon force variation [12], and the output directions indicate the force variation direction, i.e. force increase or decrease. As can be seen, sudden peaks occur when a motion was performed, meaning that a considerable force caused by muscle contractions was loaded on the sensors. Then the signals drop down quickly to the baseline by holding the motion, since there was no more force variation. When muscles were relaxed, peaks in the opposite direction occur, revealing a force decrease on the sensors. The muscle contraction strength could be estimated based on the linearity of the piezoelectret sensors.

The root mean square (RMS) is also calculated for all the output channels, and a RMS vector is thus achieved, where each element value within the vector represents the RMS for each channel. Figure 5 shows the RMS spectrums for the three motion classes tested in the experiments, and significant difference between the motions could be observed.

Table 1 shows the confusion matrix of the three lower-limb motions. As can be seen, the classification

Fig. 2 Five selected points for FMG signal acquisition

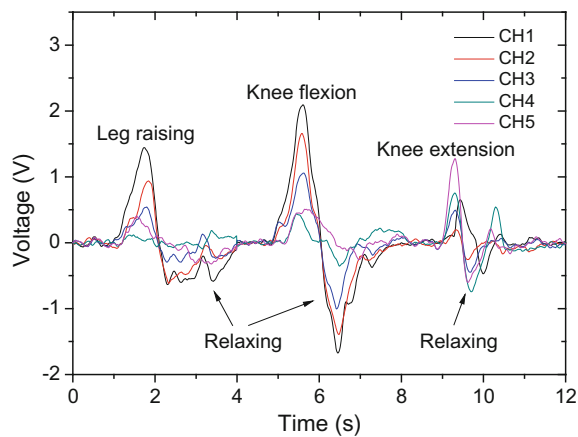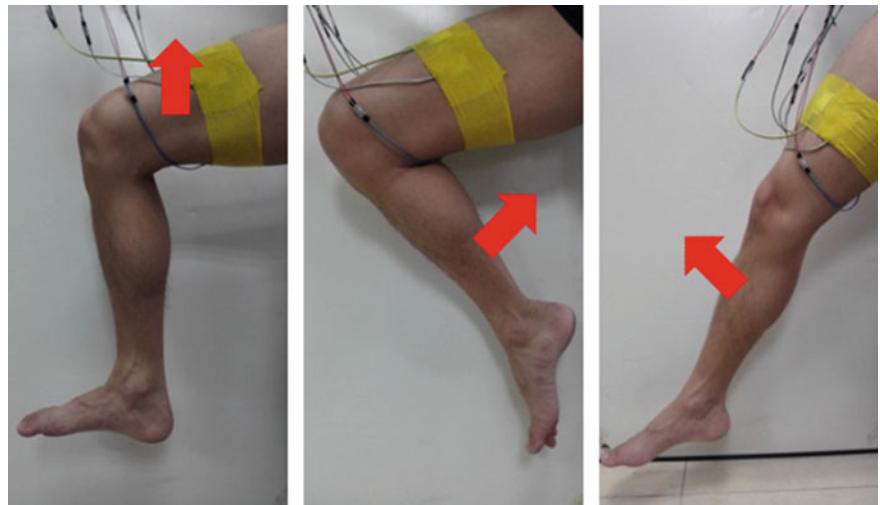**Fig. 3** Different motions of leg raising, knee flexion, and knee extension were tested in the experiments

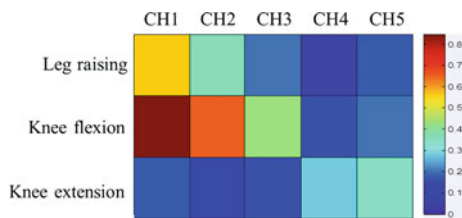**Fig. 4** Typical force distribution signals for different motions

Fig. 5 Normalized root mean square spectrums calculated from the five-channel date for different motions

accuracy of the motions of leg raising, knee flexion, and knee extension was 100%, 81.8%, and 94.4%, respectively, and the average classification accuracy over all the motions was calculated as 92.1%.

4 Discussion

This pilot study mainly focused on developing a new approach for FMG acquisition to register body motions with a novel kind of sensor. The experimental results show that FMG signals could be successfully recorded with the flexible piezoelectret sensors. By properly extracting FMG signal features and using LDA algorithm, an average classification accuracy of 92.1% was achieved over three lower-limb motions of leg raising, knee flexion, and knee extension for able-bodied subjects.

In this work, only five piezoelectret sensors were applied for signal acquisition, which might not provide enough FMG information and would subsequently limit the classification accuracy. In addition, the position for data acquisition could also be improved with an associated physiological study of human muscle structures. A sensor array with high density sensing unit would be suggested for more precise measurement of the radially directed force distribution.

Table 1 Confusion matrix of motion classes (%)

	Leg raising	Knee flexion	Knee extension
Leg raising	100	0	0
Knee flexion	18.2	81.8	0
Knee extension	5.6	0	94.4

The advantages of some special material properties of piezoelectrets may be taken into account to design an advanced FMG acquisition system. As an example, combined with their small thickness, flexibility, and stretchability, piezoelectrets could be integrated into fabrics. Instead of using wrist straps, belts, or even sockets and gloves that are cumbersome to wear, the fabric-based FMG acquisition system will be completely flexible and can be worn day and night, which may enhance the wearing comfort and free the body motions.

In future work, more subjects including limb amputees would be recruited for data acquisition to achieve a more in-depth investigation, especially for the FMG-based control of prostheses for amputees. A comparison between different body motion registration techniques, e.g. FMG and sEMG, would also be suggested.

5 Conclusion

In this work, piezoelectret sensors were applied to record FMG signals to register lower-limb motions. With their promising material and sensing performances, piezoelectret sensors could successfully capture the radially directed force distribution signals generated by the muscle contractions during leg raising, knee flexion, and knee extension. FMG signal features were extracted and an average classification accuracy of 92.1% was achieved. Some deep-going works were also suggested for future work.

References

1. B. Dobkin and A. Dorsch, The promise of mHealth: daily activity monitoring and outcome assessments by wearable sensors, *Neurorehabilitation and Neural Repair*, vol. 25, no. 9, pp. 788–798, 2011.
2. X. Zhang, X. Chen, Y. Li, V. Lantz, K. Wang, and J. Yang, A framework for hand gesture recognition based on accelerometer and EMG sensors, *IEEE Transactions on Systems, Man, and Cybernetics—Part A: Systems and Humans*, vol. 41, no. 6, pp. 1064–1076, 2011.
3. F. Lorussi, E. Scilingo, M. Tesconi, A. Tognetti, and D. De Rossi, Strain sensing fabric for hand posture and gesture monitoring, *in Proc. International Workshop on New Generation of Smart Wearable Health Systems and Applications*, Lucca, Italy, December 11–14 2003, vol. 9, no. 3, pp. 372–381.
4. P. Parker and R. Scott, Myoelectric control of prostheses, *Critical Reviews in Biomedical Engineering*, vol. 13, no. 4, pp. 283–310, 1986.
5. K. Wheeler and C. Jorgenson, Gestures as input: Neuroelectric joysticks and keyboards, *IEEE Pervasive Computing*, vol. 2, no. 2, pp. 56–61, 2003.
6. O. Armagan, F. Tascioglu, and C. Oner, Electromyographic biofeedback in the treatment of the hemiplegic hand—A placebo-controlled study, *American Journal of Physical Medicine and Rehabilitation*, vol. 82, no. 11, pp. 856–861, 2003.
7. A. Chan and K. Englehart, Continuous myoelectric control for powered prostheses using hidden Markov models, *IEEE Transactions on Biomedical Engineering*, vol. 52, no. 1, pp. 121–124, 2005.
8. N. Li, D. Yang, L. Jiang, H. Liu, and H. Cai, Combined use of FSR sensor array and SVM classifier for finger motion recognition based on pressure distribution map, *Journal of Bionic Engineering*, vol. 9, no. 1, pp. 39–47, 2012.
9. R. Abboudi, C. Glass, N. Newby, J. Flint, and W. Craelius, A biomimetic controller for a multifinger prosthesis, *IEEE Transactions on Rehabilitation Engineering*, vol. 7, no. 2, pp. 121–129, 1999.
10. M. Wininger, N. Kim, and W. Craelius, Pressure signature of forearm as predictor of grip force, *Journal of Rehabilitation Research and Development*, vol. 45, no. 6, pp. 883–892, 2008.
11. Z. Xiao and C. Menon, Towards the development of a wearable feedback system for monitoring the activities of the upper-extremities, *Journal of Neuroengineering and Rehabilitation*, vol. 11, no. 1, pp. 1–13, 2014.
12. R. Gerhard-Multhaupt, Less can be more: holes in polymers lead to a new paradigm of piezoelectric materials for electret transducers, *IEEE Transactions on Dielectrics and Electrical Insulation*, vol. 9, no. 5, pp. 850–859, 2002.
13. P. Fang, X. Qiu, W. Wirges, R. Gerhard, and L. Zirkel, Polyethylene-naphthalate (PEN) ferroelectrets: Cellular structure, piezoelectricity and thermal stability, *IEEE Transactions on Dielectrics and Electrical Insulation*, vol. 17, no. 4, pp. 1079–1087, 2010.
14. X. Zhang, X. Zhang, Q. You, and G. Sessler, Low-cost, large-area, stretchable piezoelectric films based on irradiation-crosslinked poly(propylene), *Macromolecular Materials and Engineering*, vol. 299, pp. 290–295, 2014.
15. D. Tkach, H. Huang, and T. Kuiken, Study of stability of time-domain features for electromyographic pattern recognition, *Journal of Neuroengineering and Rehabilitation*, vol. 7, paper no. 21, 2010.
16. A. Phinyomark, P. Phukpattaranont, and C. Limsakul, Feature reduction and selection for EMG signal classification, *Expert Systems with Applications*, vol. 39, no. 8, pp. 7420–7431, 2012.
17. R. Boostani and M. Moradi, Evaluation of the forearm EMG signal features for the control of a prosthetic hand, *Physiological Measurement*, vol. 24, no. 2, pp. 309–319, 2003.

Indocyanine Green Loaded, PEGylated, Reduced Graphene Oxide as a Highly Efficient Passive Targeting Contrast Agent for Photoacoustic/Fluorescence Dual-Modality Tumor Imaging

Jingqin Chen, Chengbo Liu, and Liang Song

Multi-modality imaging based on multifunctional nanocomposites holds great promise to fundamentally augment the capability of biomedical imaging, for both the diagnosis and therapy of cancer [1]. Herein, we synthesized indocyanine green (ICG) loaded, PEGylated, reduced nano-graphene oxide (rNGO-PEG/ICG), which provide excellent fluorescence imaging capability and greatly enhanced optical absorption for photoacoustic imaging (Fig. 1). In vitro confocal fluorescence microscopy study showed that the rNGO-PEG/ICG can be effectively uptaken by Hela cells. Moreover, it exhibited an excellent passive targeting capability for in vivo tumor imaging. Compared with free ICG, rNGO-PEG/ICG, upon intravenous injection, was able to provide greatly enhanced fluorescence and photoacoustic imaging contrasts of tumors in mice (Figs. 2 and 3). In addition, the circulation time of rNGO-PEG/ICG in the mouse body sustained up to six hours post injection; while after one day, no obvious accumulation of rNGO-PEG/ICG was found in any major organs (liver, spleen, kidney etc.), except the tumor regions. The demonstrated high fluorescence/photoacoustic dual-contrasts, together with its low toxicity and excellent circulation life time, suggests that the synthesized rNGO-PEG/ICG can be a promising candidate for further translational studies on both the early diagnosis and image-guided therapy/surgery of cancer.

J. Chen · C. Liu · L. Song (✉)
Research Laboratory for Biomedical Optics and Molecular Imaging, Shenzhen Key Laboratory for Molecular Imaging, Institute of Biomedical and Health Engineering, Shenzhen Institutes of Advanced Technology, Chinese Academy of Sciences, Shenzhen, 518055, China
e-mail: liang.song@siat.ac.cn
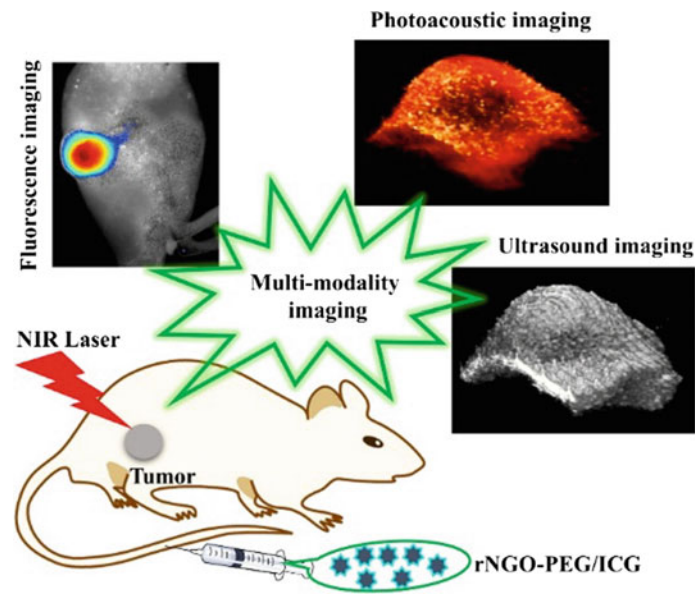
Fig. 1 The schematic illustration of multimodal imaging on tumor-bearing mouse after tail intravenous injection of rNGO-PEG/ICG
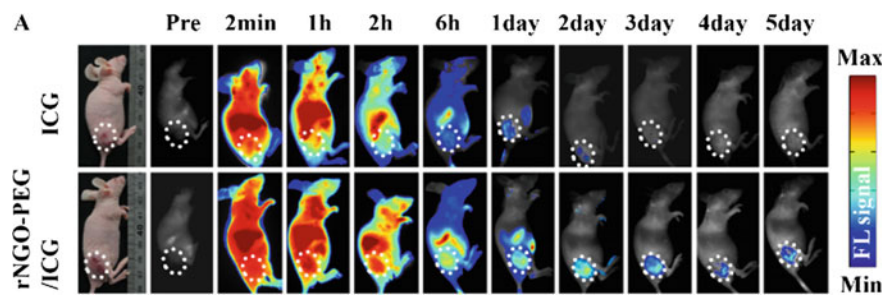
Fig. 2 In vivo fluorescence imaging. Fluorescence signal distribution within the tumor-bearing mouse body as a function of time after tail vein injection of rNGO-PEG/ICG
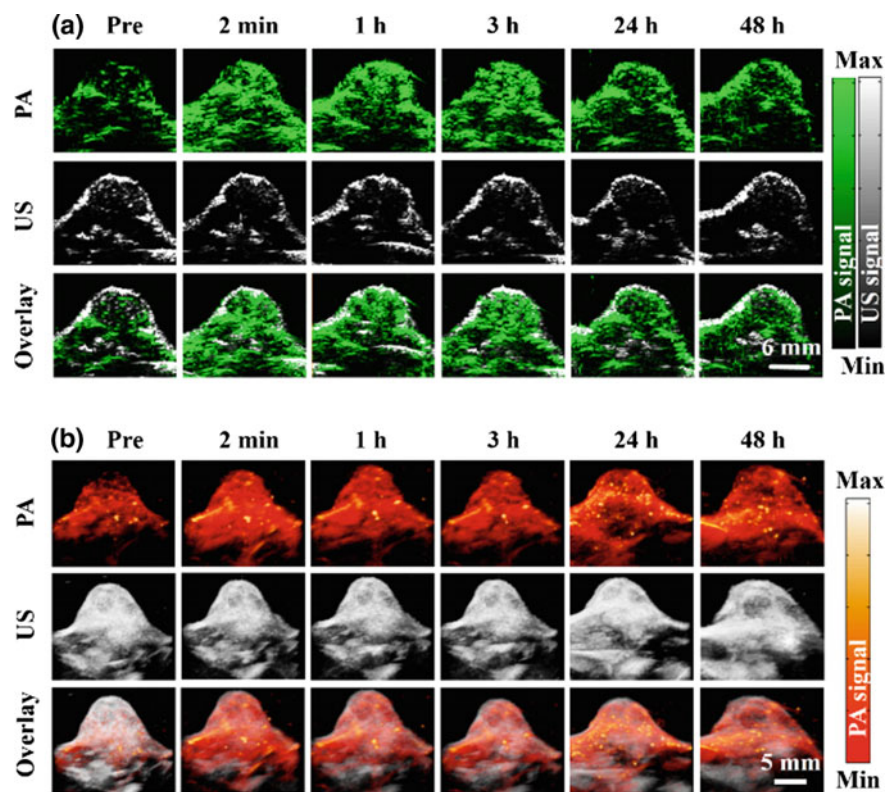
Fig. 3 In vivo photoacoustic imaging. **a** B-scan and **b** 3D ultrasound (US) and PA images of the tumor region obtained at 2 min, 1, 3, 24, and 48 h after tail vein injection of rNGO-PEG/ICG

Reference

1. L. V. Wang, Photoacoustic tomography: in vivo imaging from organelles to organs. Science, 2012, 335(6075):1458–1462.

Photoacoustic/Ultrasonic Dual-Modality Endoscopy in Vivo

Riqiang Lin, Yan Li, Jianhua Chen, and Liang Song

Abstract

Early diagnosis and treatment of cancer are of vital importance. Novel imaging methods are in great need to achieve this. Photoacoustic endoscopy (PAE) is an emerging endoscopic technology capable of providing both functional and molecular information of intact biological tissue of internal organs in vivo. With endogenous or exogenous contrast agent, cancer formation and the corresponding vascular morphology and function changes can be detected and imaged by PAE. In addition, Utilizing multi-wavelength laser excitation, a number of important physiological parameters, such as the total hemoglobin concentration, oxygen saturation of hemoglobin, and micro-hemodynamic flux, can be obtained by PAE. Such information directly correlates with vascular angiogenesis and abnormal metabolisms and thus reflects the formation and progression of many neoplasms.

In our study, a miniaturized, simple and full field-of-view photoacoustic/ultrasonic endoscopy system was developed. A flexible coil was used to transmit the rotational torque from the rotary stage, which enables a 360° field-of-view imaging in vivo, for the first time to our knowledge. The developed imaging catheter was fully encapsulated by a single-use protective polyamide tube. A B-scan rate up to 5 Hz (200 A-lines/B-scan) was achieved. Three-dimensional photoacoustic and ultrasound images of the rectum from a SD rat were acquired in vivo. The significantly improved imaging field-of-view, together with the flexible, simple and encapsulated catheter design, suggests that this PAE system can be of great interest for clinical translation for a variety of endoscopic applications, such as the urogenital, colorectal and gastrointestinal tract imaging (Fig. 1).
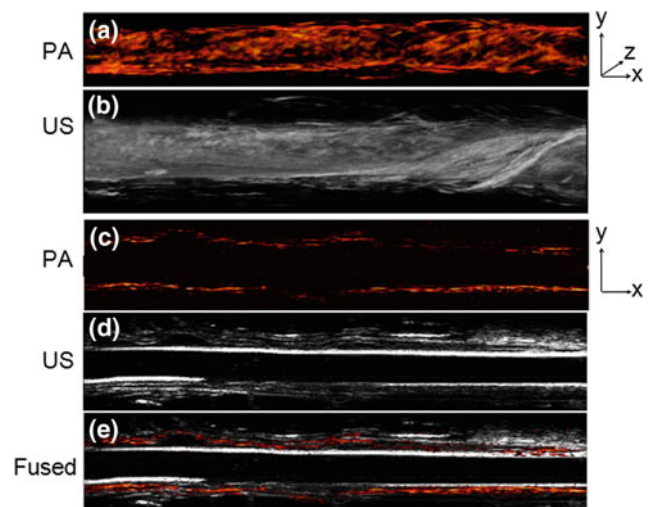
Fig. 1 Three-dimensional photoacoustic/ultrasound endoscopic imaging of a healthy rat rectum in vivo. **a** 3D PA and **b** US images of the rectum. **c** Unfolded images of (**a**), **d** unfolded images of (**b**), **e** fused images of (**c**) and (**d**)

Riqiang Lin and Yan Li are equally contributed.

R. Lin · Y. Li · J. Chen · L. Song (✉)
Research Laboratory for Biomedical Optics and Molecular Imaging, Institute of Biomedical and Health Engineering, Shenzhen Institutes of Advanced Technology, Chinese Academy of Sciences, 1068 Xueyuan Boulevard Nanshan, Shenzhen, 518055, China
e-mail: liangsong@siat.ac.cn

References

1. World Cancer Report 2014. Vol. Chapter 1.1 (World Health Organization, 2014).
2. Yao, J. J., Maslov, K. I., Zhang, Y., Xia, Y. N. & Wang, L. V. Label-free oxygen-metabolic photoacoustic microscopy in vivo. J Biomed Opt 16, doi: Artn 076003, https://doi.org/10.1117/1.3594786 (2011).
3. Yang, J. M. et al. Optical-resolution photoacoustic endomicroscopy in vivo. Biomed Opt Express 6, 918–932, https://doi.org/10.1364/oe.23.00918 (2015).
4. Yang, J. M. et al. A 2.5-mm diameter probe for photoacoustic and ultrasonic endoscopy. Opt Express 20, 23944–23953, https://doi.org/10.1364/oe.20.023944 (2012); Yang, J. M. et al. J Biomed Opt 19 (2014).
5. Bai, X. S. et al. Intravascular Optical-Resolution Photoacoustic Tomography with a 1.1 mm Diameter Catheter. Plos One 9, ARTNe9246310.1371/journal.pone.0092463 (2014).
6. Li, Y. et al. High-speed intravascular spectroscopic photoacoustic imaging at 1000 A-lines per second with a 0.9 mm diameter catheter. J Biomed Opt 20, https://doi.org/10.1117/1.jbo.20.6.065006 (2015).

A Novel Compact Linear-Array Based Photoacoustic Handheld Probe Towards Clinical Translation for Sentinel Lymph Node Mapping

Mucong Li, Chengbo Liu, and Liang Song

Abstract

Breast cancer is the leading threat to women health both in the developed and developing countries around the world. Sentinel lymph node (SLN) biopsy has become the standard of care for the staging of this disease over the past few decades. Conventional ultrasound lacks the capability to identify the SLNs. Thus, during the procedure, radioactive tracers and dyes are injected and an open surgery is required to identify the dye accumulated SLNs. As a rapidly growing technology, photoacoustic (PA) imaging is gaining widespread attention due to its excellent imaging contrast as well as high resolution for deep imaging [1, 2]. Therefore, handheld ultrasound linear array based PA systems have been developed by several groups for SLN identification over the past few years, which were demonstrated to be able to identify SLNs noninvasively, and can potentially eliminate the need for radioactive tracers and open surgeries [3]. In most of these systems, the light excitation and ultrasound detection are not designed coaxially, and thus high laser pulse energy is usually needed to produce PA images with a decent signal-to-noise ratio. For one recently reported coaxial based design, the imaging probe is very bulky and complex, making it unfriendly for clinical use and translation [4].

In this study, we developed a handheld ultrasound linear array based real-time photoacoustic tomography system. Compared with previously reported systems, our system is more compact and clinically friendly, and the excitation laser energy is more efficiently utilized. A novel optical-acoustic co-axial probe design (Fig. 1) was proposed in our system to offer the system a high signal-to-noise ratio as well as deep imaging capability, under relatively low laser energy excitation. GPU computation was also applied in the system to accelerate the imaging reconstruction speed, guaranteeing a real-time frame rate display. The system was validated in both in vitro and in vivo studies, by imaging silver needles in intra-lipid containing agar phantom as well as a rat sentinel lymph node (Fig. 2) under the skin surface in vivo, respectively.

The significantly improved imaging SNR with low laser pulse energy, high imaging depth, together with the reduced probe and optical fiber holder size, suggests that the developed handheld linear array based system is of great potential to be further translated for clinical applications.

M. Li · C. Liu · L. Song (✉)
Chinese Academy of Sciences, Shenzhen Institutes of Advanced Technology, Shenzhen, Guangdong, China
e-mail: liang.song@siat.ac.cn

M. Li
e-mail: mc.li@siat.ac.cn

C. Liu
e-mail: cb.liu@siat.ac.cn

Fig. 1 Probe schematics. **a** Side view, **b** front view and **c** photo of the handheld probe. Lens 1: Plano-convex acylindrical lens; Lens 2: Plano-concave cylindrical lens
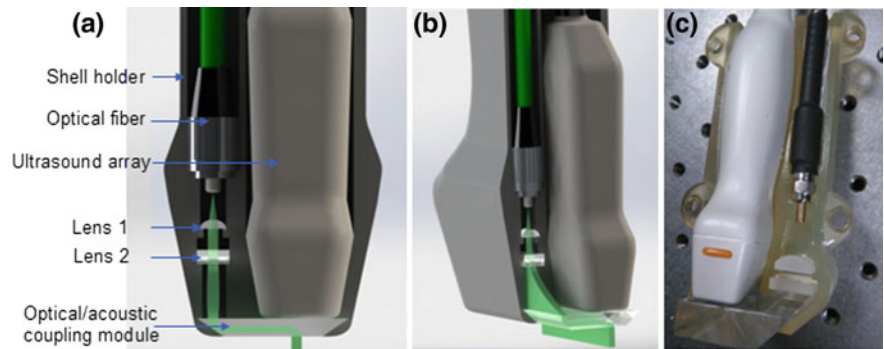
Fig. 2 Noninvasive photoacoustic mapping of the sentinel lymph node of a SD rat in vivo. **a** Before indocyanine green dye injection, **b** after indocyanine green dye injection, **c** ultrasound image, **d** anatomy photo of the SLN after imaging
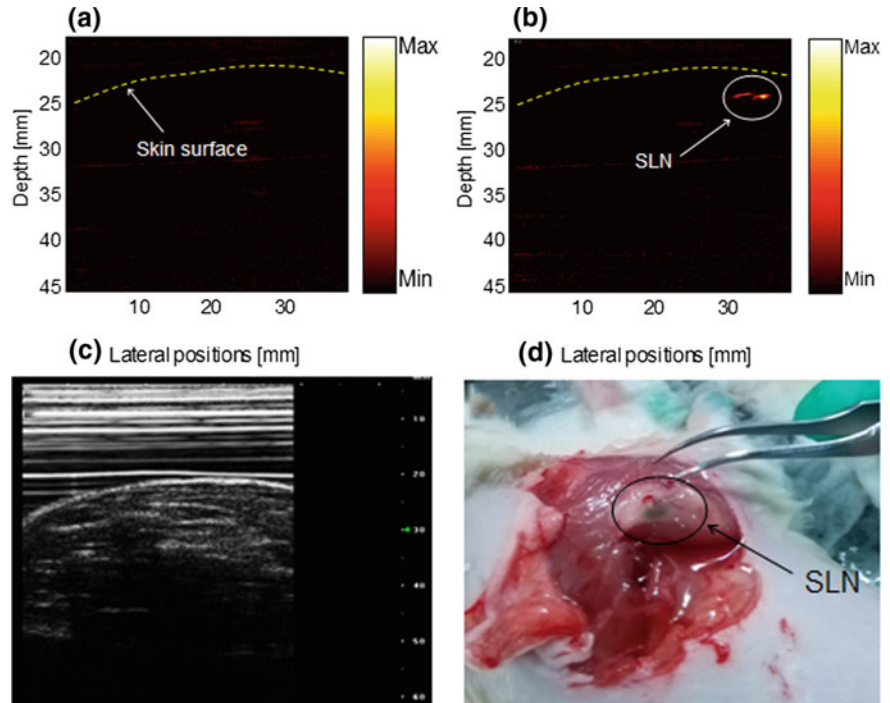
References

1. C. Kim, T. N. Erpelding, K. Maslov, "Handheld Array-based Photoacoustic Probe for Guiding Needle Biopsy of Sentinel Lymph Nodes," *Journal of Biomedical Optics*, vol. 15, no. 4, pp. 046010–046010–4, 2010.
2. L. H. V. Wang and S. Hu, "Photoacoustic Tomography: In Vivo Imaging from Organelles to Organs," *Science*, vol. 335, no. 6075, pp. 1458–1462, 2012.
3. L. G Montilla, R. Olafsson, D. R Bauer. "Real-time Photoacoustic and Ultrasound Imaging: A Simple Solution for Clinical Ultrasound Systems with Linear Arrays," *Physics in Medicine and Biology*, vol. 58, no. 1, pp. N1–N12, 2013.
4. L. Song, K. Maslov, R. Bitton, "Fast 3-D dark-field reflection-mode photoacoustic microscopy in vivo with a 30-MHz ultrasound linear array," *Journal of biomedical optics*, vol. 13, no. 5, pp. 054028–054028–5, 2008.

Estimating Blood Pressure with a Smartphone

Rong-Chao Peng, Wen-Rong Yan, and Xiao-Lin Zhou

1 Introduction

Cardiovascular disease like hypertension is one of the top killers of human's life. As the smartphone is becoming ubiquitous in the world, its application in medicine may provide an easy and low-cost approach for early detection of cardiovascular disease. Lamonaca et al. applied artificial neural network to evaluate blood pressure from the pulse wave signal acquired by the camera of the smartphone [1]. Chandrasekaran et al. proposed two vascular transit time methods to cufflessly estimate blood pressure with smartphones [2]. In this study, we proposed a novel method to estimate continuous blood pressure from heart sound signals acquired by the built-in microphone of the smartphone.

2 Methods

It is known in clinical medicine that the second heart sound (S2) has a characteristic "accentuation" in hypertensive patients. We thus infer that the pattern of the S2 is associated with the blood pressure. If the pattern of the S2 is recognized, then the blood pressure might be determined.

Thirty-two healthy subjects participated in the experiment (25 males and 7 females, age 20–32 years, height 150–185 cm, weight 44–90 kg). They were instructed to lie in the supine position on a mattress. A smartphone was used to collect the heart sound signals and simultaneously a Finometer® MIDI (Model II, Finapres Medical Systems B.V.,

The Netherlands) was used to measure continuous beat-to-beat blood pressure.

Each heart sound signal was down-sampled to 2205 Hz and its envelope of Shannon energy was calculated. The peaks of the envelope were identified by a high threshold and a low threshold, and then were classified as the first heart sound (S1) or S2 according to the clinical knowledge that the duration from S1 to S2 is shorter than that from S2 to S1.

Afterwards, the S2 of each heartbeat in the heart sound signals was truncated by a 64 ms window centered at the maximum of the S2, and its frequency spectrum was obtained by Fast Fourier transform (FFT). The spectrum was then normalized by dividing its maximum value, and the 36 spectral values with 10 Hz interval in the frequency band 50–400 Hz were chosen as features of the S2. These features were separately regressed with the systolic and diastolic blood pressure using support vector machine (SVM) developed by Chang and Lin [3]. The accuracy of the regression was evaluated using tenfold cross-validation.

3 Results

The predicted values of the systolic and diastolic blood pressure using the SVM regression were compared with the corresponding values measured by the Finometer device. Figure 1 shows that the correlation coefficients between the predicted values and the measured values were 0.893 and 0.922 for systolic and diastolic blood pressure, respectively. These results suggest that the smartphone is of potential use for cuffless and continuous blood pressure monitoring.

R.-C. Peng · W.-R. Yan · X.-L. Zhou (✉)
Chinese Academy of Sciences, Shenzhen Institutes of Advanced Technology, Shenzhen, 518055, China
e-mail: xl.zhou@siat.ac.cn

R.-C. Peng
e-mail: pengxiaotu@126.com

W.-R. Yan
e-mail: christopheryanwr@gmail.com
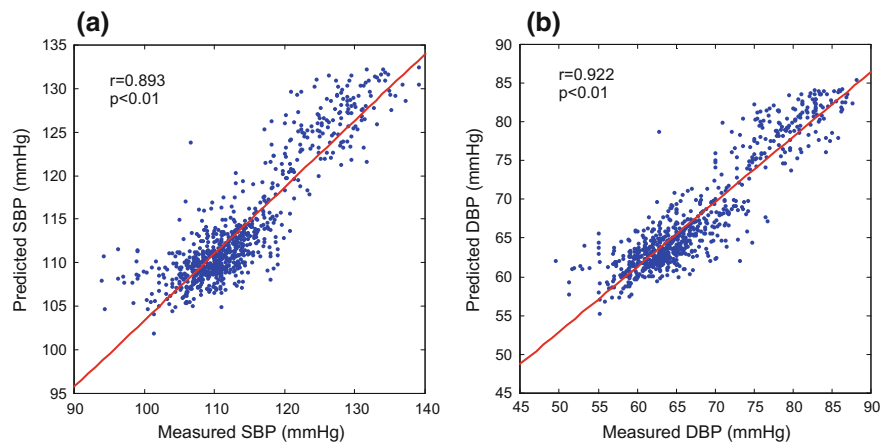
Fig. 1 Correlation analysis between predicted values and measured values for (**a**) systolic blood pressure (SBP) and (**b**) diastolic blood pressure (DBP). In each panel, the diagonal is the linear regression line. *r*, Pearson correlation coefficient

4 Conclusion

We demonstrated that the smartphone can be used to estimate blood pressure from the heart sound signals, continuously, non-invasively and cufflessly.

References

1. F. Lamonaca, K. Barbe, Y. Kurylyak, et al., "Application of the Artificial Neural Network for blood pressure evaluation with smartphones," in 2013 IEEE 7th Intl. Conf. on Intell. Data Acq. and Advanced Comput. Sys., IDAACS 2013, Sep 12, 2013 - Sep 14, 2013, Berlin, Germany, 2013, pp. 408–412.
2. V. Chandrasekaran, R. Dantu, S. Jonnada, et al, "Cuffless differential blood pressure estimation using smart phones," IEEE Trans. on Biomed. Eng., vol. 60, pp. 1080–1089, Apr 2013.
3. C.-C. Chang and C.-J. Lin, "LIBSVM: A library for support vector machines," Acm Trans. on Intell. Sys. and Tech., vol. 2, pp. 1–27, 2011.

Is Beat-to-Beat Blood Pressure Variability in Frequency Domain Associated with the Occurrence of Carotid Plaques?

Dan Wu, Huahua Xiong, Yujie Chen, Heye Zhang, and Yuan-Ting Zhang

1 Introduction

More evidences indicate that the increased blood pressure variability (BPV) has some relations with arteriosclerosis and development of plaques, also it will lead to the cardiovascular disease [1]. Blood pressure variability is usually assessed in the time domain. Standard deviation (SD), coefficient of variability (CV), average real variability (ARV) are the most used BPV indices. However, the prognostic significance of the BPV indices in frequency domain was less reported. Therefore, in this study, we will investigate whether beat-to-beat BPV in frequency domain can evaluate the occurrence of carotid plaques in the early stage.

2 Methodology

In this study, 74 subjects (mean age 56.7 ± 9.6 years) with carotid plaques and 55 subjects without plaques (mean age 53.0 ± 9.2 years) were enrolled. Beat-to-beat blood pressure monitoring and carotid artery ultrasound examination were performed in these subjects respectively. 5 min Beat-to-beat BP was recorded using Finometer® MIDI (Finapres Medical System, Amsterdam, The Netherlands). BPV was evaluated in time and frequency domain [2]. The carotid artery ultrasound was examined using a high-resolution ultrasound Doppler system (iU22, Philips Ultrasound, Bothell, WA, USA). Independent sample T-test and non-parametric test were used to compare the time and frequency domain BPV indices in two groups, respectively. All of the statistical analyses were performed using SPSS 15.0 statistical package.

3 Results

Table 1 describes the mean values of time domain BPV measures in subjects with and without plaques. It is obviously that all the BPV measures in subjects with plaques are higher than those in subjects without plaques.

D. Wu · H. Zhang (✉)
Chinese Academy of Sciences and Key Lab for Health Informatics
of the Chinese Academy of Sciences, Shenzhen Institutes of
Advanced Technology, Shenzhen, China
e-mail: hy.zhang@siat.ac.cn

D. Wu
Shenzhen College of Advanced Technology, University of
Chinese Academy of Sciences, Shenzhen, China

H. Xiong
Departments of Ultrasound, The Second People's Hospital of
Shenzhen, Shenzhen, China

Y. Chen
Institute of Clinical Anatomy, Southern Medical University,
Guangzhou, China

Y.-T. Zhang
Department of Electronic Engineering, Joint Research Centre for
Biomedical Engineering, The Chinese University of Hong Kong,
Hong Kong, China

Table 1 Mean values of time domain BPV measures in subjects with and without plaques along with statistical significance of difference

Variables (Unit)	Without plaques (N = 55)	With plaques (N = 74)	P value
SBPV (SD) (mm Hg)	5.58 ± 1.74	6.06 ± 2.07	0.163
SBPV (CV) (%)	4.17 ± 1.36	4.36 ± 1.21	0.405
SBPV (ARV) (mm Hg)	2.25 ± 0.85	2.38 ± 1.03	0.452
DBPV (SD) (mm Hg)	3.37 ± 1.12	3.78 ± 2.76	0.294
DBPV (CV) (%)	4.76 ± 2.32	4.88 ± 2.95	0.798
DBPV (ARV) (mm Hg)	1.21 ± 0.41	1.40 ± 1.43	0.349

SBPV, systolic BPV; DBPV, diastolic BPV

Table 2 Significant difference of BPV indices in frequency domain between subjects with and without plaques

BPV frequency indices (Hz)	Z	P value
SBPV_VLFn (0.02–0.07)	−2.295	0.022*
SBPV_LFn (0.075–0.15)	−0.352	0.725
SBPV_HFn (0.15–0.40)	−0.352	0.725
DBPV_VLFn (0.02–0.07)	−2.138	0.032*
DBPV_LFn (0.075–0.15)	−0.824	0.410
DBPV_HFn (0.15–0.40)	−0.824	0.410

LFn, normalized low frequency; HFn, normalized high frequency. *$P < 0.05$

However, there was no significant difference between the two groups. In contrast, for BPV indices in the frequency domain in Table 2, we found that the normalized very low frequency (VLF) band in systolic BPV ($P = 0.022$) and diastolic BPV ($P = 0.032$) were significantly different between the two groups.

4 Discussion and Conclusions

In our previous study, we found that BPV in time domain had correlation with the number of plaques [3]. In present study, we extend the existing knowledge and indicate that beat-to-beat BPV measures in frequency domain are superior to BPV measures in time domain for identifying the patients with plaques. In the future, we can use frequency domain indices of BPV to predict the occurrence of carotid plaques in the early stage. Furthermore, a large-scale follow-up study is needed in the future to confirm the predictive significance of BPV measures in the formation of plaques.

Conflict of Interest The authors declare that they have no conflict of interest.

References

1. R. Sega, G. Corrao, M. Bombelli, et al., "Blood pressure variability and organ damage in a general population: results from the PAMELA study,"*Hypertension*, vol. 39, pp. 710–714, Feb 2002.
2. H.M. Stauss, "Identification of blood pressure control mechanisms by power spectral analysis," *Clinical and Experimental Pharmacology and Physiology*, vol. 34, pp. 362–368, 2007.
3. Y.J. Chen, H.H. Xiong, Dan Wu, et al., "Relationship of short-term blood pressure variability with carotid intima-media thickness in hypertensive patients," *BioMed Eng OnLine*,vol. 14, pp. 71–86, 2015.

Power Aware Topology Management and Congestion Control Mechanism in High Medical QoS WHMNs

Fangmin Sun and Ye Li

Abstract

Wireless health monitoring networks (WHMNs) usually characterized by limited bandwidth resource and large amount of data, so to improve the network throughput of the wireless health monitoring network is a key challenge. Besides, as the data transmitted in the WHMNs are about the health or even the life of the people being monitored, so the real-time ability of the network should be ensured. In this paper, an adaptive transmission power based congestion control (Acc) mechanism was designed to achieve high throughput and real-time for a three-tier semi-self-organizing health monitoring network. The router nodes adjust their wireless transmission power according to the current network topology state and the communication state of the network adaptively to balance network load and reduce network congestion. The congestion control methods proposed in this paper have the characteristics of low power consumption and low communication overhead. Experiments have shown that the WHMN with the proposed Acc mechanism performs better than the WHMNs without the Acc in end-to-end delay and network throughput.

1 Introduction

Nowadays, wireless health monitoring networks (WHMNs) are being widely studied and have gained large advancement. WHMNs are usually worked on the ISM free licenses band, and featured by limited energy and bandwidth resource [1]. Besides, in the WHMNs the human activities are not limited, so the topology of the WHMNs is usually dynamic.

Wireless health monitoring networks usually need to monitoring tens of even hundreds of people at the same time, and the amount of data transmitted in the WHMNs is very large, to improve the network throughput of the WHMNs is an essential and urgent problem. Besides, as the data transmitted in the WHMNs are about the health or even the life of the people being monitored, so the real-time ability of the network should be ensured.

For the band limited WHMNs, network congestion are the main cause of the high end-to-end delay and low efficiency of data transmission [2]. Moreover, a good network topology can reduce congestion by balancing the network traffic.

In this paper, an Adaptive transmission power based topology management and congestion control mechanism was designed to achieve high throughput and real-time in WHMNs, and the method has been verified to be effective by the experiments.

2 Network Architecture

The WHMN we designed is a three-tier semi-self-organizing health monitoring network. The architecture is shown in Fig. 1. From bottom to top, the first tire of the network is the mobile data acquisition layer (DAL), which consists of various kinds of wearable health monitoring nodes (HMNs) to sample the physiological signal of the people being monitored. The second tire of the network is the data transporting layer, which is formed by the specially designed router nodes (RNs) and composed of the main routing path of data transmission. The third tire of the network is the data collecting layer (DCL), which is formed by the coordinator node (CN), which is connected to a personal computer to enable data collection and remote transmission to the backend sever [3, 4].

F. Sun · Y. Li (✉)
Research Centre for Biomedical Information Technology, Chinese Academy of Sciences, Shenzhen Institutes of Advanced Technology, Shenzhen, China
e-mail: ye.li@siat.ac.cn

F. Sun
e-mail: fm.sun@siat.ac.cn

Fig. 1 The architecture of the WHMN we designed
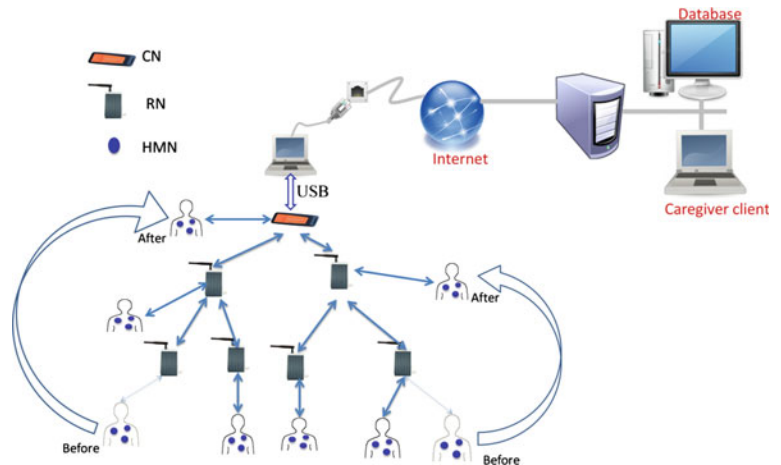
3   Congestion Control Mechanisms

Network congestion will result in serious consequences such as packet loss, throughput degradation, increasing network delay, energy waste, etc. [5]. In this paper, we solve the congestion problem from two aspects: topology optimization and congestion control mechanism.

3.1   Topology Management and Optimization Mechanism

In the network establishment stage, a transmission power based topology management and optimization mechanism has been proposed to balance the network communication load and maximize the network throughput. The router node (RN) automatically adjusts its transmission power according to the children nodes it has. If the children nodes number of a RN is greater than the threshold, the RN would adjust its transmission power according to formula (1). Conversely, the RN adjusts its power P according to formula (2).

$$P = \max\left(P_{\min}, \frac{(N_1 - 1)P_0}{(\text{nodenum} - \text{nodemax}) + N_1}\right) \quad (1)$$

$$P = \min\left(P_{\max}, \frac{N_2 P_0}{(\text{nodenum} - \text{nodemin}) + N_2}\right) \quad (2)$$

where, P_0 is the current transmission power of the RN; P_{min} is the minimum transmission power of the RN to ensure the network connectivity; P_{max} is the maximum transmission power that the RN could transmit. The threshold *nodemax* and *nodemin* are set according to the total number of the HMNs *nodetotal* and the total number of the RNs *routertotal* in the WHMN (see formula (3) and (4)). While the value of N_1 and N_2 are all set to 100.

$$\text{nodemax} = \left\lceil \frac{2 \times \text{nodetotal}}{\text{routertotal}} \right\rceil \quad (3)$$

$$\text{nodemin} = \left\lfloor \frac{\text{nodetotal}}{3 \times \text{routertotal}} \right\rfloor \quad (4)$$

The transmission power based topology management mechanism enable the HMNs evenly distributed in the network and so as to avoid the network congestion caused by network load imbalance.

3.2   Congestion Control Mechanism

In the stable data transmission stage, the RNs detect the congestion by the channel busy ratio and buffer occupancy ratio, and alleviate the congestion by adaptive power adjustment.

Congestion detection: the RNs have been in the channel listening state, through the detection of the channel busy ratio and the length of the buffer queue to detect congestion. If congestion occurs, it can reduce the number of children nodes by reducing the transmission power of the wireless signal, so as to avoid the occurrence of congestion.

Congestion avoidance and release mechanism: by adjusting its own wireless transmit power to reduce the number of its child nodes, thus avoiding or reducing the network congestion.

The buffer occupancy ratio λ, The channel busy ratio μ, If $\lambda > 80\%$ and $\mu > 80\%$, while the RN adjust its transmission power according to formula (5).

$$P = \max(P_{\min}, \lambda \mu P_0) \quad (5)$$

For the RNs whose remaining buffer space is large and the channel state is comparatively free, if $\lambda < 20\%$ and $\mu < 20\%$, the RNs would adjust the transmission power according to the formula (6).

$$P = \min\left(P_{\text{max}}, \frac{P_0}{(1 - \lambda\mu)}\right) \qquad (6)$$

where, P0 is the present transmit power of the RN and P is the transmit power after the power adjustment.

No congestion notification: because congestion notification itself can increase the bandwidth consumption and reduce the transmission efficiency of data processing, so congestion control mechanism without congestion notification is better to avoid and relieve the congestion.

4 Experiments and Results

4.1 Network Throughput

We tested the network throughput when there are different numbers of HMNs were sending ECG signals to the CN. The sampling rate of the ECG signal was 250 samples/s, and there were 4 bytes in every sample. The ECG signal was sent once per second, and the data transmission rate was 1 kbytes/s. The testing results are shown in Fig. 2.

Compared with the WHMN without the Acc mechanism, the network throughput of the WHMN improved by Acc was improved by 38.5% on the average.

4.2 End-to-End Delay

We tested the averaged end-to-end delay when there are different numbers of HMNs sending data to the CN at the same time. Each HMN sent 50 packets/s and 80 bytes in each packet. The test result is shown in Fig. 3. It can be seen that the LHRP significantly reduced the end-to-end delay compared with the HRP. When there are 30 HMNs sending data at the same time, the averaged end-to-end delay of the Acc method is 25.8% lower than the system without Acc.

End-to-end delay was test when there is 5 HMNs in the network. Each HMN sends the ECG signal to the sink node through one or more hops. The HMN sends 50 packets/s and 80 bytes in each packet; the test results is shown in Fig. 4.

Fig. 2 The network throughput varies with the number of nodes in the network

Fig. 3 End-to-end delay varies with number of HMNs

Fig. 4 End-to-end delay varies
with number of hops
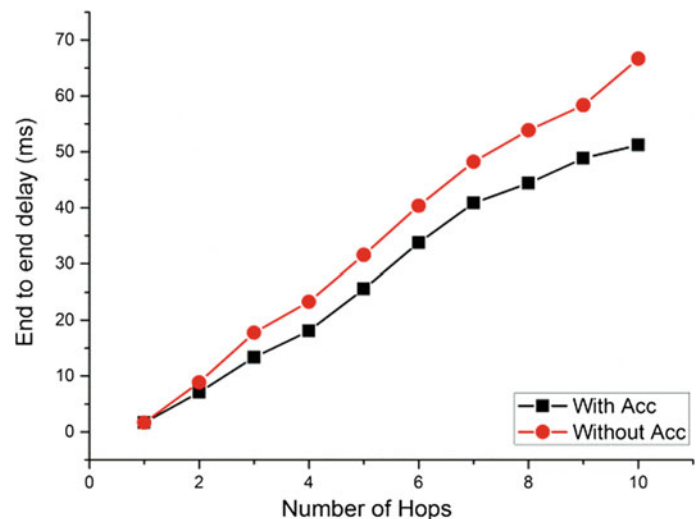
With the increase of the number of hops, the improvement
is much more significant. When data transmitted through 10
hops, the averaged end-to-end delay was reduced about 13 ms
compared with the result of the system without Acc.

5 Conclusion

In this work, a transmission power based adaptive conges-
tion control algorithm was proposed and the performance of
Acc algorithm in reducing the end-to-end delay and
improving network throughput is verified to be effective.

References

1. Chiarini G, Ray P, Akter S, et al. mHealth technologies for chronic
   diseases and elders: A systematic review. Selected Areas in
   Communications, IEEE Journal on, 31(9): pp. 6–18, 2013.
2. Xiao Y, Kim K. Congestion control of differentiated service network
   [J]. Chinese Journal of Electronics, 19(1): pp. 113–118, 2010.
3. F M Sun, Z Fang, Z Zhao, et al. A Wireless ZigBee Router with
   P-H-T Sensing for Health Monitoring[C]. Green Computing and
   Communications (GreenCom), 2013 IEEE and Internet of Things
   (iThings/CPSCom), IEEE International Conference on and IEEE
   Cyber, Physical and Social Computing, pp. 1773–1778, 20–23 Aug.
   2013.
4. F M Sun, Z Zhao, Z Fang, L D Du, et al. Implementation and
   real-time and reliability evaluation of a WHMS improved by LHRP
   and SMAM. International Journal of Distributed Sensor Networks,
   Volume 2015, Article ID 282816, 11 pages, 2015.
5. Dongho Lee, Kwangsue Chung. Adaptive duty-cycle based con-
   gestion control for home automation networks. IEEE Transactions
   on Consumer Electronics, Vol. 56, No. 1, February 2010.

DTI Quantitative Analysis on Microstructural Abnormality in Post Stroke Depression

Chenfei Ye, Jun Wu, Xuhui Chen, and Heather T. Ma

1 Introduction

Post stroke depression (PSD) is a frequent problem in stroke rehabilitation. Previous neuroimaging studies have implicated the link between particular white matter microstructures and pathophysiology of depression [1]. However, these studies reported no clear association between the lesion location and stroke-induced deterioration, and are often restricted to particular diffusion tensor imaging (DTI) image contrast like fractional anisotropy (FA) changes, lacking of multiple comparisons. In order to explore the effect of microstructural abnormalities in white matter to PSD comprehensively, we proposed a quantitative method with multiple DTI coefficient comparisons. Our result shows certain parameter changes in microstructures affected by infarct lesions are associated with depression.

2 Methodology

Thirteen PSD patients (6 men and 7 women, mean age 65 ± 7 years) and ten healthy subjects (7 men and 3 women, mean age 42 ± 11 years) as normal control (NC) were included in the current study. For PSD patients, the severity of depression was assessed using the 24-item Hamilton Rating Scale for Depression (HAMD-24) within 1 month after stroke onset. All the subjects underwent 1.5T MR imaging with T1 and DTI scanning within two weeks after stroke onset. Final infarcts were manually defined on diffusion weighted imaging (DWI) images.

C. Ye · H. T. Ma (✉)
Department of Electronic & Information Engineering, Harbin Institute of Technology Shenzhen Graduate School, Shenzhen, China
e-mail: heather.tma@gmail.com

J. Wu · X. Chen
Department of Neurology, Peking University Shenzhen Hospital, Shenzhen, China

After image preprocessing, all the subjects T1 images were parcellated through MRICloud platform, which is an atlas-based automatic T1 segmentation pipeline invented by JHU (www.mricloud.org). For atlas creation, a subset of the atlases were initially segmented using a single-subject atlas with DiffeoMap software followed by manual corrections. Then all other data were segmented by multi-atlas segmentation. For each of our subject, the parcellation maps obtained from MRICloud were registered to corresponding mean of DWI (MD), apparent diffsuion coefficient (ADC) and FA images separately with manual correction. Thus microstructures were segmented in multiple DTI images. Since superior frontal gyrus (SFG) and cingulate cortex (CC) have been reported particularly relevant to depression [2], we focus on these two microstructures as regions of interests (ROI) in our PSD study. Based on the location of main ischemic lesions greater than 5 mm axial diameter, we classified the ROIs of each PSD patients into two clusters: homolateral group (ROI and lesion in the same hemisphere) and contralateral group (ROI and lesion in the opposite hemisphere). For comparison, ROIs on each hemisphere of NC group was selected separately. For each kind of DTI coefficient images, four parameters based on intensity distribution (mean, standard deviation, skewness and kurtosis) were quantitatively measured on ROIs with ANOVA analysis.

3 Result

Several parameters with significant difference were found in statistical results. In the case of SFG, kurtosis on homolateral and contralateral MD is both lower than NC's MD ($p = 0.02$). For ADC, homolateral skewness is lower than NC's ($p = 0.045$), and homolateral and contralateral kurtosis is both lower than NC's ($p = 0.007$). As for CC, mean MD of PSD patients is lower ($p = 0.049$) while standard deviation is higher ($p = 0.001$) comparing NC. For both mean and

standard deviation of ADC, PSD patients are much higher than NC (p < 0.001).

4   Conclusions

Instead of simple observation on FA value, this study analyzed intensity distribution of multiple DTI contrasts. We identified certain diffusivity abnormalities in SFG and CC structures of PSD patients. These quantitative findings coincide well with the previous hypothesis that infarct lesions in PSD patients may lead to structural damage of neuroanatomical emotional-circuits, which contains SFG and CC. This study may provide new insights into the neuroanatomical mechanism of PSD.

References

1. Drevets WC, Price JL, Furey ML. Brain structural and functional abnormalities in mood disorders: implications for neurocircuitry models of depression. Brain Struct Funct, 213:93–118, 2008.
2. Bae JN, MacFall JR, Krishnan KR, et al. Dorsolateral prefrontal cortex and anterior cingulate cortex white matter alterations in late-life depression. Biol Psychiatry, 60: 1356–1363, 2006.

Marrow Fat Effect on Trabecular Biomechanics in Different BV/TV Subjects—A Simulation Study

Yang Chen, Liang Li, James F. Griffith, Ping-Chung Leung, and Heather T. Ma

1 Introduction

Osteoporosis is a metabolism disease characteristic with a loss of bone mass and a reduction of bone strength, patients suffering osteoporosis will have an increased probability of bone fracture [1]. BV/TV is a main factor for bone strength evaluation. Trabecular structures and bone marrow are the main components of cancellous bone, it has been reported that bone marrow may affect cancellous bone biomechanics, especially for marrow fat, which may enhance trabecular strength, but the difference of this effect in different BV/TV groups remains unknown yet.

In this study, in order to investigate the difference of marrow fat effect in different BV/TV people, three different groups finite element (FE) models were established based on three different BV/TV subjects, simulation compressive test were preformed on these models. The simulation results indicate that marrow fat may have larger contribution in low BMD people.

2 Materials and Methods

Three post-menopausalfemales were involved in this study, a quantitative CT scan of L3 lumbar spine was preformed on each subjects, bone mineral density (BMD) and BV/TV of each subjects was measured based on these QCT images. The vertebra bone structures of each slice were segmented and the segmented images were imported into Simpleware (Simpleware INC, England) for numerical models. To induce the calculation, model geometry were cropped into a 10 mm * 10 mm * 10 mm cube. For each subjects, two different models where trabecular structures with and without marrow fat were established respectively.

The trabecular structure were set as non-linear elastic material which was described in previous study [2], where marrow fat was set as elastic materials, elastic modulus and other material properties of trabecular bone were computed by its BMD. Numerical models were imported into COMSOL Multiphycis (COMSOL INC, Sweden), the boundary conditions of simulation models were the same as previous work [2]. Models were compressed to completely fracture, and the mechanical features of fractured models were extracted from the results.

3 Result and Discussion

Simulation results were in agreement with previous study, where marrow fat would enhance trabecular bone strength. In order to quantify marrow fat effect, a new parameter, stress-increased rate was introduced, which defined as the difference between the stress of models with and without marrow divided the stress of pure trabecular model. Results of stress-increased rate were shown in Fig. 1.

Form Fig. 1 we can conclude that the stress-increased rate has a negative correlation with BV/TV, which means that marrow fat contribute more in bone strength in low BV/TV subjects. This difference may indirectly explain the phenomenon that the content of marrow fat would increase in low BMD people. But this study still has some limitations, further we will extend the research subjects and a statistical

Y. Chen · L. Li · H. T. Ma (✉)
Department of Electronic & Information Engineering,
Harbin Institute of Technology Shenzhen Graduate School,
Shenzhen, China
e-mail: heather.tma@gmail.com

J. F. Griffith · P.-C. Leung
The Chinese University of Hong Kong, Hong Kong, China

Fig. 1 Stress-increased rate
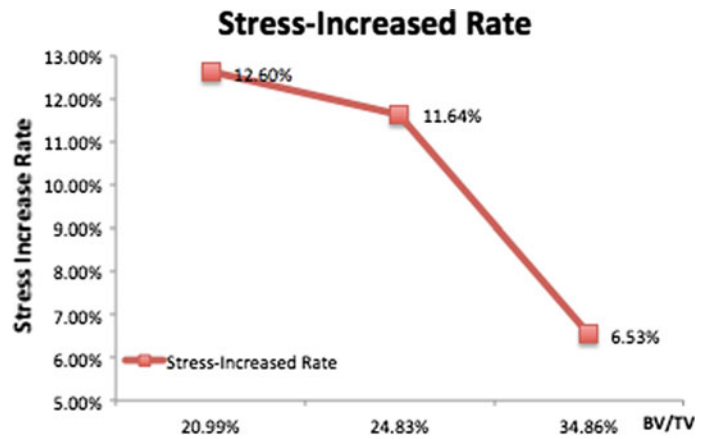
analysis will also be preformed to investigate the relationship between BV/TV and marrow fat's effect.

References

1. P. Ammann and R. Rizzoli, "Bone strength and its determinants," Osteoporosis International, vol. 14, no. 3, pp. 13–18, 2003.
2. Chen Yang, Ma H.T.Ting, et al., "A simulation study on marrow fat effect on biomechanics of vertebra bone", Procedings of 37th Annual conference of EMBS, IEEE, 2015.

A New Atlas Pre-selection Approach
for Multi-atlas Based Brain Segmentation

Hengtong Li, Chenfei Ye, Jingbo Ma, Susumu Mori, and Heather T. Ma

1 Introduction

The demographic-based multi-atlas propagation indicates that top-ranked atlas selection with mutual information (MI) similarity can result in a better segmentation performance compared to that from a random set of atlases [1]. For the purpose of speeding up this process, we propose a fast method for the atlas pre-selection in multi-atlas based segmentation. This study is based on the multiple granularity analysis, where Lite-M1 pipeline has been developed. In this pipeline, the lateral ventricle (LV) of target image is primarily labeled before the multi-atlas based segmentation. By adopting the same pipeline for segmentation, results based on the proposed pre-selection method were compared to that using MI similarity and 4 labels, which contain cerebral cortex, white matter, gray matter and lateral ventricle. This study shows that the proposed method can reduce heavy computational burden in atlas pre-selection process, while remains high accurate multi-atlas based brain segmentation.

2 Materials and Methods

2.1 Atlas Database

The atlas database in current study was selected from JHU T1 Geriatric Multi-Atlas Inventory. The atlas database contains T1 images of brain from 77 subjects (age = 34 ± 25.00). Those 77 brain images were manually parcellated into 286 structures defined in the JHU brain atlas.

A leave-one-out cross-validation was implemented by combining the pre-election method and the Lite-M1 pipeline.

2.2 Atlas Pre-selection

The scenario of pre-selection is to rank all atlases in the database according to an agreement with target image, where the top-ranked atlases are selected for segmentation process. We chose Lateral ventricle (LV) as the functional area for similarity calculation. In addition, we take advantage of the coarse segmentation result (7 labels) to propose another atlas pre-selection method. Four major labels, including white matter, gray matter, cerebral cortex, and lateral ventricle segments, were used to ranking the atlases by an overlap coefficient Dice. Dice is a statistical validation metric to evaluate the overlapping accuracy of paired structural regions.

In Lite-M1 pipeline, the target image is firstly aligned in a standard space of all atlases and its LV region is primarily labeled in the pre-processing step. In JHU brain atlas database, LV structure is an existing label and marked as atlas set $A^{LV}\left\{A_1^{LV}, A_2^{LV}, \ldots, A_{77}^{LV}\right\}$.

A new segmentation pipeline was assembled by combining the atlas pre-selection process and Lite-M1 pipeline. Dices between the LV label from the target $T1_i$ image and the rest 76 LV atlases $\left(A_i^{LV}\right)$ were calculated and sorted in ascending order. Subsets were generated by selecting the top5, top10, top15, top20 and top25 ranked atlases respectively. We adopt the same pipeline for segmentation, results based on the proposed pre-selection method were compared to that using MI similarity and 4 labels (4L), and random selection.

H. Li · C. Ye · J. Ma · H. T. Ma (✉)
Department of Electronic & Information Engineering, Harbin Institute of Technology Shenzhen Graduate School, Shenzhen, China
e-mail: heather.tma@gmail.com

S. Mori
Radiology Department, Johns Hopkins University, Baltimore, USA

3 Result and Discussion

The subcortical segmentation based on atlas pre-selection shows an overall excellent performance with the mean Dice over 0.85. Obviously, 4L- and LV-based segmentation results show a bit higher accuracy. It can be observed that with increasing number of selected atlas subsets, the segmentation accuracy would also increase in the 4L-, LV-and MI-based atlas pre-selection methods. With the pre-selection of 25 top matched atlases, the four methods give the same performance. All these comparisons demonstrate a comparable atlas pre-selection with high performance for all methods.

The proposed pre-selection method was compared to the MI-based method in terms of accuracy. For accuracy evaluation, Dice overlap of 7 subcortical regions was calculated between automatic segmentation results and manually segmented atlases. The results shows a high overall performance of 4L- and LV-based pre-selection, comparable to MI- and random-based pre-selection. All these results imply that 4L- and LV-based atlas pre-selection is a reliable method.

Reference

1. Aljabar P, Heckemann R. A, Hammers A, Hajnal J. V, and Rueckert D. Multi-atlas based segmentation of brain images: atlas selection and its effect on accuracy. Neuroimage 46, 726–738, 2009.

A Study of Alzheimer's Disease Based on DTI Gaussian Mixture Analysis

Jingbo Ma, Chun Sing Wong, and Heather T. Ma

1 Introduction

Early clinical diagnosis of Alzheimer's disease (AD) is beneficial for medications that delay its progression. However, current diagnosis of AD is still based on the observation of clinical symptoms from the family members and the MMSE score test from the doctors. Since diffusional tensor imaging (DTI) has long been used to detect microstructural changes in cerebral white matter (WM), we conducted a multi-parameter comparison on structures of WM using DTI, aiming to access the relation between neuroanatomical variations and AD onset.

2 Method

18 Alzheimer's disease patients (73.0 ± 10.0 years) and 19 healthy controls (78.7 ± 4.2 years) underwent a Philips 3T MRI Achieva scanner. A body coil for excitation and an 8-channel head coil for reception were used. DTI images were acquired with 3 b-values (0, 1000, and 2000 s/mm^2) across 32 diffusion gradient directions. Other imaging parameters were as follows: repetition time/echo time = 2000/69 ms, nominal resolution = $2.5 \times 2.5 \times 3$ mm^3, reconstruction resolution = $2 \times 2 \times 3$ mm^3, matrix size = 128×128, 33 axial slices with no inter-slice gap to cover the brain, SENSE-reduction factor is 2, and partial Fourier encoding: 3/4. The acquisition time was 15 min.

The diagnosis report was issued by experts with clinical experience. DICOM data of DWI images whose b value is 0 or 1000 was imported into the DTI-studio to do the imaging registration and calculate B0, fractional anisotropy (FA), apparent diffusion coefficient (ADC) and mean of all DWIs (MD) images. Each subject's axial T1 images were automatically segmented into 286 structures by applying MRI-Cloud pipeline, which is a state-of-the-art multi-atlas based segmentation tool. Then, the transformation matrix was calculated by registering MD images into T1 images using air linear method in the DiffeoMap software. B0, FA and ADC images were mapped into the T1 images by multiplying the transformation matrix.

According to Djamanakova's study on Alzheimer's disease [1], 27 structures showed significant difference on volume change between AD patients and age-matched healthy controls, which may be highly correlated with this disease. Thus, these 27 structures were defined as regions of interest (ROI) to be mainly analyzed on WM. For each structure, histogram was calculated and Gaussian mixture model (GMM) was applied on the histogram. Two single Gaussian curves were estimated to matching the histogram.

3 Result and Discussion

Among the anatomical structures we explored (cortical-subcortical structures, basal nuclei, thalamus and lateral ventricle), some showed visible distribution consistency is within the healthy control group while the AD patients group is not. These structures for each type of parametric images showed obvious difference between AD and control groups were listed in Table 1. For example, the difference between the two Gaussian's vertical values is much larger in AD groups. Besides, for the structures left peripheral parietal WM in MD images, although both group showed within-group consistency, a wider distribution range was observed in the healthy controls' results. All the observed results may reveal some physiological changes of

J. Ma · H. T. Ma (✉)
Department of Electronic & Information Engineering, Harbin Institute of Technology Shenzhen Graduate School, Shenzhen, China
e-mail: heather.tma@gmail.com

C. S. Wong
Li Ka Shing faculty of medicine, Department of Diagnostic Radiology, The University of Hong Kong, Hong Kong, China

Table 1 Structures that showed visible distribution difference between groups for parametric images

Images	Brain anatomical structures showed difference
B0	Posterior limb of internal capsule, caudate
FA	Hippocampus, splenium of corpus callosum, thalamus, and lateral ventricle
ADC	Genu of corpus callosum, insular
MD	Genu of corpus callosum, left peripheral temporal WM, lateral ventricle

these structures in the AD patients' brains, which could be helpful for the clinical diagnosis of AD.

Reference

1. Djamanakova A, Tang X, Li X, Faria AV, Ceritoglu C, Oishi K, Hillis AE, Albert M, Lyketsos C, Miller MI, Mori S. Tools for multiple granularity analysis of brain MRI data for individualized image analysis. Neuroimage, 101:168–76, 2014.

SVM-Based Approach for Human Daily Motion Recognition

Haitao Yang, Xinrong Zhang, Mengting Chen, and Heather T. Ma

1 Introduction

The application of human motion analysis and recognition is very extensive, involving national defense, medical, film production and many other areas. The traditional study of human motion is achieved by the video or image sequence analysis, however, it usually has a problem that the vulnerable interfering background noise may cause the body contour segmentation inaccurate results [1]. With the development of MEMS, the sensors become smaller, cheaper and cheaper. Considering the portability, accuracy and real-time, we study on design of human motion recognition system based on inertial sensors. In this study, based on support vector machine, the method of routine motion recognition shows a good generalization performance than video or image sequence analysis, which is based on the principle of structural risk minimization, such as convex objective function and efficient training algorithm and good generalization performance.

2 Methodology

2.1 Maximum Interval Classifier-SVM

SVM is a classical method in the field of pattern recognition and machine learning. For classification problems that can't be linearly separated in the input space, SVM reach a solution using a nonlinear mapping from the original input space into a high-dimensional so-called feature space, where an optimally separating hyperplane is searched.

2.2 The Dynamics of Human Motion Data

By motion capture system and posture reconstruction algorithm, we can find the three-dimensional coordinates of all the major joints of the body. In contrast, the use of three-dimensional angular spatial coordinates calculated to represent the movement, not only removes the impact of space in the absolute position and direction, as well as the input data into the lower dimensional feature vectors to reduce the amount of calculation.

2.3 Human Motion Recognition System Uses LCSS

It is extremely important to select the kernel function when we use the SVM to solve classification problems. Here we introduce the longest common subsequences (LCSS) algorithm to quantify this similarity. The time signal S[1, 2, …, m] has a certain similarity with the time signal T[1, 2, …, n]. We have:

$$R[i,j] = \begin{cases} 0 & if\ i = 0\ or\ j = 0 \\ R[i-1, j-1] + 1 & if\ \mathrm{abs}(x[i] - y[j]) < \alpha \\ & \&\ \mathrm{abs}(i-j) < \beta \\ \max(R[i-1,j], R[i,j-1]) & \text{else} \end{cases}$$

So the final similarity measure based on LCSS is:

$$\mathrm{Sim}^{LCSS}(S, T) = \frac{R(m,n)}{\max(m,n)}$$

3 Result

In experiment we use True Motion System to capture accurate human daily motion data. Ten healthy young people (7 males, 3 females, 22 to 25 years old) participated in the study. For all three groups of data, we used one of three

H. Yang · X. Zhang · M. Chen · H. T. Ma (✉)
Department of Electronic & Information Engineering, Harbin Institute of Technology Shenzhen Graduate School, Shenzhen, China
e-mail: heather.tma@gmail.com

groups as training samples, and the remaining 2 groups as test samples. using LCSS as the kernel function of SVM can achieve good recognition effect. The average recognition rate of all kinds of motion is 96.4%, and it means that the algorithm is designed reasonable. At the same time the feature extraction of the paper is effective.

4 Conclusion

We design a system to achieve human daily motion recognition based on SVM. To our knowledge, this is the first time using LCSS as the kernel function for motion recognition. We have the system in case of attitude information as possible to retain the original data to maximize compression. Although human motion recognition system has high accuracy, it still has a lot of room for improvement.

References

1. R. Green, L. Guan. Quantifying and recognizing human movement patterns from monocular video images-Part I: A new framework for modeling human motion. IEEE Transactions on Circuits and systems for Video Technology, Special Issue on Image and Video-Based Biometrics, 14: pp. 179–190, 2004.
2. I. Laptev, B. Caputo, Recognizing Human Actions: A Local SVM Approach, Pattern Recognition, 2004.

High-Speed Intravascular Spectroscopic Photoacoustic Imaging at Two Spectral Bands

Xiaojing Gong, Yan Li, Riqiang Lin, Ji Leng, and Liang Song

Abstract

The rupture of atherosclerotic plaques is the leading cause of acute coronary events. The detection of lipid content and its distribution within the plaques is critical for identifying vulnerable plaques that are prone to rupture [1]. Intravascular spectroscopic photoacoustic technology is capable of imaging the composition and structure of atherosclerotic plaques [2, 3]. To achieve accurate spectroscopic IVPA imaging, an ns-pulsed, wavelength tunable laser [e.g., optical parameter oscillator (OPO) laser] is critical. However, in previously reported IVPA systems, laser pulse energy in the order of mJ was usually required to produce decent photoacoustic signals, so the choices of laser sources were usually limited to OPO lasers of a pulse repetition rate of 10–20 Hz. The B-scan rate at a single wavelength with such lasers was 0.05–0.1 f/s (assuming 200 A-lines/B-scan); for spectroscopic imaging, the image acquisition would take several times longer. Overall, the imaging speed is becoming one of the major challenges for translating IVPA into clinical applications [4, 5]. In this study, a catheter of 0.9 mm in diameter with a novel quasi-focusing light illumination scheme is designed and developed, smaller than the critical size of 1 mm required for clinical translation. With this design, the laser fluence in the targeted imaging region was increased, which produced detectable signals with laser energy as low as ~ 30 μJ/pulse. As a result, a 1-kHz-repetition-rate, ns-pulsed optical parametric oscillator (OPO) laser was able to be utilized to achieve high-speed IVPA imaging, working at both the 1.2 and 1.7 μm spectral bands for lipid detection. Specifically, a B-scan acquisition rate of 5 Hz was achieved, ~ 100-fold faster than conventional IVPA systems operating at the similar tunable range. With the system, multi-wavelength (five wavelengths) spectroscopic IVPA imaging of both a lipid-mimicking phantom and peri-adventitial adipose tissue from a porcine vessel was demonstrated at both the 1.2 and 1.7 μm spectral bands. The significantly improved imaging speed, together with the reduced catheter size and multi-wavelength spectroscopic imaging ability, suggests that the developed high-speed IVPA technology is of great potential to be further translated for in vivo applications.

See Fig. 1.

X. Gong · Y. Li · R. Lin · J. Leng · L. Song (✉)
Shenzhen Institutes of Advanced Technology, Chinese Academy of Sciences, Shenzhen, Guangdong, China
e-mail: liang.song@siat.ac.cn

X. Gong
e-mail: xj.gong@siat.ac.cn

Y. Li
e-mail: liyan@siat.ac.cn

R. Lin
e-mail: rq.lin@siat.ac.cn

J. Leng
e-mail: ji.leng@siat.ac.cn

Fig. 1 Spectroscopic IVPA images of the peri-adventitial adipose tissue from a porcine aorta segment [inset in (**g**)]. **a–f** Representative IVPA B-scan images at both spectral bands. **g** and **h** Comparison between the IVPA spectroscopic results and the absorption spectrum of lipid. The arrows in **a–f** indicate the location of the adipose tissue, while the dashed green circles show the contour of the plastic tube (Color figure online)
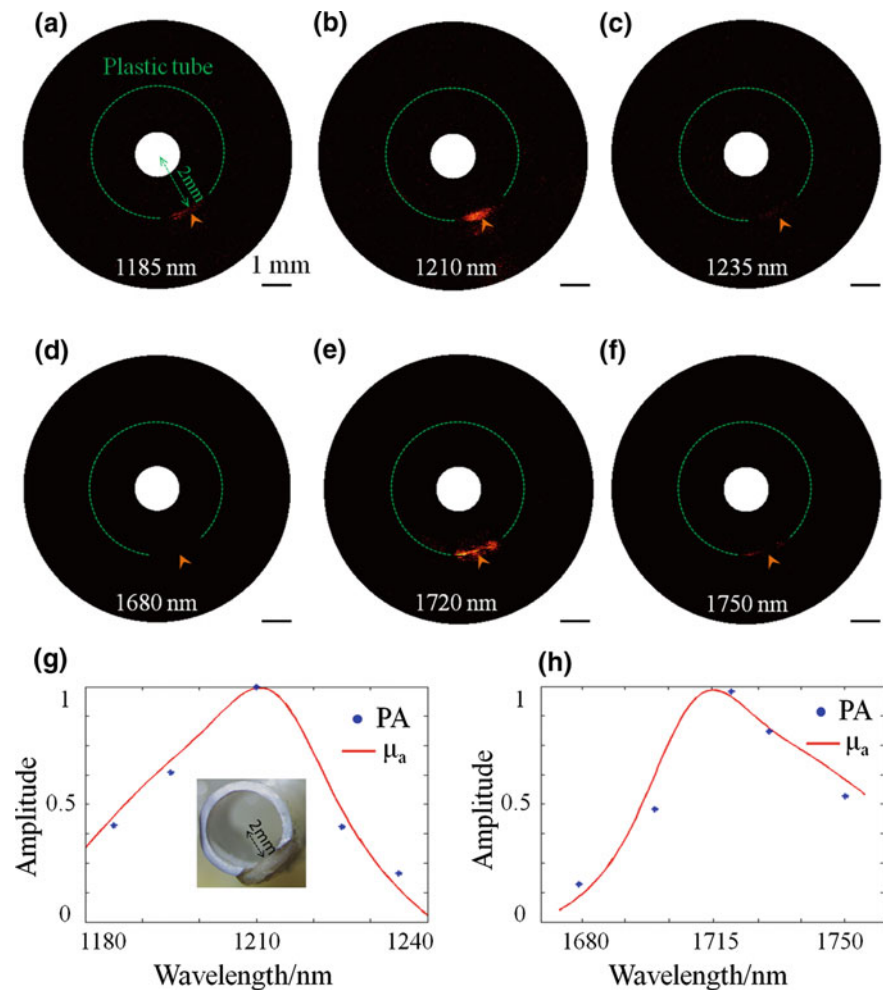
References

1. E. Falk, P. K. Shah, and V. Fuster, "Coronary Plaque Disruption," *Circulation*, vol. 92, no. 3, pp. 657–671, 1995.

2. L. H. V. Wang and S. Hu, "Photoacoustic Tomography: In Vivo Imaging from Organelles to Organs," *Science*, vol. 335, no. 6075, pp. 1458–1462, 2012.

3. K. Jansen, M. Wu, A. F. W. van der Steen, and G. van Soest, "Lipid detection in atherosclerotic human coronaries by spectroscopic intravascular photoacoustic imaging," *Opt Express*, vol. 21, no. 18, pp. 21472–21484, 2013.

4. L. Song, K. Maslov, and L. H. V. Wang, "Multifocal optical-resolution photoacoustic microscopy in vivo," *Opt Lett*, vol. 36, no. 7, pp. 1236–1238, 2011.

5. X. S. Bai, X. J. Gong, W. Hau, R. Q. Lin, J. X. Zheng, C. B. Liu, C. Z. Zeng, X. Zou, H. R. Zheng, and L. Song, "Intravascular Optical-Resolution Photoacoustic Tomography with a 1.1 mm Diameter Catheter," *Plos One*, vol. 9, no. 3, p. 0092463, 2014.

A Hybrid Non-invasive Method for the Classification of Amputee's Hand and Wrist Movements

Oluwarotimi Williams Samuel, Xiangxin Li, Xu Zhang, Hui Wang, and Guanglin Li

Abstract

The quest to develop dexterous artificial arm which supports multiple degrees of freedom for amputees has attracted a lot of study interest in the last few decades. The outcome of some of the studies had identified surface Electromyography (EMG) as the most commonly used biological signal in predicting the motion intention of an amputee. Different EMG based control methods for multifunctional prosthesis have been proposed and investigated in a number of previous studies. However, no any multifunctional prostheses are clinically available yet. One of the possible reasons would be that the residual muscles after amputations might not produce sufficient EMG signals for movement classifications. In this study, we proposed to use electroencephalography (EEG) signals recorded from the scalp of an amputee as additional signals for motion identifications. The performance of a hybrid scheme based on the combination of EMG and EEG signals in identifying different hand and wrist movements was evaluated in one transhumeral amputee. Our pilot results showed that the proposed hybrid method increased the classification accuracy in identifying different hand and wrist movements of the amputee. This suggests that the proposed method may have potential to improve the control of multifunctional prostheses.

O. W. Samuel · X. Li · G. Li (✉)
Key Laboratory of Human-Machine Intelligence-Synergy Systems, Chinese Academy of Sciences, Shenzhen Institutes of Advanced Technology, Shenzhen, 518055, China
e-mail: gl.li@siat.ac.cn

O. W. Samuel · X. Li · H. Wang
Shenzhen College of Advanced Technology, University of Chinese Academy of Sciences, Shenzhen, 518055, China

X. Zhang
Department of Biology, South University of Science and Technology, Shenzhen, China

1 Introduction

The loss of a hand or arm due to amputation or congenital deformity greatly decreases the quality of life of an individual. This is because the amputees have not only lost their grasping function, but also an important communication tool which is needed in their daily life [1]. In an attempt to restore the hope of this category of humans, several research relating to the development of assistive devices had been conducted. From the outcome of these research works, surface Electromyography (sEMG) signals recorded *Non-invasively* from muscle contractions has been identified as a major source of biological signal that could be used to control a multifunctional prosthetic device [2–4]. However, several EMG powered prosthetic control methods have been proposed recently. Despite this remarkable progress, current EMG based methods for the control of multifunctional prosthetic devices for upper limb amputees' are not yet available for clinical use [5, 6]. This is possibly due to the fact that the remaining muscles after amputation may not be able to produce sufficient EMG input signal to efficiently power the prosthesis in cases where the amputation level is severe or as a result of the presence of muscular diseases [7]. Therefore, there is need to source for an additional control signal to complement the inadequate EMG signal to efficiently classify the motion intention of amputees'.

Brain Computer Interfaces (BCIs) had been identified as a means of establishing new communication pathway between the human brain and rehabilitation devices. A variety of methods for monitoring brain activity have been proposed and they include electroencephalography (EEG), magnetoencephalography (MEG), positron emission tomography (PET), functional magnetic resonance imaging (fMRI), and optical imaging. MEG, PET, fMRI, and optical imaging methods are invasive thereby making them technically demanding and expensive. Furthermore, PET, fMRI, and optical imaging depend on blood flow and have long time constants that make them less amenable to rapid

communication [8, 9]. Among these methods, EEG seems promising because it is *Non-invasive* and has relatively short time constants that can function in most environments. In addition, EEG technique requires relatively simple and inexpensive equipment that offers the possibility of a new non-muscular communication and control channel for a practical BCI [10]. However, it has been reported in literature that prosthetic devices which solely depend on EEG signal for their control are not yet acceptable due to their relatively low level of accuracy [11]. Nevertheless, EEG signals have been proved to be strong candidate of additional inputs for the control of wearable robotics [12].

Recent advances in EMG and EEG studies are reported as follows; Shibasaki and Rothwell [13] studied the correlation between EMG-EEG mainly to investigate the cortical mechanism underlying the central motor control for voluntary movements and the physiological mechanism responsible for involuntary movements. Ferreira1 et al. [14], developed two Human-Machine Interfaces in which the first was based on acquired EMG signal and the second on EEG signal to assist people with neuromotor disability recover on time. Ramalingam et al. [15], compared the performance of EMG based prosthesis with its EEG counterpart with respect to classification accuracy when various hand movements were performed. Thilina et al. [7], reviewed the fusion of EEG and EMG for bio-robotics applications with the aim of identifying important design features in such a hybrid system. However, studies on the use of EMG and EEG signals in identifying amputees' hand and wrist movements have not been conducted. Hence, this study investigates and proposes the use of a hybrid non-invasive method based on EMG and EEG signals for the classification of amputees' hand and wrist movements.

2 Methods

2.1 Characteristics of the Recruited Subject

A 49 years old male transhumeral amputee whose left hand was amputated 3 years ago was recruited as the subject in this study. The subject was properly examined to ensure he meets up with the requirements of the study. Meanwhile, the length of his residual arm was measured to be 20 cm. The subject was given written informed consent and he provided permission for the publication of his photographs for scientific and educational purposes. Lastly, the protocol of this study was approved by the Shenzhen Institutes of Advanced Technology Institutional Review Board, Chinese Academy of Sciences, China.

2.2 Equipment Setup and Data Acquisition

A 64 Channel standard EEG recording cap with tin electrodes of 6 mm central opening in its middle was placed on the scalp of the subject in order to acquire EEG data corresponding to hand and wrist movement tasks such as; hand close (HC), hand open (HO), wrist extension (WE), wrist flexion (WF), and no movement (NM) as shown in Fig. 1.

The cap's electrode sites were placed according to standard 10–20 EEG system. Figure 1a is a pictorial representation of the experiment setup in readiness for EEG and EMG data acquisition. The EEG device was connected to Neuroscan software (version 4.3).

A High Density (HD) EMG system (REFA 128 model, TMS International, REFA, Oldenzaal, The Netherlands) was used for EMG data collection. The REFA 128 model is a stationary system measuring multiple monopolar electrophysiological variables. The REFA system has a special reference amplifier and a shielded input cable to eliminate main interference or movement artifact caused by the cables. In this study, only 32 channels of the HD EMG system were used, and the electrodes were placed in a grid format around the biceps brachii and triceps muscle of the amputee's residual arm (Fig. 1a). In addition, an electrode which denotes the ground electrode was placed on the wrist of the right intact arm of the subject.

After setting up the EEG and EMG data acquisition devices, the subjects was introduced to the five classes of movements (HC, HO, WE, WF, and NM) and as well given some time to practice performing the movements. During the experiment, the subject performed each class of movement for 5 s and rested for another 5 s before observing the preceding class of movement. The 5 s rest between two consecutive class of movements was to prevent the subject from undergoing both muscle and mental fatigue. In each experiment, the data were acquired in five consecutive trials. Meanwhile, in each trial, all classes of hand and wrist movements were repeated 10 times and held for 5 s, producing 50 s of EEG and EMG recordings per class. Lastly, the EEG and EMG data corresponding to the 5 classes of movements were simultaneously recorded and stored.

2.3 Data Processing and Pattern Recognition

All the recorded data were analyzed offline with Matlab version 8.3, R2014a (The Mathworks, Massachusetts). A sample model of the acquired EMG data is represented by Eq. 1.

Fig. 1 **a** EEG and EMG Equipment setup for data collection; while **b**, **c**, **d**, **e**, and **f** are the classes of hand movements
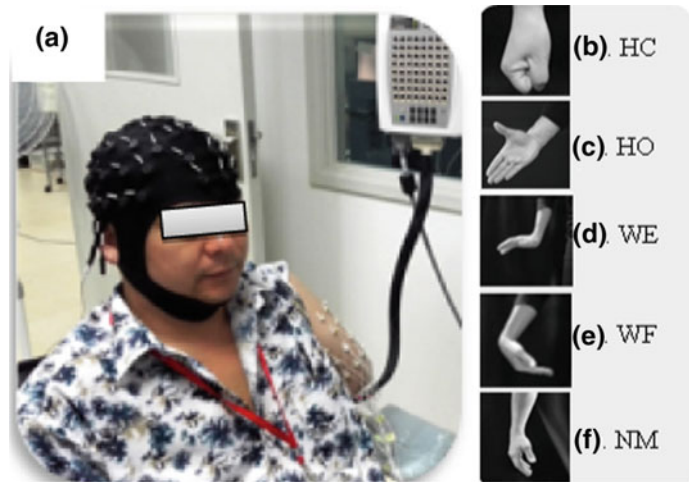
$$x_{emg}(n) = \sum_{r=1}^{N-1} h(r)e(n-r) + w(n) \qquad (1)$$

where $x_{emg}(n)$ is the modeled EMG signal, e(n) is the point processed which represents the firing impulse, h(r) denotes the motor unit action potential which represents a combination of all muscle fibers of a single motor unit, w(n) denotes the zero mean additive white Gaussian noise, while N represents the number of motor unit firing at a particular point in time. All channels of the EMG signals were filtered with a band-pass filter (cut-off frequency from 10 to 500 Hz) and then sampled at the rate of 1024 Hz. Meanwhile a model which represents the integrated acquired EEG signal is presented in Eq. 2. This signal is calculated as a summation of values of the EEG signal amplitude and noise over time from all the electrode channels.

$$x_{eeg}(n) = \sum_{r=1}^{n} x_r + A(r) \qquad (2)$$

where $x_{eeg}(n)$ denote the overall recorded EEG signal, x_r represents the EEG signal obtained from the rth electrode channel, A(r) denotes the noise in the EEG signal, and n is the total number of EEG electrode channels considered. EEGLAB version 10.0 toolbox (Free Software Foundation, Inc. 1991) was used to preprocess the EEG data in order to remove the baseline from each channel and extract relevant EEG epochs from the data. The recorded EEG signals were band-pass filtered between 0.05 and 100 Hz and as well sampled at the rate of 1000 Hz. A notch filter of 50 Hz was used to remove the power-line noise from the EEG and EMG recordings. Both preprocessed data (EMG and EEG)

were later combined into a single dataset and thereafter segmented into a series of 150 analysis window at a time increment of 100 ms. Four commonly used time domain features: mean absolute value (MAV), number of zero crossings (ZC), waveform length (WL), and number of slope sign changes (SSC) were extracted from each analysis window [16]. A matrix containing the four extracted features was obtained and passed to a 5-fold cross validation function. Figure 2 presents a diagram of the proposed hybrid method. This figure simply shows the key stages involved in the realization of the proposed hybrid method for hand and wrist movement classification.

The concept of linear discriminant analysis (LDA) which has been widely applied in the field of pattern classification [17], was used to build a classifier to classify the hand and wrist movements in this study. In order to ensure proper performance of the classifier, a 5-fold cross validation technique was used to partition the matrix of the extracted four time domain features into training, testing, and validation sets before feeding them into the classifier. The LDA classifier then performs the classification task. The performance of the trained LDA classifier in identifying the different classes of hand and wrist movements was computed using the formula presented in Eq. 3.

$$CA_{trained\,LDA} = \frac{\sum_{i=1}^{N} CCS_i}{\sum_{i=1}^{n} TS_i} * 100\% \qquad (3)$$

where $CA_{trained\,LDA}$ represents the classification accuracy of the trained LDA classifier, CCS_i is the ith correctly classified sample, N denotes number of correctly classified samples, TS_i is the ith testing sample, and n represents the number of testing samples.

Fig. 2 Architecture of the proposed hybrid method
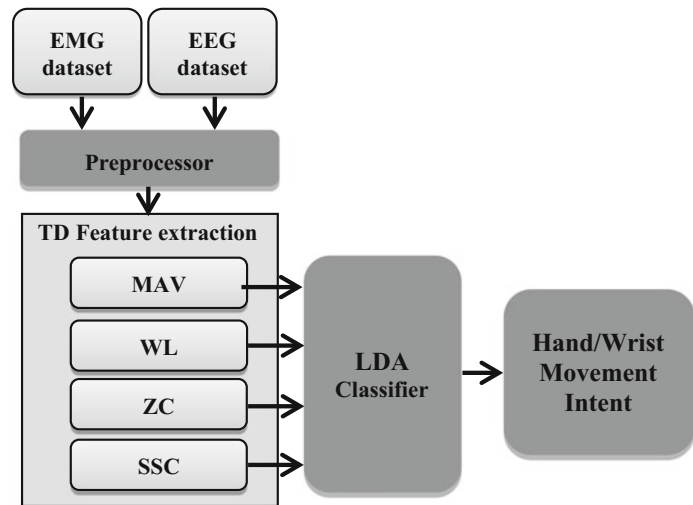
3 Results and Discussion

From the outcome of our experiments, the classification performances of EMG, EEG, and the hybrid (EMG + EEG) methods with various configurations across the five classes of hand and wrist movements are presented in the confusion matrices shown in Tables 1, 2 and 3. From the results presented in Tables 1, 2 and 3, the diagonal of each confusion matrix denotes the classification accuracy of the five categories of hand and wrist movements.

Meanwhile, in each confusion matrix, the value marked in red represents the class of hand/wrist movement with the

Table 1 Classification accuracy with ONLY 32 EM G electrodes (%)

	HC	HO	WE	WF	NM
HC	84.600	4.3800	6.9200	0.5900	3.5000
HO	6.3300	68.730	6.5800	14.670	3.6900
WE	6.1800	5.4800	82.630	2.6700	3.0400
WF	2.9200	20.660	6.8000	63.360	6.2600
NM	8.3700	10.300	5.4600	13.320	62.520

Table 2 Classification accuracy using only 64 EEG electrodes (%)

	HC	HO	WE	WF	NM
HC	74.390	9.7800	2.5400	4.4900	8.7900
HO	8.3900	76.620	7.5100	3.8100	3.6600
WE	3.6200	9.8300	81.870	2.3400	2.3400
WF	6.3200	7.1100	3.1400	80.570	2.8600
NM	7.2300	5.0900	2.3700	2.3300	82.990

Table 3 Classification accuracy with the combination of 32EMG + 64EEG electrodes (%)

	HC	HO	WE	WF	NM
HC	93.840	1.9400	1.3200	1.1600	1.7400
HO	1.9600	89.290	3.6800	3.1300	1.9400
WE	1.5700	2.7400	94.310	1.9000	1.1900
WF	1.7600	4.0100	1.3400	89.920	2.9700
NM	3.6300	3.4900	9.4000	2.3300	89.610

highest classification accuracy. For instance, hand close (HC) has the highest classification accuracy (**84.6%**), while no movement (NM) has the lowest classification accuracy (**62.5%**) as shown in Table 1. The average classification accuracy for each category of upper limb movement across the three configuration technique is presented in Fig. 3.

From the plot shown in Fig. 3, it is observed that wrist extension attained a classification accuracy of 86.3% which is the highest among the others while hand open had the least (68.7%) classification accuracy. The overall average performance of the three examined electrode configuration methods is reported as follows in Table 4.

From Table 4, when 32-EMG electrodes were used, the average classification accuracy was 72.4% which is the least among the others, with a 64-EEG electrode configuration, an average classification accuracy of 79.3% was recorded which shows an improvement over the 32-EMG configuration. With all the 96 (32EMG and 64EEG) electrodes, an average classification accuracy of 91.4% was attained which is the highest of all the electrode configurations. Going by the analysis of the results obtained from various electrode configurations, it is obvious that EMG signal alone is not sufficient to effectively classify multiple classes of hand/wrist

Fig. 3 Average classification accuracy of the hand movements across the three electrode configuration
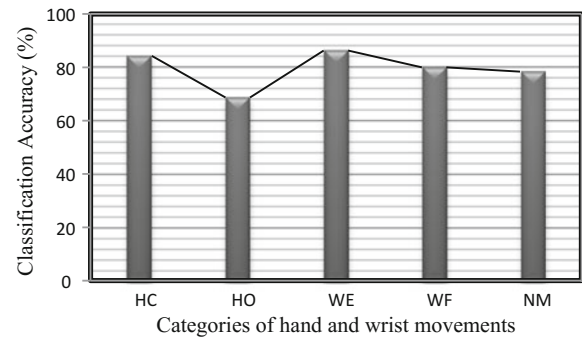

Table 4 Average classification accuracy of 5 classes of hand/wrist movements across all electrode configurations (%)

Methods	Hand/Wrist movements					Average
	HC	HO	WE	WF	NM	
32-EMG	84.6	68.7	82.6	63.4	62.5	72.4
64-EEG	74.4	76.6	81.9	80.6	82.9	79.3
32EMG + 64EEG	93.8	89.3	94.3	89.9	89.6	91.4

movements likewise the EEG signal alone. Rather, the combination of both the EMG and EEG signals looks promising in the identification of multiple classes of hand/wrist movements.

4 Conclusion

Several studies have proposed different strategies for the control of multifunctional prosthesis for upper limb amputees'. However, currently, multifunctional prosthetic devices are not yet available for either clinical or commercial use. This is because the performance of the existing control strategies are not satisfactory enough to meet the modern day clinical and commercial needs. This study has investigated the use of EEG signal as an additional input to the commonly used EMG signal for the identification of five classes of hand and wrist movements of a transhumeral amputee. Experimental results show that the proposed hybrid method has better performance in terms of classification accuracy compared with the individual (EMG or EEG) methods. The overall performance of the hybrid method seems promising and could aid the development of practical multifunctional prostheses.

Conclusively, in our future work, more amputees will be recruited and the optimal electrode channels shall be determined in order to further validate the effectiveness and as well increase the acceptability of the proposed hybrid method.

References

1. T.A. Kuiken, G. Li, B.A. Lock, et al, "Targeted Muscle Reinnervation for Real-time Myoelectric Control of Multifunction Artificial Arms," The Journal of the American Medical Association, vol. 301, no. 6, pp. 619–628, 2009.
2. G. Li, and T.A. Kuiken, "EMG Pattern Recognition Control of Multifunctional Protheses by Transradial Amputees," 31st Annual International Conference of the IEEE EMBS, pp. 6914–6917, 2009.
3. U. Sahin and F. Sahin, "Pattern Recognition with surface EMG Signal based on Wavelet Transformation," IEEE Int. Conf. on Systems, Man, and Cybernetics, Oct. 14–17, 2012, COEX, Seoul, Korea, pp. 295–300.
4. M. Asghari, O.H. Hu, "Myoelectric control systems: A survey", Biomedical Signal Processing and Control, pp. 275–294, 2007.
5. G. Li, A.E. Schultz, and T.A. Kuiken, "Quantifying Pattern Recognition-Based Myoelectric Control of Multifunctional Transradial Prostheses," IEEE Transactions on Neural Systems and Rehabilitation Engineering, vol. 18, no. 2, pp. 185–192, 2010.
6. Y.U. Huang, K. Englehart, and B. Hudgins, "A Gaussian mixture model based classification scheme for myoelectric control of powered upper limb prostheses," IEEE Transactions on Biomedical Engineering, vol. 52, no. 11, pp. 1801–1811, 2005.
7. D.L. Thilina, T. Kenbu, H. Yoshiaki, and K. Kazuo, "Towards Hybrid EEG-EMG-based control approaches to be used in bio-robotics applications: current status, challenges, and future directions," Paladyn Journal of Behavioral Robotics, vol. 4(2), pp. 147–154.

8. J.R. Wolpaw, N. Birbaumer, D.J. McFarland, G. Pfurtscheller, and T.M. Vaughan, "Brain Computer Interfaces for Communication and Control," Clinical Neurophysiology 113 (2002), pp. 767–791.

9. D.J. McFarland, L.M. McCane, and J.R. Wolpaw, "EEG-based communication: short-term role of feedback," IEEE Transactions on Rehabilitation Engineering, vol. 6, pp. 7–11, 1998.

10. N. Birbaumer, "Breaking the silence: Brain—computer interfaces (BCI) for communication and motor control," Psychophysiology, 43 (2006), pp. 517–532.

11. R.W. Jonathan, B. Niels, J.M. Dennis, P. Gert, M.V. Theresa, "Brain-computer interfaces for communication and control," Clinical Neurophysiology, 113(2002), 767–791.

12. K. Kiguchi and Y. Hayashi, "Motion Estimation based on EMG and EEG Signals to Control Wearable Robots," IEEE International Conference on Systems, Man, and Cybernetics, pp. 4214–4218, 2013.

13. H. Shibasaki and J.C. Rothwell, "EMG-EEG Correlation," Recommendations for the Practice of Clinical Neurophysiology: Guidelines of the International Federation of Clinical Physiology (EEG Suppl. 52), pp. 269–274, 1999.

14. A. Ferreira1, W.C. Celeste1, F.A. Cheein, T.F. Bastos-Filho, M. Sarcinelli-Filho, and R. Carelli, "Human-machine interfaces based on EMG and EEG applied to robotic systems," Journal of NeuroEngineering and Rehabilitation 2008, 5:10.

15. V.V. Ramalingam, S. Mohan, V. Sugumaran, "A Comparison of EMG and EEG signals for prostheses control using decision tree," International Journal of Research in Computer Applications & Information Technology, vol. 1, no. 1, pp. 01–08, 2013.

16. G. Li, Y. Li, L. Yu, and Y. Geng, "Conditioning and sampling issues of EMG signals in motion recognition of multifunctional myoelectric prostheses," Annals of Biomedical Engineering., vol. 39, no. 6, pp. 1779–1787, 2011.

17. L.J. Hargrove, G. Li, K.B. Englehart, and B.S. Hudgins, "Principal Components Analysis Preprocessing for Improved Classification Accuracies in Pattern-Recognition-Based Myoelectric Control," IEEE Trans. on Biomedical Engineering, vol. 56, no. 5, pp. 1407–1414, 2009.

The Research and FPGA Implementation of ECG Signal Preprocessing

Wenjun Su, Yunping Liang, Mengni Li, and Ye Li

Abstract

In this paper, we studied ECG signal preprocessing and implemented it into a Field Programmable Gate Array (FPGA). The processing includes band pass filter, pseudo differential identification and mathematical morphology transform.

1 Instruction

ECG signal is generally millivolt level [1] and it contains three parts noises and pseudo different is not to be ignored which can cause misjudgment of R wave. In our previous work, we developed a handheld device named Mini Holter used to sample ECG signals and transmit signals to cloud computing platform as shown in Fig. 1a. Now, we proposed a System-on-Chip (SOC) scheme integrating the ECG signal processing into an ECG signal special chip shown in Fig. 1b. This paper presents a FPGA implementation based on the ECG biomedical embedded system and Xilinx technology, and performs ECG pre-processing [2].

In this paper, Sect. 2 presents the main algorithms design of ECG signal preprocessing. The conclusion and the recommendation for future work are discussed in Sect. 3.

2 ECG Preprocessing Algorithms

2.1 FIR Band Pass Filter

FIR band pass filter is used to filter out three parts noises. We chose the pass band of FIR filter in 5–45 Hz. The effect of filter denoising is good. The structure of FIR band pass filter was implemented by pipe-line.

2.2 Pseudo Differential Identification

Pseudo differential identification is used to do more filtration for the ECG signal after denoising, which designed to reduce and remove the normal pseudo differential that helpful for reducing misjudgment of R wave. The basic idea of the algorithm is by refreshing the threshold value range to decide the ECG mean square difference.

2.3 Mathematical Morphology Transform

The mathematical morphology transform is to transform the denoising ECG data, to extrude the QRS complex, thus easily to determine the position of QRS wave. The morphology transform takes the structure function as the triangle, runs the erosion and dilation operation. The hardware implementation of mathematical morphology transforms adopted the method of pipe-line. The pipeline design chart is shown in Fig. 2.

W. Su · Y. Liang · M. Li · Y. Li (✉)
Research Centre for Biomedical Information Technology,
Shenzhen Institutes of Advanced Technology, CAS, Shenzhen,
China
e-mail: ye.li@siat.ac.cn

W. Su · M. Li
School of Software Engineering, University of Science and
Technology of China, Hefei, China
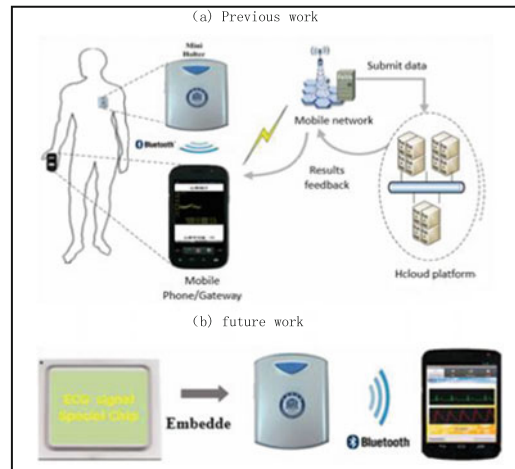
Fig. 1 ECG signal acquisition and analysis sketch
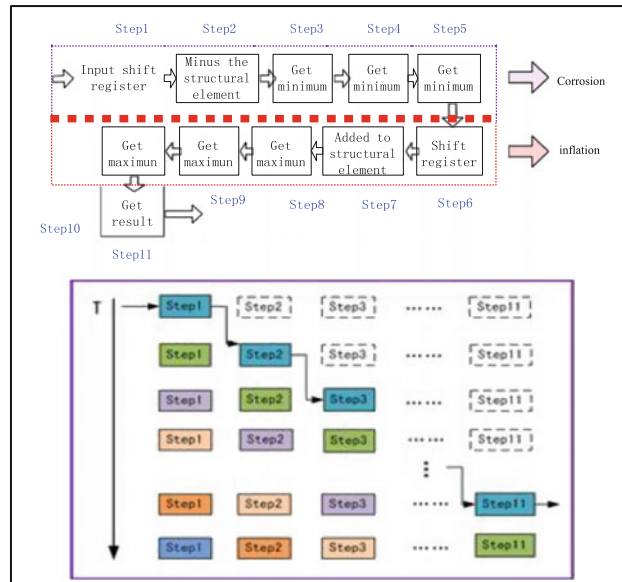
Fig. 2 Mathematical morphology transforms pipe-line flow

3 Conclusion

In the future, we will design the algorithm of R wave extraction and HRV analysis.

References

1. Thakor N, Webster JQ, Tompkius WJ. Estimation of QRS complex powerSpectra for design of QRS filter. IEEE Transactions on BME. 1984, 31(11): 702–706.
2. Chia-Ching Chou, et al. A novel wireless biomedical monitoring system with dedicated FPGA-based ECG processor [J]. Consumer Electronics (ISCE), 2012 IEEE 16th International Symposium on.

Comparison of the Correlation of Different Pulse Transit Time Parameters to Blood Pressure

Wan-Hua Lin, Oluwarotimi Williams Samuel, Qing Liu, Yuan-Ting Zhang, and Guanglin Li

Abstract

Estimation of blood pressure (BP) based on pulse transit time (PTT) is of great interest since it can estimate BP continuously and cufflessly. In previous studies, different character points were available in ECG and in photoplethysmogram (PPG) for calculating PTT. The present study aimed at comparing the correlation of BP to different PTT parameters calculated using different character points of ECG and PPG. PTT parameters were calculated as the time interval from R peak, Q valley, or S valley of ECG to the peak or valley of the first derivative of the PPG. Correlations of beat-to-beat BP to the different beat-to-beat PTT parameters were calculated for the selected 13 datasets with a total of 3910 heart beats data. The results showed that the PTT as the time interval from Q valley of the ECG to the peak of the first derivative of the PPG gave the best parameter which correlates with both the systolic blood pressure (SBP, $r = -0.62 \pm 0.14$) and the diastolic blood pressure (DBP, $r = -0.45 \pm 0.18$). Therefore, this method of determining PTT would be useful to improve the accuracy of estimating BP continuously and cufflessly.

W.-H. Lin · O. W. Samuel · G. Li (✉)
Key Laboratory of Human-Machine Intelligence-Synergy Systems, Shenzhen Institutes of Advanced Technology, Chinese Academy of Sciences, Shenzhen, 518055, China
e-mail: gl.li@siat.ac.cn

W.-H. Lin · O. W. Samuel
Shenzhen College of Advanced Technology, University of Chinese Academy of Sciences, Shenzhen, 518055, China

Q. Liu · Y.-T. Zhang
Joint Research Center for Biomedical Engineering, The Chinese University of Hong Kong, Shatin, N.T., Hong Kong

Y.-T. Zhang
Apple Inc., Silicon Valley, CA, USA

1 Introduction

ESTIMATION of blood pressure (BP) based on pulse transit time (PTT) is of great interest since it can estimate BP continuously and cufflessly [1–11]. PTT is defined as the transmission time of the blood pulse wave from the cardiac aortic valve to the peripheral artery, and is commonly calculated as the time interval from a character point of ECG to a character point of photoplethysmogram (PPG) captured from the peripheral. It is based on the principle that the higher the BP is, the shorter time it would take for the transmission of the blood pulse wave from the heart to the peripheral. In previous studies, different character points were available in ECG and in PPG for calculating PTT. The present study is aimed at comparing the correlation of BP to different PTT parameters calculated using different character points of ECG and PPG.

2 Methods

2.1 Protocol

Nine healthy adults (aged 28 ± 4 years) were recruited for the experiment. Five data sets of ECG, PPG, and continuous BP waves were captured continuously at a sample rate of 1000 Hz during the experiment for each subject. The first dataset was captured for 5 min when the subject was sitting on a chair quietly after arrival. Another 5 min of dataset was recorded while the subject maintained the same initial sitting position. Thereafter, three data sets were recorded for 5 min after each bout of exercise (running on a treadmill) for three times, respectively. During the experiment, ECG and finger PPG were recorded by an in-house system. Continuous BP wave was captured by Finapres® (Finapres Medical System, The Netherlands). Details of the experimental procedure can be found in a previous study [12].

2.2 Data Analysis

R peak, Q valley and S valley points of the ECG, peak and valley points of the first derivative of the PPG, peak (i.e., SBP) and valley (i.e., DBP) points of the BP wave were identified by procedures automatically, and were double-checked manually. The procedures were performed by the combinations of following processes: industry frequency interference cancelation, wavelet transform, amplitude threshold setting, extreme maximum points and extreme minimum points detection, redundant points cancelation, and missed points supplement. Several PTT parameters were calculated as follows: PTT1 was calculated as the time interval from R peak of the ECG to the peak of the first derivative of the PPG. PTT2 was calculated as the time interval from R peak of the ECG to the valley of the first derivative of the PPG. PTT3 was calculated as the time interval from Q valley of the ECG to the peak of the first derivative of the PPG. PTT4 was calculated as the time interval from Q valley of the ECG to the valley of the first derivative of the PPG. PTT5 was calculated as the time interval from S valley of the ECG to the peak of the first derivative of the PPG. PTT6 was calculated as the time interval from S valley of the ECG to the valley of the first derivative of the PPG. The definitions of the PTT parameters are shown in Fig. 1. In order to avoid the influence of noise, only the dataset that contained more than 50 continuous heart beats available were used for the analysis. A total of 3910 heart beat data from 13 datasets were eligible for analysis. Correlation coefficients were calculated between beat-to-beat BP series and different beat-to-beat PTT series for each dataset. Thereafter, Mean ± SD were calculated among the results of the eligible 13 datasets. All the analysis were performed off-line using Matlab®

3 Results

Figure 2 shows the results of the character points detected in the ECG, in the first derivative of the PPG, and in the BP wave from a 5-min length of dataset. R peak (denoted with black plus sign), Q valley (denoted with blue plus sign) and S valley (denoted with green plus sign) points of the ECG, peak (denoted with black plus sign) and valley (denoted with blue plus sign) points of the first derivative of the PPG, peak (denoted with black plus sign) and valley (denoted with blue plus sign) points of the BP wave were respectively derived. The values of the peak points of the BP wave represent the beat-to-beat SBP, while valley points represent the beat-to-beat DBP.

Figure 3 illustrates the results of the beat-to-beat SBP, DBP, PTT1–PTT6 series that were calculated from the same dataset as in Fig. 2. As can be seen from the Fig. 3, the PTT series fluctuated contrary to the SBP and DBP series.

Table 1 presents the correlation coefficients (which are expressed as Mean ± SD) between BP and different PTT parameters of the entire 13 datasets. All the six PTT parameters showed negatively correlated with SBP and DBP. Of the six PTT parameters, PTT3, which is calculated as the time interval from Q valley of the ECG to the peak of the first derivative of the PPG, was the best parameter to correlate with SBP and DBP. The correlation coefficients were −0.62 ± 0.14 (Mean ± SD) between SBP and PTT3, and −0.45 ± 0.18 between DBP and PTT3, respectively.
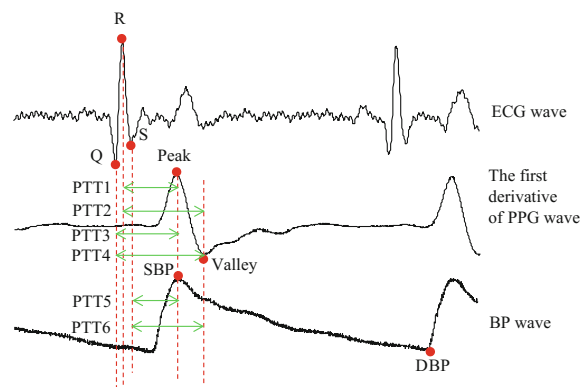
Fig. 1 The definitions of the PTT parameters. PTT indicates pulse transit time; PPG, photoplethysmogram; BP, blood pressure; SBP, systolic blood pressure; DBP, diastolic blood pressure

Fig. 2 An example of detecting character points of the ECG, the first derivative of the PPG, and the BP wave from a 5-min length of dataset. PPG indicates photoplethysmogram; BP, blood pressure
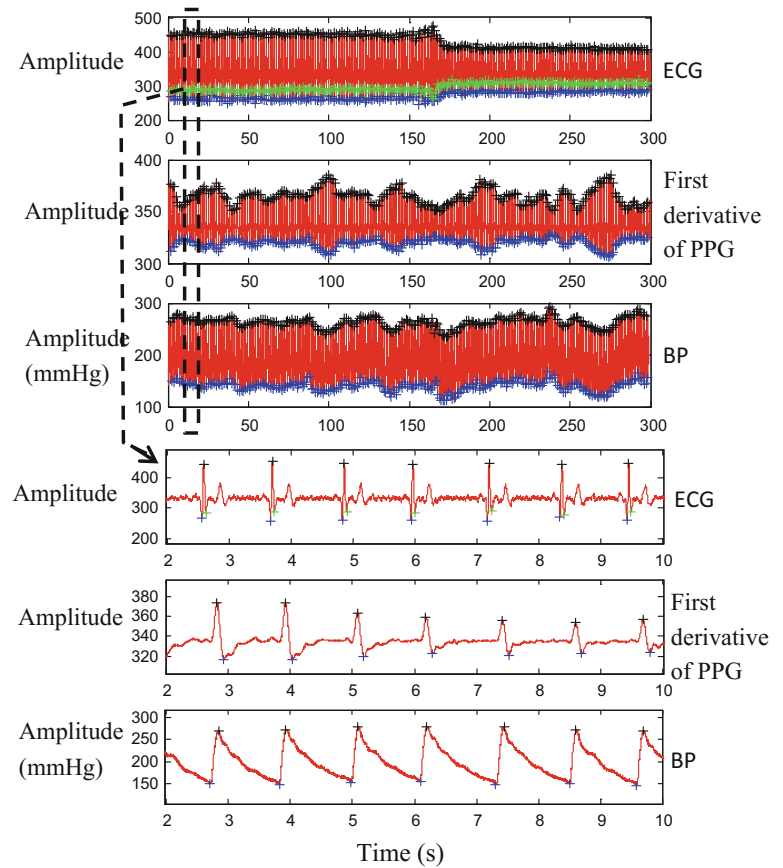
Fig. 3 An example of the BP and PTT series that were extracted from the 5-min length of dataset as in Fig. 2. PTT indicates pulse transit time; SBP, systolic blood pressure; DBP, diastolic blood pressure
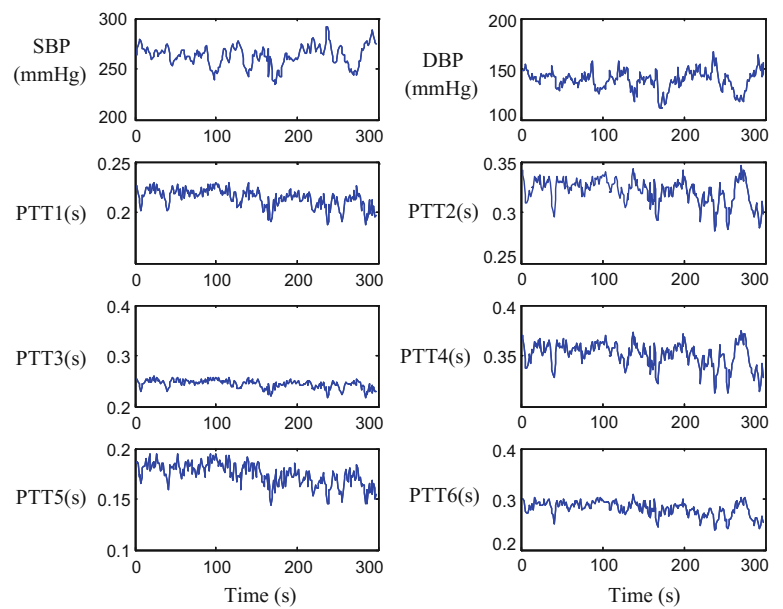
Table 1 Correlation coefficients between pulse transit time parameters and blood pressure

	SBP	DBP
PTT1	-0.62 ± 0.16	-0.44 ± 0.19
PTT2	-0.59 ± 0.14	-0.42 ± 0.16
PTT3	**-0.62 ± 0.14**	**-0.45 ± 0.18**
PTT4	-0.60 ± 0.13	-0.43 ± 0.16
PTT5	-0.56 ± 0.15	-0.39 ± 0.18
PTT6	-0.57 ± 0.14	-0.39 ± 0.17

PTT indicates pulse transit time; *SBP* systolic blood pressure; *DBP* diastolic blood pressure

4 Conclusions and Discussions

The present study compared the correlation of different PTT parameters to BP, and concluded that PTT3, which is calculated as the time interval from Q valley of the ECG to the peak of the first derivative of the PPG, is the best parameter to correlate with the SBP and DBP.

Though PTT was widely used for estimating cuffless BP in the laboratory [1–11], it has been hardly used in clinical practice since the accuracy still needs to be optimized. In previous studies, different character points in the ECG and PPG were used for calculating the PTT. Some previous studies proposed the use of vessel transit time (VTT), which is calculated by deducting the pre-ejection period (PEP) time from the PTT, for BP estimation [1], while some studies used the time interval from the R peak of the ECG to different character points of the PPG for BP estimation [6]. The definitions of the time indices are different in different studies. In another study, they defined pulse arrival time (PAT) as the time interval between the R peak of the ECG and the foot/onset of the PPG, which is the same as the definition of PTT1 in our study and the same as PPT in the study of [1]. The time index (they defined it as PTT) used in that study is also calculated by the subtraction of PEP [1], which is the same as the definition of VTT in the study of [13]. Until now, time index by the subtraction of PEP is not well correlated with BP. Over all, PTT1, which is calculated as the time interval from the R peak of the ECG and the foot of the PPG, that is, the peak of the first derivative of the PPG, is the most widely accepted method for estimating BP [3]. The correlation coefficients were -0.62 ± 0.16 between PTT1 and SBP, and -0.44 ± 0.19 between PTT1 and DBP in this study. The results are better than those of PTT2, PTT4, PTT5, and PTT6. However, the correlation of PTT3 to SBP/DBP is a litter better than the widely used PTT1 in this study.

In future studies, more efforts need to be directed towards improving the accuracy of BP estimation in order to facilitate their use in clinical and commercial applications. Beside optimizing the calculation of PTT, there are some other promising methods that can be used to improve existing BP estimation algorithm, such as the morphology features of the PPG wave [14].

References

1. C. Ahlstrom, *et al.*, "Noninvasive investigation of blood pressure changes using the pulse wave transit time: a novel approach in the monitoring of hemodialysis patients," *J Artif Organs,* vol. 8, pp. 192–7, 2005.
2. F. Barcelo-Rico, *et al.*, "Adaptive calibration algorithm for plasma glucose estimation in continuous glucose monitoring," *IEEE J Biomed Health Inform,* vol. 17, pp. 530–8, May 2013.
3. Y. Choi, *et al.*, "Noninvasive cuffless blood pressure estimation using pulse transit time and Hilbert-Huang transform," *Computers & Electrical Engineering,* vol. 39, pp. 103–111, Jan 2013.
4. H. Gesche, *et al.*, "Continuous blood pressure measurement by using the pulse transit time: comparison to a cuff-based method," *European Journal of Applied Physiology,* vol. 112, pp. 309–315, Jan 2012.
5. I. C. Jeong and J. Finkelstein, "Optimizing Non-Invasive Blood Pressure Estimation Using Pulse Transit Time," *Medinfo 2013: Proceedings of the 14th World Congress on Medical and Health Informatics, Pts 1 and 2,* vol. 192, pp. 1198–1198, 2013.
6. Y. Li, *et al.*, "Characters available in photoplethysmogram for blood pressure estimation: beyond the pulse transit time," *Australas Phys Eng Sci Med,* vol. 37, pp. 367–76, Jun 2014.
7. Q. Liu, *et al.*, "Attenuation of systolic blood pressure and pulse transit time hysteresis during exercise and recovery in cardiovascular patients," *IEEE Trans Biomed Eng,* vol. 61, pp. 346–52, Feb 2014.
8. C. C. Poon and Y. T. Zhang, "Cuff-less and noninvasive measurements of arterial blood pressure by pulse transit time," *Conf Proc IEEE Eng Med Biol Soc,* vol. 6, pp. 5877–80, 2005.
9. S. Puke, *et al.*, "Blood pressure estimation from pulse wave velocity measured on the chest," *Conf Proc IEEE Eng Med Biol Soc,* vol. 2013, pp. 6107–10, 2013.

10. X. F. Teng and Y. T. Zhang, "An evaluation of a PTT-based method for noninvasive and cuffless estimation of arterial blood pressure," *Conf Proc IEEE Eng Med Biol Soc,* vol. 1, pp. 6049–52, 2006.

11. M. Y. Wong, *et al.*, "An evaluation of the cuffless blood pressure estimation based on pulse transit time technique: a half year study on normotensive subjects," *Cardiovasc Eng,* vol. 9, pp. 32–8, Mar 2009.

12. Q. Liu, *et al.*, "Time-frequency analysis of variabilities of heart rate, systolic blood pressure and pulse transit time before and after exercise using the recursive autoregressive model," *Biomedical Signal Processing and Control,* vol. 6, pp. 364–369, Oct 2011.

13. J. Proenca, *et al.*, "Is Pulse Transit Time a good indicator of Blood Pressure changes during short physical exercise in a young population?," *2010 Annual International Conference of the Ieee Engineering in Medicine and Biology Society (Embc),* pp. 598–601, 2010.

14. H. Fukushima, *et al.*, "Cuffless Blood Pressure Estimation using only Photoplethysmography based on Cardiovascular parameters," *2013 35th Annual International Conference of the Ieee Engineering in Medicine and Biology Society (EMBC),* pp. 2132–2135, 2013.

Relative Analysis Between Curative Effect Evaluation and Electroencephalograph of Stroke Patient in Convalescence

Xiao-Mao Fan, Xing-Xian Huang, Ye Li, Hai-Bo Yu, and Yun-Peng Cai

Abstract

Assessment of stroke mainly depends on clinical symptoms, however, it can only detect static reaction of brain function. Electroencephalograph (EEG) with no-invasive and dynamic is an important means to monitor electrophysiological pathological states of the cerebral cortex. To get insights into the correlation between factors of EEG and factor of curative effect evaluation, 84 stroke patients in convalescence less than 6 months were recruited. All of them received twice 19 leads EEG examinations of patients in hospital before and after the discharge as well as scale of evaluation criteria for strokes of Traditional Chinese Medicine (TCM). Pearson's correlation analysis method was used for EEG data on 114 factors, which 23 were found to be relative with curative effect evaluation factor (p value < 0.05).

Keywords

Relative analysis • EEG • Stroke

1 Introduction

Recently, Electroencephalogram (EEG) becomes one of the first diagnostic tools available in hospital to reflect patients' brain activity and syndrome of stroke [1]. However, assessment of stroke mainly depends on clinical symptoms such as Computed Tomography (CT), Magnetic Resonance Imaging (MRI), which can only detect static reaction of brain function. And EEG with no-invasive and dynamic is an important means to monitor electrophysiological pathological states of the cerebral cortex. To get insights into the correlation between EEG and curative effect evaluation of stroke patient in convalescence, this paper uses Pearson's correlative analysis method to analyze EEG data and curative effect evaluation.

2 Methods

84 patients in convalescence less than 6 months were recruited. All of them received twice 19 leads EEG examinations of patients in hospital before and after the discharge as well as scale of evaluation criteria for strokes of Traditional Chinese Medicine (TCM). 266 factors were removed from 380 of EEG factors based on the suggestions from medical expert. The dependent factor was calculated by curative effect evaluation before-after scores from evaluation criteria scale for strokes of TCM.

3 Results

23 related EEG factors with curative effect evaluation were found, especially alpha and delta rhythms. Alpha rhythms are the major brain electrical activity of normal person. It disappears or decreases under pathological condition. Delta rhythms show positive correlation with relative power of alpha rhythms and exist in frontal region, central region, parietal region, occipital region, temporal region, especially in central region (CZ, PZ). Most of patients have the motor and sensory dysfunction after stroke. The central region (CZ, FZ) is relative with the motor and sensory function and not effects by the nidus of stroke.

X.-M. Fan · Y. Li · Y.-P. Cai (✉)
Shenzhen Institutes of Advanced Technology, Shenzhen, 518055, China
e-mail: yp.cai@siat.ac.cn

X.-X. Huang · H.-B. Yu
Shenzhen Chinese Traditional Medicine Hospital, Shenzhen, 518033, China

4　Conclusion

This paper found 23 relative EEG factors with curative effect evaluation, especially alpha and delta rhythms. Alpha rhythms are the major brain electrical activity of normal person, which disappear or decrease under pathological condition. This paper shows positive correlation between curative effect evaluation with alpha rhythms, and negative correlation with delta rhythms. So, EEG can be one of the electrophysiological examinations to evaluate the curative effect evaluation of stroke, especially alpha and delta rhythms.

References

1. Zhang S, Ke Z, Li L, et al. EEG patterns from acute to chronic stroke phases in focal cerebral ischemic rats: correlations with functional recovery[J]. Physiological measurement, 2013, 34(4): 423.

Big Data Analysis of Hypertension Complications Bases on Shenzhen Medical Information Management Platform

Yu-Jie Yang, Qi Li, and Yun-Peng Cai

Abstract

In recent years, the prevalence of hypertension in China increases continuously, and hypertension has become the first risk factor of the total death of Chinese population. At the same time, with the progression of hypertension condition, it may induces stroke, coronary heart disease, kidney failure and other severe complications, endangering the safety of life and property seriously. However, in China, hypertension patients have "three low"—low awareness rate, low treatment rate and low control rate, thus analyzing the significant risk factors and pathogenesis has certain clinical significance for prevention and treatment of complications of hypertension. In this paper, we screen approximately 2.2 million copies of hypertensive patients from medical information management platform, analyzing the risk factors by General Linear Model, selecting the factors of high significance for statistical analysis.

1 Introduction

Shenzhen's hypertension situation is particularly severe. According to the epidemiology investigation in 2009, the hypertension prevalence rate of people over 35 years old was about 20.9%, which showed an apparently upward momentum compared to 1997s. After "139 project" building, Shenzhen has been built Shenzhen City health data center, information sharing and exchange platform, and several business application systems based on the platform, creating more than 10 million residents of electronic health records, covering 60 public hospitals and more than 600 community health centers. As of the end of 2014, the total management of hypertensive patients is over 340 thousand people.

In this paper, we screened 343435 hypertensive patients from Shenzhen medical information management platform, including basic information, regular physical examination data, outpatient records, major disease records, hypertension follow up records, etc.

2 Risk Analysis

We choose general physical examination record as the main features, combined with the patient's personal data, hypertension data, life style and the hypertension follow-up data, etc. According to the clinic records or major disease records, the total patients will be divided into the experimental group (severe complication group) and the control group (stable group). After date preprocessing, we chose 28 features to build risk model, such as age, marriage status, education level, BMI, SBP, DBP, drink, smoke, sport, etc. GLM (Generalized Linear Model [1]) algorithm was used to analyze the risk of complications in hypertensive patients with p-value < 0.5. The results showed that waistline, SBP, DBP, marital status, gender, compliance behavior and age are the main risk factors of hypertension complications. Figure 1 shows the age distribution of the two group people.

Y.-J. Yang · Q. Li · Y.-P. Cai (✉)
Shenzhen Institutes of Advanced Technology, Shenzhen, 518055, China
e-mail: yp.cai@siat.ac.cn

Fig. 1 Age distribution (the stable group vs. the severe complication group)
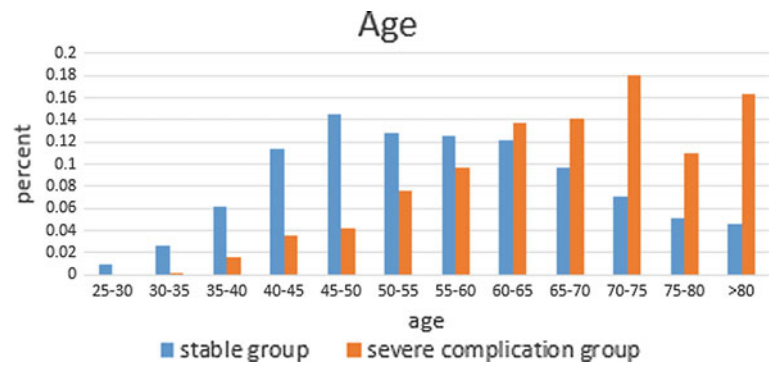
3   Conclusion

According to analysis, the risk of hypertension is relevant to a series of health condition and life style, such as Waistline, SBP, DBP and Compliance behavior are high risk factors.

References

1. Nelder John, Wedderburn Robert (1972). "Generalized Linear Models". Journal of Royal Statistical Society, Series A (General) (Blackwell Publishing) 135(3):370–384.

Vital Signs Analysis for Oceanauts in Deep Sea Submerged Environment: A Case Study

Fen Miao, Ye Li, and Lu Shi

Abstract

The oceanauts often suffer a lot from psychological dysfunction in the narrow and complicated deep sea environment. This paper aims to analyze the vital signs for oceanauts in submergence work with one case as an example. Four vital signs including heart rate, blood pressure, SDNN and LF/HF derived from ECG and blood pressure signals were analyzed to demonstrate the physiological status in submergence work.

Keywords

Deep submergence • Heart rate variability
Blood pressure

1 Introduction

Manned deep submergence is indispensable to deep ocean exploration [1]. Scientists and engineers are carried to the deep sea topography to perform different kinds of tasks. The deep sea environment is characteristic of darkness, noise, acceleration and abnormal temperature difference. In such a narrow and complicated space, the oceanauts often suffer a lot from great mental stress and psychological dysfunction with long-term continuous work and complex instrument operation. Some vital signs, such as heart rate variability (SDNN, LF/HF) and blood pressure were presented to be important markers for stress and health [2]. Therefore, vital signs monitoring and analysis is very important to detect the abnormal physiological status for the oceanauts.

2 Methods

Our study is based on the physiological signals detected from one submariner during the submersible process. Four vital signs including heart rate, blood pressure, SDNN and LF/HF derived from ECG and blood pressure signals were analyzed to demonstrate the change of mental stress during the submersible work. Five time points, including before submersible, going deep, in work, driving back and after the submersible, were analyzed.

3 Results

Figure 1 gives the value of four vital signs during the five time points. From Fig. 1 we can see, there are significant increases for the four signs in the submersible process, and the signs begin to decrease while driving back. In other words, the oceanaut suffers from significant mental stress during the submersible work.

F. Miao · Y. Li (✉)
Key Laboratory for Health Informatics of the Chinese Academy of Sciences (HICAS), Shenzhen Institutes of Advanced Technology, Shenzhen, 518055, China
e-mail: ye.li@siat.ac.cn

L. Shi
Shanghai Jiao Tong University, Shanghai, China
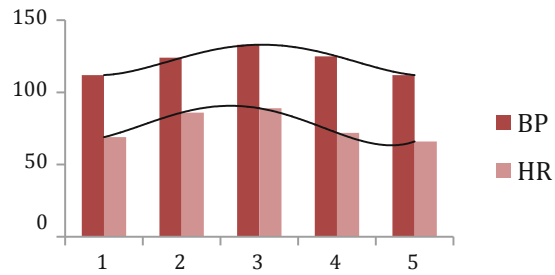
(a) Blood pressure and heart rate
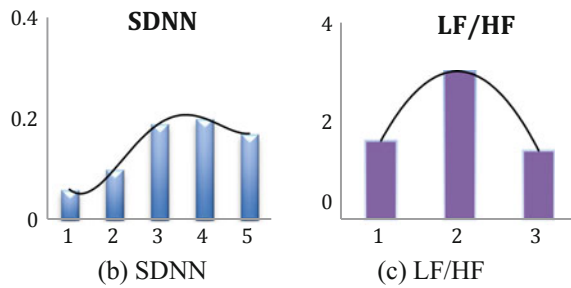
(b) SDNN

(c) LF/HF

Fig. 1 Vital signs comparison during five processes

example. It can be easily explained that as the oceanaut feel nervous with the deeper and deeper environment, the physiological signs that reflect mental stress would be changed.

Conflict of Interest There is no conflict of interest.

References

1. Liu F, Cui W C, Li X Y. China's first deep manned submersible, JIAOLONG [J]. Science China Earth Sciences, 2010, 53(10): 1407–1410.
2. Thayer J F, Åhs F, Fredrikson M, et al. A meta-analysis of heart rate variability and neuroimaging studies: implications for heart rate variability as a marker of stress and health [J]. Neuroscience & Biobehavioral Reviews, 2012, 36(2): 747–756.

4 Discussion and Conclusion

Four vital signs including heart rate, blood pressure, SDNN and LF/HF were demonstrated to be with significant increases in the submersible process with one oceanaut as an

Correlation Analysis of the Time Difference Between Multi-wavelength PPG

Jing Liu and Yuan-Ting Zhang

Abstract

This work developed a four-channel photoplethysmogram (PPG) acquisition system to collect the multi-wavelength PPG signals of red, yellow, green and blue light at the fingertip simultaneously. Eight subjects including 4 females took part in the experiment, and the multi-wavelength PPG signals from their fingertip were recorded. Since different PPG signal carries the blood pulsation information in different depth of the tissue, the time differences between multi-wavelengths was examined to investigate their relationships. The result shows the three time difference between yellow PPG and other PPGs (red PPG, green PPG and blue PPG) are highly correlated with each other ($|r| > 0.7$).

1 Introduction

Photoplethysmography is an optical measurement technique that can be used to detect pulsatile blood volume in the microvascular bed of tissue [1].

In this work, a four-channel PPG signal acquisition system was developed to collect the PPG waveforms of red, yellow, green and blue light simultaneously at the same body site of the subject. The correlation relationships between the time differences of different wavelength PPG were investigated in the study.

2 Methods

A quad wavelength PPG acquisition system was developed to collect and process four-channel PPG signals simultaneously as shown in Fig. 1.

The beat-to-beat time delay between the peaks of different PPG during the same cardiac cycle was extracted from the signals recorded from 8 subjects at rest. The peak delays between different PPG signals were denoted as R-Y, R-G, R-B Peak, Y-G Peak, Y-B Peak, G-B Peak in which R, Y, G, B were short for red PPG, yellow PPG, green PPG and Blue PPG respectively.

J. Liu
Department of Electronic Engineering, Joint Research Centre for Biomedical Engineering, The Chinese University of Hong Kong, Shatin, Hong Kong

Y.-T. Zhang (✉)
Department of Electronic Engineering, The Chinese University of Hong Kong, Shatin, Hong Kong
e-mail: ytzhangmdbs@gmail.com
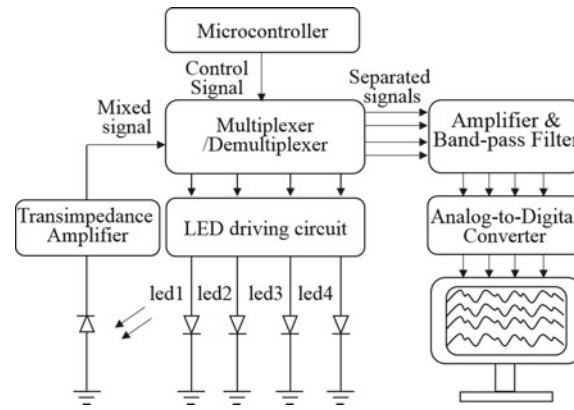
Fig. 1 Block diagram of the multi-wavelength PPG acquisition system

Table 1 The average correlation coefficients of the multi-wavelength PPG time differences

Correlation coefficient	R-Y	R-G	R-B	Y-G	Y-B	G-B
R-Y	1.00	0.16	0.21	−0.87[a]	−0.91[a]	0.02
R-G	–	1.00	0.51	0.27	0.03	−0.70*
R-B	–	–	1.00	0.02	0.12	0.21
Y-G	–	–	–	1.00	0.91*	−0.31
Y-B	–	–	–	–	1.00	0.05
G-B	–	–	–	–	–	1.00

[a] Denotes strong correlation relationship ($|r| > 0.7$)

3 Results and Discussion

The average correlation coefficients between different parameters of all the subjects were shown in Table 1.

It can be noted that when the peak of yellow PPG acts as a benchmark, the three time differences calculated from yellow PPG and other PPGs, i.e. R-Y, Y-G and G-B were highly correlated with each other. It can be speculated that time delay between yellow PPG and other PPGs may carry some information about tissue properties which can be explored in the future work.

References

1. A. Challoner, "Photoelectric plethysmography for estimating cutaneous blood flow," *Non-invasive physiological measurements,* vol. 1, pp. 125–151, 1979.

Epidermal Bioelectronics Toward Oximetry and Health Care Applications

Jie Zhang, Huihua Xu, Ningqi Luo, and Ni Zhao

Abstract

Cardiovascular diseases are among the most dangerous illnesses to human being, especially to the aged people. Therefore precaution and surveillance of cardiovascular diseases, empowered by prompt diagnosis and treatment of abnormal physiological conditions, have become growingly important and are expected to play essential roles in people's daily life. In this work, we developed low power photoplethysmogram (PPG) sensing system containing a flexible inorganic LED device and a high-sensitivity, ultra-thin phototransistor to monitor physiological parameters such as heart rate variability and oxygen saturation. The ultra-thin flexible LED and phototransistor overcome the roughness of human skin and allow conformal contact between the devices and the skin surface to realize high signal-to-noise ratio and resistance to motion artifact. The fabrication protocol of the LED and phototransistors will be described, followed by a detailed characterization on the device performance.

1 Introduction

ONE PPG sensing system requires both flexible light emission source and photodiode to form conformal contact with human skin with ultra-thin thickness [1–3].

In this work, flexible LED device is developed as light emission source to promise effective conformal lamination with human skins. The physical characteristics of LED device compared with commercial LED are investigated.

2 Method

A low-temperature solution-processed method is applied to develop efficient flexible LED devices as shown in Fig. 1.

The infrared light emission LED chips (ES-SASFPN42A) is fabricated on silicon substrate. After the substrate is removed by solution etching process, the electrode is re-deposited to reduce contact resistance. The flexible LED device is finally transferred to other flexible substrate to form light emission source in one PPG sensing system.

3 Results and Disscusion

The current density-voltage and light intensity-voltage curves of commercial LED device and flexible LED device are shown in Fig. 2.

The turn-on voltage for flexible LED device is slightly reduced compared with commercial LED device. It is supposed that the silicon substrate in commercial LED device is not highly conductive and the substrate will consume part of voltage when LED device is lighted up. However the buffer layer in device might be deteriorated in the solution etching process and the light intensity is weaken at the same drive voltage for the flexible LED device.

J. Zhang · H. Xu · N. Luo · N. Zhao (✉)
Department of Electronic Engineering, The Chinese University of Hong Kong, Shatin, New Territories, Hong Kong
e-mail: nzhao@ee.cuhk.edu.hk

J. Zhang
e-mail: zjcszjcxm@gmail.com
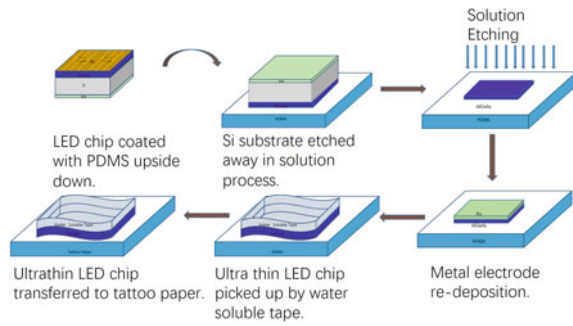
Fig. 1 Ultra-thin LED devices fabrication diagram
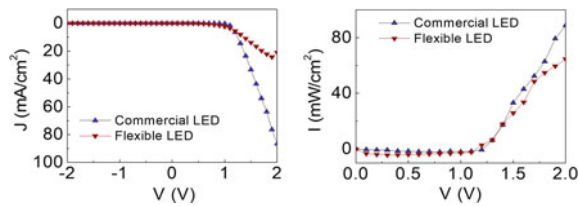
Fig. 2 (Left) Current density versus voltage and (right) light intensity versus voltage for commercial LED chip and flexible LED chip

References

1. L. Gao, Y. Zhang, V. Malyarchuk, L. Jia, K. I. Jang, R. C. Webb, H. Fu, Y. Shi, G. Zhou, L. Shi, D. Shah, X. Huang, B. Xu, C. Yu, Y. Huang, and J. A. Rogers, "Epidermal photonic devices for quantitative imaging of temperature and thermal transport characteristics of the skin," *Nat. Commun.,* vol. 5, pp. 4938, 2014.
2. C. M. Lochner, Y. Khan, A. Pierre, and A. C. Arias, "All-organic optoelectronic sensor for pulse oximetry," *Nat. Commun.,* vol. 5, pp. 5745, 2014.
3. C. Pang, J. H. Koo, A. Nguyen, J. M. Caves, M. G. Kim, A. Chortos, K. Kim, P. J. Wang, J. B. Tok, and Z. Bao, "Highly skin-conformal microhairy sensor for pulse signal amplification," *Adv. Mater.,* vol. 27, no. 4, pp. 634–640, 2015.

An Investigation of Time Difference Between Epidermal Pressure Pulse and PPG Signal

Wen-Xuan Dai, Ni Zhao, and Yuan-Ting Zhang

Abstract

This work investigates the time difference between epidermal pressure pulse and PPG signal over the radial artery. 8 healthy subjects including 4 females participated in the experiment with their PPG signals and epidermal pressure pulses recorded at wrist simultaneously by a multi-modal pulse sensing patch. The arrival times of two signals are marked by three different characteristic points. The result shows that there is a significant delay between the peaks of epidermal pressure pulse and PPG signal.

1 Introduction

The advent of technology has offered multiple methods to monitor the pulse wave of blood vessel continuously and unobtrusively. Photoplethysmography is an optical technique that measures the pulsatile blood volume change [1], while pressure sensor measures the epidermal pressure pulse on the skin surface. The arrival times of both signals are intensely studied to calculate the pulse transit time for blood pressure estimation [2, 3].

In this work, a multi-modal pulse sensing patch combining a PPG sensor and a flexible pressure sensor was developed to collect the blood volume pulse and epidermal pressure pulse at the same site of subjects simultaneously. Time differences between two pulse signals characterized by three different characteristic points were examined under controlled applied force.

2 Methodology

A multi-modal pulse sensing patch was developed using a 3 mm * 3 mm flexible pressure sensor as well as a PPG sensor (an LED and a photo detector with a 5 mm interval in between), as shown in Fig. 1.

PPG and epidermal pressure signals were recorded simultaneously over the radial artery from 8 healthy subjects at rest. The arrival times were extracted from each pulse using three characteristic points, i.e. minimum point, maximum upslope point and maximum point, denoted as $T_{min}, T_{slope}, T_{max}$, respectively.

3 Result and Discussion

The average time differences between epidermal pressure pulse and PPG signal of all the subjects using different time markers are shown in Fig. 2.

It can be seen that there is no big difference between the T_{min} and T_{slope} of two signals. However, the peak of epidermal pressure pulse arrives about 16.7 ± 11.0 ms later

W.-X. Dai · N. Zhao · Y.-T. Zhang (✉)
Department of Electronic Engineering, The Chinese University of
Hong Kong, Shatin, Hong Kong
e-mail: ytzhangapple@icloud.com; ytzhangmdbs@gmail.com
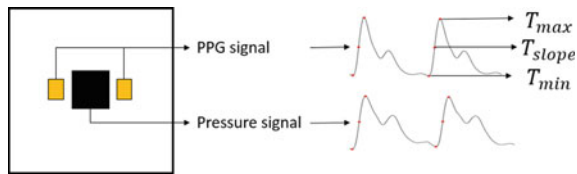
Fig. 1 Structure of the multi-modal pulse sensing patch
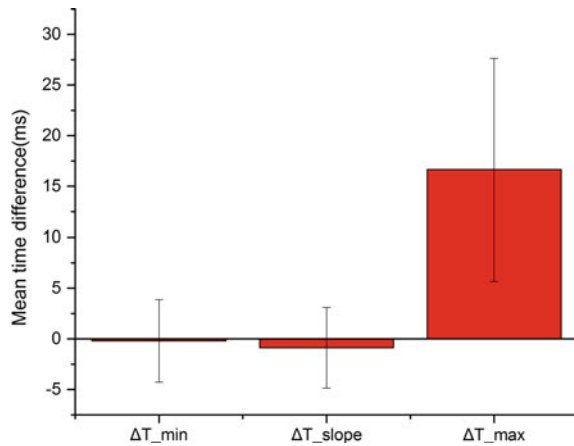
Fig. 2 Time differences between epidermal pressure pulse and PPG signal using different time markers $\left(\Delta T = T_{pre} - T_{ppg}\right)$

than the peak of PPG signal averagely. The delay may represent some local tissue properties which can be explored in the future study.

References

1. Allen J. "*Photoplethysmography and its application in clinical physiological measurement*" [J]. Physiological measurement, 2007, 28(3): R1.
2. Poon C C Y, Zhang Y T. "*Cuff-less and noninvasive measurements of arterial blood pressure by pulse transit time*" [C]//Engineering in Medicine and Biology Society, 2005. IEEE-EMBS 2005. 27th Annual International Conference of the. IEEE, 2006: 5877–5880.
3. Ding X R, Dai W X, et al. "*A Flexible Tonoarteriography-Based Body Sensor Network for the Cuffless Measurement of Arterial Blood Pressure*" [C]// Body Sensor Networks (BSN), 2015 12th International Conference on. IEEE, 2015.

Automatic Co-registration of MEG-MRI Data Using Multiple RGB-D Cameras

Shih-Yen Lin, Chin-Han Cheng, Li-Fen Chen, and Yong-Sheng Chen

Abstract

Integration of functional and structural modalities is essential to functional brain mapping. This paper presents an automatic co-registration system for aligning the coordinate systems between magnetoencephalography/ electroencephalo-graphy (MEG/EEG) and magnetic resonance image (MRI) using multiple off-the-shelf RGBD cameras. The system was constructed by using multiple Kinects for Windows V2, which were calibrated for the integration of the captured data of subjects' heads from multiple views. The integrated point clouds of the head surface captured by Kinects played an intermediate role between MEG/EEG and MRI. MEG/EEG-to-Kinect co-registration was conducted by using 3D locations of three anatomical landmarks, whereas Kinect-to-MRI co-registration was performed by using Gaussian mixture model to align facial part of points automatically segmented from both Kinect data and MRI. Combination of these two co-registration results yields the MEG/EEG-to-MRI transformation. Our evaluation results showed that the proposed system can achieve coordinate system alignment with high accuracy.

S.-Y. Lin (✉) · Y.-S. Chen (✉)
Department of Computer Science, National Chiao Tung University, Hsinchu, Taiwan
e-mail: dxxx861124@gmail.com

Y.-S. Chen
e-mail: yschen@cs.nctu.edu.tw

C.-H. Cheng
Institute of Biomedical Informatics, National Yang-Ming University, Taipei, Taiwan
e-mail: chinhan21@gmail.com

L.-F. Chen
Institute of Brain Science and Institute of Biomedical Informatics, National Yang-Ming University, Taipei, Taiwan
e-mail: lfchen@ym.edu.tw

L.-F. Chen
Integrated Brain Research Unit, Department of Medical Research, Taipei Veterans General Hospital, Taipei, Taiwan

1 Introduction

In brain research fields, noninvasive functional brain mapping using magnetoencephalography (MEG) or electroencephalography (EEG) requires to map the neuronal activity measured on the head surface into the stereotactic space inside the brain, which is called source localization technique. Because source localization requires the locations of EEG electrodes or MEG sensors in the stereotactic coordinate system of magnetic resonance image (MRI), it is essential to align the coordinate system of MEG or EEG to that of MRI in order to integrate the functional activity to the structure of the brain obtained by MRI. Moreover, the accuracy of the coordinate system alignment strongly affect the accuracy of source localization as well as the subsequent interpretation of brain function.

Various methods have been proposed to co-register MEG/EEG and MRI coordinate systems. Conventional methods uses locations of anatomical landmarks (left preauricular, or LPA; right preauricular, or RPA; nasion, or NAS) or fiducial points in both modalities to determine a unified coordinate system [1, 2]. Typically, these landmarks are localized using a 3-D digitizer and those in the MRI space are manually specified through visual inspection. Localizing these landmarks is a labor-intensive and operator-dependent task. Poor repeatability is usually another concern, even for an experienced operator. To avoid intensive manual operations, automatic co-registration methods were proposed in the literature. For example, surface-based co-registration methods [3, 4] involves localizing subjects' head surfaces in MEG/EEG and MRI coordinate through 3-D digitizer and image segmentation respectively, and coordinate trans-formation are estimated using co-registration between these two head surfaces. Although this type of method provide higher stability, measuring head surfaces is still highly operator-dependent and thus the accuracy of head surface localization are subject to the skill of the operators.

3D camera systems are considered as reliable, operator-independent alternatives to 3D digitizer for capturing face shapes or landmarks. Localization using 3D cameras can be done in a much shorter time and with a higher sampling density. In addition, camera-based localization require less manual operations, which increases the convenience of the system and can also reduce the operator dependency as well. Several camera-based co-registration methods have been proposed and these works have shown the advantages of methods of this type [5, 6]. However, previous camera-based co-registration methods are based on single-camera setups. Thus it is inconvenient to apply these existing methods when the landmarks/electrodes cannot be captured in a single camera view, which is the case in nearly all experiments using EEG caps. In light of these facts, it is beneficial to adopt a multi-camera co-registration system. However, most commercialized 3D-camera systems and multi-camera systems for MEG/EEG localization are very expensive. In this regard, the Kinect for Windows V2 may serve as an affordable alternative to the multi-camera co-registration system. It also features high-precision depth estimation as well as high-resolution color image.

This study aims to develop an automatic co-registration system for aligning MEG/EEG and MRI modalities based on multiple Kinects for Windows V2. This co-registration system is convenient and efficient to use and can reduce errors due to manual operations.

2 Methods

2.1 Overview

The purpose of MEG/EEG-MRI co-registration is to estimate the coordinate system transformation from MEG (or EEG) coordinate system to MRI coordinate system, $^{\mathrm{MRI}}T_{\mathrm{MEG}}$ (or $^{\mathrm{MRI}}T_{\mathrm{EEG}}$ for EEG system). For this purpose we decompose the transformation into the compositions of two

coordinate transformations: (1) Kinect-to-MRI transformation $\left(^{\mathrm{MRI}}T_{\mathrm{Ki}}\right)$, (2) MEG-to-Kinect (or EEG-to-Kinect) transformation $\left(^{\mathrm{Ki}}T_{\mathrm{MEG}},\,\mathrm{or}\,^{\mathrm{Ki}}T_{\mathrm{EEG}}\right)$:

$$^{\mathrm{MRI}}T_{\mathrm{MEG}} = {}^{\mathrm{MRI}}T_{\mathrm{Ki}}{}^{\mathrm{Ki}}T_{\mathrm{MEG}}, \quad ^{\mathrm{MRI}}T_{\mathrm{EEG}} = {}^{\mathrm{MRI}}T_{\mathrm{Ki}}{}^{\mathrm{Ki}}T_{\mathrm{EEG}} \quad (1)$$

Each of the two transformation components is estimated using a separate procedure. Figure 1 shows the flowchart of the proposed system. For estimating Kinect-to-MRI transformation, we first extract the 3D points on the face of subject using Kinect and in the MRI data of the subject and then align these two sets of 3D facial points. For MEG/EEG-to-Kinect transformation, the MEG/EEG subject coordinate system (or CTF coordinate system) is defined by specifying three anatomical landmarks: LPA, RPA, and NAS. The 3D coordinates of these landmarks as well as all MEG head position indicators (HPIs) or EEG electrodes are localized using Kinects from multiple views. Once the locations of the landmarks in Kinect coordinate system are known, the transformation from subject coordinate system to Kinect coordinate system can be estimated.

2.2 Design of Multiple-Camera System

We will first describe the general locations of EEG electrodes and MEG HPIs in each type of experiments. In MEG experiments, the four HPIs are located at the forehead and behind the two ears, which can be captured with only three views (front, left, and right, as shown in Fig. 2a). In EEG experiments, on the other hand, subject is asked to wear a cap with EEG electrodes covering nearly all upper part of the head (Fig. 2b), so the EEG-dedicated camera system should be able to cover the front, left, right, rear as well as the top view of the head. Regarding this, we designed a 3-camera MEG-dedicated system (Fig. 2c) and a 5-camera EEG-dedicated system (Fig. 2d). These systems were made of stable steel frames with static camera mounts.

Fig. 1 Flow chart of the proposed automatic co-registration of MEG/EEG-MRI data using multiple RGB-D cameras
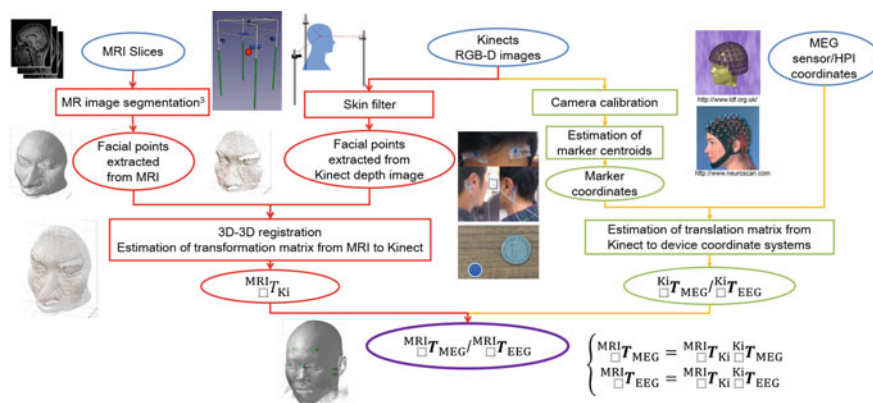
Fig. 2 Locations of MEG HPIs and EEG electrodes **a** HPIs of MEG experiment are located at the forehead and behind two ears. **b** EEG cap covers the upper parts of the head (*source* http://www.neuroscan.com). **c** The design of 3-Kinect camera mount for MEG-dedicated co-registration system. **d** The design of 5-Kinect camera mount for EEG-dedicated co-registration system

2.3 Kinect Head Image Acquisition

Prior to acquisition, Kinects were calibrated using calibration boards with checkerboard pattern. We used a rigid-transformation estimation based on least-square-error criterion to calculate the coordinate system transformation from each Kinect to the main Kinect mounted in the front of the seat. These calibrated Kinects would provide integrated 3D information from multiple views. And in order to automatically localize the landmarks and HPIs (or EEG electrodes) in later steps, blue markers were pasted on all landmarks as well as HPIs (or EEG electrodes on the EEG cap) prior to Kinect image acquisition. For the purpose of noise reduction, one acquisition are the average of 20 consecutive frames. When acquiring a 3D head image, subjects were instructed to remain still for one second in order to ensure image quality.

2.4 MRI Acquisition

All MRIs were acquired on Siemens MAGNETOM Trio, A Tim System 3T scanner (Siemens Medical Solution, Erlangen, Germany) with 12-Channel head coil. We used a magnetization Prepared Rapid Gradient Echo (MPRAGE) sequence (TR = 2530 ms, TE = 3.03 ms, TI = 1100 ms, field of view = 224×256, matrix size = 224×256 and 192 continuous slices). The slice thickness is 1 mm, and voxel size is $1 \times 1 \times 1$ mm^3.

2.5 Data Pre-processing

(1) *Segmentation of facial points from MRI*

We used the gray value thresholding to find the scalp surface. Similar to [6], the gray value threshold was defined as a fraction of the largest gray value (threshold = 0.04). The segmented facial points were down-sampled (down-sample rate = 3) to increase the time efficiency.

(2) *Segmentation of facial points from Kinect data*

The first step of segmentation involves a depth threshold to segment the head points (X_{head}) from the all 3D Kinect points (X_{Ki}). The threshold is defined as 0.15 m larger than the smallest depth value in the point cloud, i.e. 0.15 m behind the tip of the subject's nose:

$$X_{head} = \left\{ x | x_z < \min_z + 0.15, x \in X_{Ki} \right\} \qquad (2)$$

After the depth thresholding, we utilized a skin-color filter to exclude the regions of hair and cheek. Facial skins were segmented according to the rules proposed in [7, 8]. Subsequently, the lower part of the face (i.e. parts below the tip of the nose) were excluded. The reason for this is that these regions are liable to movements and will potentially undermine the accuracy of Kinect-to-MRI co-registration.

(3) *Automatic marker localization using Kinect data*

The first step is to estimate the transformation from Kinect camera coordinate system to the CTF coordinate system. To do this, three landmark markers (LPA, RPA, NAS) were localized manually on the color images, and the transformation from Kinect coordinate system to CTF coordinate system were estimated using rules proposed in [9]. And all 3D information acquired were converted to CTF coordinate system.

The second step is the automatic segmentation of potential markers. The color model of markers are defined using the color of the three landmark markers, Dissimilarity measure between color of pixel a (c_a) and the color model (c_{model}) are defined as the weighted Euclidean distance between two colors in HSV color space:

$$\varepsilon(c_a, c_{model}) = \left\| w_{hsv}^T \left(c_{a,hsv} - c_{model,hsv} \right) \right\|_2 \qquad (3)$$

The weighting vector w_{hsv}^T is for scaling the relative strictness of each color component. In our work we empirically set the weighting vector to a ratio of 150:20:2 for H, S and V components, respectively. The pixels of potential markers are pixels whose dissimilarity from the color model is below an empirical threshold (see Fig. 3b). Subsequently, connected components of these pixels are identified as possible individual markers. These potential markers would underwent further exclusion criterion: marker size (components with sizes dissimilar to that of an actual marker were excluded), ovality (markers at ill-conditioned angles were excluded) as well as CTF coordinates (marker far from the CTF origin were excluded) (see Fig. 3c).

After potential markers are found, the third step is to pairing actual markers with the identified potential markers. To do this, we use a template of marker locations (identified manually on color images) in CTF coordinates. The template are scaled to fit the size of the subject's head. Potential markers within a threshold of spatial distance are identified and paired with the actual marker. If multiple potential markers are found from different views, the one with smaller ovality will be chosen, since rounder shape indicates smaller view angle and potentially higher depth confidence (see Fig. 3d). If there are unpaired markers due to either lighting issues or occlusion of EEG signal wires, markers can also be localized manually in our system.

2.6 Co-registration Between Coordinate Systems

(1) *Kinect-to-MRI Co-registration*

Kinect-to-MRI co-registration is done through aligning the extracted 3D facial point sets obtained from MRI and Kinect. We used a point-to-point based registration algorithm, Gaussian mixture model (GMM) registration [10] to do this task.

(2) *MEG/EEG-to-Kinect Co-registration*

Co-registration from EEG CTF coordinate to Kinect coordinate system is done through finding the Kinect coordinate of the landmarks defining CTF coordinate system, and the coordinate system transformation were estimated using rules in [9]. Co-registration from MEG coordinate to Kinect coordinate system is done through estimating the spatial
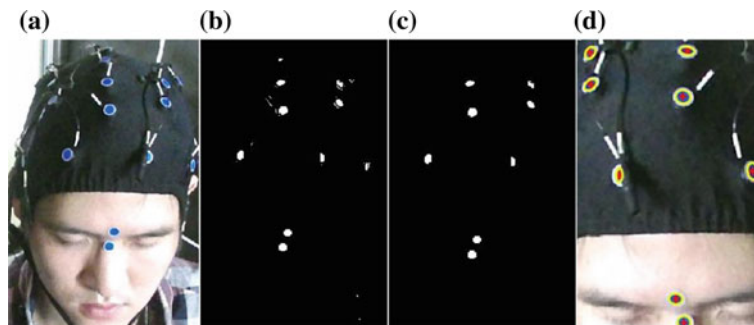

Fig. 3 An example of automatic marker segmentation. **a** Original color image. **b** Potential markers after applying color similarity threshold. **c** Potential markers after applying threshold on marker size, ovality and CTF coordinates. **d** Pairing detected potential markers with actual markers (Color figure online)

transformation from the HPIs' MEG device coordinates to their corresponding Kinect coordinates. For this purpose, ICP algorithm was used.

(3) *MEG/EEG-to-MRI Co-Registration*

Finally the coordinate transformation from MEG/EEG coordinate system to MRI coordinate system can be calculated by the multiplication of MEG/EEG-to-Kinect transformation by the Kinect-to-MRI transformation (Eq. 1).

3 Preliminary Results

3.1 Evaluation: Accuracy of Kinect-to-MRI Co-registration

The error measure of Kinect-to-MRI co-registration is defined as the shortest Euclidean distances between a Kinect facial point (x) co-registered to the MRI coordinate system and the facial surface defined by MRI facial points $\left(S_{\text{face}}^{(\text{MRI})}\right)$:

$$\varepsilon_{\text{K2M}}\left(x, S_{\text{face}}^{(\text{MRI})}, {}^{\text{MRI}}T_{\text{Ki}}\right) = dist\left(S_{\text{face}}^{(\text{MRI})}, {}^{\text{MRI}}T_{\text{Ki}}x\right) \quad (4)$$

To estimate the distance MRI-derived surface from MRI-derived points set, we use Marching Cubes to compute triangulated mesh and build up the MRI surface.

Fig. 4 Box plot of Kinect-to-MRI co-registration error. The central red lines are the medians, the edges of the box are the 25th and 75th percentiles, and whiskers represent 1.5 times the interquartile ranges. Data beyond the whisker (red crosses) are regarded as outliers

The dataset for this evaluation include acquisitions of 3 participants. As shown in Table 1 and Fig. 4, the mean error are below 1 mm. However, a large number of outliers exists. Figure 5 illustrates the distribution of error in various portions of the face. As can be seen, regions with highest error values are predominantly non-rigid parts of face like cheek and eyelid, while rigid parts like forehead demonstrate lower error value and errors within these regions are mostly lower than 1 mm.

Table 1 Error statistics of Kinect-to-MRI co-registration

	Mean (mm)	Std. dev. (mm)	Median (mm)
Subject 1	0.77	0.71	0.53
Subject 2	0.91	0.96	0.55
	0.82	0.85	0.85	0.54

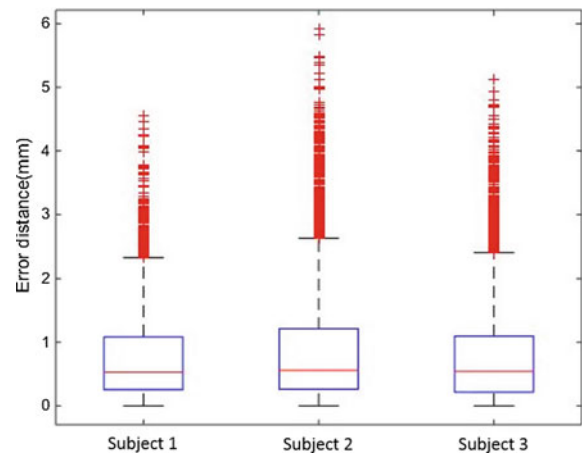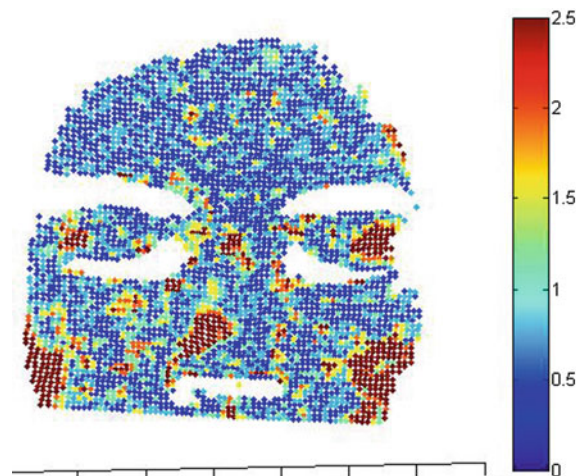**Fig. 5** The error range distribution of Kinect-MRI registration on Kinect-derived face. Color represents the error value at the respective location (Color figure online)

4 Discussion and Conclusions

We have proposed an automatic system for MEG-MRI and EEG-MRI co-registration based on multiple Kinect for Windows V2. Through utilizing multiple Kinects and automatic segmentation algorithms, the amount of manual operations needed is greatly reduced, resulting in higher time-efficiency as well as lesser errors due to manual operations. Utilizing off-the-shelf Kinect for Windows V2 makes our system much more affordable compared to other dedicated co-registration systems. This work demonstrated our preliminary effort to construct an affordable, fully-automatic co-registration system, and this system is planned to undergo further improvements (possible improvements includes advanced noise reduction/correction for 3D localization and more accurate registration algorithms), and would be further validated using EEG/MEG experimental data.

Conflicts of Interests The authors declare that there are no conflicts of interest.

References

1. J. George, P. Jackson, D. Ranken, and E. Flynn, "Three-dimensional volumetric reconstruction for neuromagnetic source localization," in *Advances in biomagnetism*, Springer, 1989, pp. 737–740.
2. H. J. Wieringa, MEG, EEG and the integration with magnetic resonance images: HJ Wieringa, 1993.
3. S. J. Williamson and L. Kaufman, "Advances in neuromagnetic instrumentation and studies of spontaneous brain activity," *Brain Topography*, vol. 2, pp. 129–139, 1989.
4. S. J. Williamson, Z.-L. Lü, D. Karron, and L. Kaufman, "Advantages and limitations of magnetic source imaging," *Brain topography*, vol. 4, pp. 169–180, 1991.
5. N. Hironaga and A. Ioannides, "Accurate co-registration for MEG reconstructions," in *Proceedings of the 13th International Conference on Biomagnetism*. VDE Verlag, Berlin, 2002, pp. 931–933.
6. V. Napadow, R. Dhond, D. Kennedy, K. K. Hui, and N. Makris, "Automated brainstem co-registration (ABC) for MRI," *NeuroImage*, vol. 32, pp. 1113–1119, 2006.
7. P. Peer and F. Solina, "An automatic human face detection method," in *Proceedings of Computer Vision Winter Workshop (CVWW'99)*, Rastenfeld, Austria. 1999.
8. F. Solina, P. Peer, B. Batagelj, and S. Juvan, "15 seconds of fame-an interactive, computer-vision based art installation," in *Proceedings of the 7th International Conference on Control, Automation, Robotics and Vision*, pp. 198–204, 2002.
9. Coordinate systems. Available: http://neuroimage.usc.edu/brainstorm/CoordinateSystems.
10. N. Baka, C. Metz, C. Schultz, R.-J. van Geuns, W. J. Niessen, and T. van Walsum, "Oriented gaussian mixture models for nonrigid 2D/3D coronary artery registration," *IEEE Transactions on Medical Imaging*, vol. 33, pp. 1023–1034, 2014.

Comparison of Heart Rate Variability and Pulse Rate Variability of Respiratory Control

Yi Han, Wen-Chen Lin, Sheng-Cheng Huang, Cheng-Lun Tsai, and Kang-Ping Lin

Abstract

Heart rate variability (HRV) can be applied to observe the autonomic nervous system activity of human beings. With the development of wearable device technology, PPG signal is often applied to measure pulse rate, and furthermore to analyze the pulse rate variability (PRV), which is considered to be equivalent to HRV. However, regular heart rate will be affected by breath volume and breath rate that causes different results when HRV and PRV are measured in different situations. This paper presents a study based on the characteristics of the respiratory sinus arrhythmia (RSA), the heart rate and tide volume of breath and the variabilities from PPG and ECG which were measured by PSG simultaneously. Furthermore, according to the measurement of PTT based on PPG and ECG signals, the characteristics of peripheral arteries were evaluated. From the results, it was found that the significance ($p < 0.05$) is shown between HRV and PRV when normal young groups are controlled at different tide volume of breath. No significance is shown on the PRV obtained from four limbs. In summary, the PRV and HRV show different characteristics at different breath controls. There are no differences between each PRV when PPG signals are obtained from four limbs.

Keywords

Respiratory sinus arrhythmia • Heart rate variability
Pulse rate variability • Photoplethysmography

Y. Han · W.-C. Lin · S.-C. Huang · K.-P. Lin (✉)
Department of Electrical Engineering, Chung Yuan Christian University, Taoyuan City, Taiwan
e-mail: kplin@cycu.edu.tw

C.-L. Tsai
Department of Biomedical Engineering, Chung Yuan Christian University, Taoyuan City, Taiwan

1 Introduction

Photoplethysmography (PPG) is used in many clinical applications, including blood oxygen saturation, heart rate, blood pressure, etc. Heart rate, which is used widely in clinical settings, is the most important physiological parameter [1]. Heart rate variability (HRV) is determined by R-R interval of electrocardiography (ECG) as an index of the cardiovascular autonomic nervous system. The analysis of HRV is common in time domain or frequency domain [2, 3]. Some studies agreed that the results from pulse rate variability (PRV) were as good as which from HRV [4, 5]. However, differences between PRV and HRV are shown in few studies [6].

The development of wearable device technology has become the mainstream. More and more wearable photoplethysmographic biosensors are developed and used in heart rate estimation. HRV is estimated by PRV mostly in the stationary state, and whether or not PRV could replace HRV still leave exploring space [7].

Respiratory sinus arrhythmia (RSA) is caused by the reciprocal effect of respiration and blood pressure. Respiration would change HRV and postural change would cause venous return [8]. The respiratory fluctuations affecting signals from pulse wave are more than which from ECG. The velocity of pulse wave would be changed by cardiac output and varying aortic transmural pressure with a mechanical respiratory influence [9]. Constant et al. [9] indicated that respiratory pulse rate does not reflect respiratory heart rate precisely in standing subjects and patients with low HRV.

The accuracy of PRV as an estimation of HRV depends on the health and status (resting or moving) of subjects. Many studies suggest that HRV is somewhat overestimated by PRV. The reason is the coupling effects between respiration and cardiovascular system. The agreement of PRV and HRV would be impaired if subjects had physical activity and some mental stressors [10].

In this study, we evaluated differences between HRV and PRV based on the respiratory frequency and volume. Standard deviation of normal to normal intervals (SDNN), and standard deviation of all peak to peak intervals (SDPP) were parameters for analysis.

2 Methods

2.1 Subjects and Signal Acquisition

We studied 12 subjects with mean age of 27 years old (year range: 23–55 year). Each subject was sitting with a comfortable posture while being tested in the experiment. PPG and ECG signals were recorded by PSG (Alice 6 LDx, Philips) with sampling frequency 250 Hz and 12 bit ADC. The ECG signal was from Lead II, and the PPG signals were from the left hand (LH), right hand (RH), left leg (LL) and right leg (RL). The signals were analyzed by a personal computer (Fig. 1).

2.2 Experimental Protocol

In this study, the parameters are R-R interval (RRI) in ECG, peak to peak interval (PPI) and pulse transit time (PTT) in PPG, which is shown in Fig. 2.

Experimental protocol of breathing was designed in five states, including static frequency breathing (SFB), rapid and deep breathing (RDB), slow and deep breathing (SDB), rapid and shallow breathing (RSB), and slow and shallow breathing (SSB). The duration of each state was 1 min, and was defined as the followings (Fig. 3):

SFB   Each subject was breathing at the range of personal tidal volume with the frequency of 15 num./min.
RDB   Each subject was breathing at the range between inspiratory reserve volume and expiratory reserve volume with the frequency of 30 num./min.
SDB   Each subject was breathing at the range between inspiratory reserve volume and expiratory reserve volume with the frequency of 5 num./min.
RSB   Each subject was breathing at the range smaller than tidal volume with the frequency of 30 num./min.

Fig. 2 The related measuring points among the parameters of RRI, PPI and PTT

SSB   Each subject was breathing at the range smaller than tidal volume with the frequency of 5 num./min.

2.3 HRV and PRV Analysis

In Fig. 4, the length of ECG signal is represented by L, and the positions of R peak are determined by the R peak detection. Peaks of PPG were found in the relation of R peak positon. All the detection results were confirmed artificially. The RRI, PPI and PTT were determined by results of the algorithm.

R peak detection algorithm is refereed to double difference methods as the fallowing equation [11]:

$$S_{d1}(n) = X_{ecg}(n) - X_{ecg}(n-1) \tag{1}$$

$$S_{d2}(n) = S_{d1}(n) - S_{d1}(n-1) \tag{2}$$

$$d(n) = [S_{d2}(n)]^2, n = 1, 2, \ldots, L \tag{3}$$

where $X_{ecg}(n)$ is the input ECG signal, $S_{d1}(n)$ is the first difference, $S_{d2}(n)$ is the second difference of the input signal. $d(n)$ is defined as the square of the signal $S_{d2}(n)$.

The positions of R peaks are determined as:

$$R = \{k | d(n-1) < d(k=n) \langle d(n+1) \cap d(n) \rangle Th\} \tag{4}$$

where Th is a threshold value, R is the position of R peak. If $d(n)$ is known as a peak at the time sequence k and the value

Fig. 1 Flow chart of signal acquisition
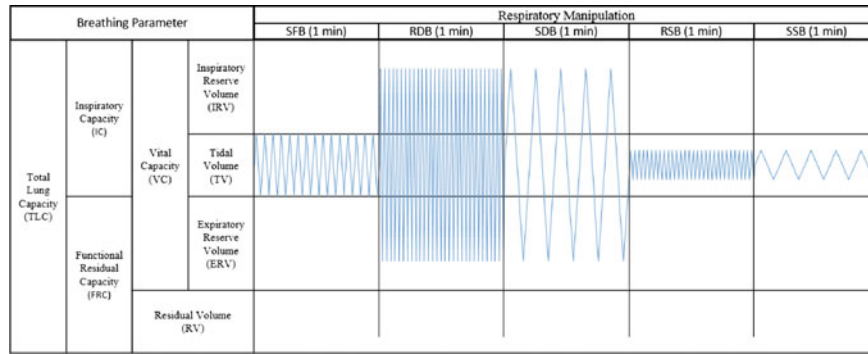
Fig. 3 Experiment protocol of breathing control. Experimental protocol of breathing was designed in five segments, including static frequency breathing (SFB), rapid and deep breathing (RDB), slow and deep breathing (SDB), rapid and shallow breathing (RSB),and slow and shallow breathing (SSB)
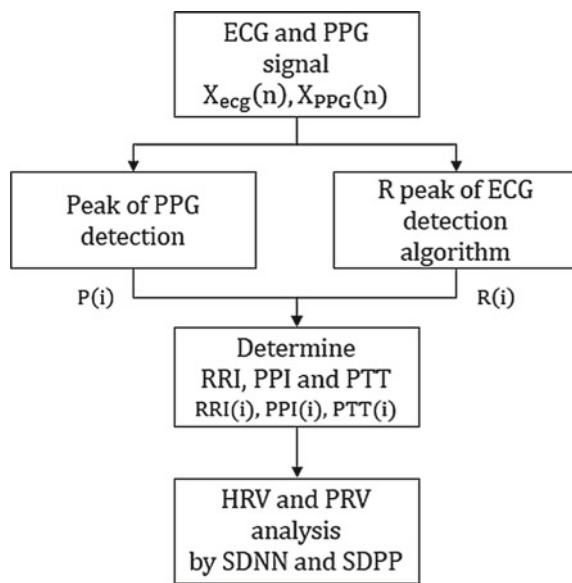
Fig. 4 Definitions of RRI, PPI and PTT

is greater than h, k is the position of R peak. There are N numbers of R peak.

The peak positions of PPG are determined by using the position of R peak in ECG, which is written as:

$$P = \{k | \max X_{PPG}(k = n), n = R(i), \ldots, R(i+1)\} \quad (5)$$

P is the peak position of PPG. If PPG signal $X_{PPG}(n)$ has a maximum at the time sequence k in the range between R(i) and R(i + 1), k is the peak position of PPG. There were N numbers of peak.

The RRI, PPI and PTT are defined as the followings:

$$RRI(i) = R(i) - R(i - 1) \quad (6)$$

$$PPI(i) = P(i) - P(i - 1) \quad (7)$$

$$PTT(i) = P(i) - R(i), i = 1, 2, \ldots, N \quad (8)$$

In order to analyze HRV and PRV in this study, standard deviation of all normal to normal intervals (SDNN) and standard deviation of all peak to peak intervals (SDPP) are defined as the followings:

$$SDNN = \sqrt{\frac{1}{N} \sum_{i=1}^{N} RRI(i) - \overline{RRI}} \quad (9)$$

$$SDPP = \sqrt{\frac{1}{N} \sum_{i=1}^{N} PPI(i) - \overline{PPI}} \quad (10)$$

3 Results and Discussions

Table 1 shows the results from analysis of HRV and PRV by using SDNN and SDPP. The mean value of HRV and PRV in SDB was almost 2 times than which in RDB. The mean value of HRV and PRV in SSB was about 1.5 times than which in RSB. The mean value of HRV and PRV in RDB was similar to which in RSB. The mean value of HRV and PRV in SDB was about 1.2 times than which in SSB. The mean value in SDB was greater than other breathing interval, which showed that the frequency had more impacts than volume of breathing on HRV and PRV. As a result, SDB had the most impact on the breathing interval. Conversely, SSB had fewer impacts on the breathing interval. When the breath was manipulated, the psychological effect reached the rapid breathing rate. Subjects might feel nervous or excited (sympathetic activation) because of the stress. Conversely, slow breathing was less stressful.

Table 2 shows that HRV and PRV were compared with each other in all the breathing experiments. The comparison results of HRV and PRV indicated that the p value was smaller than 0.05 in all the breathing experiments, which showed the differences between HRV and PRV is significant in the breathing interval. In addition to the measurement

Table 1 Measurement results of HRV and PRV

	HRV (ms)	PRV (ms)			
		LH	RH	LL	RL
NFB	38.15 ± 16.65	40.15 ± 16.33	39.79 ± 16.34	39.41 ± 16.2	39.95 ± 16.17
RDB	35.73 ± 11.68	38.72 ± 11.81	38.81 ± 10.13	37.91 ± 14.39	37.32 ± 11.7
SDB	65 ± 30.78	67.26 ± 31.04	66.75 ± 31.38	67.05 ± 31.77	67.2 ± 31.47
RSB	37.58 ± 17.54	39.43 ± 18.06	39.85 ± 18.77	39.66 ± 18.49	39.23 ± 17.62
SSB	54.32 ± 19.95	57.18 ± 20.48	58.95 ± 21.06	56.26 ± 20.66	56.45 ± 20.31

Note Four limbs refer to left hand (LH), right hand (RH), left leg (LL), and right leg (RL)

Table 2 The results of comparison with HRV and PRV

P value		PRV			
		LH	RH	LL	RL
HRV	SFB	0.00583**	0.00234**	0.01047*	0.00202**
	RDB	0.00068**	0.0264*	0.04151*	0.00867**
	SDB	0.00294**	0.00191**	0.00032**	0.00006**
	RSB	0.01317*	0.00727**	0.00194**	0.00730**
	SSB	0.00176**	0.02318*	0.00003**	0.00007**

Note The symbol "*" means p value and was smaller than 0.05
The symbol "**" means p value and was smaller than 0.01

Table 3 The results of comparison with PRV from four limbs

P value		RH	LL	RL
SFB	LH	0.10808	0.12799	0.38941
	RL	0.39107	0.18288	
RDB	LH	0.46949	0.2602	0.06014
	RL	0.13514	0.32764	
SDB	LH	0.09909	0.38692	0.45627
	RL	0.17904	0.34935	
RSB	LH	0.25349	0.39952	0.39764
	RL	0.25195	0.25313	
SSB	LH	0.22662	0.12136	0.19692
	RL	0.11127	0.32225	

Table 4 The results of comparison with PTT from four limbs

P value		RH	LL	RL
SFB	LH	0.41293	0.22443	0.37483
	RL	0.45421	0.38948	
RDB	LH	0.41145	0.19042	0.37284
	RL	0.49803	0.16965	
SDB	LH	0.12180	0.49670	0.23148
	RL	0.40471	0.20859	
RSB	LH	0.21425	0.17192	0.47584
	RL	0.24589	0.21678	
SSB	LH	0.39275	0.13564	0.18069
	RL	0.15304	0.46750	

error, the difference in vessel status would lead to the influence in paths of pulse transmission personally. Therefore, the measurement results in PRV would not be replaced in HRV.

Table 3 shows that PRV from four limbs were compared with each other in all the breathing experiments. Table 4 shows PTT from four limbs were compared with each other in all the breathing experiments. In Tables 3 and 4, the

p value of PRV and PTT from four limbs is greater than 0.05 in the breathing experiments. The results showed that the differences between PRV and PTT from four limbs are not significant in the breathing interval.

4 Summary

In this study, it was found that controlling breath rate shows instant impact on HRV and PRV comparing to which on changing the volume of breaths. As a result, SDB has the most impact on the breathing states. Conversely, SSB has fewer impacts on the breathing interval. The comparison results of HRV and PRV in all the breathing experiments, which shows the differences between HRV and PRV, are significant in the breathing states. In addition to the measurement error, the differences in vessel status would lead to the influence in paths of pulse transmission personally. Therefore, the measuring result of PRV would not be properly and directly replaced as the same means of which of HRV.

References

1. J. Allen, "Photoplethysmography and its application in clinical physiological measurement," *Physiol. Meas*. 28, R1–R39. 2007.

2. Task Force of the European Society of Cardiology and The North American Society of Pacing and Electrophysiology, "Heart rate variability—Standards of measurement, physiological interpretation and clinical use," *European Heart Journal*, vol. 17, pp. 354–381. 1996.

3. J. L. A. Carvalho, "A Tool for Time-Frequency Analysis of Heart Rate Variability," (in Portuguese), M.Sc. dissertation, Publication ENE.DM-156N03, Department of Electrical Engineering, Universidade de Brasilia, Brasilia, Brazil, 2003.

4. J. Hayano, A. K. Barros, A. Kamiya, N. Ohte, and F. Yasuma, "Assessment of pulse rate variability by the method of pulse–frequency demodulation," *Biomed. Eng. Online*, vol. 4, p. 62, 2005.

5. P. S. McKinley, P. A. Shapiro, E. Bagiella, M. M. Myers, R. E. De Meersman, I. Grant, and R. P. Sloan, "Deriving heart period variability from blood pressure waveforms," *J. Appl. Physiol.*, vol. 95, no. 4, pp. 1431–1438, Oct. 2003.

6. F. Chang, C. Chang, C. Chiu, S. Hsu, Y. Lin. "Variations of HRV analysis in different approaches," *Comput Cardiol*, vol. 34, pp. 17–20. 2007.

7. Asada, H. Harry, et al. "Mobile monitoring with wearable photoplethysmographic biosensors," *Engineering in Medicine and Biology Magazine*, vol. 22.3, pp. 28–40. 2003.

8. A. Schäfer, J. Vagedes, "How accurate is pulse rate variability as an estimate of heart rate variability? A review on studies comparing photoplethysmographic technology with an electrocardiogram," *International Journal of Cardiology*, vol. 166, pp. 15–29. 2013.

9. I. Constant, D. Laude, I. Murat, J.L. Elghozi, "Pulse rate variability is not a surrogate for heart rate variability," *Clin Sci.*, London, vol. 97, pp. 391–397. 1999.

10. J. K. Triedman, J. P. Saul, "Blood Pressure Modulation by Central Venous Pressure and Respiration Buffering Effects of the Heart Rate Reflexes," *Circulation*, vol. 89, pp. 169–179. 1994.

11. D. Sadhukhan, M. Mitra, "R-peak detection algorithm for ECG using double difference and RR interval processing," *Procedia Technology*, vol. 4, pp. 873–877. February 2012.

Pilot Project: ICT System for Management and Self-management of Diabetes

Sara Zulj, Luka Celic, Mladen Grgurevic, Manja Prasek, and Ratko Magjarevic

Abstract

Diabetes is one of the leading health problems in the world and its treatment typically requires a lot of interactions between healthcare professionals and patients. Patients are advised to self-monitor their blood glucose in order to achieve a specific level of glycemic control, to prevent hypoglycemia and to help healthcare professionals to adjust their treatment. In order to help patients and healthcare professionals provide better self-management and management of diabetes, we have developed new system. The system comprises a device for connecting and communicating with glucose meters, data management software for data acquisition and visualization, and database. The system is endorsed through the pilot project by Croatian Health Insurance Fund and Croatian Ministry of Health. We present some features of the collected data from the first one hundred patients.

1 Introduction

DIABETES is one of the leading public health problems in the world. The number of diabetic patients is expected to rise to 366 million by 2030 [1]. In 2012, WHO estimated that 1.5 million deaths were directly caused by diabetes [2].

Diabetes is a chronic disease and its treatment typically requires a lot of interactions between healthcare professionals and patients. It is known that optimal diabetes management requires an organized, patient-centered, systematic approach and the involvement of a coordinated team of dedicated healthcare professionals [3].

Patients are advised to self-monitor their blood glucose in order to achieve a specific level of glycemic control, to prevent hypoglycemia and to help healthcare professionals to adjust their treatment. Although there is a kit comprising data cable and management software for most glucose meters available and sold separately on the market, this self-monitoring data is rarely reviewed by patients. Handwritten diabetes diaries, however, often include inaccurate or missing data and are therefore often not reliable source of data for health care professionals [4].

In a feasibility study we have performed a few years ago, we have shown the benefits of integration of different measurement devices (glucose meters, scale, blood pressure meter, activity sensors etc.) used for monitoring of their status by diabetics into a cloud based expert system [5]. In order to enable healthcare professionals to provide better management of diabetes, while at the same time making the self-management easier for patients, we have further developed a scalable ICT system for acquisition, management and storage of blood glucose data for national health care providers in Croatia.

2 ICT System For (Self-)Management of Diabetes

2.1 System Design

More than 42 types of glucose meters from 17 manufacturers are currently available on the Croatian market. Meters vary in appearance, memory capabilities, hardware interface, communication protocol, and data management software. Most of the available meters are approved by the Croatian Health Insurance Fund as medical devices for diabetic patients. Due to non-standardized features of glucose meters' hardware interfaces and communication protocols, in order to read the data on measured glycemia from glucose meters

S. Zulj · L. Celic · R. Magjarevic (✉)
Faculty of Electrical Engineering and Computing,
University of Zagreb, Zagreb, Croatia
e-mail: Ratko.Magjarevic@fer.hr

S. Zulj
e-mail: sara.zulj@fer.hr

M. Grgurevic · M. Prasek
Vuk Vrhovac University Clinic for Diabetes, Endocrinology and
Metabolic Diseases, Zagreb University School of Medicine,
Zagreb, Croatia

memory, professional users were forced to use a large number of different accessories and different software for practically each model of glucose meter on the market. The examination process and the communication between the physicians and the patients was suffering because of inappropriate infrastructure in the infirmary. Therefore, we developed an ICT system for data acquisition, management, visualization and storage.

The system comprises a device for connecting and communicating with currently available meters, data management software for data acquisition and visualization, and database for long term storage. This system is available in two versions, *clinic version*—designed for healthcare professionals for desktop use with a computer, and *mobile version*—designed for patients for self-monitoring.

Once transferred into the system, by either health care professional or patients themselves, the data is stored and is available to authorized persons for viewing at any time. Transferred self-monitoring glucose data contain all the information that can be digitally obtained from the glucose meter through communication, such as date and time of the measurement, measurement value and flag (before meal, after meal, fasting, etc.)

In data visualization view, healthcare professionals are given statistics for the immediate patient in a chosen time span (e.g. total number of blood glucose measurements, minimal, maximal and average value of measurements, number of days without measurement and average number of measurements per day). More important, it provides a measure of glycemic variability and the number of hypoglycemic episodes as recommended by ADA [6] for better glycemic control evaluation.

As a tool for better management of the disease and treatment, we present to the user a *standard day graph* to provide a pattern in the daily glucose profile (Fig. 2), and a *trend graph* to show trending glycemic control over a larger time span, e.g. 3 months (Fig. 2). Standard day graph shown on Fig. 1 could support the health care professional in making a decision regarding patients therapy. For example, if the patient suffers from hypoglycemic episodes during early morning, the doctor can make a decision to prescribe lower dosage of insulin in the evening, and if the hyperglycemic event occurs mostly in the evening, higher dosage of insulin could be prescribed in the morning.

2.2 The Pilot Stage

Croatian Health Insurance Fund and Croatian Ministry of Health endorsed the project with the aim of planning a better management and self-management of diabetic patients. The system was installed at the Vuk Vrhovac University clinic for diabetes, endocrinology and metabolic diseases, and at two general practice clinics.

3 Results

In the first 9 months of the pilot project, we have acquired 182.338 blood glucose measurements from 523 patients. The data were downloaded from 19 different glucose meter types. Around 70% of the data were obtained from three types of glucose meters: Accu-Check Performa (24%), Bayer Contour (20%), newer version Bayer Contour XT (18%), and Abbott Freestyle Optium (8%).

We have analyzed the data of the first one hundred subjects; 41 type 1 Diabetes Mellitus patients (T1DM)—22 male and 19 female, and 59 type 2 Diabetes Mellitus patients
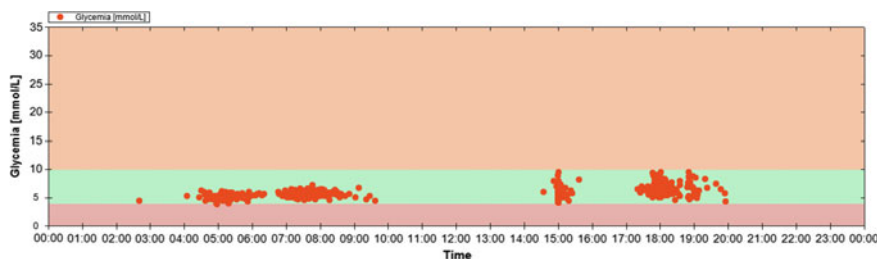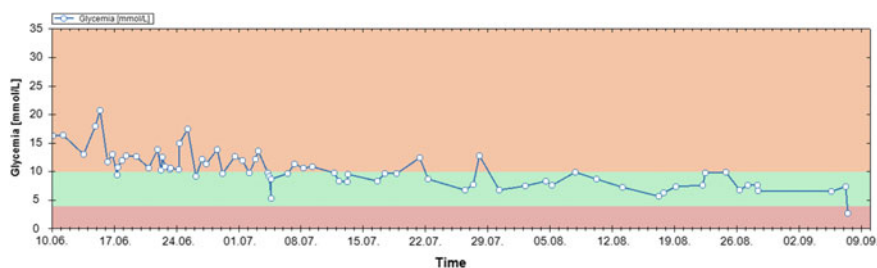
Fig. 1 Standard day graph

Fig. 2 Trend graph

(T2DM)—25 male and 34 female. Blood glucose measurements in the last 90 days prior to visit to the clinic were considered in this analysis. HbA1c value is taken at the time of the visit. We have also included body mass index (BMI), blood pressure, prescribed therapy, duration of the disease and duration of the therapy.

3.1 Body Mass Index

In the T1DM group, body mass index was 26.2 ± 3.4 for the male and 24.3 ± 4.0 for the female subgroup. 12 (54%) male and 4 (21%) female subjects were overweight ($25 \leq$ BMI < 30), 3 (14%) male and 3 (16%) female subjects were obese (BMI ≥ 30).

In the T2DM group, body mass index was 29.2 ± 3.2 for the male and 30.2 ± 6.2 for the female subgroup. 13 (52%) male and 11 (32%) female subjects were overweight, 11 (44%) male and 15 (44%) female subjects were obese.

No association between BMI and mean blood glucose or standard deviation of blood glucose was found.

3.2 Prescribed Therapy

Prescribed therapy was noted as: diet, diabetes pills, insulin therapy of 1 dose per day, 2–3 doses per day or intensive insulin therapy (4–5 doses per day).

The T1DM group has an average number of measurements per day 3.5 ± 1.4, which corresponds well with prescribed intensive insulin therapy of 4–5 doses.

The T2DM group values are given in Table 1. Those average values for each group fit in with the prescribed therapy, where number of measurements per day should be equal or more than the number of doses of insulin. For subjects prescribed on diet or diabetic pills, the significance of these results is smaller due to small number of subjects.

Table 1 T2DM group: number of measurements per day

Prescribed therapy	Mean number of measurements per day	Standard deviation
Insulin—1 dose	0.4	0.2
Insulin—2–3 doses	2.3	0.9
Intensive insulin therapy —4–5 doses	3.0	1.1
Diet	0.9	1.0
Pills	0.7	0.6

3.3 HbA1c

We included HbA1c at the time of a visit and compared it to the average of blood glucose measurements transferred from the glucose meter. The results are given in Table 2. Good correlation between HbA1c and mean blood glucose level in the past 90 days is shown among the subjects who on average performed more than 4 measurements per day (Fig. 3), whereas this correlation is non-existent among subjects who performed less than 4 measurements per day (Fig. 4).

3.4 Blood Pressure

According to WHO guidelines on hypertension [7] (systolic blood pressure ≥ 140 mmHg or diastolic blood pressure ≥ 90 mmHg), 21 male and 27 female subjects are shown to have raised blood pressure.

T1DM subjects had lower average blood pressure (128.4 ± 17.3 over 78.9 ± 9.3 mmHg) than T2DM subjects (135.9 ± 19.3 over 85.8 ± 11.1 mmHg).

Although more female subjects were classified as high blood pressure, both T1DM and T2DM male subjects have higher average blood pressure.

3.5 Duration of the Disease and Duration of the Therapy

No significant association between either the duration of therapy or the duration of disease and mean blood glucose or standard deviation of blood glucose was found.

3.6 Inaccurate Time of Measurements

During the analysis, it has been noticed that around 10% of the subjects misconfigured their glucose monitor devices which led to false date and time results stored in database.

4 Conclusion and Future Work

The system successfully connected 19 different glucose meters with a single data management system. By acquisition of the patient data we are able to provide better insight into the population glycemic control.

Table 2 Comparison of mean HbA1c and mean SMBG

Subgroup	Mean HbA1c (%)	StdDev HbA1c (%)	Mean SMBG[a] (mmol/l)	StdDev SMBG (mmol/l)
T1DM—all	**7.11**	**0.89**	**8.30**	**3.84**
Male	7.24	0.79	8.25	3.69
Female	6.95	1.00	8.37	4.01
T2DM—all	**7.35**	**0.78**	**9.22**	**2.88**
Male	7.22	0.81	9.01	2.55
Female	7.44	0.75	9.37	3.12

[a]SMBG—Self-monitored blood glucose from last 90 days obtained from glucose meter

Fig. 3 Correlation between HbA1c and mean blood glucose value in prior 90 days for subject who measured 4 or more times per day on average
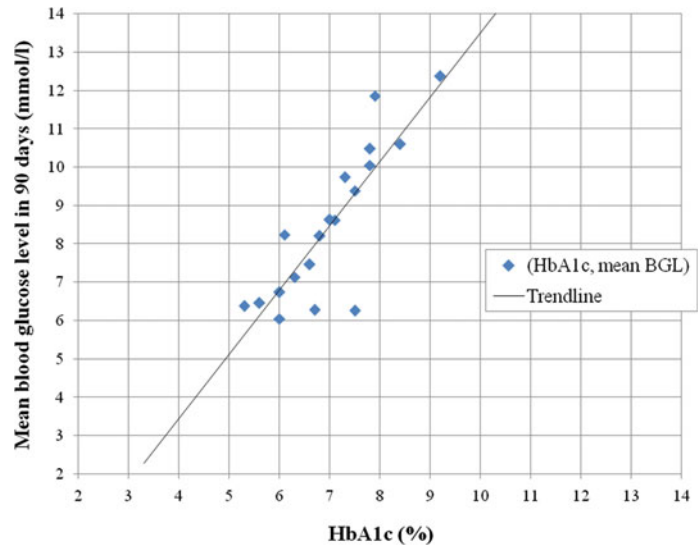
Fig. 4 Correlation between HbA1c and mean blood glucose value in prior 90 days for subject who measured less than 4 times per day on average
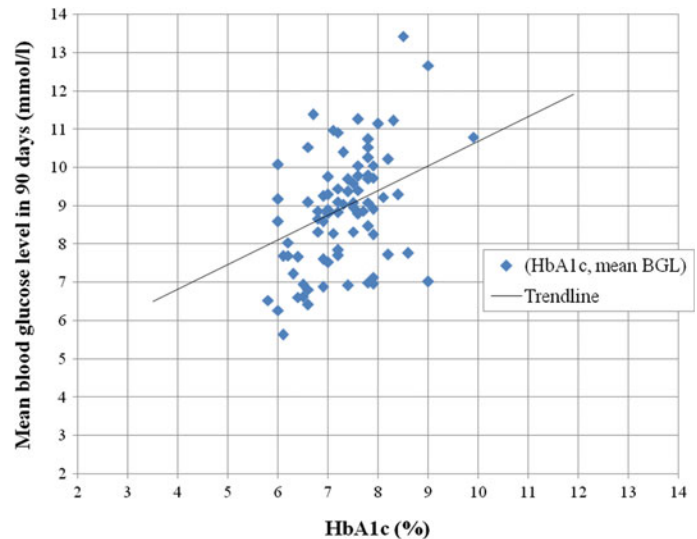
From the data analysis on the first one hundred patients, we were able to see that both BMI and blood pressure are higher in T2DM subjects, as well as good correlation between HbA1c values and mean blood glucose values among patients who measured 4 or more times per day.

In the context of data accuracy, we have notices an issue with data accuracy due to glucose meter misconfiguration.

In the next phase, we aim to further develop and test mobile system for personal use of a patient, which will give more information about patient's glycemic control including

nutrition information, medication/insulin intake, exercise and physical activity.

Conflict of Interest The authors declare that they have no conflict of interest.

References

1. S. Wild, G. Roglic, R. Sicree, and H. King, "Global prevalence of diabetes: estimates for the year 2000 and projections for 2030," Diabetes Care, vol. 27, 5, pp. 1047–1053, 2004.
2. Global status report on noncommunicable diseases 2014. Geneva, World Health Organization, 2012.
3. Strategies for Improving Care, Diabetes Care. 2015 Jan; 38, Suppl: S5–7, American Diabetes Association, 2015.
4. M. Prasek, "Self Control Diary – Challenges of New Technological Possibilities", IFMBE Proceedings 37, Budapest, 2011, p. 972–973.
5. L. Celic; D. Trogrlic; I. Paladin; M. Prasek; R. Magjarevic. "Integration of Measurement Devices Supporting Diabetic Patients into a Remote Care System", IFMBE Proceedings 37, Budapest, 2011, p. 39–42.
6. Glycemic Targets, Diabetes Care 2015;38(Suppl. 1):S33–S40, American Diabetes Association, 2015.
7. Whitworth JA, World Health Organization, International Society of Hypertension Writing Group: 2003 World Health Organization (WHO)/International Society of Hypertension (ISH) statement on management of hypertension. J Hypertension, 21, 2003.

Detection of Atrial Fibrillation Using 12-Lead ECG for Mobile Applications

Ricardo Jorge dos Santos Couceiro, Paulo Carvalho, Jorge Henriques, Rui Paiva, and Manuel Jesus Antunes

Abstract

Atrial Fibrillation (AF) is the most common arrhythmia and is associated with an increased risk of heart-related deaths and the development of conditions such as heart failure, dementia, and stroke. Affecting mostly elderly people, AF is associated with high comorbidity, increased mortality and is a major socio-economic impact in our society. Therefore, the detection of AF episodes in personalized health (p-Health) environments can be decisive in the prevention of major cardiac threats and in the reduction of health care costs. In this paper we present a new algorithm for detection of AF based on the assessment of the three main physiological characteristics of AF: (1) the irregularity of the heart rate; (2) the absence of the P-wave and (3) the presence of fibrillatory waves. Several features were extracted from the analysis of 12-lead electrocardiogram (ECG) signals, the best features were selected and a support vector machine classification model was adopted to discriminate AF and non-AF episodes. Our results show that the inclusion of features from the analysis of the recovered atrial activity was able to increase the performance of the algorithm: sensitivity of 88.5% and specificity of 92.9%.

R. J. dos. S. Couceiro · P. Carvalho · J. Henriques ·
R. Paiva
Department of Informatics Engineering, Science and Technology,
Centre for Informatics and Systems, University of Coimbra,
Pólo II, Coimbra, Portugal
e-mail: rcouceir@dei.uc.pt

P. Carvalho
e-mail: carvalho@dei.uc.pt

J. Henriques
e-mail: jh@dei.uc.pt

R. Paiva
e-mail: ruipedro@dei.uc.pt

M. J. Antunes (✉)
Centre of Cardio-Thoracic Surgery of the University Hospital of
Coimbra, Coimbra, Portugal
e-mail: antunes.cct.huc@sapo.pt

In the WELCOME project it is being designed a novel light vest with an integrated sensor system that collects several signals, including 12-lead ECG signals. The proposed algorithm is currently integrated in the WELCOME feature extraction module, which is responsible for receiving raw signals, extraction higher level features (e.g. occurrence of AF episodes) and provide them to the clinical decision process.

1 Introduction

ATRIAL FIBRILLATION (AF) is the most common sustained cardiac arrhythmia and is associated with significant morbidity, mortality and decreased life quality, specially in elderly, where its prevalence increases to 8% [1]. It is predicted that by 2060 AF will affect 17.9 million people in Europe and 6–12 million in United States by 2050 [2]. Despite not being lethal, AF is associated with an increased risk of heart failure, dementia, and stroke.

AF results from multiple re-entrant wavelets in the atria, which leads to its partial disorganization. In the electrocardiogram, AF can be recognized by the absence of the P-wave before the QRS-complex, which is replaced by a "sawtooth" shaped wave, and by the appearance of an irregular cardiac frequency, or both.

Based on these characteristics, several methods have been proposed in literature to detect AF using single-lead or multi-lead ECG signals. To assess the irregularity of the heart rhythm, methods based on the analysis of a Hidden Markov Model transition probabilities [3], linear and non-linear analysis of auto-regressive (AR) models [4] and histogram-based statistical analysis [5] have been proposed. To extract the atrial activity (AA), two main directions have been followed: (i) single-lead ECG analysis and multi-lead ECG analysis. Techniques such as blind source separation, spatio-temporal cancellation and artificial neural networks are the most promising in these two research fields. In

single-lead ECG analysis, the main approaches for QRS-T cancelation are based on wavelet transforms [6, 7] and template-based approaches (e.g. [8]), while in the multi-lead ECG analysis, the main methods are based on the blind source separation techniques, such as independent component analysis (ICA) [9]. However, the majority of the studies proposed lack of proper analysis regarding the extraction of relevant features from the extracted AA, capable of being used in the discrimination between AF and non-AF episodes.

In our previous work [10] we proposed an algorithm for detection of AF based on the single-lead ECG analysis and combining features assessed from heart rate (HR) and atrial activity.

In this paper, we propose a novel algorithm for the detection of AF, which is based on the assessment of the HR irregularity and on the atrial activity, using a 12-lead ECG approach. In this algorithm, the atrial activity is retrieved using ICA and several frequency domain features were extracted. The relevance of the extracted features was evaluated using the F-score metric and the best features (three from HR analysis, one from P-wave detection and four from AA analysis) were selected for classification purposes.

The remainder of the paper is organized as follows. In Sect. 2 the algorithm structure and feature extraction are presented. The data collection and main results are presented and discussed in Sect. 3. In Sect. 4 the main conclusions are outlined.

2 Methods

The proposed method consists of two main phases, which are: (1) the feature extraction and; (2) the classification. In the feature extraction phase, the ECG signals are processed and analyzed in order to extract relevant features for the discrimination between AF and non-AF episodes, which are used downstream during the classification phase.

2.1 Feature Extraction

The first step of the proposed algorithm is the segmentation of the MLII-lead ECG signal, i.e. the detection of its characteristics waves (P-wave, QRS-complex and T-wave). Here, an algorithm similar to the one proposed by Sun et al. [11] has been adopted.

(1) *Heart rate analysis*

In heart rate (HR) analysis the main objective is the extraction of features that are able to quantify the regularity of the RR intervals in the ECG. To this matter, the RR
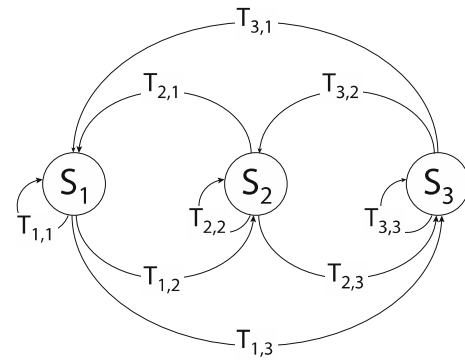

Fig. 1 Structure of the Hidden Markov model used to analyze the HR
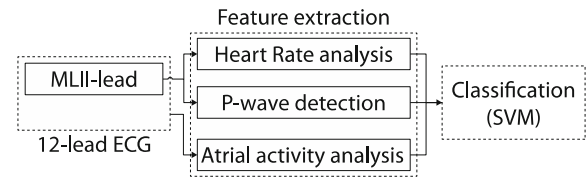

Fig. 2 Structure of the proposed algorithm

sequence was modelled using a Markov process (see Fig. 1) with three states [3]: small (S_1), regular (S_2) and long (S_3) RR intervals (Fig. 2).

From the transition probabilities between each state, one constructed a transition probability (TrP) matrix, which characterizes the regularity (or irregularity) of the heart cycles. The probability of the state S_2 and the probability of transition from S_2 to S_2 state quantifies the regularity of the heart rate, i.e. a high S_2-to-S_2 probability shows that is very likely to find two consecutive RR intervals with the same (regular) length. In fact, these are the first features (F_1 and F_2) that characterize the RR regularity:

$$F_1 = P(S_2) \tag{1}$$

$$F_2 = P(S_i, S_j) = P(S_i|S_j) \times P(S_i) \tag{2}$$

where $i = 2$ and $j = 2$ are the labels corresponding to the second state (regular RR interval).

From the analysis of the TrP matrix we found that AF and non-AF episodes present very characteristic distributions. While the TrP matrices corresponding to non-AF episodes present a dirak-impulse-like distribution concentrated around the S_2-to-S_2 transition, the TrP matrices from AF episodes present a much flatter probabilistic distribution, i.e. it is more likely to find transitions between RR intervals with different lengths during AF episodes. Based on this finding we proposed the assessment TrP matrix dispersion by measuring its entropy (H), as defined in (3).

$$F_3 = \sum_{i=1}^{3} P(S_i) \times \sum_{j=1}^{3} P(S_j|S_i) \times log_2 P(S_j|S_i) \qquad (3)$$

Additionally, the similarity between a probabilistic distribution under analysis and a model representative of AF episodes (collected from MIT-BIH Atrial Fibrillation database) was also assessed using the Kullback–Leibler divergence, as defined in (4).

$$F_4 = \sum_{x=1}^{3} \sum_{y=1}^{3} P(x,y) log \left(\frac{P(x,y)}{P_{AF}(x,y)} \right) \qquad (4)$$

where $\overline{P_{AF}(x,y)}$ is the defined AF model and $P(x,y)$ is the distribution under analysis. More details about these features can be found in [10].

(2) *P-wave detection*

The first step in the analysis of the atrial activity is to search for the presence of P-waves before the QRS complex. While during non-AF episodes the P-waves are commonly distinguishable, during AF episodes the P-waves are replaced by a "sawtooth" like waveform resultant from the fibrillatory process. To correctly evaluate the presence or absence of P-waves, the Pearson correlation (ρ) coefficient is calculated between the segmented P-waves and a P-wave model and the rate of P-waves per window (F_6) is assessed by:

$$F_5 = R_{Pwaves} = \frac{N_{SP}}{N_{RR}} \qquad (5)$$

where N_{SP} is the number of selected P waves (with ρ greater than 0.2) and N_{RR} is the number of cardiac cycles detected in the analysed window.

(3) *Atrial activity analysis*

The third main characteristic of AF is the discoordination of the atrial activation, which is a result of the disorganization in the path of the electrical impulses in the atria. In the ECG, the result is the replacement of the commonly seen P-waves by fibrillatory waves, with typical frequencies ranging from 5 to 8 Hz (herein defined as AF_{int}). Moreover, the spectrum of AF episodes presents no harmonics and the amplitudes above 15 Hz are minimal [9].

In order to analyse this process, it is essential to retrieve the signal components related with the AA, i.e. to cancel or extract the QRS complex and the T wave (QRST) from the

analysed signals. To recover the atrial components of the ECGs, we applied independent component analysis (ICA) as proposed in [9].

First, all the ECG signals were upsampled to 1 kHz using a shape-preserving piecewise cubic interpolator, aiming the improvement of the frequency resolution in the subsequent analysis. Next, the signals were normalized regarding their amplitude and preprocessed. In the preprocessing, the power line interference is canceled using a 50 Hz notch filter, while the baseline wandering and thermal noise are reduced using a 0.5–60 Hz band-pass filter. The separation process was performed using the FastICA algorithm in consecutive 10 s windows, shifted by 10 s increments. The identification of the components related with the AA was performed using a kurtosis-based source reordering, where the components with sub-Gaussian statistical properties ($k < 0$) were assigned to AA, and the components with Gaussian ($k = 0$) and super-Gaussian properties ($k > 0$) were assigned to noise (and/or artifacts) and VA, respectively. After the separation process is concluded, the components corresponding to the AA are summed into a single AA source and the power spectral density (PSD) was estimated using the Welch's (WOSA) method. In the PSD estimation one used a Hamming window with 4096 samples, a section overlap of 2048 samples and a discrete Fourier transform (DFT) with 8192 points.

From the analysis of the estimated PSDs, five features were extracted. Although AF episodes are characterized by a spectrum peak within the AF frequency region, occasionally, due to difficulties in the separation process or in the peak detection, no peak is found within this region. Therefore, the first AA feature (F_6), was defined as the distance from the spectrum maximum peak to the frequency interval characteristic of AF episodes, i.e. 5–8 Hz.

In contrast with AF spectrums, which present a very characteristic frequency spectrum with a major peak in the AF_{int}, non-AF episodes present a spectrum dispersed along a wider frequency range. This observation leads to the definition of more two AA features, which are the entropy of the spectrum (F_7) and the Kullback–Leibler divergence between the spectrum and a generalized bell-shaped membership function (F_8):

$$f(x, a, b, c) = \frac{1}{1 + \left| \frac{x-c}{a} \right|^{2b}} \qquad (6)$$

where the parameters $a = 2$, $b = 6$ and $c = 6$ control the shape and position of the function in the AF_{int}. Let $P(w)$ be the spectrum under analysis and $Q(w)$ be the aforementioned

bell-shaped function, the features F_7 and F_8 are defined as follows:

$$F_7 = -\sum_{w \in W} P(w) \times log_2 P(w) \tag{7}$$

$$F_8 = -\sum_{w \in W} P(w) log \frac{P(w)}{Q(w)} \tag{8}$$

where w is the frequency bin and W is the range of spectrum frequencies.

Additionally, the dispersion of the spectrum was also assessed by the number of spectrum peaks above half height the maximum peak (F_9) and by the weight of the main peak spectrum frequencies (F_{10}), as defined in (9) and (10)

$$F_{10} = \frac{\sum_{w \in W} P(w) \times Q(w)}{\sum_{w \in W} P(w)} \tag{9}$$

where W_P is the range of frequencies corresponding to the main spectrum peak.

To assess the weight of the spectrum frequencies above 15 Hz the last feature was defined as:

$$F_{11} = \frac{\sum_{w > 15} P(w)}{\sum_{w \in W} P(w)} \tag{10}$$

In Fig. 3 we illustrate the main characteristics of the AF and non-AF spectra and the rationale behind the extracted features.

Fig. 3 Spectra of AF and non-AF episodes and corresponding extracted features
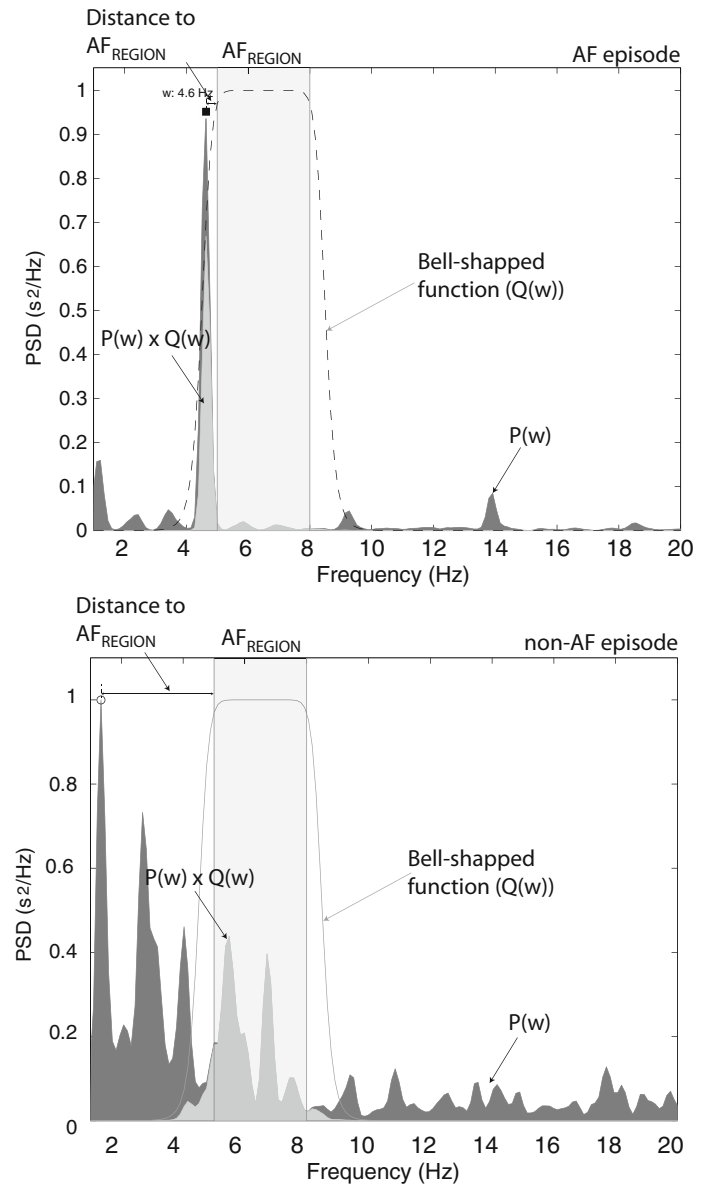
Table 1 Results achieved by the proposed multi-lead and single-lead AF detection algorithms

Algorithm	SE (%) avg ± std	SP (%) avg ± std	PPV (%) avg ± std
Single-lead algorithm [10]	79.0 ± 3.0	91.4 ± 0.5	86.6 ± 2.2
Multi-lead algorithm	88.5 ± 1.4	92.9 ± 0.3	90.6 ± 1.4

2.2 Classification

The classification between AF and non-AF episodes was performed on a 10 s window basis using a support vector machine classification model (C-SVC algorithm) with a radial basis function.

3 Results and Discussion

3.1 Study Protocol

In this study AF and non-AF episodes from 12 patients were considered. From those, 1 episode (2 records of 30 min.) was selected from the "St.-Petersburg Institute of Cardiological Technics 12-lead Arrhythmia Database" and 11 episodes (11 records of 60 min.) were selected from the 12-lead ECG database collected under the project "Cardiorisk—Personalized Cardiovascular Risk Assessment through Fusion of Current Risk Tools".

The selected records were partitioned into records of 5 min leading to the construction of a dataset consisting of 144 records of 5 min length, in which 72 records present AF and 72 records present other rhythms other than AF.

3.2 Feature Selection

The selection of the features most suitable for detection of AF episodes was performed based on the F-score metric. A ROC analysis was performed for each feature using a sixfold cross validation approach, leading to the selection of eight features. The best features were extracted from the HR analysis (F_4 and F_3), followed by three features from the AA analysis (F_6, F_8 and F_{10}). Three features from both HR and AA analysis (F_2, F_9, F_{11}) presented a F-score below the 50% and therefore were not selected.

3.3 Validation

The validation of our algorithm was performed using a sixfold cross validation approach, where the dataset was randomly partitioned into 6 equal size subsets. From the 6 subsets, 5 subsets were used for training (with episodes from 10 patients) and 1 subset (with episodes from the remaining 2 patients) was used for testing. The cross-validation process was repeated 6 times for each of the 6 subsets. This process was repeated 20 times and the average and standard deviation (avg ± std) of the sensitivity (SE), specificity (SP) and positive predictive value (PPV) was evaluated.

In Table 1 we present the results achieved by the single-lead [10] and multi-lead algorithms in the testing subsets. It is possible to observe that the multi-lead algorithm performed better than the single-lead algorithm. The analysis of AA recovered from 12-lead source separation provided relevant features that enabled the increase of approximately 9% the algorithms SE, 1% in the algorithms SP and 4% in the algorithms PPV. These results show that source separation techniques such as ICA can provide a valuable insight about AA and enable the extraction of reliable features for AF detection.

Conclusions

In this paper we presented a novel algorithm for detection of AF episodes based on the analysis of 12-lead ECG signals. The proposed algorithm is based on the analysis of the three main characteristics of AF: the irregularity of the RR interval, the absence of the P-wave and the presence of the fibrillatory wave. The extraction of features from the separated atrial activity is the main innovative aspect of the proposed algorithm. Experimental results showed that the extracted features are relevant to this topic and the algorithm was able to achieve better discrimination performance when compared to the previously proposed single-lead solution. Based on these evaluations, it is possible to conclude that the extraction and analysis of atrial activity from multi-lead ECG signals is an important contribution to the enhancement of AF detection problem.

The proposed algorithm is currently integrated in the WELCOME feature extraction module, which is responsible for the off-line extraction of higher level features in a cloud server and for providing them to the clinical decision process.

Conflict of Interest The authors declare that they have no conflict of interest.

References

1. R. C. Davis, F. D. R. Hobbs, J. E. Kenkre, A. K. Roalfe, R. Iles, G. Y. H. Lip, *et al.*, "Prevalence of atrial fibrillation in the general population and in high-risk groups: the ECHOES study," *EP Europace,* vol. 14, pp. 1553–1559, 2012-11-01 00:00:00 2012.

2. R. B. Schnabel, X. Yin, P. Gona, M. G. Larson, A. S. Beiser, D. D. McManus, *et al.*, "50 year trends in atrial fibrillation prevalence, incidence, risk factors, and mortality in the Framingham Heart Study: a cohort study," *The Lancet,* vol. 386, pp. 154–162.

3. G. B. Moody and R. G. Mark, "A new method for detecting atrial fibrillation using R-R intervals.," in *Computers in Cardiology*, 1983, pp. 227–230.

4. S. Cerutti, L. T. Mainardi, A. Porta, and A. M. Bianchi, "Analysis of the dynamics of RR interval series for the detection of atrial fibrillation episodes," in *Computers in Cardiology 1997*, 1997, pp. 77–80.

5. K. Tateno and L. Glass, "A method for detection of atrial fibrillation using RR intervals," in *Computers in Cardiology 2000*, 2000, pp. 391–394.

6. L. Senhadji, F. Wang, A. Hernandez, and G. Carrault, "Wavelets extrema representation for QRS-T cancellation and P wave detection," in *Computers in Cardiology, 2002*, 2002, pp. 37–40.

7. C. Sanchez, J. Millet, J. J. Rieta, F. Castells, J. Rodenas, R. Ruiz-Granell, *et al.*, "Packet wavelet decomposition: An approach for atrial activity extraction," in *Computers in Cardiology, 2002*, 2002, pp. 33–36.

8. S. Shkurovich, A. V. Sahakian, and S. Swiryn, "Detection of atrial activity from high-voltage leads of implantable ventricular defibrillators using a cancellation technique," *Biomedical Engineering, IEEE Transactions on,* vol. 45, pp. 229–234, 1998.

9. J. J. Rieta, F. Castells, C. Sanchez, V. Zarzoso, and J. Millet, "Atrial activity extraction for atrial fibrillation analysis using blind source separation," *Biomedical Engineering, IEEE Transactions on,* vol. 51, pp. 1176–1186, 2004.

10. R. Couceiro, P. Carvalho, J. Henriques, M. Antunes, M. Harris, and J. Habetha, "Detection of atrial fibrillation using model-based ECG analysis," in *ICPR 2008. 19th International Conference on Pattern Recognition, 2008*, 2008, pp. 1–5.

11. Y. Sun, K. Chan, and S. Krishnan, "Characteristic wave detection in ECG signal using morphological transform," *BMC Cardiovascular Disorders,* vol. 5, pp. 1–7, 2005.

A Multi-feature Approach for Noise Detection in Lung Sounds

Adriana Leal, César Teixeira, Ioanna Chouvarda, Nicos Maglaveras, Jorge Henriques, Rui Paiva, and Paulo Carvalho

Abstract

During the acquisition of lung sounds, several sources of noise can interfere with the recordings. Therefore, the detection of noise present in lung sounds plays an important role in the correct diagnosis of several pulmonary disorders such as in chronic obstructive pulmonary diseases. Denoising tools reported so far focus mainly in the detection of abnormal lung sounds from the background noise (usually vesicular background) or even just in the discrimination of normal from abnormal lung sounds. Algorithms for heart sound cancellation have also been proposed. However, it can be noticed that there is a lack of signal processing methods to efficiently detected and/or remove artifacts introduced in the acquisition environment or produced by the subject (e.g., speech). The present study focuses in the analysis of lungs sounds recorded in two different populations containing events of cough, speech and other artifacts from the surrounding environment. Feature extraction and binary classification were performed achieving, on average, values of a sensitivity and specificity ranging from 76 to 97% for the classification of cough, speech and other artifacts and from 83 to 90% for the specific detection of cough events. The detection of artifacts achieved sensitivity and specificity values of 84% and 61%, respectively for one population and 88% and 52% for another population.

1 Introduction

The acquisition of lung sounds (LSs) using the stethoscope is considered an important, fast and noninvasive method in the detection of pulmonary disorders, namely chronic obstructive pulmonary diseases (COPD) [1]. The presence of abnormal LSs in the normal respiratory cycle is an indicator that leads to a positive diagnosis.

LS is a biological signal characterized by a stochastic nonstationary behavior, with sudden variations in short periods of time over the signal [1, 2]. The signal's bandwidth typically ranges from 50 to 2500 Hz (when signals are acquired on the chest) [3, 4]. In fact, the morphology of the LS can vary from subject to subject, depending on the chest size and on the body mass, and it is also influenced by the variations in the air flow rate and on the position where the stethoscope is attached in the chest [5, 6].

However, LSs can be contaminated with noise coming from the acquisition environment and also with physiological interferences, such respiratory muscle and heart sounds (HSs) [3, 4]. Specifically, concerning HSs interference, it is known that the predominant frequency components typically detected in those signals may overlap the frequency range of the LSs, making it hard to distinguish both types of sound [5, 7].

Then, in order to truthfully conclude about the clinical state of a subject, concerning pulmonary disorders, the LSs should ideally be free of any type of noise. Following that

A. Leal · C. Teixeira · J. Henriques · R. Paiva · P. Carvalho (✉)
Center for Informatics and Systems, Polo II, University of
Coimbra, 3030-290 Coimbra, Portugal
e-mail: carvalho@dei.uc.pt

A. Leal
e-mail: adriana.leal@student.fisica.uc.pt

C. Teixeira
e-mail: cteixei@dei.uc.pt

J. Henriques
e-mail: jh@dei.uc.pt

R. Paiva
e-mail: ruipedro@dei.uc.pt

I. Chouvarda
Laboratory of Medical Informatics, Medical School, Aristotle
University of Thessaloniki, 54124 Thessaloniki, Greece
e-mail: ioanna@med.auth.gr

N. Maglaveras
Laboratory of Medical Informatics, Medical School, Institute of
Applied Biosciences, Center for Research and Technology,
Aristotle University of Thessaloniki, 54124 Thessaloniki, Greece
e-mail: nic-mag@med.auth.gr

211

purpose, several approaches in literature have been proposed to detect abnormal LSs from the vesicular background (considered the background noise) present in the original LS. Those methods include higher-order statistics (HOS), fuzzy logic, wavelet transform (WT), empirical mode decomposition (EMD) and fractal dimension (FD) [1, 4]. In most of the studies, one infers that the acquisitions take place in controlled clinical environments, where external noise is intentionally reduced or just nonexistent.

There is also a wide number of authors who presented algorithms developed to remove HSs from the original LSs, using mainly adaptive HOS, WT, recursive least squares and time-frequency spectrum analysis [4].

However, only few articles were found to report signal processing methods to detect and remove artifacts from LSs, in m-Health environments. Two papers reported algorithms based on spectral subtraction of a noise estimate obtained from: a period when the patient sustained breathing [8] or a reference sensor that solely and simultaneously recorded the ambient noise [6]. In another study a denoising filter based on a combination of EMD and FD was described, returning 91.8% of sensitivity and 97.7% of specificity [1].

The aforementioned methods can be of great usefulness when LSs need to be acquired in unpredictable noisy environments. In other words, denoising tools for LSs are required in telemonitoring systems that could provide continuous monitoring of patients with pulmonary disorders.

Herein, we analyze LSs that were deliberately contaminated with periods of cough followed by speech performed by each patient. Furthermore, other sources of noise can be heard that include voices and cough from other subjects in the room and hair rub. The purpose of the study is the detection of all types of artifact, to allow the further interpretation of the LSs. We follow a multi-feature approach to face the problem of noise detection in LSs.

2 Materials and Methods

2.1 Data Collection

Pulmonary signals were recorded in two different populations: at the (1) George Papanikolaou General Hospital of Thessaloniki and (2) General Hospital of Imathia-Health Unit of Naoussa, Greece (see Table 1). All subjects comprising the Thessaloniki dataset were diagnosed with COPD. Wheezes or wheezes and crackles were identified in the LSs of six subjects of the Naoussa population. The ethical committee of both hospitals authorized the acquisition of the data.

Auscultation was performed with the participants in a sitting position, using six channels that were set in different positions: four in the back and two in the front of the chest. During the acquisition, the volunteers were asked to simulate cough and next to count from one to ten. The different events were annotated in the timeline by the physicians who supervised the acquisition and we assigned them to four distinct classes: (1) cough and speech, (2) artifact, (3) abnormal LSs, and (4) normal LSs (see Table 1). Cough and speech periods last on average 5–6 s in the Thessaloniki population and are also the predominant events in the Naoussa dataset.

2.2 Feature Extraction

The features were computed for each individual channel, since each channel corresponds to different positions in the chest and also to different recording times.

Four different features were tested in the analysis of LSs and will be briefly described in this section. The LSs signals were windowed, with a given percentage of overlap. The size of the window and the overlap were defined for the highest specificity and sensitivity, depicted in a receiver operating characteristic (ROC) curve.

(1) *Teager-Kaiser energy operator* (*TKEO*): As a nonlinear energy operator, this feature is useful to highlight sudden discontinuities (either in amplitude or frequency) and reduce smooth transitions occurring in the signal [9].

In (1) the discrete version of TKEO is computed for the signal x_n. Energy is obtained for each window in each instant and depends on the strength of the previous and next sample [9]. So far only another author used this feature for the detection of crackles [10].

$$E_n = x_n^2 + x_{n-1}x_{n+1} \tag{1}$$

(2) *Katz fractal dimension* (*KFD*): This feature is a measure of the complexity of a signal in the time domain. KFD is estimated in (2), where L is the sum of the Euclidean distance between successive points, d is the distance between the first point of the window and the point of the window at which the distance is maximal, n is the number of steps in the window ($n = N - 1$), and N is the length of the input data [4, 11, 12].

Table 1 Population description

Population	Thessaloniki	Naoussa
Sampling rate (Hz)	10,000	4000
Stethoscope	3M Littman 3200	Meditron
Number of subjects	7	9
Mean signal duration (s)	70	19
Abnormal lung sounds	Wheezes, fine crackles, coarse crackles	
Artifacts	External voice, cough with artifacts	Speech background, cough background, hair rub

$$KFD = \frac{\log_{10}(n)}{\log_{10}\left(\frac{d}{L}\right) + \log_{10}(n)} \tag{2}$$

(3) *Mel-frequency cepstral coefficients (MFCC)*: The cepstral coefficients are obtained from the inverse cosine transform of the logarithm of the short-time Fourier transform (STFT) of each window and are given by (3):

$$c_n = \sum_{k=1}^{M} \log(E_k)\left(n(k-0.5)\frac{\pi}{M}\right) \tag{3}$$

where $n = 1, 2, \ldots, L$, L is the desired number of cepstral coefficients, M is the number of frequency subbands and E_k is the respective filter bank energy. This approach uses a different weighting frequency scale that closely resembles how human ear perceives sounds. The cepstrum, in addition to the spectrum which informs about the predominant frequencies present in the signal, allows to know how those frequencies change across time [6, 13]. The extracted feature corresponds to the coefficient with the highest module of specificity and sensitivity in the ROC curve.

(4) *Normalized mutual information* (*NMI*): Mutual information quantifies the statistical dependence between random variables or, in other words, the amount of information shared by those variables. The I between two variables X and Y, denoted $I(X; Y)$, is obtained using the corresponding entropies, $H(X)$ and $H(Y)$ and the joint entropy $H(X, Y)$ [14]:

$$I(X; Y) = H(X) + H(Y) - H(X, Y) \tag{4}$$

$H(X)$ and $H(Y)$ are given by:

$$H(X) = -\sum_{x \in X} p(x) \log p(x) \tag{5}$$

With x taking any of the non repeated values in the variable X and $p(x)$ corresponding to the frequency counts of the discrete variable X. Joint entropy is given by:

$$H(X, Y) = -\sum_{x,y} p(x, y) \log p(x, y) \tag{6}$$

In order to scale the values of $I(X; Y)$ between 0 (statistically independent variables) and 1 (variables with the same information) normalization was performed:

$$NMI = \frac{I(X; Y)}{H(X)} \tag{7}$$

NMI was computed for a reference window, free of noise, and for each of the windows into which the LS was segmented (named test windows). The final feature corresponds to the comparison between the NMI of the reference window and each of the test windows. This method of finding a reference window was developed in another study which purpose was the detection of artifact in phonocardiogram signals [15]. However, this algorithm to denoise HSs has suffered slight changes aiming to adapt it to the study of LSs. Shortly, the algorithm comprises two steps: (1) search for a reference window considered free from noise and (2) comparison of the reference window with all the windows into which the signal was segmented (named test windows), in order to distinguish contaminated from clean windows.

In the first phase, differently from the HSs' algorithm, the LSs signal is windowed and the TKEO is computed for each window. The reference window will correspond to the window with the minimum value of TKEO. Other two features, spectral similarity (R) and PSD ratio, described in [15], were also computed for the LSs.

2.3 Classification

Detection of artifacts is performed in three stages. Firstly, events other than LSs (cough, speech and other artifacts) were classified using different features (TKEO, KFD, MFCC, R, and PSD ratio). In the second part, the events of cough were classified using features NMI and MFCC, depending on dataset. In the final phase, the detection of artifact, including the speech segments, took place using the output of the two previous classifications (see Fig. 1).

The binary classification outputs a vector of 0s and 1s (called "detected"), where one corresponds to the detection of the artifact and zero to a non detected event, respectively. Consequently, classification only takes place if a fixed
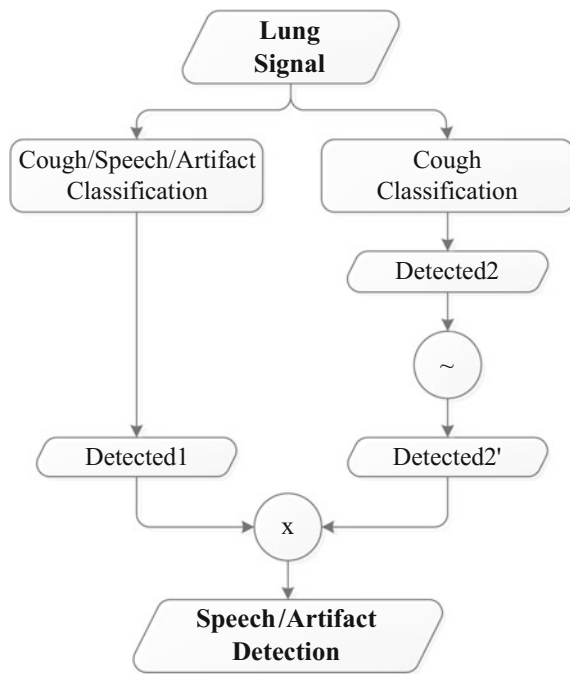
Fig. 1 Multi-stage algorithm for the classification of artifact

threshold is set for each of the features. If the value of the feature in the test window is above this threshold, that window is classified as contaminated. In order to obtain the best values of specificity and sensitivity for each feature several thresholds were tested and further analyzed using the ROC curve. The 100 tested thresholds ranged from the minimum to the maximum of the feature. In other words, the tested thresholds were a percentage of the signal, making them adaptive thresholds. The discrimination capacity of the features was assessed in terms of specificity and sensitivity, by comparing the output of the classification, the "detected", with the target (annotated by the physicians).

The algorithm was implemented in Matlab R2013b on Windows 8.1 using an Intel® Core™ i7-4790 K CPU at 4 GHz.

3 Results and Discussion

Tables 2 and 3 contain the results of the classification in terms of sensitivity and specificity, averaged across the subjects for each one of the parameter combination (window, overlap and threshold).

3.1 Detection of Cough, Speech and Artifact Events

The detection results obtained for the five features previously described in Sect. 2.2 are presented in Table 2. The best results were obtained for the features TKEO and KFD in the Thessaloniki dataset and MFCC in the Naoussa population. Naoussa signals were of lower size comparing to the files from Thessaloniki, explaining the variation in the window size across the two populations.

Table 2 Classification results for cough, speech and artifact detection

Population	Feature	Window (s)	Overlap (%)	Threshold[a]	SS (%)	SP (%)
Thessaloniki	TKEO	3.9	90	9	92.04	97.24
	KFD	4	90	10	90.91	99.24
	MFCC	4	80	58	86.52	93.71
	SPEN	4	80	9	85.98	92.81
	R	4	90	5	86.14	96.37
Naoussa	TKEO	2.3	60	57	63.09	99.50
	KFD	2.8	70	53	69.18	98.79
	MFCC	1	90	64	84.66	96.40
	SPEN	1	90	20	78.47	94.18
	R	0.5	90	3	84.38	96.29

[a]Percentage of the features' amplitude

Table 3 Classification results for cough detection

Population	Feature	Window (s)	Overlap (%)	Threshold[a]	SS (%)	SP (%)
Thessaloniki	NMI	4	90	81	84.49	83.05
Naoussa	MFCC	0.5	90	83	90.36	90.09

[a]Percentage of the features' amplitude

Table 4 Classification results for speech and artifacts detection

Population	SS (%)	SP (%)
Thessaloniki	84.39	61.54
Naoussa	87.72	56.38

3.2   Detection of Cough Events

Cough is an important manifestation of several pulmonary diseases (e.g. pulmonary fibrosis, COPD, lung cancer, etc.). Consequently, counting and classification of cough is considered a useful diagnostic tool [16]. The cough events were classified using the NMI and MFCC features in the Thessaloniki and Naoussa populations, respectively. Unlike other tested features, NMI and MFCC (the latter using a different window size) allowed the identification of the cough events rather than the detection of both cough and speech segments. Results are presented in Table 3.

3.3   Detection of Speech and Artifact Events

For this classification the "detected" vectors obtained in Sects. 3.1 and 3.2 were used to compute the "detected" for the third phase of the algorithm (see Fig. 1). The results of the classification of the class speech and artifact versus the class cough and LSs are presented in Table 4.

The results are strongly dependent on the annotations (which will influence the target definition). Moreover, the detection of artifact, the main purpose of this study, was affected by the size of the windows selected through the ROC curve. In the specific case of the Thessaloniki dataset, using a 4s window lead to good results in the classification of cough and speech since those events' duration is superior to the window used to segment the signal. On the contrary, other artifact events such external voices or hair rub last less than 4 s making these type of events hard to detect when cough and speech are the predominant segments in the signal.

4   Conclusions

The detection of artifact in lung sounds becomes an important step when those signals need to be acquired in unpredictable conditions, e.g., when there are different sources of noise in the acquisition environment. Therefore, in the search for a suitable methodology to identify interferences in LSs, several features were tested and optimal parameters were selected. The features analyzed reached a high detection capacity in the classification of cough, speech and other artifacts occurring in uncontrolled environments.

This performance was reflected in the values of sensitivity and specificity, which average value for all the features was 88% and 96%, respectively for Thessaloniki population and 76% and 97%, respectively for the Naoussa dataset. The results for the classification of cough were equally high, with sensitivity and specificity ranging, respectively from 83% to 90% in both populations. The classification of artifact, including speech against the other events, lead to lower sensitivity (ranging from 84 to 88%) and even lower specificity (ranging from 61 to 56%) in both populations.

As future work, the set of features tested will be considered as inputs of more complex classifiers able to define more flexible, nonlinear decision boundaries. Data from each channel, i.e., each position of the stethoscope can also be analyzed separately in order to conclude about the more suitable locations to detect noise. Finally, it must be noticed that a careful inspection of the annotations of the events will have a significant impact in the specificity and sensitivity.

References

1. L. Hadjileontiadis, Empirical mode decomposition and fractal dimension filter: a novel technique for denoising explosive lung sounds, *IEEE Engineering in Medicine and Biology Magazine*, no. 1, pp. 30–39, Jan.
2. A. Bohadana, G. Izbicki, and S. S. Kraman, Fundamentals of lung auscultation. *The New England journal of medicine*, no. 8, pp. 744–751, Feb.
3. A. Gurung, C. G. Scrafford, J. M. Tielsch, O. S. Levine, and W. Checkley, Computerized lung sound analysis as diagnostic aid for the detection of abnormal lung sounds: a systematic review and meta-analysis. *Respiratory medicine*, no. 9, pp. 1396–1403, Sep.
4. L. J. Hadjileontiadis, Lung sounds: an advanced signal processing perspective. *Synthesis Lectures on Biomedical Engineering*, no. 1, pp. 1–100, Jan.
5. Z. Moussavi, Fundamentals of respiratory sounds and analysis. *Synthesis Lectures on Biomedical Engineering*, no. 1, pp. 1–68, Jan.
6. G. -C. Chang and Y. -F. Lai, Performance evaluation and enhancement of lung sound recognition system in two real noisy environments. *Computer methods and programs in biomedicine*, no. 2, pp. 141–150, Feb.
7. T. H. Falk and W. -Y. Chan, Modulation filtering for heart and lung sound separation from breath sound recordings. *Conference proceedings: Annual International Conference of the IEEE Engineering in Medicine and Biology Society. IEEE Engineering in Medicine and Biology Society. Annual Conference*, pp. 1859–1862, Jan.
8. A. Yadollahi and Z. Moussavi, On arithmetic misconceptions of spectral analysis of biological signals, in particular respiratory sounds. *Conference proceedings: Annual International Conference of the IEEE Engineering in Medicine and Biology Society.*

IEEE Engineering in Medicine and Biology Society. Annual Conference, pp. 388–391, Jan.

9. E. Kvedalen, Signal processing using the Teager Energy Operator and other nonlinear operators, Jul.

10. L. Mendes, P. Carvalho, C. A. Teixeira, R. P. Paiva, and J. Henriques, Robust features for detection of crackles: an exploratory study. *Conference proceedings: Annual International Conference of the IEEE Engineering in Medicine and Biology Society. IEEE Engineering in Medicine and Biology Society. Annual Conference*, pp. 1473–6, Aug.

11. L. Hadjileontiadis and I. Rekanos, Detection of explosive lung and bowel sounds by means of fractal dimension, *IEEE Signal Processing Letters*, no. 10, pp. 311–314, Oct.

12. S. Charleston-Villalobos, G. Dorantes-Méndez, R. González-Camarena, G. Chi-Lem, J. G. Carrillo, and T. Aljama-Corrales, Acoustic thoracic image of crackle sounds using linear and nonlinear processing techniques. *Medical & biological engineering & computing*, no. 1, pp. 15–24, Jan.

13. M. Bahoura, Pattern recognition methods applied to respiratory sounds classification into normal and wheeze classes, *Computers in Biology and Medicine*, no. 9, pp. 824–843, Sep.

14. G. Brown, A. Pocock, M. -J. Zhao, and M. Luján, Conditional likelihood maximisation: a unifying framework for information theoretic feature selection, *The Journal of Machine Learning Research*, no. 1, pp. 27–66, Jan.

15. D. Nunes, A. Leal, R. Couceiro, J. Henriques, L. Mendes, P. Carvalho, and C. Teixeira, A low-complex multi-channel methodology for noise detection in phonocardiogram signals, 37th Annual International Conference of the Ieee Engineering in Medicine and Biology Society, p. 4.

16. C. Lucio, C. Teixeira, J. Henriques, P. de Carvalho, and R. P. Paiva, Voluntary cough detection by internal sound analysis, *2014 7th International Conference on Biomedical Engineering and Informatics*. 1em plus 0.5em minus 0.4em IEEE, pp. 405–409, Oct.

Reconstruction and in Silico Simulation Towards Electricigens Metabolic Network of Electronic Mediator

Yuhe Wang, Zhenglin Tong, and Jianming Xie

Abstract

Microorganisms have drawn our attention for its distinguished capacity of electron transportation. Recently microbial fuel cells (MFC) have emerged as a novel biochemical catalytic device, the electron transfer mechanisms are of our primary concern to improve the efficiency of extracellular electron transfer (EET). Here we reconstruct the genome-scale metabolic network of Shewanella oneidensis MR-1 by merlin. Based on text mining, we focus on the electronic mediators, then we complete the reconstruction of the metabolic sub-network. We have identified the key reactions of EET process combined with the utilization of COBRA Toolbox, the simulated gene and reaction knockouts provided guidance to the strain genetic modification to a certain level.

1 Introduction

The low rate of reaction, high internal resistance and fast energy consumption hinder the industrial application of MFC. Scientists have worked on the mechanism of electrogenesis for decades.

There are 3 main pathways, (a) the mediated transfer mode (MET) involving a mediator-used process, (b) the direct transfer mode (DET) containing c-type cytochrome and nanopili, (c) the pathway relying on the self-secreted flavins. We employ methods of omics and system biology, perform de novo assembly algorithms to analyze *Shewanella oneidensis* MR-1, figured out the key reactions with its corresponding mode and genes.

2 Methods

We utilized Merlin to reconstruct expected sub-network [1], as shown in Fig. 1.

Combined with text mining, verified major electron carrier as FMN, riboflavin, ubiquinone, menaquinone and NADH. We selected relevant reactions of KEGG to generate metabolic network relating electronic mediator.

The use of COBRA Toolbox to perform flux balance analysis (FBA) [2] on genome scale metabolic model (GSMM) iSO783 [3] got primary reactions of EET pathway.

3 Results and Discussion

This sub-network contains various reactions relating cytochrome c, indicates that cytochrome c applies a vast number of substrates to transfer electron. We have identified important reactions via FBA, which were listed in Table 1.

In addition, reactions as SO3DE, AKGD, MDH and PDH, were not included in FBA, which were contrary to Ong's research [3], thus we need further exploration.

Y. Wang · Z. Tong · J. Xie (✉)
Department of Biomedical and Science Engineering, Southeast University, Nanjing, China
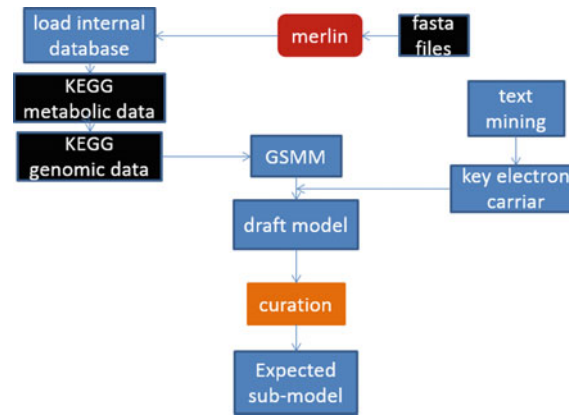e-mail: xiejm@seu.edu.cn

Fig. 1 The process of metabolic network reconstruction using Merlin

Table 1 Key reactions of different EET routes

Mode	Key reaction	Abbreviation
DET	(2.0) focytcc[c] + (4.0) h[c] + (0.5) o2[c] ➜ (2.0) ficytcc[c] + (2.0) h[e] + h2o[c]	CYOO2
	(2.0) ficytcc[c] + (2.0) h[c] + ubq8h2[c] ➜ (2.0) focytcc[c] + (4.0) h[e] + ubq8[c]	CYOR7
MET	(2.0) fe3[e] + mql7[c] ➜ (2.0) fe2[e] + (2.0) h[e] + mqn7[c]	FER3
	[c]:nad + nadph ➜ nadh + nadp	THD5
	[c]:icit + nad ➜ akg + co2 + nadh	ICDHXI
Flavins	[c]: (2) dmlz ➜ 4r5au + ribflv	RBFSB
	[c]: atp + ribflv ➜ adp + fmn + h	RBFK
	[c]: fmn + h + nadh ➜ fmnRD + nad	FMNRX

References

1. Oscar D, Hill EA, Geydebrekht OV, et al. "Reconstructing genome-scale metabolic models with merlin" [J], *Nucleic Acids Res*, 2015, 43, 8: 3899–3910.

2. Orth JD, Thiele I, Palsson BO, et al. "What is flux balance analysis?" [J], *Nat Biotechnol*, 2010, 28(3):245–248.

3. Ong WK, Vu TT, Lovendahl KN, et al. "Comparisons of Shewanella strains based on genome annotations, modeling and experiments" [J], *BMC Systems Biology*, 2014, 8: 31–41.

An Attempt to Define the Pulse Transit Time

Xiao-Rong Ding, Jing Liu, Wen-Xuan Dai, Paulo Carvalho,
Ratko Magjarević, and Yuan-Ting Zhang

Abstract

Pulse transit time (PTT) is promising for various clinical applications. This paper attempts to discuss different terminologies used for PTT and reveals the research discontinuity among different groups, with the aim to describe the definition of PTT and propose solutions to clarify the usage of PTT.

1 Introduction

EACH contraction of the heart produces a pressure pulse which travels from the left ventricular into the peripheral circulation through the arterial walls. Pulse transit time (PTT) refers to the time it takes a pulse wave to travel between two places in the cardiovascular system. PTT is a powerful physiological parameter that has been widely used for various clinical applications, such as the measurement of respiratory effort [1], evaluation of arterial stiffness, and estimation of blood pressure (BP), etc. [2], because of its noninvasive, reliable, low-cost and ease of use properties. Particularly, PTT has been extensively studied for unobtrusive and continuous BP measurement.

However, there are distinct differences between research groups in terms of the PTT definition, and PTT has been usually mixed up with pulse arrival time (PAT). Although the usage of PTT has been increasing in science and engineering during the past 50 years, there is still a lack of

X.-R. Ding · J. Liu · W.-X. Dai · Y.-T. Zhang (✉)
Department of Electronic Engineering, Joint Research Centre for Biomedical Engineering, The Chinese University of Hong Kong, Shatin, Hong Kong
e-mail: ytzhangmdbs@gmail.com

P. Carvalho
Departamento de Engenharia Informática, Universidade de Coimbra, Coimbra, Portugal

R. Magjarević
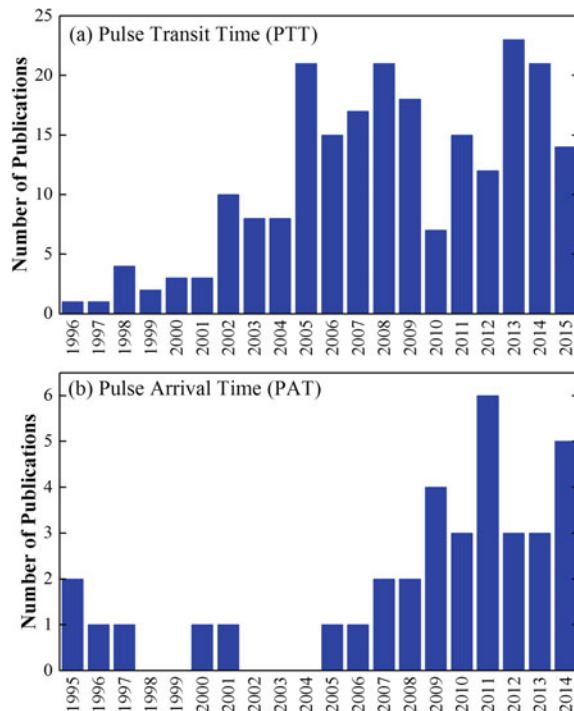Faculty of Electrical Engineering and Computing, University of Zagreb, Zagreb, Croatia

common terminology for PTT. This paper proposes the definition and terminology of PTT to resolve the difficulties and confusion within the scientific community.

2 Terminology

2.1 Pulse Transit Time (PTT)

The usage of PTT can be dated back to 1964, when Weltman et al. [3] devised the pulse wave velocity computer by "utilizing the EKG complex and a downstream pulse signal to define pulse transit time over a known arterial length". To the best of our knowledge, this is the first time the word "pulse transit time" being used and defined. In 1976, Steptoe [4] reported the "transit time"—the interval between R wave of the electrocardiogram (ECG) and the proximal pulse, as a modification of the interval between pulse arrivals at two sites on the same major artery for the sake of convenience. In 1978, Obrist et al. [5] measured PTT as the time between the initiation of the pre-ejection period (PEP) (formally PEP is defined as the time span between the Q wave of the ECG and the onset of the opening of the aortic valve; in practice the R wave of the ECG is usually used as the reference point since its determination is more easier and precise) and the peak of the pulse wave. In 1980, Weiss et al. [6] defined PTT as the interval between ventricular electrical activity and the peripheral appearance of the pulse. In the same year, Marie et al. [7] mentioned the time interval of ECG R wave to peripheral pulse as PTT absolute measures, while that between two peripheral pulses as PTT differences measures, which were referred as ECG-initiated transit time (ECG-TT) and arterial PTT respectively by Redman et al. [8] in 1983.

2.2 Pre-ejection Period (PEP)

The PTT calculating from ECG and peripheral pulse includes PEP [5]. Ever since 1981, there have been some studies

taking PTT as the interval between pulse arrivals between two arterial sites. For example, in the studies [9, 10], PTT was measured as the interval between two arterial sites, meanwhile the time difference between the R wave of ECG and the peripheral pulse was called ECG-pulse interval or PAT.

According to Thomson Reuters Web of Science, the total number of references for "pulse transit time" was 270, with the sum of times cited was 2380, among which PTT was commonly used not only as the time difference from R wave of ECG to peripheral pulse but also as the time intervals between two peripheral pulses; while the total number of references for "pulse arrival time" was 49 with the sum of times cited was 396. As shown in Fig. 1, the number of publications in the recent 20 years for "PTT" is increasing with years more than "PAT". We did a survey of PTT studies during 1964–2015. Among 270 publications with title including "pulse transit time", PTT that defined and calculated as the time interval between R wave of ECG and peripheral pulse is dominant.

3 Definition of Pulse Transit Time

The word "transit" is defined as "carrying of people or things from one place to another" according to Oxford Dictionaries. Accordingly, the definition of PTT—"The time for the carrying of pulse wave information by pulse signal from one 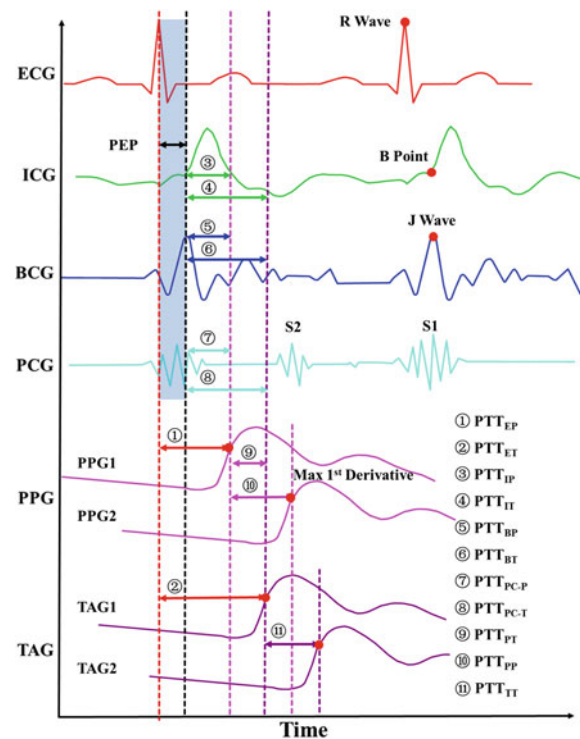location to another in the cardiovascular system"—is a more broad definition which covers the transit times determined by different approaches, such as the time intervals between R wave of the ECG and the photoplethysmogram (PPG)/ tonoarteriogram (TAG) [11] which includes the PEP, impedance cardiogram (ICG)/ballistocardiogram (BCG)/ ph-onocardiogram (PCG) to PPG/TAG, PPG to TAG, or by two PPGs/TAGs at different arterial sites, etc. However, "arrival" should be referred to the pulse in the same form of energy from the starting point to the arrival point, suggesting PAT is not equivalent of PTT.

4 Terminologies of Pulse Transit Time

In order to clarify the ambiguity on the usage of PTT, we propose to label PTT calculated from different methods, with the indexes consisting of the first one/two letter(s) of the starting signal and the arrival signal. Most of the current PTT calculation methods are summarized in Fig. 2.

5 Conclusion

In this abstract, PTT has been defined according to its measuring methods to resolve the confusion regarding PTT usage. We should clarify the PTT to overcome the disconnection between different groups and save the researchers' efforts.

References

1. R. P. Smith, et al., "Pulse transit time: an appraisal of potential clinical applications," *Thorax*, vol. 54, pp. 452–457, May 1999.
2. J. E. Naschitz, et al., "Pulse transit time by R-wave-gated infrared photoplethysmography: review of the literature and personal experience," *Journal of Clinical Monitoring and Computing*, vol. 18, pp. 333–42, Dec 2004.
3. G. Weltman, et al., "The continuous measurement of arterial pulse wave velocity," *Medical electronics and biological engineering*, vol. 2, pp. 145–154, 1964.
4. A. Steptoe, et al., "Pulse-Wave Velocity and Blood-Pressure Change - Calibration and Applications," *Psychophysiology*, vol. 13, pp. 488–493, 1976.
5. P. A. Obrist, et al., "Pulse transit time: Relationship to blood pressure," *Behavior Research Methods & Instrumentation*, vol. 10, pp. 623–626, 1978.
6. T. Weiss, et al., "Pulse transit time in the analysis of autonomic nervous system effects on the cardiovascular system," *Psychophysiology*, vol. 17, pp. 202–207, 1980.
7. G. V. Marie, et al., "The Relationship between Pulse Transit-Time and Blood-Pressure," *Biological Psychology*, vol. 11, pp. 298–298, 1980.
8. S. Redman and J. Dutch, "Classical-Conditioning of Arterial Pulse Transit-Time and Ecg-Initiated Transit-Time with the Cold Pressor as Unconditioned Stimulus," *Physiological Psychology*, vol. 11, pp. 87–90, 1983.
9. L. A. Geddes, et al., "Pulse Transit-Time as an Indicator of Arterial Blood-Pressure," *Psychophysiology*, vol. 18, pp. 71–74, 1981.
10. M. H. Pollak and P. A. Obrist, "Aortic-Radial Pulse Transit-Time and Ecg Q-Wave to Radial Pulse-Wave Interval as Indexes of Beat-by-Beat Blood-Pressure Change," *Psychophysiology*, vol. 20, pp. 21–28, 1983.
11. X. Ding, et al., "A Flexible Tonoarteriography-Based Body Sensor Network for the Cuffless Measurement of Arterial Blood Pressure," *in Proceedings of the 2015 IEEE International Conference on Body Sensor Networks (BSN)*, Boston, United States, 2015.